



HAL
open science

Evaluation of therapeutic strategies based on radiations and nanoparticles using a 3D cell model

Pauline Maury

► **To cite this version:**

Pauline Maury. Evaluation of therapeutic strategies based on radiations and nanoparticles using a 3D cell model. Medicinal Chemistry. Université Paris-Saclay, 2021. English. NNT : 2021UPASF016 . tel-04527809

HAL Id: tel-04527809

<https://theses.hal.science/tel-04527809>

Submitted on 31 Mar 2024

HAL is a multi-disciplinary open access archive for the deposit and dissemination of scientific research documents, whether they are published or not. The documents may come from teaching and research institutions in France or abroad, or from public or private research centers.

L'archive ouverte pluridisciplinaire **HAL**, est destinée au dépôt et à la diffusion de documents scientifiques de niveau recherche, publiés ou non, émanant des établissements d'enseignement et de recherche français ou étrangers, des laboratoires publics ou privés.

Evaluation of therapeutic strategies based on radiations and nanoparticles using a 3D cell model

Thèse de doctorat de l'université Paris-Saclay

École doctorale n° 571 Sciences chimiques : molécules, matériaux, instrumentation et biosystèmes (2MIB)

Spécialité de doctorat: Chimie

Unité de recherche : Université Paris-Saclay, Institut des Sciences Moléculaires d'Orsay, 91405, Orsay, France

Référent : Faculté des Sciences d'Orsay

Thèse présentée et soutenue à Paris-Saclay,
le 30/03/2021, par
Pauline MAURY

Composition du Jury

M. Eric DEUTSCH

Professeur des universités – Praticien hospitalier, HDR

Institut Gustave Roussy,

Université Paris Saclay, Villejuif, France

Président

Mme Marie-Anne HERVE DU PENHOAT

Maître de conférences, HDR

Institut de Minéralogie de Physique des Matériaux et cosmo chimie,

Sorbonne Université, Paris, France

Rapporteur & Examinatrice

Mme Charlotte RIVIERE

Maître de conférences, HDR

Institut Lumière Matière,

Université Claude Bernard, Lyon, France

Rapporteur & Examinatrice

M. Ryoichi HIRAYAMA

Chargé de recherche,

National Institute for Quantum and Radiological Science and
Technology,

National Institute of Radiological Sciences, Chiba, Japan

Examineur

Mme Sandrine LACOMBE

Professeur des universités, HDR

Institut des Sciences Moléculaires d'Orsay,

Université Paris Saclay, Orsay, France

Directrice de thèse

Mme Erika PORCEL

Maître de conférences,

Institut des Sciences Moléculaires d'Orsay,

Université Paris Saclay, Orsay, France

Co-encadrante de thèse

ACKNOWLEDGEMENTS

Alors que je m'apprête à quitter le milieu étudiant pour basculer dans le monde des adultes, j'ai d'abord une pensée pour tous les professeurs qui m'ont guidée, conseillée et permis d'arriver aujourd'hui jusqu'au doctorat. De l'école Beauregard au lycée Jean Vigo de Millau, de l'université de Toulouse à celle d'Orsay, l'enseignement que j'ai reçu et le soutien qu'ils m'ont donné m'ont poussé à continuer toujours d'étudier encore un peu.

La thèse aura été une formidable aventure et je voudrais tout d'abord remercier les membres de mon jury d'avoir accepté de participer à l'aboutissement de ce travail. Un grand merci à Marie-Anne Hervé du Penhoat et Charlotte Rivière pour le temps que vous avez consacré à la lecture de mon manuscrit et pour les échanges constructifs que nous avons eus autour de celui-ci. Thanks to Ryoichi Hirayama for sharing with me his expertise and participating in this important moment even it was late in Chiba. My travels in Japan and the experiences that we led together will stay unforgettable. Enfin, merci à Eric Deutsch d'avoir accepté de présider mon jury de thèse et de me permettre à présent de rejoindre l'Institut Gustave Roussy pour écrire la suite de mon aventure professionnelle.

Je voudrais ensuite remercier ma directrice de thèse, Sandrine Lacombe, pour m'avoir permis de travailler durant ces trois années sur cette thématique passionnante. Sandrine, je te remercie de m'avoir inclus dans de nombreux projets de recherche stimulants et d'avoir partagé avec moi ton enthousiasme pour la recherche et ton goût du challenge. Merci de m'avoir ouvert à des horizons inconnus en permettant à la petite aveyronnaise d'aller manipuler à l'autre bout du monde et de découvrir le Japon. Merci aussi pour la liberté que tu m'as accordée pour mener à bien ces travaux et pour la confiance que tu m'as témoignée.

Un immense merci à Erika Porcel, mon encadrante. Notre rencontre à Orsay il y a 6 ans aura pour moi été déterminante. D'abord en stage, puis en thèse, c'est toi qui m'a permis de découvrir le monde de la recherche. Merci pour ton soutien, ta présence quotidienne et pour tout ce que tu m'as apporté. Nous avons vécu ensemble des moments forts que je n'oublierai jamais. Je garderai en mémoire toutes ces nuits de manips, en France ou au Japon, et cette atmosphère si particulière, entre adrénaline et fatigue, que j'ai tellement appréciée. Je suis heureuse d'avoir appris à tes côtés et d'avoir partagé avec toi des moments complices et parfois insolites.

Une pensée pour Charles qui prend le relai. Merci d'avoir veillé au bon déroulé de cette thèse en comodal et pour l'aide précieuse que tu m'as apportée dans la dernière ligne droite. Je te souhaite de te plaire ici autant que je me suis plu, et je suis sûre que tout se passera bien. Je sais que tu seras bien entouré comme je l'ai été et je voudrais à ce propos remercier Charlotte Robert qui a eu aussi dans cette thèse une place cruciale.

Charlotte, j'ai toujours pu compter sur toi, professionnellement, personnellement aussi, et du fond du cœur je te remercie pour ton soutien sans faille, à chaque étape importante.

J'ai également une pensée très reconnaissante pour nos collaborateurs à Polytechnique (Marie-Claire Schanne Klein, Pierre Mahou et Isabelle Lamarre) ainsi que Michele Mondini à l'IGR qui ont partagé avec moi leur savoir-faire et qui m'ont épaulé avec beaucoup de bienveillance. J'ai eu beaucoup de chance de vous rencontrer et je vous remercie d'avoir également été présents dans les difficultés, notamment lorsque nous n'avions plus de L2.

Un grand merci aussi à François Lux pour ta gentillesse et pour l'intérêt que tu as porté à mes travaux, j'ai vraiment apprécié les échanges que nous avons eus au cours de ces différents projets et j'espère que nous serons amenés à nous recroiser ici ou là.

Enfin, merci à Gérard Baldacchino d'avoir partagé avec moi (avec bonne humeur) un peu de ton expertise sur la chimie sous rayonnement.

Durant les trois années passées, j'ai eu la chance d'évoluer dans un environnement bienveillant où j'ai pu trouver ma place et me sentir bien. Je voudrai pour cela remercier Bernard Bourguignon et Thomas Pino, directeurs de l'ISMO de m'avoir permis de réaliser ma thèse dans ce laboratoire auquel je resterai très attachée. Mais je voudrais aussi et surtout prendre le temps de remercier du fond du cœur, toutes les personnes qui par leur petits mots, sourire et plaisanteries ont participé à rendre mon quotidien heureux.

Bien évidemment, cela commence par un merci très fort à Michel, Satchin et Gilles. Je voulais juste vous dire que j'ai vraiment adoré tous les moments passés avec vous ; c'était vraiment fun et vous me manquez énormément. Un grand merci également à Sandrine Lévêque-Fort car pendant ces 3 ans tu n'étais jamais très loin, ce que j'ai beaucoup apprécié. Dans la difficulté (expérimentale ou sportive), tu m'as donné plein de bons conseils et prêté une oreille attentive.

Je voudrai également remercier les collègues avec lesquels j'ai travaillé. Un merci respectueux à Ruxandra Gref. La collaboration que nous avons eue m'a beaucoup apportée, et je te remercie pour ce que tu m'as appris sur les MOFs. Merci aussi à Xue Li pour ta gentillesse et tes conseils.

Un clin d'œil aux AP, Christophe, Thierry, Farah bien sûr pour tous les petits services qu'on s'est rendus et puis surtout Ludivine, Marie Poppins de la bio et tai chi girl accomplie.

Une pensée également pour Sylvie, notre secrétaire de compétition qui a toujours fait son maximum pour nous aider notamment dans les moments de stress à l'autre bout du monde.

Un merci à Madhan qui, pendant 3 ans, a rythmé mes arrivées au labo avec un « Salut Pauline » chaleureux qui lançait le top départ de la journée.

Je voudrai aussi exprimer toute ma gratitude à Céline Dablemont qui m'a permis d'enseigner la thermodynamique dans les meilleures conditions possibles et qui m'a épaulé dans ces premières expériences de monitorat avec beaucoup de sollicitude.

Enfin, et ce n'est pas des moindres, un clin d'œil complice à la team des doc' du labo. Si ces trois années ont été si agréables, je sais que c'est aussi parce qu'on était tous ensemble au 520 et qu'on aura bien rigolé. D'abord, un grand merci à ma team diabète : Bibiche et Jojo qui entre deux cabines d'essayage ou 3 cuillères de gâteaux sont toujours des acolytes au top. Hâte de retrouver tout ça avec vous bientôt ! Merci aussi au reste de la bande : Ozan, Oliver, Olivia, Joffrey, Delphine, Adrien, JB, Xiaomin et tous les autres pour les bonnes soirées qu'on a partagées. Enfin une pensée particulière pour mon Pierrot. Merci pour les fois où tu as été là. Tout n'aura pas été simple, tout n'aura pas heureux mais je sais que les moments partagés étaient forts et que nous garderons pour toujours des « secondes de souvenirs dans le crâne » : une Tour Eiffel qui brille, des trottinettes dézinguées et beaucoup de pizzas, toujours trop salées.

Ces remerciements ne seraient pas tout à fait complets sans une pensée sincère pour Cătălin, sans qui je n'en serai sans doute pas là. Merci pour tout ce que tu m'as donné et pour le bout de chemin que nous avons partagé ensemble.

L'aboutissement de ce travail de thèse est aussi l'occasion pour la première fois de remercier ma famille, même si c'est un peu impudique. Je voudrais simplement vous dire que vous êtes ce que j'ai de plus précieux et que vous serez toujours avec moi, dans tout ce que je fais. Je sais au fond de moi que le pays natal a des griffes et que la maison familiale restera toujours mon refuge et ma soupape de décompression. Je voudrais que vous sachiez qu'à chaque fois que je ne sais pas trop où je vais, je regarde d'où je viens et je voudrais vous dire qu'après ça, ça va toujours beaucoup mieux. Maman, merci pour ton pragmatisme lucide et papa, merci pour ton optimisme confiant. Ensemble, vous me donnez l'équilibre et la stabilité dont j'ai tant besoin. Merci de me soutenir toujours, dans chacun de mes choix, même lorsqu'ils sont difficiles ou pas forcément logiques.

Merci aussi au sang de la veine, mes trois frères, parce qu'avec vous à mes côtés, il me semblerait souvent pouvoir tout affronter. Une pensée enfin pour mes belles sœurs adorées, en particulier Alice, très présente dans cette aventure ; un confinement et une rédaction de thèse auront contribué à rendre le lien indéfectible.

Merci également à mes oncles et tantes pour leurs petits sms d'encouragement et de soutien à chaque étape-clé. Je ne peux, dans ce moment si important pour moi, m'empêcher d'avoir enfin une pensée émue pour mes grands-parents si aimants et si présents, qui ont contribué à nous transmettre le goût des plaisirs simples et le sentiment profond de savoir d'où l'on vient.

Enfin, un dernier mot pour mes amis, en particulier pour mes copines d'enfance : Anaïs, Mathilde, Sophie et Julie qui suivent depuis tant d'années mon devenir personnel et professionnel. Je sais qu'on peut faire beaucoup de choses par amitié : renoncer au Nutella qui tue les grands singes, danser sur Maitre Gims, partir à l'aventure, faire les portes ouvertes des labos de recherche et mille autres choses encore. Dans tous les cas, je voudrais vous dire merci car tout cela compte pour moi !

Un grand merci aussi à ma bande des beaux gosses : Damien, Natha, Flavien, Quentin et Christian pour les moments de franche rigolade que nous partageons ensemble.

Enfin, je voudrai remercier Laëtitia, Mery et surtout Isabelle qui sont les meilleurs exemples prouvant que des collègues de travail peuvent également devenir des amitiés sincères. Isabelle, merci pour ton précieux soutien et à très vite à l'IGR !

DEDICATION

A ma maman, qui croit si fort en la science,

A sa force et son courage,

TABLE OF CONTENT

DEDICATION	V
TABLE OF CONTENT	VII
LIST OF TABLES	XI
LIST OF FIGURES	XIII
ACRONYMS & ABBREVIATIONS	XVII
PREFACE	VIII
CHAPTER 1. INTRODUCTION.....	1
1. MOTIVATION	3
2. OBJECTIVES	4
3. STATE-OF-THE-ART.....	5
3.1. <i>Processes involved in the NPs' activation</i>	5
3.1.1. Physical stage	5
3.1.2. Chemical stage	13
3.1.3. Biological stage.....	14
3.1.4. Summary	16
3.2. <i>Studies on the effects of NPs combined with radiations</i>	17
3.2.1. <i>In vitro</i> experiments	17
3.2.2. <i>In vivo</i> experiments	18
3.2.3. Clinical trials	19
3.2.4. Summary	19
3.3. <i>Limitation of the 2D in vitro and in vivo models – Role of ECM on NPs and radiation effects</i>	20
3.3.1. 2D <i>in vitro</i> models	20
3.3.2. <i>In vivo</i> models.....	20
3.3.3. Summary: Towards a 3D model to fill the gap between 2D <i>in vitro</i> and <i>in vivo</i> models	21
3.4. <i>Overview of the 3D preclinical models</i>	23
3.4.1. Spheroids.....	24
3.4.2. Organoids	24
3.4.3. Organs-on-chips	25
3.4.4. Three-Dimensional Bioprinting	25
3.4.5. Scaffolds and hydrogels.....	25
3.4.6. Summary	26
3.5. <i>Summary of the state-of-the-art</i>	30
CHAPTER 2. A 3D COLLAGEN-BASED TISSUE-LIKE MODEL TO EVALUATE THERAPEUTIC STRATEGIES	31
1. INTRODUCTION	33
2. ABSTRACT.....	34
3. CORPUS	35
3.1. <i>Introduction</i>	35
3.2. <i>Material and Methods</i>	36
3.2.1. Sample preparation	36
3.2.2. Microscopy methods	37
3.2.3. Cell activity in 3D-CCM	38
3.2.4. Oxygen tunability in 3D-CCM	39
3.2.5. Nanoagent monitoring in 3D-CCM	39
3.2.6. Cell response to radiation treatment in 3D-CCM	40
3.3. <i>Results and discussion</i>	41

3.3.1.	Structural characterization	41
3.3.2.	Cell activity	44
3.3.3.	Oxygen control	45
3.3.4.	Evaluation of drugs/nanoagents uptake in living cells	46
3.3.5.	Quantification of radiation effect on cell survival	47
3.4.	<i>Conclusion</i>	49
4.	ACKNOWLEDGEMENTS	50
5.	SUPPLEMENTARY MATERIALS	50
5.1.	<i>Segmentation and analysis of nuclei</i>	50
5.2.	<i>Uptake calculation</i>	52
5.3.	<i>Clonogenic assay</i>	52
CHAPTER 3. EVALUATION OF TREATMENT COMBINING AGuIX AND RADIOTHERAPY		55
1.	INTRODUCTION	57
2.	ABSTRACT.....	58
3.	CORPUS	58
3.1.	<i>Introduction</i>	58
3.2.	<i>Materials and methods</i>	59
3.2.1.	Workflow of the present study	59
3.2.2.	Nanoparticle quantification in the patients	60
3.2.3.	Preparation and characterization of 3D-CCMs.....	62
3.2.4.	Irradiation protocols of the 3D-CCMs.....	62
3.2.5.	Clonogenic assay	63
3.3.	<i>Results</i>	64
3.3.1.	Calibration curve of T_1 as a function of AGuIX [®] concentration.....	64
3.3.2.	Determination of AGuIX [®] concentrations used in clinic	64
3.3.3.	Preparation of AGuIX [®] loaded 3D HeLa cells models.....	68
3.3.4.	Evaluation of the AGuIX [®] effect on the radiotoxicity.....	69
3.4.	<i>Discussion</i>	71
3.5.	<i>Conclusion</i>	72
CHAPTER 4. EVALUATION OF GEM-LOADED NANOMOFs COMBINED WITH HADRONTHERAPY		73
1.	INTRODUCTION	75
2.	CORPUS	76
2.1.	<i>Introduction</i>	76
2.2.	<i>Materials</i>	77
2.2.1.	NanoMOFs Synthesis and Gemcitabin incorporation.....	77
2.2.2.	Cell cultures.....	78
2.3.	<i>Methods</i>	78
2.3.1.	Characterization of the nanoMOFs toxicity.....	78
2.3.2.	Characterization of the nanoMOFs localization by fluorescence microscopy.....	79
2.3.3.	Quantification of the nanoMOFs in the samples.....	79
2.3.4.	Irradiation experiments.....	80
2.4.	<i>Results</i>	82
2.4.1.	Toxicity of nanoagents	83
2.4.2.	Localization of nanoMOFs	83
2.4.3.	Quantification of nanoMOFs	84
2.4.4.	Impact of nanoMOFs, Gemcitabin and Gem-loaded nanoMOFs on radiation effects: comparison of normoxic and hypoxic conditions (in 2D cell cultures)	85
2.4.5.	Impact of nanoMOFs, Gemcitabin and Gem-loaded nanoMOFs on radiation effects: impact of the matrix (3D cell cultures)	89
2.5.	<i>Discussion</i>	91
2.5.1.	Molecular processes induced by irradiation	91

2.5.2. Mechanisms induced in presence of Gemcitabin	92
2.6. <i>Conclusions</i>	94
3. SUPPLEMENTARY DATA	95
3.1. <i>Dependance of the LET</i>	96
3.2. <i>Summary of the radiobiological values</i>	96
CHAPTER 5. CONCLUSIONS & PERSPECTIVES	98
1. GENERAL CONCLUSIONS	100
2. PERSPECTIVES	101
LIST OF REFERENCES.....	102
SUPPLEMENTARY SECTION.....	121
1. SUPPLEMENTARY INFORMATIONS	121
1.1. <i>Liquid overlay & Low adhesion plates</i>	121
1.2. <i>Hanging drop method</i>	121
1.3. <i>Agitation-based approaches</i>	122
1.4. <i>Micro-/nano patterned surfaces</i>	122
2. SUPPLEMENTARY RESULTS.....	123
3. PUBLISHED PAPERS	123

LIST OF TABLES

TABLE 1 – ADVANTAGES AND DISADVANTAGES OF THE PRECLINICAL MODELS	29
TABLE 2. QUANTIFICATION OF AGUIX [®] DETERMINED BY ICP-MS.....	47
TABLE 3. CALCULATED RADIOBIOLOGICAL COEFFICIENTS.....	48
TABLE 4. MEAN AGUIX [®] CONCENTRATION IN PATIENTS’ GTV CORRECTED OF THE BASELINES. THE VALUES WERE DETERMINED FROM MRI 2 AND 3 (PERFORMED DURING EBT, AFTER NP INJECTION) ACCORDING TO THE TWO DIFFERENT METHODS. RELATIVE DIFFERENCE IS REPORTED (COLUMN 4).....	67
TABLE 5. MEAN AGUIX [®] CONCENTRATION IN PATIENTS’ BLADDER CORRECTED OF THE BASELINES. THE VALUES WERE DETERMINED FROM MRI 2 AND 3 (PERFORMED DURING EBT, AFTER NP INJECTION) ACCORDING TO THE TWO DIFFERENT METHODS. RELATIVE DIFFERENCE IS REPORTED (COLUMN 4)	67
TABLE 6. COMPARISON OF THE SURVIVAL FRACTIONS OBTAINED IN PRESENCE OF GEM FREE OR 5% GEM LOADED NANOMOFs.	83
TABLE 7. RADIOBIOLOGICAL VALUES EXTRACTED FROM THE CELL SURVIVAL CURVES FOR THE CONTROL (C) AND GEM LOADED NANOMOFs (MG) DEPENDING ON THE EXPERIMENTAL CONDITIONS (BEAM, CELL CYTOARCHITECTURE, OXYGENATION CONDITIONS). THE VALUES IN BOLD ARE THOSE FOR THE DIFFERENCE BETWEEN THE CONTROL AND MG ARE SIGNIFICANT TAKING INTO ACCOUNT THE STANDARD DEVIATION OF EACH OF THE PARAMETERS	96

LIST OF FIGURES

FIGURE 1.1 - PROCESSES INVOLVED IN THE INTERACTION OF PHOTONS WITH MATTER AS A FUNCTION OF THE INCIDENT ENERGY AND THE ATOMIC NUMBER OF THE TARGET.....	6
FIGURE 1.2 - PHOTOELECTRIC EFFECT	7
FIGURE 1.3 - COMPTON EFFECT.....	7
FIGURE 1.4 - PHYSICAL INTERACTION PROCESSES OF NP WITH INCIDENT IONS.....	8
FIGURE 1.5 – ACTIVATION OF NP BY SECONDARY ELECTRONS.....	9
FIGURE 1.6 – DE-EXCITATION PROCESSES	10
FIGURE 1.7 - SIMULATION OF THE LOCAL DOSE DEPOSITION AFTER IRRADIATION OF THE MEDIUM CONTAINING NP EXTRACTED FROM LUX ET AL., 2015 ACCORDING TO THE METHOD DEVELOPED BY MCMAHON ET AL., 2011.....	11
FIGURE 1.8 - CHARGE TRANSFER ON A POSITIVELY CHARGED NP	12
FIGURE 1.9 - CHEMICAL STEP LEADING TO THE PRODUCTION OF RADICALS.....	13
FIGURE 1.10 - BIOLOGICAL DAMAGE INDUCED IN THE CELL CYTOPLASM, IN THE VICINITY OF THE NP	15
FIGURE 1.11 - CASCADE OF PROCESSES TAKING PLACE FROM THE RADIATION INTERACTION TO THE IMPACT ON THE BIOLOGICAL SYSTEM, IN THE PRESENCE OF NP. ADAPTED FROM BALDACCHINO ET AL., 2019 AND TUBIANA ET AL., 1986.....	17
FIGURE 1.12 - PIPELINE OF A TREATMENT EVALUATION: FROM BENCH TO BEDSIDE.....	17
FIGURE 1.13 - EXPOSURE TO NPs OF A 2D CELL CULTURE AND A 3D MODEL.....	22
FIGURE 1.14 – SCHEME REPRESENTING THE CURRENT PRECLINICAL MODELS: 2D CELL CULTURES, 3D CELL MODELS AND IN VIVO MODELS.....	23
FIGURE 2.1 - SET OF SPECIFICATIONS FOR THE 3D CELL MODEL OPTIMIZED FOR THE PRESENT STUDIES	33
FIGURE 2.2 – GRAPHICAL ABSTRACT: 3D CELL COLLAGEN-BASED MODEL WITH TUNABLE ENVIRONMENT CONDITIONS (OXYGEN CONCENTRATION, NANODRUG EXPOSURE, RADIATIONS).....	34
FIGURE 2.3 - (A) THICKNESS OF 3D-CCMs COMPOSED OF HeLa CELLS (N=7), (B) COMPARISON OF THE COEFFICIENT OF VARIATION (CV) OBTAINED FROM THE 3D-CCM THICKNESS MEASUREMENTS (BLUE DASHED LINE) WITH THE CVs REPORTED IN THE LITERATURE FOR SPHEROIDS OF UNIFORM SIZES OBTAINED BY DIFFERENT METHODS: PELLET CULTURE (IN PINK), MICROWELL ARRAYS (IN GREEN), MICROFLUIDIC DEVICES (IN RED), HANGING DROP METHOD (IN BLACK) OR OTHER (IN YELLOW). THE USE OF VARIATION BARS INSTEAD OF SQUARE POINTS ILLUSTRATES THE DEPENDENCY OF THE CV TO DIFFERENT PARAMETERS (CELL SEEDING DENSITY, SIZE OF THE WELL...)	42
FIGURE 2.4 - HeLa CELLS MORPHOLOGY IN (A) 2D CULTURE AND (B) 3D CELL COLLAGEN-BASED MODEL. NUCLEI AND PLASMA MEMBRANE ARE STAINED IN BLUE AND GREEN RESPECTIVELY. IMAGES (A) AND (B) WERE OBTAINED BY CONFOCAL MICROSCOPY (RESPECTIVE FOV OF 82 μM X 84 μM AND 123 μM X 83 μM AND RESPECTIVE PIXEL SIZE SIDE OF 0.186 μM OR 0.312 μM).	42
FIGURE 2.5 - (A) 2PEF/SHG IMAGES OF HeLa NUCLEI (IN BLUE) EMBEDDED IN THE FIBRILLARY COLLAGEN MATRIX (IN GREEN) (FOV OF 350 μM X 350 μM, PIXEL SIZE OF 0.192 μM SIDE), (B) NUMBER OF NUCLEI AS A FUNCTION OF DEPTH FOR HeLa IN 3D-CCMs (N=3, SAMPLE 1 IN RED, SAMPLE 2 IN BLUE, SAMPLE 3 IN GREEN), (C) NUMBER OF NUCLEI AS A FUNCTION OF DEPTH FOR FIBROBLASTS IN 3D-CCMs (N=3, SAMPLE 1 IN GREY, SAMPLE 2 IN PURPLE, SAMPLE 3 IN YELLOW)	43
FIGURE 2.6 - MINIMUM DISTANCE BETWEEN TWO NUCLEI AS A FUNCTION OF DEPTH FOR 3D-CCMs COMPOSED OF (A) HeLa CELLS (B) FIBROBLASTS (N=3).....	44
FIGURE 2.7 - (A) CELL VIABILITY IN 3D-CCMs MEASURED 28 H AFTER MODEL CREATION. (B) EVOLUTION OF THE MITOCHONDRIAL ACTIVITY IN 3D-CCMs (IN GREEN) QUANTIFIED BY MTT ASSAY AS FUNCTION OF THE TIME IN THE SAMPLE. THE NEGATIVE CONTROL IS SHOWN (IN RED)	45
FIGURE 2.8 - PO ₂ MEASURED IN 3D AND 2D SAMPLES (RED BOLD BAR) (N=10). IT IS COMPARED TO PO ₂ REPORTED IN THE LITERATURE (McKEOWN, 2014) FOR TUMORAL (SQUARE) AND HEALTHY TISSUES (CIRCLE), SUCH AS PANCREAS (BLUE), CERVIX (GREEN), HEAD & NECK (BLACK), PROSTATE (ORANGE) AND BREAST (PINK). FOR THE VALUES REPORTED FROM LITERATURE, AN ERROR BAR WAS REPRESENTED WHEN SEVERAL STUDIES WERE CONSIDERED.	46

FIGURE 2.9 - CONFOCAL MICROSCOPY IMAGES OF HELa CELLS EXPOSED TO AGUIX [®] IN (A) A 2D CULTURE (FOV OF 110 μM X 101 μM, PIXEL SIZE OF 0.229 μM SIDE) AND (B,C) 3D-CCMs (FOV OF 140 μM X 140 μM AND 41 μM X 41μM, PIXEL SIZE OF 0.273 μM AND 0.080 μM SIDE). EACH IMAGE RESULTS FROM SUPERIMPOSITION OF THE TRANSMISSION AND FLUORESCENCE IMAGES. NUCLEI AND NPs ARE LABELLED IN BLUE AND RED RESPECTIVELY. THE BLACK HOLES CORRESPOND TO CELLS (ABSENCE OF COLLAGEN).	47
FIGURE 2.10 - SURVIVAL FRACTIONS OF HELa CELLS IRRADIATED IN 2D CULTURE (DASHED CURVE/EMPTY TRIANGLES) AND IN 3D-CCMs (SOLID CURVE/SOLID TRIANGLES). THE INFLUENCE OF AGUIX [®] ON RADIOTOXICITY WAS INVESTIGATED USING 3D-CCMs (RED CURVE). THE THEORETICAL UNCERTAINTIES (AREA) WERE DETERMINED ACCORDING TO THE STANDARD DEVIATIONS OF THE α AND β PARAMETERS. F-STATISTICAL TESTS, BASED ON THE MAXIMUM LIKELIHOOD METHOD (SEE DETAILS IN SUPPLEMENTARY MATERIALS, 7.3), WERE PERFORMED TO COMPARE 2D AND 3D MODELS, AND, MODELS WITH OR WITHOUT AGUIX [®] . THE DIFFERENCES WERE SIGNIFICANT WITH A P VALUE OF 1.099 E-07 (P< 0.05) AND 0.03 (P< 0.05)	48
FIGURE 2.11 - VARYING THE THRESHOLD WITH IMAGING DEPTH. GREEN, ORANGE AND BLUE CURVES RESPECTIVELY INDICATE THE MEDIAN OF THE IMAGE AT EACH STACK, THE SUM OF THE MEDIAN AND THE STANDARD DEVIATION, AND THE ADAPTIVE THRESHOLD. IN THIS EXAMPLE, THE THRESHOLD WAS 1.0*STD_DEV + 535.	50
FIGURE 2.12 - EXAMPLE OF THE CLUSTERING OF INDIVIDUAL CELLS IN 2D: (A) CELL IMAGE AT A FIXED STACK, (B) RESULTING CLUSTERING IMAGE WHERE EACH COLOR INDICATES A DIFFERENT CELL.....	51
FIGURE 2.13 - GLOBAL PYTHON CODE WORKFLOW. THE ADAPTIVE THRESHOLD IS APPLIED TO GENERATE A 3D BINARY IMAGE. THIS IMAGE IS CLEANED VIA AN OPENING, AND PARAMETERS ARE EXTRACTED FOR INDIVIDUAL REGIONS. AFTER A FINAL FILTERING OF OUTLIERS, PLOTS AND HISTOGRAMS ARE GENERATED.	51
FIGURE 2.14 – SURVIVAL CURVES AND RADIOBIOLOGICAL COEFFICIENTS EXTRACTED FROM THE R SOFTWARE	53
FIGURE 3.1 - CONTRIBUTION OF THE STUDY IN THE FRAMEWORK OF NANOENHANCED IMAGE-GUIDED RT	57
FIGURE 3.2 - OVERVIEW OF THE NANOCOL PROTOCOL	59
FIGURE 3.3 - WORKFLOW OF THE PRESENT STUDY: FROM THE PATIENT MRI TO THE AGUIX [®] EFFECT	60
FIGURE 3.4 - (A) EXPERIMENTAL SETUPS FOR EBT (UPPER IMAGE) AND HDR (LOWER IMAGE) SHOWING THE IRRADIATION OF THE 3D-CCM BY THESE TWO MODALITIES (SAMPLE SURROUNDED BY RED DOTTED LINE). THE SAMPLE WAS PLACED IN A BOLUS AND CENTERED IN THE PHANTOM USING POSITIONING LASERS (RED DOTTED LINES). DOSE DISTRIBUTIONS AND DOSE VOLUME HISTOGRAMS (DVH) FOR (B) EBT AND (C) HDR. IRRADIATION OF THE 3D-CCM WAS PERFORMED DELIVERING AT LEAST 95% OF THE PRESCRIBED DOSE TO 99% OF THE SAMPLE.....	63
FIGURE 3.5 - CALIBRATION CURVE OF T ₁ MEASURED WITH THE VFA SEQUENCE AS A FUNCTION OF THE AGUIX [®] CONCENTRATION IN THE PHANTOM SYRINGES. EXPERIMENTAL POINTS ARE REPRESENTED IN BLACK AND THE FIT CORRESPONDS TO THE RED DOTTED LINE.....	64
FIGURE 3.6 - MR IMAGES (T2-PROPELLER) OF THE GTV (RED LINE) OF PATIENT 4 ACQUIRED (A) WITHOUT INJECTION OF AGUIX [®] (AT D ₀ OF THE TREATMENT-P4/T1) AND (B) AFTER 30 MG/KG AGUIX [®] INJECTION (AT D ₀ OF THE RADIOTHERAPY-P4/T2) ...	65
FIGURE 3.7 - EVOLUTION OF THE TUMOR VOLUME (REDUCTIONS OF 53%, 37%, 75% AND 91% BETWEEN MRI 1 AND 4 FOR THE PATIENTS 1, 2, 3 AND 4 RESPECTIVELY) (A) AND T ₁ VALUE IN HEALTHY FAT TISSUES (B) , IN THE BLADDER (C) AND IN THE GTV (D) , AT EACH TIME POINT, FOR THE 4 PATIENTS INCLUDED IN THE CLINICAL TRIAL (BLUE, ORANGE, GREEN AND RED). PATIENTS 1, 2, 3 HAVE RECEIVED AN INJECTION OF 30 MG/KG WHILE A DOSE OF 50 MG/KG WAS DELIVERED TO PATIENT 4.	65
FIGURE 3.8 - (A) GAUSSIAN DISTRIBUTIONS OF T ₁ VALUES MEASURED IN THE GTV FOR THE PATIENT 2 AT THE TIME POINTS MR 2 AND MR 3. (B) MAXIMUM AGUIX [®] CONCENTRATIONS IN PATIENT'S GTV	68
FIGURE 3.9 - (A) CONFOCAL IMAGES OF 3D-CCMs TREATED WITH 0.5 MMOL/L AGUIX [®] FOR 24 H. CELLS ARE IDENTIFIED AS BLACK HOLES IN THE COLLAGEN MATRIX, THEIR NUCLEI ARE LABELLED IN BLUE AND AGUIX [®] IN RED. (B) ICP-MS DOSAGES OF Gd IN THE SAMPLES (IN GREEN) OR IN CELLS EXTRACTED FROM THE SAMPLES (IN BLUE) FOR THE TWO INCUBATION TIMES (4H OR 24H) .	69
FIGURE 3.10 - SURVIVAL CURVES OBTAINED AFTER IRRADIATION OF HELa CELLS IN 3D-CCM TREATED BY (A) EBT (B) HDR WITH AND WITHOUT NPs. RESULTS OF THE F-TEST WERE F=3.003 (P VALUE OF 0.08) FOR MV+4H NPs, F=6.42 (P VALUE OF 0.007) FOR MV+24H-NPs AND F=9.16 (P VALUE OF FOR 0.001) kV+24H NPs. (C) RADIOBIOLOGICAL PARAMETERS EXTRACTED FROM THE LQ MODEL FIT AND DEF VALUE. (D) EVALUATION OF THE COMBINED TREATMENTS (SER VALUES) FOR THE THREE IRRADIATION CONDITIONS.	70

FIGURE 4.1 – **(A)** LOCALISATION OF 17 $\mu\text{G}/\text{ML}$ NANOMOFs INCUBATED A- IN MONOLAYER CULTURES FOR 6H OR B-C-D- IN 3D-CCMs FOR 18H. NANOMOFs ARE LABELLED IN RED, COLLAGEN IS GREEN AND NUCLEI ARE BLUE. B- AND C- IMAGES REPRESENT THE SAME AREA IN THE SAMPLE : B IS THE MERGED IMAGE (SHG+2PEF) WHILE C REPRESENTS THE NANOPARTICLE CHANNEL IN 2PEF EXCLUSIVELY AN ACQUISITION IN THE Z-DEPTH OF THE AREA FRAMED IN ORANGE WAS PERFORMED. IMAGES EXTRACTED FROM THE STACK ARE GIVEN IN D-. SHG IMAGES WERE CAPTURED WITH A PIXEL SIZE OF 0.192 μM , AN ACQUISITION FREQUENCY OF 400 HZ AND A Z-STEP OF 1 μM . **(B)** EVALUATION OF THE CYTOTOXICITY OF NANOMOFs LOADED WITH GEMCITABIN BASED ON THE MITOCHONDRIAL ACTIVITY MEASUREMENT OF CELLS CONTAINED IN 3D-CCM (IN BLACK) COMPARED TO POSITIVE (GREEN) AND NEGATIVE (RED) CONTROLS. **(C)** QUANTIFICATION OF NANOMOFs AMOUNT IN 3D-CCM AND CELLS AFTER AN INCUBATION OF THE SAMPLES WITH 17 $\mu\text{G}/\text{ML}$ NANOMOFs FOR 18H..... 85

FIGURE 4.2 – **(A)** SURVIVAL CURVES OBTAINED WITH CARBON ION IRRADIATION IN NORMOXIC (LEFT) AND HYPOXIC (RIGHT) CONDITIONS. THE CONTROL IS LABELLED IN PINK AND THE RESPONSE OF THE CELLS INCUBATED WITH NANOMOFs, FREE GEMCITABIN OR GEMCITABIN-LOADED NANOMOFs IS REPRESENTED IN BLUE, RED OR BLACK RESPECTIVELY. THE P VALUE BETWEEN THE CONTROL AND THE SF CURVE WITH GEMCITABIN IS < 0.001 (***) AND THE P VALUE BETWEEN THE CONTROL AND THE SF CURVE WITH GEM-LOADED NANOMOFs IS < 0.1 (.). **(B)** ANALYSIS PARAMETERS EXTRACTED FROM THE SURVIVAL CURVES. TOP: RADIOBIOLOGICAL PARAMETERS VALUES (A IN Gy^{-1} AND B IN Gy^{-2}). BELOW: QUANTIFICATION OF THE RADIOSENSITIZING EFFECT INDUCED BY THE PRESENCE OF FREE GEMCITABIN (G) OR GEMCITABIN-LOADED NANOMOFs (MG), IN NORMOXIC (SMOOTH) AND HYPOXIC (HATCHING) CONDITIONS. SER VALUES WERE CALCULATED FOR IRRADIATION DOSES OF 2, 4 AND 6 Gy. 87

FIGURE 4.3 – **(A)** SURVIVAL CURVES OBTAINED WITH HELIUM IONS IRRADIATION IN NORMOXIC (LEFT) AND HYPOXIC (RIGHT) CONDITIONS. CONTROL IS LABELLED IN PINK AND THE RESPONSE OF THE CELLS INCUBATED WITH NANOMOFs, FREE GEM OR GEM-LOADED NANOMOFs IS BLUE, RED OR BLACK RESPECTIVELY. THE P VALUE BETWEEN THE CONTROL AND THE SF CURVE WITH GEM IS < 0.001 (***) AND THE P VALUE BETWEEN THE CONTROL AND THE SF CURVES WITH GEM-LOADED NANOMOFs IS < 0.05 (*) FOR NORMOXIC AND < 0.1 (.) FOR HYPOXIC CONDITIONS. **(B)** ANALYSIS PARAMETERS EXTRACTED FROM THE SURVIVAL CURVES. TOP: RADIOBIOLOGICAL PARAMETERS VALUES (A IN Gy^{-1} AND B IN Gy^{-2}). BELOW: QUANTIFICATION OF THE RADIOSENSITIZING EFFECT INDUCED BY THE PRESENCE OF FREE GEM OR GEM-LOADED NANOMOFs, IN NORMOXIC (SMOOTH) AND HYPOXIC (HATCHING) CONDITIONS. SER VALUES WERE CALCULATED FOR IRRADIATION DOSES OF 2, 4 AND 6 Gy AND DEF FOR A SURVIVAL FRACTION OF 10%. **(C)** ISOBOLOGRAMM ANALYSIS FOR NORMOXIC CONDITIONS AND GRAPHICAL REPRESENTATION GIVING THE VALUES OF DM. COMBINATION INDEX VALUES ARE REPORTED SHOWING ADDITIVE (CI=1.0) OR SYNERGISTIC EFFECT (CI<1.0) 89

FIGURE 4.4 - **(A)** SURVIVAL FRACTIONS OF HELA CELLS EXTRACTED FROM 3D-CCMs IRRADIATED WITH CARBON IONS (LEFT) AND HELIUM IONS (RIGHT), IN THE PRESENCE OF NANOMOFs (BLUE), FREE GEM (RED) AND GEM LOADED NANOMOFs (BLACK). P VALUES FOR GEM AND GEM LOADED NANOMOFs WERE 2E-4 AND 4E-10 FOR CARBON IONS IRRADIATION AND 1E-2 AND 2E-8 WITH HELIUM IONS IRRADIATION. **(B)** RADIOBIOLOGICAL PARAMETERS (A IN Gy^{-1} AND B IN Gy^{-2}). **(C)** QUANTIFICATION OF THE ENHANCEMENT EFFECTS (SER) OF CARBON IONS (BLACK AND DARK RED) AND HELIUM IONS (GRAY AND LIGHT RED) BEAMS INDUCED BY THE PRESENCE OF GEM (RED) OR GEM-LOADED NANOMOFs (BLACK AND GRAY). 90

FIGURE 4.5 – SURVIVAL CURVES FOR CONTROLS AND CELLS TREATED BY **(A)** CARBON IONS AND **(B)** HELIUM IONS USING MONOLAYER CULTURES UNDER NORMOXIC ($\text{pO}_2=20\%$, IN RED) AND HYPOXIC ($\text{pO}_2=0.5\%$, IN BLUE) CONDITIONS. **(C)** OER REPORTED BY SCIFONI ET AL. 92

FIGURE 4.6 – SURVIVAL CURVES FOR CONTROLS AND CELLS TREATED BY **(A)** CARBON IONS AND **(B)** HELIUM IONS USING MONOLAYER CULTURES INCUBATED WITH GEM-LOADED NANOMOFs (0.85 $\mu\text{G}/\text{ML}$ IN 17 $\mu\text{G}/\text{ML}$) UNDER NORMOXIC ($\text{pO}_2=20\%$, IN RED) AND HYPOXIC ($\text{pO}_2=0.5\%$, IN BLUE) CONDITIONS. 94

FIGURE 4.7 - SURVIVAL CURVES FOR THE CONTROLS (FROM A TO C) AND FOR CELLS INCUBATED WITH GEM-LOADED NANOMOFs (FROM D TO E) AND TREATED BY CARBON IONS (DARK PURPLE AND BLACK CURVES) AND HELIUM IONS (LIGHT PINK AND GREY CURVES). THREE EXPERIMENTAL CONDITIONS ARE PRESENTED: IRRADIATIONS OF MONOLAYER CELLS IN NORMOXIA (A-D), IRRADIATION OF MONOLAYER CELLS IN HYPOXIA (B-E) AND IRRADIATION OF 3D-CCMs (C-F) 96

ACRONYMS & ABBREVIATIONS

3D-CCMs: 3D cell collagen-based model

2PEF: 2 Photons Emission Fluorescence

2D: Two dimensional

AGuIX[®]: Activation-Guided Irradiation by X-ray, Gd-based nanoparticles

ATCC: American Type Culture Collection (non-profit organization)

Au: Gold

CDD: Complex DNA Damage

CI: Combination index

CT: Computed Tomography

CV: Coefficient of Variation

Cy5: Cyanine 5

C⁶⁺: Carbon ions

DEA: Dissociative Electron Attachment

DEF: Dose Enhancement Factor

DMEM: Dubelcco's Modified Eagle Medium

DNA: Deoxyribonucleic acid

EBT: External Beam Therapy

ECM: Extracellular matrix

EDTA: Ethylenediaminetetraacetic acid

EPR : Enhanced Permeability Retention

FBS: Foetal Bovine Serum

FOV: Field of view

Gd: Gadolinium

Gem: Gemcitabin

GEMs: Genetically engineered models

GTV: Gross Tumor Volume

Gy: Gray

He²⁺: Helium ions

HDR: High Dose Rate

LET: Linear Energy Transfer

Linac: Linear Accelerator

LMDS: Locally Multiply Damaged Site

LQ: Linear Quadratic

MCTS: Multicellular Tumor Spheroid

ML: Maximum Likelihood

nanoMOF: nanoagents of Metallic Organic Framework

MRI: Magnetic Resonance Imaging

OAR: Organ at risk

OER: Oxygen Enhancement Ratio

PDX: Patient-Derived Xenografts

PE: Plating Efficiency

PEG: Poly(ethylene glycol)

P/S: Penicillin Streptomycin

Pt: Platinum

ROS: Reactive Oxygen Species

SER: Sensitizer Enhancement Ratio

SF: Survival Fraction

SHG: Second Harmonic Generation

SOBP: Spread Out Bragg Peak

SRT: Stereotactic Radiotherapy

TPS: Treatment Planning System

UT2A: Ultra Trace Analyses Aquitaine (Pau, France)

VFA: Variable Flip Angle

VMAT : Volumetric Modulated Arc Therapy

PREFACE

PhD director : Pr. Sandrine Lacombe (Université Paris Saclay)

Co-supervisor : Dr. Erika Porcel (Université Paris Saclay)

PhD thesis : from 01/01/2018 to 31/03/2021

Context of the thesis:

My thesis was carried out at Université Paris-Saclay, CNRS, Institut des Sciences Moléculaires d'Orsay, 91405, Orsay, France.

The thesis was supported by a Grant of the French government (Ministry of Higher Education and Research) attributed by the doctoral school 2MIB (Sciences Chimiques: Molécules, Matériaux, Instrumentation et Biosystèmes). In the framework of this PhD, teaching in Thermodynamics and Thermochemistry was carried out at Polytech Paris Sud (PeiP1) and Université Paris Saclay (L1).

This thesis work was performed in the frame of the Strategic Research Initiative (IRS) funded by Université Paris Saclay 'NanoTheRad'.



My thesis resulted in :

- 3 publications

G.J. Sánchez, **P. Maury**, L. Stefancikova, O. Campion, G. Laurent, A. Chateau, F.B. Hoch, F. Boschetti, F. Denat, S. Pinel, J. Devy, E. Porcel, S. Lacombe, R. Bazzi, S. Roux, Fluorescent radiosensitizing gold nanoparticles, *Int. J. Mol. Sci.* 20 (2019). doi.org/10.3390/ijms20184618.

P. Maury, E. Porcel, S. Lacombe, G. Baldacchino, Comprendre et améliorer les effets cliniques de la hadronthérapie, *l'Actualité Chimique*, numéro spécial N° 460-461 Mars-Avril 2021, p.76-83.

P. Maury, E. Porcel, A. Mau, P. Mahou, F. Lux, O. Tillement, P. Mahou, M-C Schanne-Klein, S. Lacombe, Rapid Evaluation of Novel Therapeutic Strategies Using a 3D Collagen-Based Tissue-Like Model, *Frontiers in Bioengineering and Biotechnologies*, section Tissue Engineering and Regenerative Medicine. (2021). doi 10.3389/fbioe.2021.574035

- 2 papers in the process of submission or preparation:

P. Maury, A. Darricau, M. Shahin, C. Chargari, S. Ammari, S. Bockel, M. Mondini, A. Rouyar-Nicolas, F. Lux, O. Tillement, S. Lacombe, E. Deutsch, C. Robert, E. Porcel, Treatment of locally advanced cervical cancer using Gadolinium nanoparticles: MR quantification and in vitro insights based on the NANOCOL clinical trial, *Theranostics* (in preparation)

P. Maury, E. Porcel, R. Hirayama, X. Li, P. Mahou, M-C Schanne-Klein, R. Gref, S. Lacombe, Synergistic effect of Gemcitabin-loaded metal organic nanoparticles with hadrontherapy (in preparation)

CHAPTER 1. INTRODUCTION



Rythmes,
Robert Delaunay, 1934, Musée National d'Art Moderne, Paris

*“Je suis de ceux qui pensent que la science est d’une grande beauté.
Un scientifique dans son laboratoire est non seulement un
technicien : il est aussi un enfant placé devant des phénomènes
naturels qui l’impressionnent comme des contes de fées”*

*Marie Curie (1867-1934),
Madame Curie, Eve Curie, éd. Gallimard (1938)*

Contents

1. MOTIVATION	3
2. OBJECTIVES.....	4
3. STATE-OF-THE-ART.....	5
3.1. PROCESSES INVOLVED IN THE NPS' ACTIVATION	5
3.1.1. <i>Physical stage</i>	5
3.1.2. <i>Chemical stage</i>	13
3.1.3. <i>Biological stage</i>	14
3.1.4. <i>Summary</i>	16
3.2. STUDIES ON THE EFFECTS OF NPS COMBINED WITH RADIATIONS.....	17
3.2.1. <i>In vitro experiments</i>	17
3.2.2. <i>In vivo experiments</i>	18
3.2.3. <i>Clinical trials</i>	19
3.2.4. <i>Summary</i>	19
3.3. LIMITATION OF THE 2D <i>IN VITRO</i> AND <i>IN VIVO</i> MODELS – ROLE OF ECM ON NPS AND RADIATION EFFECTS	20
3.3.1. <i>2D in vitro models</i>	20
3.3.2. <i>In vivo models</i>	20
3.3.3. <i>Summary: Towards a 3D model to fill the gap between 2D in vitro and in vivo models</i>	21
3.4. OVERVIEW OF THE 3D PRECLINICAL MODELS	23
3.4.1. <i>Spheroids</i>	24
3.4.2. <i>Organoids</i>	24
3.4.3. <i>Organs-on-chips</i>	25
3.4.4. <i>Three-Dimensional Bioprinting</i>	25
3.4.5. <i>Scaffolds and hydrogels</i>	25
3.4.6. <i>Summary</i>	26
3.5. SUMMARY OF THE STATE-OF-THE-ART	30

1. MOTIVATION

Treatment of cancer is one of the greatest challenges of the 21st century. Responsible for 1 in 6 deaths, cancer remains the second leading cause of mortality worldwide (Bray et al., 2018). Faced with the growing number of cases, Europe has identified the fight against cancer as a public health priority (Horizon program) (European commission, n.d.). In France, 382 000 patients were diagnosed in 2018 (Defossez et al., 2019). Hopefully, the considerable improvements in understanding, detection and treatment of the disease in recent years lead to the hope of a curable treatment for the majority.

Surgery, radiation therapy and drug therapies (chemo-, hormone, immuno- or targeted therapies) are the mainstream methods to treat cancer (Kwatra et al., 2013). These standard modalities are used either alone or in combination, with the purpose to establish a personal treatment protocol as a function of the cancer characteristics (location, type, stage).

Radiation treatments (RT) are based on the use of ionizing radiations to kill cancer cells and prevent the progression and recurrence of tumors (Song et al., 2017). Currently, they occupy a major place in clinical therapies as 50% of the cancerous patients are treated with RT, which represents in France more than 190 000 people per year (Inca). RT includes internal and external radiotherapies. For internal RT, radioactive sources are directly placed in contact with the patient tumor using minimally invasive procedures such as direct infusion through a catheter (brachytherapy). On the other hand, external beam radiotherapy (EBT) is conventionally delivered by high-energy photon beams (6-25 MV), generated by linear electron accelerators, rotating around the patient.

Lack of tissue specificity remains the main disadvantage of the EBT. The radiation dose delivered to the tumor volume is limited by the irradiation of the surrounding healthy tissues, which may cause side effects due to collateral damage. Thus, the major challenge of the RT is to maximize the "therapeutic ratio", to increase the probability of tumor control while limiting the toxicity at the organs at risk (OAR). Recently, innovative modalities such as volumetric modulated arc therapy (VMAT) or stereotactic radiotherapy (SRT) have improved the radiation dose conformity. However, dose escalation remains an important clinical challenge (Detappe., 2017). Conventional RT treatments (based on photons) are also limited by the radioresistance of highly aggressive cancers. In particular, hypoxic tumors - where the oxygen concentration is lower than 2.5 mmHg - are associated with high probabilities of relapse and high risks of metastasis (Horsman and Overgaard, 2016; Thariat et al., 2018).

To improve the therapeutic index of treatments, novel strategies are needed to optimize tumor targeting and fight against radioresistance.

Nanomedicine in particular has opened up new horizons. With sizes ranging from 1 to few hundred nanometers, nano-objects accumulate preferentially in tumors exploiting the enhanced permeability retention effect (EPR). High-atomic number (Z) nanoparticles (NPs) such as gold (Au), Gadolinium (Gd) or Platinum (Pt) nanoagents have attracted much interest because of their capacity to amplify radiation damage via the production of secondary electrons and oxidative species (Kuncic and Lacombe, 2018). They are named "radio-enhancers". These NPs may also act as contrast agents, for magnetic resonance imaging (MRI) or computed tomography (CT). When the NPs cumulate the two properties, they are qualified as "theranostic agents" (Song et al., 2017). Among these theranostic agents, there is AGuIX[®] (Activation and Guidance of Irradiation by X-rays), a sub-5nm Gd-based NP developed by NH TherAguix company (Lyon, France).

Other nanomaterials are proposed as "drug delivery carriers". In this case, the nanoagents are used to transport fragile drugs to the tumor and protect them from degradation when traveling free in

the body. This transportation method also prevents concentration of the drugs in healthy tissues, thus reducing side effects (Lammers et al., 2008; Torchilin, 2012). Among these “nanocarriers”, “cage”-like particles recently drew special attention for chemoradiotherapy applications (Song et al., 2017). Recently, the group at ISMO, in collaboration with Ruxandra Gref, has shown that metal organic frameworks (nanoMOFs) loaded with Gemcitabin (Gem) are able to amplify radiation effects and also to bring the drug to the tumor. They are “multimodal agents”.

Beyond radiotherapy, improvement of advanced radiation therapies such as particle therapy, remains a challenge. Charged particles beams (mainly protons and carbon ions of several hundred MeV/amu) strongly improve the local control due to the ballistic property of ions : the radiation dose deposition at the end of the track (Bragg peak) (Durante et al., 2017). As a result, the damage induced behind the tumor is drastically reduced and healthy tissues are preserved. A second advantage of charged particle beams, carbon beams in particular, is their high biological efficacy compared to photons. These beams are used to treat radioresistant tumors for which conventional treatments are not effective (Durante et al., 2017). A major drawback of this modality is the damage induced in the tissues before the tumor. This limitation may be overcome by using multimodal nanoagents to enhance the effects at the tumor and decrease the total dose given to the patient, using radioenhancers and/or radiosensitizers.

The aim of my PhD was to evaluate two new strategies with a perspective of fast transfer from bench to bedside. The first is the combination of AGuiX[®] nanoagents associated with radiotherapy and brachytherapy, currently applied in clinic to treat locally advanced cervical cancers (LACC). The second consists in the association of newly developed nanoMOFs with medical particle beams. Monolayer (2D) cell cultures are currently used to rapidly test strategies and characterize biological mechanisms. In this case, the role of the cell microenvironment in tumors is not considered both in terms of their spatial organization and physiology (Duval et al., 2017; Lv et al., 2017). In particular, the extracellular matrix (ECM) plays a crucial role *in vivo* and the absence of ECM distorts the predictions of cell response to irradiation and nanogent exposure.

So, in this work, a 3D cell model has been optimized in terms of cell density and oxygen concentration to evaluate the two treatment strategies with a system that better reproduces tumor features than 2D cultures, while avoiding constraints of *in vivo* models.

2. OBJECTIVES

My work aimed to:

- (i) optimize an *in vitro* model with best characteristics to reproduce tumor conditions and adapted to the rapid evaluation of medical strategies;
- (ii) help improve the efficiency of a therapeutic strategy currently applied in clinic based on the association of Gd-based NPs and photonic radiation, by using the *in vitro* model to fasten the analysis and prediction of the NPs effects;
- (iii) evaluate the efficiency of the therapeutic strategy associating newly developed Gem-loaded nanoMOFs and ion radiations, by using the *in vitro* model to fasten the selection of such nanoagents for the scope of cancer therapy.

The manuscript is organized in five chapters. After this introduction focused on the motivation and objectives of my work, the state-of-the-art positioning the work is presented (chapter 1). The results of the work are presented in three chapters (chapters 2, 3 and 4) organized in articles

already published or in preparation. The chapter 2 is the copy of my first paper accepted for publication in *Frontiers in Bioengineering and Biotechnology* concerning the production and characterization of the 3D model. The chapter 3 is the paper submitted to the journal *Theranostics*, concerning the effects of AGuIX® on the chemo and radiation protocol tested in clinic to treat cervical tumors. The chapter 4 is the draft reporting the evaluation of the Gem-loaded nanoMOFs combined with particle beam exposure. These chapters contain a heading and full paper information (introduction, material and methods, results and conclusion). Final conclusions and perspectives of my work are exposed in Chapter 5.

3. STATE-OF-THE-ART

3.1. Processes involved in the NPs' activation

The processes involved in the interaction of ionizing radiations with biological matter, water in particular, are well described elsewhere (Joiner and Van der Kogel, 2016, 2009; Tubiana et al., 1986). Here, I focus on the processes induced or amplified by high-Z NPs. Note that the processes of drug delivery, which are not related to the action of radiation, are not explained in this work.

The influence of high-Z NPs on radiation induced cell killing is strongly depends on the incident radiation characteristics, including type and energy of the incident beam (W. B. Li et al., 2020). This section aims at providing prerequisites to better describe the processes occurring at the molecular and cellular scales observed in the presence of NPs. Radioenhancement effects are commonly believed to impact the three following stages: physical, chemical and biological, characterized by their timeline and their impact on the medium (Figure 1.1 - Processes involved in the interaction of photons with matter as a function of the incident energy and the atomic number of the target).

3.1.1. Physical stage

The physical stage consists in the interaction of the primary beam (incident photons or ions) and the secondary particles (photons and electrons produced along the incident track) with the medium containing the NPs. The primary processes include excitations (transfers of an electron to a more energetic bound state) or ionizations (extractions of electrons from the atoms). They take place in the 10^{-18} - 10^{-14} s range (Kuncic and Lacombe, 2018). The probability for these processes to occur depends on the radiation type: photons or charged particles (ions and electrons).

a. Interactions of photons with high-Z NPs

Photon beams interact with NPs via absorption or diffusion (elastic, i.e. without energy transfer or inelastic, i.e. with energy transfer).

In the context of the radiation therapy, high energy photons beams (6-25 MeV) are used. Incident photons interact with the electrons of the target (photonuclear interactions neglected). In this energy range, two interaction processes are predominant: the photoelectric effect (absorption) and the Compton scattering (inelastic diffusion). The probability for these processes to occur is determined by their cross section, σ .

As summarized in Figure 1.1, the photoelectric effect is the dominant interaction process for incident beams of keV energies (typically up to ~500 keV) interacting with high-Z atoms ($Z \sim 60-80$ amu). For instance, this process is predominant when Gd-based NPs (yellow horizontal line) are activated by preclinical irradiation with 220 kV X-rays. The Compton scattering becomes the most probable for photon energies higher than 500 keV, for Z below 60-70 amu. For example, Compton effect predominates when Gd-based NPs are coupled with a radiotherapy beam of 6 MV.

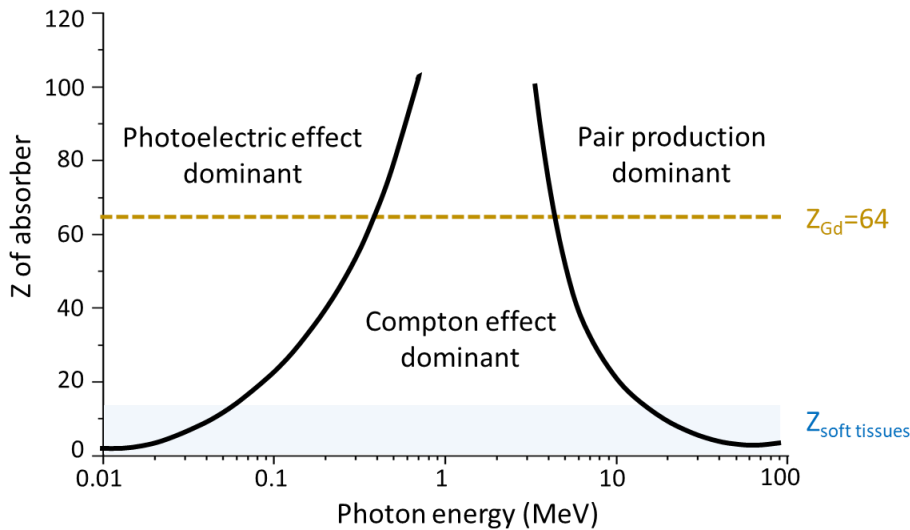


Figure 1.1 - Processes involved in the interaction of photons with matter as a function of the incident energy and the atomic number of the target (Gazis, 2019).

Photoelectric effect

The photoelectric effect consists in the complete absorption of an incident photon by an electron. The transfer of energy results in the ejection of an electron, called photoelectron (secondary electron) (Figure 1.2). This process occurs only if the energy of the photon ($E_0=h\nu$) is greater than the binding energy (W) of the electron in the target atom, which in turn gets ejected from the atom with a kinetic energy $T_e = E_0 - W$. In this energy range, the photons interact preferentially with electrons of the deepest layer (inner shell).

The highest probability of interaction is observed for $E_0=W$. It increases with the mass of the targeted atom and decreases with the energy of the incident photon according to the relation: σ (cross-section) $\propto \left(\frac{Z}{E}\right)^n$ with $n \cong 3-4$ (Hubbell, 1971; Kuncic and Lacombe, 2018). The photoelectric effect results in the production of a photoelectron and an ionized atom left in an excited state (vacancy in the inner layer). The latter is promptly submitted to relaxation processes via redistribution/rearrangement of electronic states (see section d).

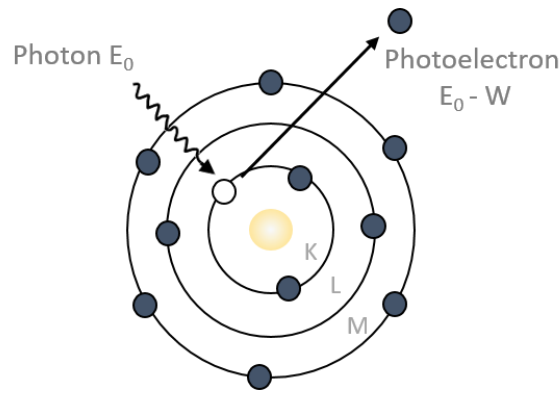


Figure 1.2 - Photoelectric effect

Compton effect

The Compton scattering is the most important primary interaction in the energy range of photon-based RT. It is the result of an interaction between a photon (E_0) and an electron located on an outer shell of the target atom (Figure 1.3). Thus, because the electrons are viewed quasi-free, the probability for Compton scattering (i.e. the electronic cross section) does not depend on Z but only on the electron density (Khan, 2014). The cross section of the Compton effect depends on the energy of the incident photon as shown by Klein and Nishina (Eq. 1) (Klein and Nishina, 1929).

$$\sigma = 2\pi r_e^2 \left(\frac{1+\alpha}{\alpha^2} \left[\frac{2(1+\alpha)}{1+2\alpha} - \frac{\ln(1+2\alpha)}{\alpha} \right] + \frac{\ln(1+2\alpha)}{2\alpha} - \frac{1+3\alpha}{(1+2\alpha)^2} \right) \quad \text{Eq. 1}$$

where r_e is the classical electron radius given by $r_e = e^2 / (m_0 c^2) = 2.819 \times 10^{-15} \text{ m}$.

The electron that has received part of the photon energy is ejected (recoil electron considered as secondary electron) with an energy W_e while the incident photon is deflected and its energy is reduced to E_d . The energy E_d of the scattered photon is given by the following equation:

$$E_d = \frac{E_0}{1 + \alpha(1 - \cos \theta)} \quad \text{Eq. 2}$$

where $\alpha = \frac{E_0}{m_0 c^2}$ and m_0 is the rest mass of electron.

It is noteworthy to mention that, after Compton interaction, scattered photons may have energies so that photoelectric effects are induced (Detappe, 2017).

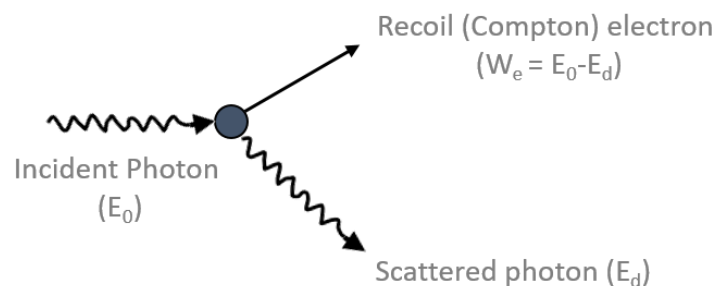


Figure 1.3 - Compton effect

b. Interactions of high energy ions with high-Z NPs

The processes induced when ions interact with high-Z NPs are different than for photons. These processes are schematized in Figure 1.4 below. Charged particles interact with NPs by Coulomb interactions. At therapeutic energies (incident energy per nucleon > 1 MeV/uma), elastic interactions with the atomic nuclei and radiative losses (bremsstrahlung) are minor.

Coulomb interactions

The cross section of Coulomb interactions between atomic charged particles beam and NPs depends on the kinetic energy and charge of the incident beam, and on the impact parameter (Khan, 2014). The probability of extracting electrons from the NP is the highest when the beam slows down in matter and the ions have a kinetic energy comparable to the one of target electrons (Lacombe et al., 2017). The emitted electrons have energy of several eV to a few tens of keV. However, on the conditions of particle therapy, the probability (geometrical cross section) of direct interaction between the incident ions and the NP is very low ($\sim 10^{-3}$ to 10^{-4}) (Wälzlein et al., 2014).

Plasmons

Solov'yov and co-workers simulated that the interaction of the external electrical field produced by the incident ion beam with NP free electrons (metals) may induce the collective oscillation of the electron plasma (plasmon and collective 5d-electrons excitations) (Bolsa Ferruz, 2017; Surdutovich and Solov'yov, 2017). However, the low probability to have direct interaction of incident ions with NPs with the concentrations used, makes this process very unlikely, with a production of secondary electrons of very low energy (secondary electrons of very low energy \sim some eV) (Haume et al., 2018; Verkhovtsev et al., 2015b, 2015a).

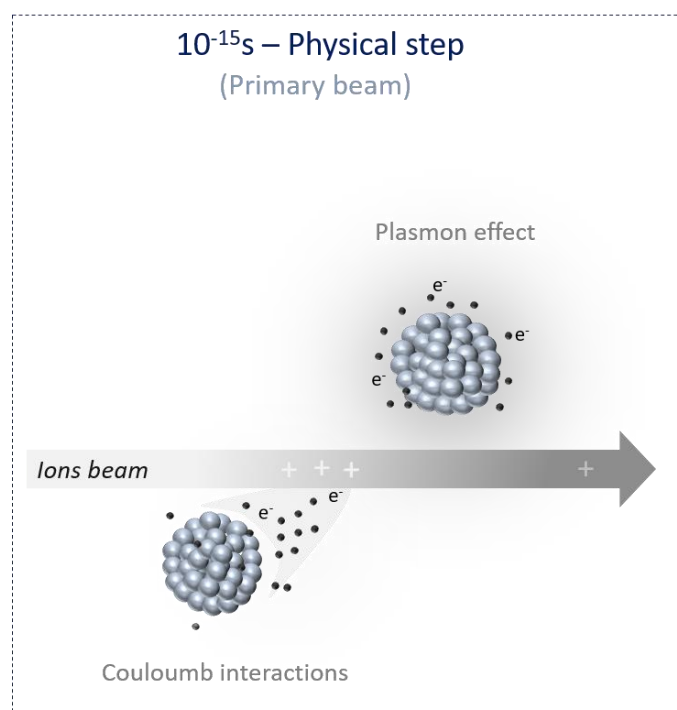


Figure 1.4 - Physical interaction processes of NP with incident ions

c. Interactions of electrons with high-Z NPs

Secondary electrons of several keV down to few eV are emitted due to the ionization induced by the interaction of photons or ions with the medium. These electrons can in turn interact with matter. As illustrated in Figure 1.5, electrons produced in the primary track or secondary electrons emitted from a neighbouring NP can interact with the NP. These Coulomb interactions of secondary electrons with the electrons of the medium can induce elastic or inelastic scattering.

By elastic scattering, secondary electrons conserve their energy E_0 but are strongly deviated. This process is more important for low energy electrons (few hundred eV). The cross-section of elastic scattering increases with Z of the medium and decreases with E_0 (Mehnaz et al., 2019).

By inelastic scattering, secondary electrons transfer partially their kinetic energy to electrons of the medium. The probability of interaction is proportional to $\frac{Z}{E_0^2}$. Hence, the medium is ionized. The incoming secondary electron is scattered and an electron is emitted, leaving a vacancy on the shell.

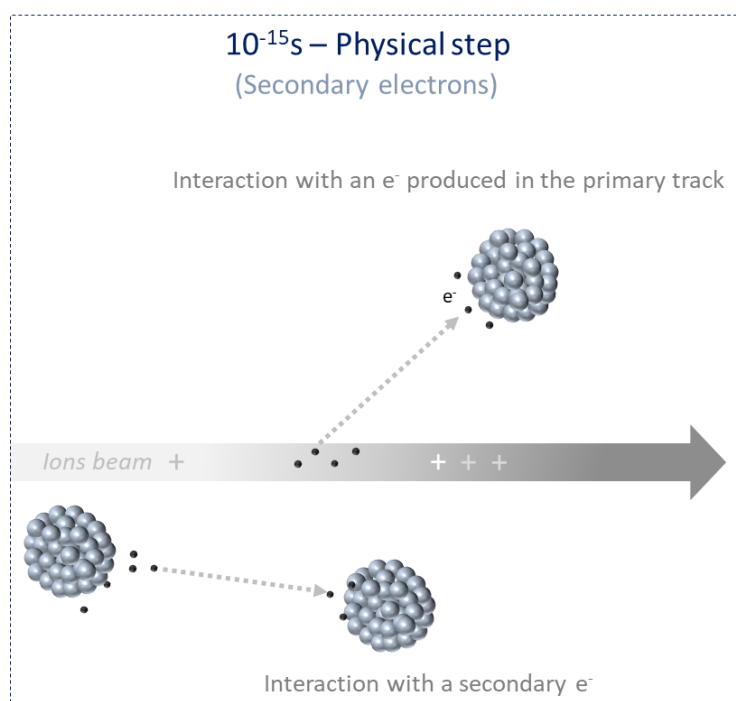


Figure 1.5 – Activation of NP by secondary electrons

Bremsstrahlung (mainly due to deflection by the electromagnetic field of the nucleus) can also cause energy losses but the process is unlikely because secondary electrons have energies below MeV.

d. De-excitation processes

The de-excitation of NPs after ionization by either photons or charged particles (ions, electrons), results in the reorganization of the electronic shells to bring the system back to its fundamental state.

The main processes involved in this relaxation are : fluorescence, Auger electron emission (Robley Evan, 1956) and potentially, electron capture from the medium to the ionized NPs (Figure 1.7). The relative importance of each process (fluorescent photon or Auger electron emission) depends on the

target atomic number Z . In the case of K-shell vacancies, the fluorescence yield increase with the atomic number of the target (Figure 1.6). However, for light elements (main constituents of the biological systems), the Auger effect becomes dominant (Krause, 1979).

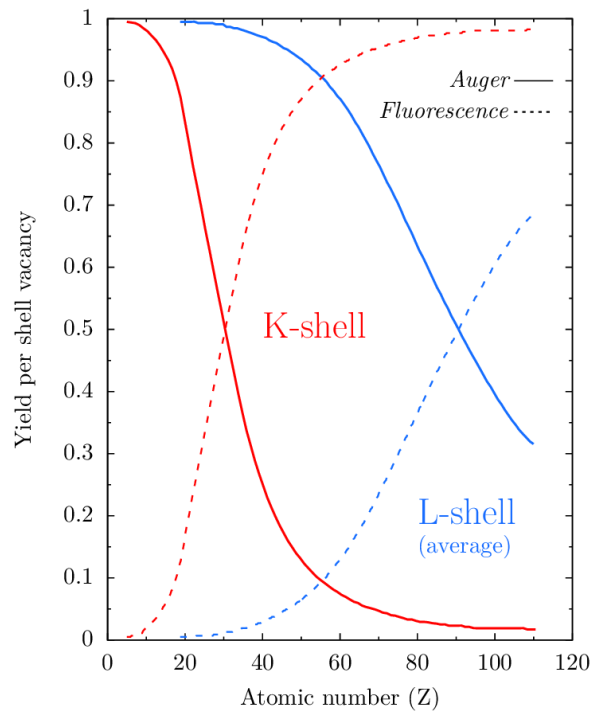


Figure 1.6 – Fluorescence and Auger yield for atoms with $Z < 120$. (Krause, 1979)

The fluorescence photon emission (radiative process) is predominant when the vacancy is produced in the K-shell. Auger electron emission (non-radiative process) which occurs after a vacancy is induced in an inner shell other than the K-orbital.

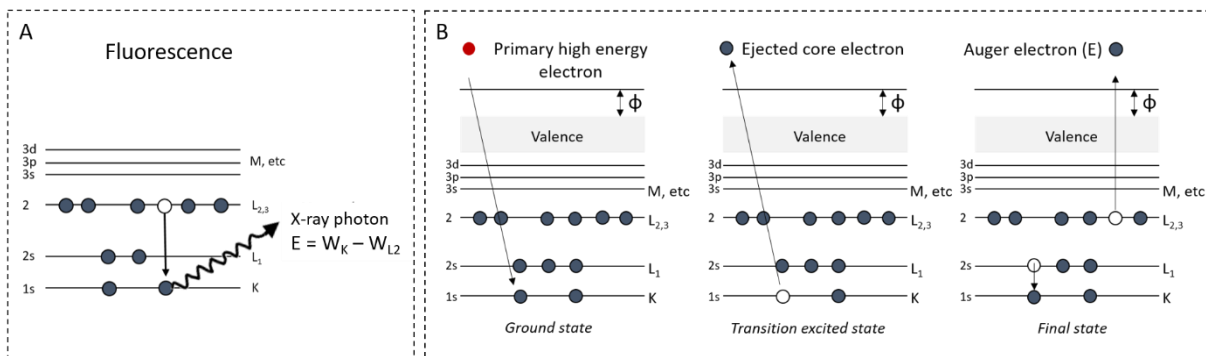


Figure 1.7 – De-excitation processes

Fluorescence processes

The energy of the emitted photon (E) is equal to the difference of energies between the binding energy of the emitted electron from the K-shell orbital and the binding energy of the re-located electron (from an upper shell, for instance L_2) (Eq. 3).

$$E = W_K - W_{L_{2,3}}$$

Eq. 3

Auger processes

Auger process can take place when inner shells are ionized. The ionization of an inner shell is followed by Auger de-excitation and emission of Auger electrons (Figure 1.7B). The energy of the Auger electrons is also determined as follows (Eq. 4). In this example, the Auger electron is emitted with a kinetic energy E:

$$E = W_K - W_{L1} - W_{L2,3} \quad \text{Eq. 4}$$

Where W_K , W_{L1} and $W_{L2,3}$ are the binding energies of the K, L_1 and $L_{2,3}$ electron shells

For high-Z compounds, Auger process dominates for shells above the K-shell.

The energy of the Auger electrons depends on the ionised atom and the involved layers. For example, for gold (K alpha transition energy), Auger electrons can have energies of few hundred eV and a range of about 10 nm in tissues (Kuncic and Lacombe, 2018). The energy dose deposition due to this process is thus very localized in the immediate vicinity of the NP compared to the dose deposition of the fluorescence photons that travel longer distances (several cm in tissue) (Schuermann et al., 2016).

As introduced by McMahon, the modelling of the radioenhancement effect is explained as an heterogeneous enhancement of the dose at nanoscopic scale, in the vicinity of the NPs (energy spikes) or their aggregates (Figure 1.8). However, the chemical and biological consequences of these local dose depositions are still under investigations (Poignant et al., 2020).

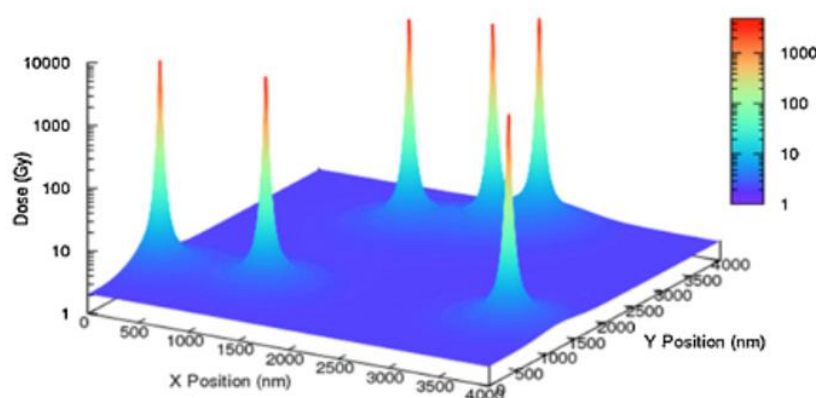


Figure 1.8 - Simulation of the local dose deposition after 80 keV photons irradiation (2 Gy) of the medium containing gadolinium NPs. (Extracted from Lux et al., 2015 according to the method developed by McMahon et al., 2011)

Charge transfer

After ionization (such as after Auger cascade), atoms of the NPs are positively charged and can capture electrons from surrounding molecules of the medium (H_2O). This strong perturbation is expected to rapidly induce electronic rearrangement in the close environment (Figure 1.9) (Stumpf et al., 2016). This type of local electronic rearrangement has been proposed by Kuncic and coworkers (Kuncic and Lacombe, 2018). Interestingly, this step begins to be taken into account in the models that describe the physical stage (Schuermann et al., 2019).

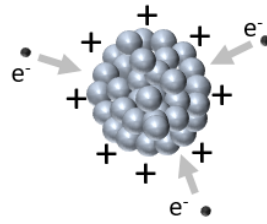


Figure 1.9 - Charge transfer on a positively charged NP

e. Stopping power and restricted Linear Energy Transfer

The charged particles beam is slowed down by these inelastic collisions with electrons of water which account formost of the energy losses. In the context of medical applications, Bremsstrahlung can be neglected.

Thus, the stopping power, S , defined as “the average energy dissipated by ionizing radiation in a medium per unit path length of travel of the radiation in the medium” can be reduced to an electronic stopping power, S_{el} , defined by the Bethe and Bloch formula provided in Eq. 5 (ICRU, 2005):

$$\frac{S_{el}}{\rho} = -\frac{1}{\rho} \left(\frac{dE}{dx} \right)_{el} = K \frac{z^2 Z}{\beta^2 A} \left[\ln \left(\frac{2m_e c^2 \beta^2 \gamma^2}{I} \right) - \beta^2 - \frac{\delta}{2} - \frac{C}{Z} \right] \quad \text{Eq. 5}$$

Where K is a constant equal to $0.307 \text{ MeV} \cdot \text{g}^{-1} \cdot \text{cm}^2$, z and βc are the atomic number and the speed of the incident ions (incident particles dependence), Z and A are the atomic number and relative atomic mass of the target atom (medium dependence). I is the mean excitation potential, γ is the Lorentz factor, δ is a charge density correction and C/Z is shell correction needed for energy loss at low energies (Berger et al., 1993).

The term $\frac{z^2}{\beta^2}$ states that the stopping power increases when the charge of the ions increases or its velocity decreases. The particles will lose more and more energy as they slow down, causing a sharp dose deposition at the end of the track, called Bragg peak.

While the stopping power considers the total amount of the energy lost by a particle, regardless the energy localization, the restricted linear energy transfer (LET) has been introduced as a concept to describe the energy loss along the linear track (Schneider, 2020). It is expressed as:

$$\text{LET}_{\Delta} = \frac{dE_{\Delta}}{dl} \quad \text{Eq. 6}$$

where dE_{Δ} is the mean energy lost by the charged particles due to electronic interactions in traversing a distance dl , minus the mean sum of the kinetic energies greater than Δ of all the electrons released by the charged particles (Seltzer et al., 2011). The variable Δ can be thought of as a threshold where only particles with a kinetic energy $\leq \Delta$ are included in the LET. If no energy cut off is imposed the unrestricted linear energy transfer, LET_{Δ} is equal to S_{el} .

The LET can be approximated by the ratio $\frac{z^2}{v^2}$, where z and v are the ion charge and speed respectively. When the ions slow down, the LET increases, reflecting an increased ionizing density, in the Bragg peak. In addition, because of their charge, carbon ions have LET higher than protons. In general, low LET (0-10 keV/ μm) are distinguished from high LET values (>10keV/ μm) (Marples, 2015). Note that these values of LET, commonly reported in the literature represent track average LET and don't take into account the fact that LET changes as the particle slows down and so is not constant along the track (Baldacchino et al., 2019a). However, it allows to get order of magnitude and compare different radiation types. In my PhD, I worked with two beams of different average LETs, namely carbon ions of 290 MeV/amu, (LET of 50 keV/ μm) and helium ions of 150 MeV/amu (LET of 12 keV/ μm).

3.1.2. Chemical stage

The living organisms are composed of water for more than 60%. Thus, incident radiations interact with water molecules mainly, which leads to the production of secondary electrons and to the excitation and ionization of water molecules along the track (water radiolysis). The consecutive interaction of secondary electrons with water is also responsible for water radiolysis (Tubiana et al., 1986). As a consequence, water molecules dissociate, which leads to the production of free radicals and water byproducts (HO^\bullet in particular) in the 10^{-12} - 10^{-6} s time frame (Figure 1.10 - Chemical step leading to the production of radicals).

Another way of producing water radicals is the Dissociative Electron Attachment (DEA), namely the attachment of low energy electrons (<25 eV) on water molecules. The result is a transient negative ion of water molecule. This species may de-excite in two ways: either by self-detachment of the electron or by dissociative detachment. The latter case leads to the production of hydrogen and hydroxyl fragments (Simpson et al., 1998).

As shown above, the presence of NP may amplify the production of electrons. In addition, electron capture from water molecules to positively charged NPs (see d) may increase water ionization. Thus, the presence of NPs is expected to enhance the production yields of water radicals. These free radicals have an unpaired electron, they are very unstable and highly reactive. The generation of ROS is suggested to be a crucial step that may connect the physical effect to the biological consequences (Schuemann et al., 2016).

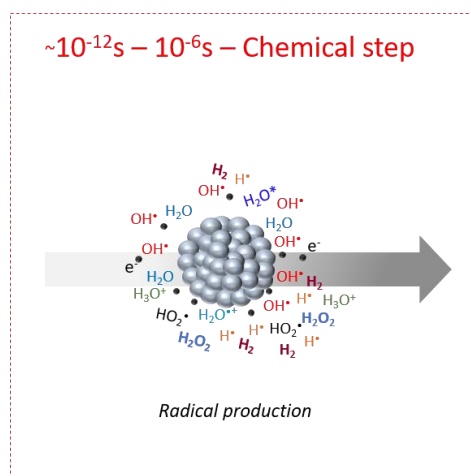


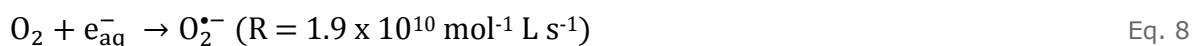
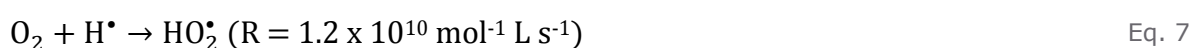
Figure 1.10 - Chemical step leading to the production of radicals

Hydroxyl radical (HO^\bullet) is a key component of radioenhancement phenomenon because it is a powerful oxidant (Schuermann et al., 2016; Usami et al., 2008). On the other hand, e^-_{aq} is a powerful reductant. These species start to migrate in the biological medium after 10^{-12} s.

Reaction between radicals may occur, leading to the formation of more stable molecular species such as H_2 or H_2O_2 , known to be toxic.

In the particular case of incident ions beams, the LET has an influence in the competition between the processes of formation and diffusion of the radicals. Indeed, when the LET increases, the spurs (small clusters of nanometers size of excited and ionized molecules) can overlap along the propagation axis of the incident beam. The formation of molecular species (H_2 , H_2O_2) is favoured leading to a decrease of the yields of radicals species (Baldacchino et al., 2019a).

The presence of molecular oxygen dissolved in the biological environment plays a crucial role in the induction of damages. Reactions with O_2 produce hydroperoxyl HO_2^\bullet and superoxide ion $\text{O}_2^{\bullet-}$ (see Eq. 7 and Eq. 8). These radicals are less oxidative than HO^\bullet but they may travel further. They are highly cytotoxic.



Some simulation tools as Geant 4-DNA were developed to study the radical effects. Unfortunately, the Monte Carlo simulations ignore the effects of molecular oxygen. The community started recently to include this step in the description of the elementary processes (Schuermann et al., 2016).

3.1.3. Biological stage

The detrimental effect of radiation on DNA molecule or some other cellular components critical to the survival of the cell (such as cellular membrane) are usually categorized as:

(i) direct effect - the primary radiation or secondary electrons directly interact with a biomolecule such as cellular DNA or organelles.

(ii) indirect effect - a biomolecule is damaged by the free radicals produced through the ionization and/or excitation of water molecules (solvent-mediated effects) (see section 3.1.2) (Tubiana et al., 1986).

The indirect action constitutes the majority of radiation-induced cellular damage (Saha, 2013) (Figure 1.11).

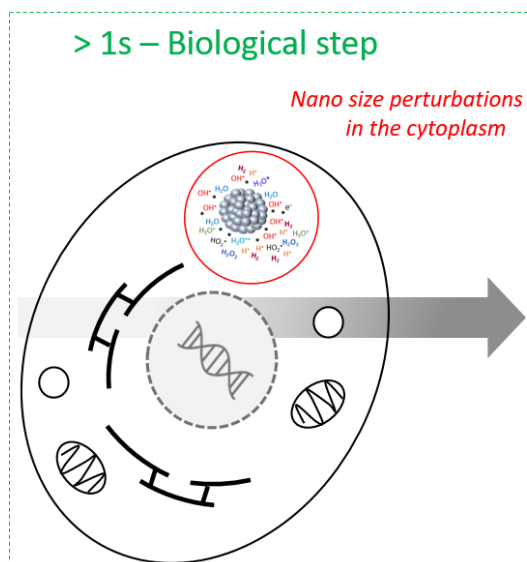
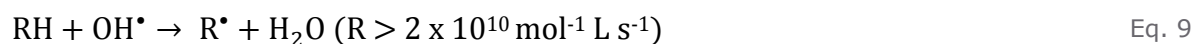


Figure 1.11 - Biological damage induced in the cell cytoplasm, in the vicinity of the NP

Hydroxyl radicals (HO^\bullet) produced during the radiolysis phase account for 60-90% of the amplification of cell killing induced by high-Z compounds activated by high energy photons or ions (Usami et al., 2008). It also induces an increase of nanosize lesions (Porcel et al., 2010; Schlathölter et al., 2016). After its production, HO^\bullet undergo reactions with the main organic constituents (RH) of biological systems (nucleic acids, proteins, lipids...). This leads to the production of carbon-centred radicals (R^\bullet), which are highly reactive and short lived organic radical (Schuemann et al., 2016) (Eq. 9).



Other water byproducts like H^\bullet or e^- can also lead to the creation of radical R^\bullet

Two reactions involving R^\bullet are in competition:

- (i) Reaction of R^\bullet with oxidative species (Eq. 10):

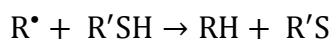
R^\bullet reacting with O_2 yields peroxy radicals RO_2^\bullet .



Peroxy radicals result in the “fixation” of the damage which is potentially lethal for cells (Chapman et al., 1973; Schuemann et al., 2016). For example, peroxy radicals formed from DNA (RO_2^\bullet with R corresponding to a nucleic acid chain) induce unrepaired DNA damage (Rodriguez and Akman, 1998). Peroxy radicals formed from unsaturated lipid (RO_2^\bullet with R corresponding to a lipidic chain) create additional toxic substances of the peroxide family (ROOH and ROOR), which accumulate during irradiation and increase the cytotoxicity (Sonntag, 1987).

- (ii) Reaction of R^\bullet with radical reductant (Eq. 11):

R^\bullet can also be annihilated by electron donors (radical scavengers) which produce a protective effect called “chemical repair”. For example, R^\bullet can react with glutathione, a sulfhydryl compound abundantly present in cell, according to the Eq. 11.



Eq. 11

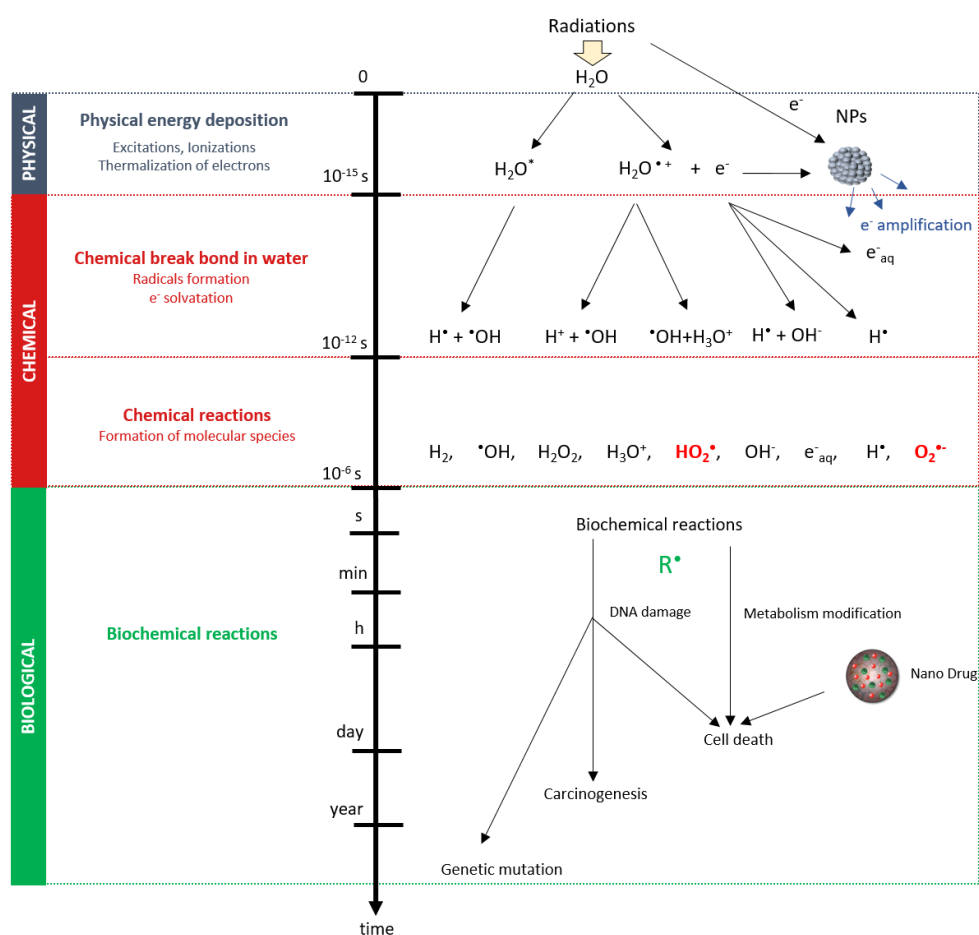
In hypoxic conditions, the role of O_2 in the radical cascade decreases. Reactions of R^{\bullet} with radical reducing species dominate, explaining that the radiations induce less damage.

However, with high LET beams, the influence of O_2 concentration is reduced because O_2 can be produced radiolytically in the ions track (Baldacchino et al., 2019b; Gervais et al., 2005). In addition, the phenomenon of radical stabilization by O_2 has much less influence when the damage produced is directly lethal (which is the case with high LET) (Baldacchino et al., 2019b; Chapman et al., 1973). In addition, in the case of ions beam, the localized energy deposition result in an increase of the complexity of DNA damage (Durante et al., 2017) and clustered DNA lesions, (also called CDD for Complex DNA Damage or LMDS for Locally Multiply Damaged Sites). These damage are more difficult to repair, leading to a higher biological efficiency of the treatment (Sage and Shikazono, 2017).

The damaged biological molecules will modify the normal cellular metabolism leading either to a faithful repair of the damage, or mutation, or death. The super production of ROS can disrupt the cell by generating oxidative stress which can also lead to cell death (Migdal and Serres, 2011).

3.1.4. Summary

The cascade of early stage processes induced by interaction of radiations (photons, charged particles) with the biological medium loaded with NPs (physical stage), consecutive chemical reactions including water radiolysis and also contribution of molecular oxygen (chemical stage) and



resulting biological damage (biological stage) are summarized in Figure 1.12.

Figure 1.12 - Cascade of processes taking place from the radiation interaction to the impact on the biological system, in the presence of NP. Adapted from Baldacchino et al., 2019 and Tubiana et al., 1986

Various experimental models have been used to disentangle the effects of NPs. Ultimately, they aim to evaluate these strategies, predict and control their effects on patients.

From the simple to more complex model, one may recall the approach adopted so far. *In silico* models were set up to study the impact of various parameters (e.g. radiation type, oxygen) on the elementary processes (physical and chemical stages). *In vitro* models, mainly 2D cell cultures were commonly used to characterize the NPs toxicity and internalization and predict their impact on radiation-induced cell killing. *In vivo* experiments were performed to study the biodistribution of NPs and the effect of this distribution on tumor release. Finally, very few clinical trials managed to bring such a combined strategy to its end, e.g. to patient treatment. An overview of the experiments and the preclinical models implemented today is exposed below.

3.2. Studies on the effects of NPs combined with radiations

This part aims at presenting how the preclinical models can be deployed to underpin the search for therapeutic strategies using radiations and nanoagents. The standard process for clinical translation is presented in (Figure 1.13). Currently, the pipeline is the following: (1) preliminary tests on 2D *in vitro* assays (2) efficacy tests and regulatory toxicity on animal models (3) clinical trials.

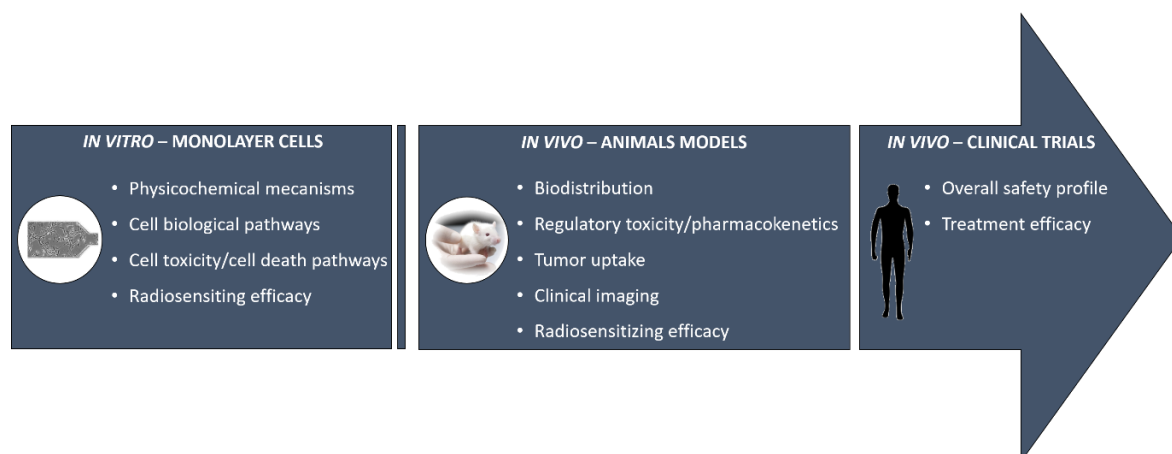


Figure 1.13 - Pipeline of a treatment evaluation: from bench to bedside

Here, we provide a state-of-the-art of the main advances and answers brought by each of the models in the context of treatments associating NPs and radiations.

3.2.1. *In vitro* experiments

In vitro studies are needed to characterize cellular scale impact of NPs including cell toxicity, uptake dynamics and radiation-induced cell survival.

The principle of radioenhancement was first demonstrated using metallic complexes to increase the effects of high energy photons (Usami et al., 2005).

Since, the potential of many other NPs has been demonstrated at the cellular scale. It is the case for the Gd-based NPs that I used in my PhD work. The radiosensitizing effects of AGuIX[®] on clinical irradiator at 6 MV have been demonstrated in a number of cell lines including cervical carcinoma (Lux et al., 2015), glioblastoma (Mowat et al., 2011), and pancreatic adenocarcinoma (Luchette et al., 2014).

A first proof of efficiency was also provided by our group, which demonstrated that the addition of AGuIX[®] also increases cell-killing when treated with carbon ion radiation (290 MeV/u, LET = 13 keV/μm) (Porcel et al., 2014).

The microscopy studies based on monolayer cultures have also revealed the sites of action of the NPs. Several studies published by our group have shown that the different metallic-based NPs (Gd, Pt, Au) were found in the cytoplasm of the cells (Porcel et al., 2014; Sánchez et al., 2019; Štefančíková et al., 2014) confirming that the primary mechanisms responsible for the enhancement of cell-killing are initiated out of the nucleus.

It was also shown that the internalization biological pathways of the NP are cell line dependant (Ivošev et al., 2020).

Monolayers cultures are essential tools to probe and better understand the physico-chemical mechanisms exposed in section 3.1. Pioneer studies led by Usami and coworkers have demonstrated at molecular and later at cellular scales (Usami et al., 2008), the importance of the production of water radicals in the NP radiosensitization. The key role of molecular oxygen in the radiation effects in the presence of AuNPs was also highlighted in our group (Bolsa Ferruz, 2017).

The biological impacts of NPs have also been studied using 2D cell cultures. In particular, they allowed to demonstrate the important role of mitochondria in NP (Au) mediated radiosensitization (Taggart et al., 2014) and the key role of oxidative stress on the response to radiation damage (Butterworth, 2013).

3.2.2. *In vivo* experiments

Several combined treatment strategies have been evaluated *in vivo*.

In vivo studies allow to evaluate the treatment effectiveness on real bodies, for example to determine the median survival time of the subject (life span) and/or the volume reduction. Hainfeld and coworkers were the first to demonstrate that AuNPs prolongate the life of mice treated with 100 kV X-rays (Hainfeld et al., 2004). Since then, it has also been shown that the use of AGuIX[®] combined with kV-beam (mean energy of 90 keV) leads to significant tumor growth suppression (~3-fold decrease in tumor volume) and improves the mice overall survival (from 45 d to 85 d) (Dufort et al., 2016). In the context of particle therapy, Kim and coworkers have first demonstrated the effectiveness of high-Z NPs (gold or iron) to improve the performance of proton radiation (Kim et al., 2012). They confirmed that the amplification of tumor regression and mice survival is related to ROS production, which is in agreement with the *in vitro* studies.

On the one hand, *in vivo* studies are also used to characterize the NP biodistribution. Performed on healthy animals, they aim at determining the behaviour of NPs in the body. For example, concerning AGuIX[®] which are injected intravenously, rapid tumor uptake was observed with long retention time (up to 24h after injection). This result was attributed to an enhanced permeability and retention (EPR) effect, reported for the first time in 1986 and observed with numerous NPs (Bort et al., 2020; Matsumura and Maeda, 1986). For most of the small metallic NP, an elimination of the NP by the kidneys was reported (Al Zaki et al., 2014; Lux et al., 2018). Studies on brain

tumor-bearing animals showed the capacity of the NPs to cross the blood-brain barrier when the blood brain barrier is damaged (Kotb et al., 2016; Le Duc et al., 2011).

On the other hand, *in vivo* studies allow to investigate theranostic properties of NPs. In 2013, Hainfeld and coworkers showed that injection of AuNPs in mice enhance the contrast of CT images (Hainfeld et al., 2013). Detappe observed that this is also the case with AGuIX[®] complexed with bismuth (Detappe et al., 2017). In line with these observations, Miladi and coworkers demonstrated that AuNPs with Gd chelates can be monitored by MRI, improving delineation of tumor margins (Miladi et al., 2015).

Last but not least, a follow up of the animal during the *in vivo* studies allows to control the toxicities and ensures that no adverse clinical signs were observed during the treatment period. The maximum tolerable dose was determined as a basis for clinical trials (Lux et al., 2018).

3.2.3. Clinical trials

Some clinical trials using a combination of high Z-NPs with radiations are being transferred to the clinic. A review of the literature up to March 2020 shows that two NPs stood out for their use in clinic in combination with radiotherapy (Scher et al., 2020). Phase 1/2 aims at studying the safety and feasibility of the NP injection. The first objective is to identify the maximum tolerated dose (determined as high a dose as possible without causing important toxicities). Phase 2/3 allows a first evaluation the treatment response (treatment efficacy).

AGuIX[®] injected intravenously in bodies, were evaluated in six phase 1/2 clinical trials for the treatment of brain metastasis and cervical cancer (Scher et al., 2020; Verry et al., 2020a). In the first-in-man performed at Grenoble, a significant MRI signal enhancement was observed two hours after AGuIX[®] iv injection for all types of brain metastases and all assessed dose (15 to 100 mg/kg) (Bort et al., 2020; Lux et al., 2018). Interestingly, the enhancement of the signal increased with the AGuIX[®] injected dose (Verry et al., 2020a). The theranostics properties of AGuIX[®] were clearly confirmed in human. AGuIX[®] (as NBTXR3) showed an absence of toxicity, with an overall safety profile similar to the control arm. The first evaluation was very promising. Based on the data currently available in the literature, no significant acute toxicity of NP combined with radiotherapy was reported (Scher et al., 2020). All the results and observations made it possible to confidently start the phase 2 clinical trials.

NPs composed of Hafnium oxide -NBTXR37 (Nanobiotix company, Paris, France), injected in tumors, were used in three phase 1/2 trials on sarcoma, head and neck squamous cell carcinoma or liver cancer and one phase 2/3 trial (Bonvalot et al., 2017). First evidence of superior efficacy of radiotherapy in the presence of NP was demonstrated with NBTXR3 (Bonvalot et al., 2019). A phase 2/3 trial (randomized, multicentre and international) was conducted between 2015 and 2017 with 176 patients. The objective was to compare preoperative RT alone versus an investigational arm involving intratumoral NBTXR3 injection prior to RT NBTXR3. The results show a significant improvement in pathological complete response (16% vs 8%; $p=0.044$) and R0 resection (84% vs 70%; $p=0.030$) with NBTXR3 in comparison with radiotherapy alone (Scher et al., 2020; Vilotte et al., 2019).

3.2.4. Summary

A myriad of experimental approaches were used across the research pipeline, from simple reductionist models dedicated to evaluate the effects of NPs and their impact on cells, to complex animal models for studying the biodistribution, pharmacokinetics and efficacy of the NP (Robertson

et al., 2019). The use of preclinical models has considerably improved our knowledge of the NPs effect and potential. Yet, the transfer to the clinic of two NPs only shows that other models are needed to fasten the selection of products and protocols. New preclinical models are essential to evaluate, simulate the impact of NPs with conditions that mimic at best biological conditions of tumors.

3.3. Limitation of the 2D *in vitro* and *in vivo* models – Role of ECM on NPs and radiation effects

3.3.1. 2D *in vitro* models

Most of the *in vitro* experiments are based on the use of two-dimensional (2D) cell culture, in which the cells grow in monolayer onto a rigid planar surface. In this case, the extra cellular matrix (ECM) is not reproduced. It's a well-established method and a convenient culture mode allowing many biological investigations. However, despite their accessibility and low cost, they do not faithfully mimic *in vivo* tissue conditions (Achilli et al., 2012; Lazzari et al., 2017).

Simple spatial organization appears as a major drawback, resulting in a loss of tissue-specific architecture. The predominance of the cell-surface attachment allows the adherent cells to spread, which modifies their morphology and their behavior (Eke and Cordes, 2011). In addition, cells are bathed in a standard cell culture medium whose composition differs from the one of the *in vivo* microenvironment.

In these conditions, cells receive completely different environmental signals compared to native tissues, causing radical modification in cell functions (Mirbagheri et al., 2019). In particular, cell proliferation is faster than *in vivo* and differentiated capacities of stem cells are often reduced. 2D culture also alters gene expression and activation of cell signaling pathways, compared to the *in vivo* tumor tissues (Costa et al., 2016; Pinto et al., 2020). Moreover, due to uniform exposure of the monolayer to culture medium, the cells tend to exhibit a synchronized cell cycle (Mirbagheri et al., 2019).

Another failure of this model is the simulation of the oxygen environment. Monolayer cells have direct access to molecular oxygen. In this case, mass transport and diffusion phenomena are too simplistic and not representative of the various conditions encountered in the cytoarchitecture of tissues.

In conclusion, although useful, fast and cheap, monolayer cultures are too simplistic which limits obtaining accurate assessment of the biological performance of treatments (Table 1).

3.3.2. *In vivo* models

At the other end of the experimental continuum, animal models allow evaluation of the treatment efficacy in living organisms.

As they are capable to reproduce tumor architecture (cell-cell interactions, presence of microenvironment) with specific *in vivo* characteristics (vasculature, kidney clearance and sometimes immune status...), mice models are believed to offer relevant predictive insights into clinical outcomes when evaluating the efficacy of novel therapeutic strategies.

Over 95% of the *in vivo* studies are conducted in mice (Vandamme, 2014). Mice included in the treatment protocols can be xenografted or genetically engineered. On the one hand, Patient-Derived Xenografts, called PDX, are based on the transfer of cancerous tissue (single-cell suspension or tissue fragment) directly from a patient's tumor into an immunodeficient mouse (Siolas and Hannon, 2013). On the other hand, genetically engineered models (GEMs) are organisms in which specific genes have been altered (added or ablated) to accurately recapitulate the genetic, biochemical, and phenotypic features of specific human malignancies (Becher and Holland, 2006).

With either method, the development of animal models is costly and time consuming process, with a development of progressively growing tumors which can take several months (Siolas and Hannon, 2013). Despite increased complexity compared to 2D cultures, animal models not accurately reproduce human tumor. For example, because a limited number of genes is targeted, GEMs don't fully reflect the tumor heterogeneity (Jung et al., 2018; Richmond and Yingjun, 2008).

The influence of the murine environment is also important. For example, the stromal component of xenograft is not of human origin, PDX are immune deficient mice or the rate of tumoral growth is higher in mice than in human (Pinto et al., 2020). These biologic differences can partly explain the inconsistency of the responses observed (efficiency, side-effects, metastatic progression, interactions with immune system) between mice and humans (Brancato et al., 2020).

More obvious brackets are associated with animal models, such as ethical and financials constraints, as well as the need for specialized equipment (animal facilities) and specialized personnel.

In conclusion, *in vivo* models are complex. Even if they do not completely reproduce the human tumor microenvironment, they provide a 3D physiological context which allows more reliable predictions of treatments. However, these models result from a long process (from animal creation to follow-up after treatments) and require both facilities and specific skills (Table 1).

3.3.3. Summary: Towards a 3D model to fill the gap between 2D *in vitro* and *in vivo* models

Translational research is essential to find new therapeutic strategies able to improve cancer treatments. The development of preclinical models more representative of tumor reality than monolayer cultures while overcoming certain *in vivo* constraints is a new challenge explored in this work. Several studies have shown that the efficacy and toxicity of many treatments presented differences according to the model used (2D or 3D) (Khaitan and Dwarakanath, 2006; Shield et al., 2009; Zietarska et al., 2007).

ECM is commonly defined as the non-cellular component of tissue that provides both essential structural and biochemical support for its cellular constituents (Qiu et al., 2017; Walker et al., 2018). *In vivo*, ECM is composed of several high molecular weight proteins, proteoglycans, and polysaccharides molecules self-arranged into fibers and networks (Vigier and Fülöp, 2016). The exact composition of the ECM surrounding the tumor depends on the tissues (Ferreira et al., 2018). The matrix provides a structural support for the cells while acting as natural penetration barrier. These mechanical framework allows a maintenance of the cell morphology (including cytoskeletal organization and cell stiffness) similar to their *in vivo* behavior (Ghosh et al., 2007; Pedersen and Swartz, 2005; Qiu et al., 2017). ECM can also serve as binding sites, controlling the adhesion and the movement of cells (Walker et al., 2018).

ECM is also a physiologically active component with and through which cells can interact (cell-cell and cell-ECM communications). It is involved in the transmission of biochemical signals and communication pathways, participating in the regulation of numerous cell functions such as cell

proliferation, differentiation and gene expression (Even-Ram and Yamada, 2005; Walker et al., 2018). ECM can also regulate diffusion processes which occur *in vivo* (such as nutrients, oxygen, CO₂, waste, drug...).

In the context of an evaluation of treatments combining NP and radiations, the role of the ECM is thus crucial.

Firstly, the presence of an ECM affects the response to nanoagents. It slows down the diffusion and obstructs the free penetration of nanoagents through the whole mass. In this way, it better reproduces the reduced tissue penetration observed in tumor after extravasation from the blood vessels (Pratiwi et al., 2021).

Several studies have shown that in presence of collagen, the tissue resistance to macromolecule transport is strongly affected, possibly by binding and stabilizing the glycosaminoglycan component of the ECM (Goodman et al., 2007; Netti et al., 2000). Steric factors and electrostatic interactions due to repulsion and binding to the ECM components also influence the nanoagents rate of movement (Tchoryk et al., 2019a).

The internalization of NPs in a 3D architecture can also be modified compared to monolayer cells (Figure 1.14). When cells are embedded in an ECM, their surface available for NP uptake is increased compared with monolayer culture where cells adhere to the rigid plastic substrate. In addition, the morphology of the cells, which differs between 2D and 3D cultures, is a parameter that can also affect the internalisation pathways of NPs, and therefore their effect (Belli et al., 2017b).

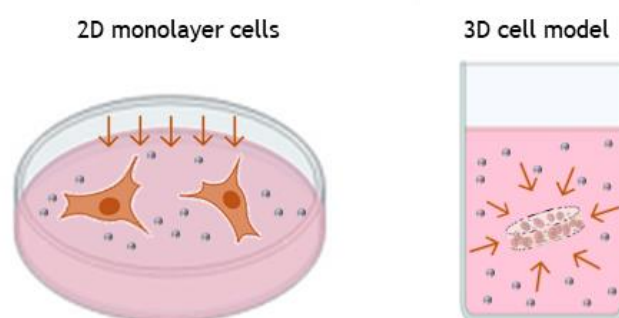


Figure 1.14 - Exposure to NPs of a 2D cell culture and a 3D model

Secondly, the presence of a matrix can also modify the response of cells to irradiation. ECM is involved in modifications of intrinsic cellular mechanisms upon DNA damage cell such as repair kinetics, cycle arrest induction or evasion of apoptosis. (Acheva et al., 2014; Asaithamby et al., 2011; Langhans, 2018; Qiu et al., 2017). Adhesion between cells and ECM proteins is an important factor known to modulate the response to radiations-based therapies (Langhans, 2018). Moreover, the establishment of gradients (in particular oxygen level) can induce hypoxia, known to be a factor of radioresistance.

Based on these considerations, there is an urgent need to evaluate the treatments combining NP with medical beam with an *in vitro* model which restores a tumor microenvironment, in particular the presence of an ECM. In this goal, *in vitro* 3D cell models have emerged. They allow rapid experimental manipulations and testing of hypotheses, without ethical and financial constraints of *in vivo* experiments. Experimentation process is faster and reproducible. 3D models bring *in vitro*

experiments one stage closer to the *in vivo* application. If it's not always an alternative, 3D cultures may at least be a quick filter before embarking on *in vivo* studies.

However, despite the initial promise of such advanced *in vitro* models in drug screening, the use of such models in the context of treatment combining radiations therapies and NP was poorly explored (Neuer et al., 2020). Only recent works based on the 3D models focused on the effects of photothermal or dynamic therapy (Darrigues et al., 2020; Mapanao et al., 2021; McCabe-Lankford et al., 2018; Mohammad-Hadi et al., 2018; Yang et al., 2019). It constitutes the main objective of my thesis.

3.4. Overview of the 3D preclinical models

Many advances have been made in recent year in cell biology, microfabrication techniques and tissue engineering to enable the development of a wide variety of models. Some of them are extremely complex and can be created from samples taken directly from the patient (such as organoids).

Even if the vasculature and immune system lack, as they can be patients-derived, they may allow to eliminate species differences that often impede interpretation of the preclinical outcomes (Fang and Eglen, 2017). In recapitulating the complex features of the primary tumor, sometimes better than animal models, they give a useful evaluation of efficacy and toxicity of drugs (Boghaert et al., 2017; Brancato et al., 2020; Halfter et al., 2016).

They can be used as *in vitro* platform to rapidly estimate the potential of new nanoagents.

However, rapid assessment of treatment effectiveness and improved predictive capability open up also new perspectives in the landscape of personalized medicine. For instance, predictive assays led on 3D models could directly guide clinical therapeutic decisions after identification of the most effective therapy (Halfter et al., 2016; Jeon and Cheong, 2019; Roy et al., 2017). This brings possibilities of patient-specific biobank creation, used to perform drug screening or facilitate treatment development (Kim et al., 2020).

Here, we provide an overview of the most commonly reported 3D cell models (Figure 1.15).

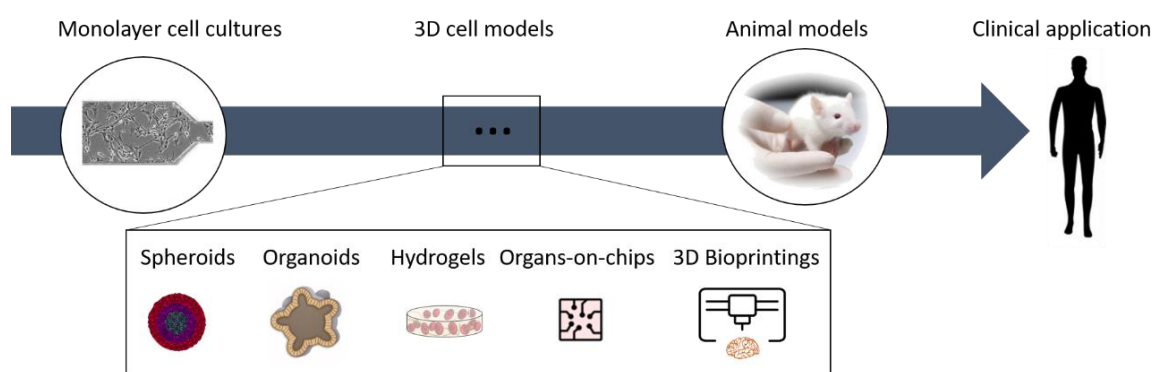


Figure 1.15 – Scheme representing the current preclinical models: 2D cell cultures, 3D cell models and *in vivo* models

3.4.1. Spheroids

Multicellular tumor spheroid (MCTS) are micro-sized self-assembled aggregates of cancer cells (co-cultured or not) (Lazzari et al., 2017). They were introduced by Sutherland and coworkers in the 1970s to recapitulate the functional phenotype of human tumor cells and their responses to radiotherapy (Sutherland RM, McCredie JA, 1971). The four main methods for creating spheroids, to which we will compare our 3D model in Chapter II, are provided in the supplementary section 1.

MCTS formation is attributed to cell adhesion and/or cell differentiation.

Basically, cells are drawn closer to form loose aggregates due to ECM-integrin binding. Direct cell-cell contact produced by initial aggregation results in upregulated cadherin expression which accumulate at the membrane surface. Homophilic cadherin-cadherin binding generate a compaction of cells into solid aggregates (i.e. spheroid) (Cui et al., 2017; Lin et al., 2006). Thus, the ECM in spheroids is composed of proteins produced by cells during the formation of the culture.

The physiological communication and the signaling established allows to reproduce the main features found in solid tumors *in vivo* such as: (i) cell-to-cell and cell-to-microenvironment interactions (ii) reproduction of gradients inducing heterogeneous cell populations (proliferation rates, oxygen, pH...) (iii) growth kinetics (iv) gene expression (v) drug resistance (Costa et al., 2016; Lazzari et al., 2017).

The main limitations of these systems are the lack of reproducibility (depending on the method of production) (Lazzari et al., 2017; Lin and Chang, 2008) and the difficulty to transfer sample (Benien and Swami, 2014). These problems are blocking points for the irradiation experiment that we conduct.

3.4.2. Organoids

Organoids, also termed “organ buds”, are advanced cellular model which represent a realistic microanatomy (Fang and Eglén, 2017). An organoid is a collection of organ-specific cell types that develops from stem cells or organ progenitors and self-organizes through cell sorting and spatially restricted lineage commitment in a manner similar to *in vivo* (Fang and Eglén, 2017; Lancaster and Knoblich, 2014). They can be created from patient biopsy or surgical section (tissue organoids) or from pluripotent stem cells (stem cell organoids) (Ramani et al., 2018).

To be considered an organoid, the cell model must meet three criteria: (i) more than one cell type of the organ modelled contained inside, (ii) organization similar to the organ itself, (iii) exhibition of organ specific functions. Organoids have been successfully developed for multiple organs including digestive (pancreas, liver, stomach, intestine) or cerebral models.

This model presents considerable advantages. It is a human model, patient-specific, and which reflects the complexity of the tumor (cell type heterogeneity). However, it is not possible to reproduce the vascularization processes. In addition, some organoids may lack key cell types found *in vivo* or are not able to mimic later stages of organ development (such as neurogenesis). Thus, the reproduction of *vivo*-like complexity and screening-compatible reproducibility stays still a technical challenge (Fang and Eglén, 2017).

3.4.3. Organs-on-chips

An organ-on-a-chip refers to a physiological organ biomimetic system built on a microfluidic chip (Fang and Eglén, 2017; Wu et al., 2020). Key parameters including position, shape and function of the cells in cultures can be precisely controlled using microfluidics. Chemical and physical microenvironment can be also regulated such as concentration gradients, shear force or cell patterning (Quan et al., 2020; Wu et al., 2020)

A wide range of organs- on-chips has already been developed including lung, liver, heart and kidneys. This complex technology, which can recreate organ-level physical microenvironments, tissue-tissue interfaces and vascular perfusion, is a powerful tool to study human biology. The devices, still in development, are complex and significant variation and inconsistency are observed between different manufacturers or users (Ingber, 2018). So, considering the equipment required, this model was not selected for this work.

3.4.4. Three-Dimensional Bioprinting

3D bioprinting is a process of fabricating of biocompatible materials, living cells and supporting components into complex 3D functional living tissues (Murphy and Atala, 2014; Vijayavenkataraman et al., 2018). This technology is based on an accumulation layer-by-layer of biomaterials and cells, which are spatially controlled during the entire printing process (Murphy and Atala, 2014). The challenge is to reproduce the complex micro-architecture of ECM components and the multiple cells types in sufficient resolution to recapitulate biological function (Ma et al., 2018). These are several approaches to 3D bioprinting, including biomimicry, autonomous self-assembly and mini-tissue building block (Murphy and Atala, 2014). The approach allows rapid printing of personalized tissues/organs and co-culture ability. However, challenge remain associated with cell and material requirement. The tissue maturation and functionality is not yet fully mastered (Fang and Eglén, 2017). Then, the overly complex process of creation and the expensive device prevent its use in our work context.

3.4.5. Scaffolds and hydrogels

Scaffold-based models have emerged as a promising model since they reproduce the dynamic interactions that occur *in vivo* between the cells of the tumor microenvironment and the surrounding ECM. In particular, they mimic salient elements of the ECM, support cell adhesion and protein sequestration (Caliari and Burdick, 2016). They can also trigger signaling events capable of stimulating *in vivo* like morphology and gene expression (Chen et al., 2012; Ferreira et al., 2018).

In contrast to spheroids that produce their own ECM after a period of culture maintenance, scaffold-based 3D models dispose of a pre-existing matrix (Caliari and Burdick, 2016; Costa et al., 2016; Ferreira et al., 2018). Sometimes called hydrogels because of their capacity to retain significant amount of water, these 3D network structures can be classified in two categories: the synthetic or natural scaffolds (Catoira et al., 2019).

On the one hand, the synthetic hydrogels are based on the use of biocompatible polymeric materials such as poly(ethylene glycol) (PEG). They present advantages of better stability, lower batch-to-batch variability and higher mechanical properties than natural ones (Caliari and Burdick, 2016). On the other hand, natural scaffolds mostly use natural compounds derived from ECM such as Matrigel and collagen. Matrigel, a basement membrane-derived preparation extracted from mouse sarcoma tumors, is widely used in cell studies while collagen is gaining widespread popularity due to its abundance in the native ECM (Caliari and Burdick, 2016). It is the main structural protein of

most hard and soft tissues, representing 25% by dry wet of total protein *in vivo* (Antoine et al., 2014; Dong and Lv, 2016). Thereby, collagen exhibits strong biomimetic properties. Biocompatible, biodegradable and non-toxic, it provides a native viscoelastic environment for embedded cells, mimicking physiological conditions (Antoine et al., 2014; Caliri and Burdick, 2016; Catoira et al., 2019; Curtin et al., 2018; Dong and Lv, 2016).

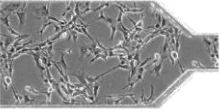
These 3D systems are easy to handle and fast to create. They can be kept in culture for several weeks. They are highly reproducible and can be easily transferred.

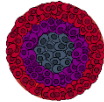

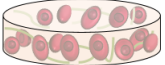
However, the main drawbacks of the collagen-based models stay their properties that may vary depending on parameters of fabrication (collagen source and batch-to batch variability, influence of the temperature, pH and concentration on the polymerization process...). In addition, because of the diffuse capacity of collagen, the diffusion gradients are low (nutrients, oxygen, other soluble bioactive molecules ...) (Antoine et al., 2014; Sarem et al., 2019). Regarding our set of specifications, these constraints do not appear as major obstacles. Experimental solutions may be proposed to overcome these weaknesses.

3.4.6. Summary

To fill the gap and bring *in vitro* experiments one stage closer to the *in vivo* application, several 3D cells models have emerged. These cultures circumvent the limitations imposed by 2D monolayer cultures such as their inability to reproduce the tumor microenvironment. 3D models restore the presence of an ECM and enhance the reliability and predictability of clinical efficacy while avoiding ethical and financial constraints of animal experiments.

As summarized in Table 1 - Advantages and disadvantages of the preclinical models, many 3D cell models exist, from the simplest to the most complicated, and none is perfect. The degree of complexity and predictability seems to bear an inverse relationship (Khaitan and Dwarakanath, 2006). The more complex the model, the less straightforward it will be to dissect clear mechanisms because of increased heterogeneity and diversity of signals. Therefore, it is necessary to balance the inevitable trade-offs in selecting a model that fits research question (Robertson et al., 2019). With regard to our experimental constraints (see our set of specifications at the beginning of chapter 2), the hydrogel model seems to us the most compatible with our constraints.

MODELS	ADVANTAGES	DISADVANTAGES
<p>2D CULTURES</p> 	<ul style="list-style-type: none"> Easy handling Fast replication Long-term cultures Low cost Good reproductibility Known characterization 	<ul style="list-style-type: none"> Loss of tissue-specific architecture (flat and stretched morphology, adhesion to the plastic substrate) Loss cell-to-cell and cell-to matrix interactions Loss of mechanical and biochemical cues (influencing proliferation, differentiation, gene expression) Lack of vasculature (supporting nutrient and waste transport) and immune system Synchronization of cell cycles Inaccurate assessment of the <i>in vivo</i> response
<p>3D CULTURES</p>	<ul style="list-style-type: none"> Microenvironmental features of human tissues Cell-cell and cell-ECM interactions Restoration of communication signaling pathways Reproduction of a penetration barrier Maintenance of cell morphology (including shape, cytoskeletal organization and types of cell adhesion) Restoration of biological functions (Gene Expression, Growth, Motility, Differentiation) Ability of co-culture Doubling time representative of <i>in vivo</i> cells 	<ul style="list-style-type: none"> Lack of vasculature (supporting nutrient and waste transport) and immune system Reproduction of static or short-term conditions

	<p>Elimination of species differences</p> <p>Rapid experimental manipulations</p> <p>Reproducible experimentation</p>	
<p>Spheroids</p> 	<p>Development of gradients (O₂, nutrients, waste...)</p> <p>Heterogeneous cell populations</p> <p>Specific gene expression</p> <p>Representation of drug resistance</p>	<p>Not standardized methods</p> <p>Maintenance of cultures</p> <p>Difficulty to transfer the sample</p> <p>Non-uniform size (depending on the creation method)</p>
<p>Organoids</p> 	<p>Human organ development</p> <p>Patient specific tumor</p> <p><i>In vivo</i> like complexity and cell heterogeneity</p>	<p>Need of stem cells or organ progenitors</p> <p>May lack key cell types</p> <p>Difficulty to reach <i>in vivo</i> maturity</p> <p>Limited availability</p> <p>Variability in the production</p> <p>Non-trivial analyses</p> <p>Ethical restrictions (human tissue)</p>
<p>Hydrogels</p> 	<p>Easy to use</p> <p>Fast process of creation</p> <p>High reproducibility of created samples</p> <p>Applicability to microplates</p>	<p>Simplistic architecture</p> <p>Limited reproduction of gradients</p> <p>Low mechanical properties (lack of covalent cross- linking)</p> <p>Batch-to-batch variability</p>


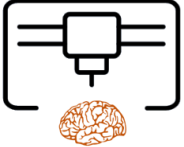

	Enzymatic degradation allowing embedded cells liberation	
<p>Organs-on-chips</p> 	<p>Good reproducibility of the created samples</p> <p>Structural and functional complexities of human organ</p>	<p>Expensive devices</p> <p>Specific skills (microfluidics/microfabrication technics)</p> <p>Non-trivial analyses/Difficult to adapt</p>
<p>3D bioprinting</p> 	<p>Custom-made architecture (patient specific)</p> <p>Presence of chemical and physical gradients</p> <p>High-throughput production</p> <p>Rather fast process</p>	<p>Challenges with cells/materials</p> <p>Highly complex</p> <p>Expensive devices</p> <p>Non-trivial analyses/Difficult to adapt</p> <p>Issues with tissue maturation</p>
<p>IN VIVO</p> 	<p>Conservation of the malignant phenotype and genotype</p> <p>Complexity and cell heterogeneity</p> <p><i>In vivo</i> characteristics (kidney clearance, tumor vasculature, competent immune system for GEMs...)</p>	<p>Ethical constraints</p> <p>High experimental cost</p> <p>Specific installations and specialized skills</p> <p>Long process (from animal creation to monitoring)/Mice availability</p> <p>Influence of the murine microenvironment (PDX)</p> <p>Differences with human response (efficiency, side effects, progression...)</p> <p>Tumor heterogeneity partly restored (GEMs)</p> <p>Tumoral variability: frequency, latency, growth (GEMs)</p>

Table 1 – Advantages and disadvantages of the preclinical models

3.5. Summary of the state-of-the-art

The presence of NPs in cells coupled with irradiation induces processes at different scales (physical, chemical and biological). The characterization of these mechanisms and their impact is an important challenge to better predict and evaluate the efficacy of a new therapeutic strategy, prior to clinical trials. Translational research, which aims at transforming a scientific concept into a clinical application, requires new preclinical models adapted to the strategies based on the combination of NPs with radiations.

2D are too simple because they don't reproduce the influence of the native tumor microenvironment. *In vivo* studies allow to capture the three dimensions of tumor architecture and to reproduce important signaling dynamics that occur in patients (cell-cell and cells-to-ECM interactions). They provide information on biodistribution and treatment efficacy, which is of great interest for clinical transfer. However, they are expensive and time-consuming.

In this context, 3D cells models have been proposed to bring *in vitro* experiments on a stage closer to the *in vivo* application, circumventing the barriers imposed by animal studies. In the field of treatments combining NPs and radiations, the presence of an ECM impacts both the NP internalization as well as the effectiveness of radiations.

Various models have been developed. Their choice is the result of a compromise between reproducibility, predictability and ease to use.

Based on this state-of-the-art, we chose a 3D model adapted to our need. It will be presented in the next chapter which includes its production process and its complete characterization.

The content of this chapter has been accepted for publication to the journal *Frontiers in Bioengineering and Biotechnologies*, section *Tissue Engineering and Regenerative Medicine* as follows:

Maury P., Porcel E., Mau A., Lux F., Tillement O., Mahou P., Schanne-Klein MC. and Lacombe S. (2021) *Rapid Evaluation of Novel Therapeutic Strategies Using a 3D Collagen-Based Tissue-Like Model*. doi 10.3389/fbioe.2021.574035

CHAPTER 2. A 3D COLLAGEN-BASED TISSUE-LIKE MODEL TO EVALUATE THERAPEUTIC STRATEGIES



Femme au béret et à la robe quadrillée (Marie-Thérèse Walter)
Pablo Picasso, 1937, Collection privée

“Essentially, all the models are wrong but some are useful”

– Georges Box
Statisticien américain

Contents

1. INTRODUCTION	33
2. ABSTRACT	34
3. CORPUS	35
3.1. INTRODUCTION.....	35
3.2. MATERIAL AND METHODS	36
3.2.1. <i>Sample preparation</i>	36
3.2.2. <i>Microscopy methods</i>	37
3.2.3. <i>Cell activity in 3D-CCM</i>	38
3.2.4. <i>Oxygen tunability in 3D-CCM</i>	39
3.2.5. <i>Nanoagent monitoring in 3D-CCM</i>	39
3.2.6. <i>Cell response to radiation treatment in 3D-CCM</i>	40
3.3. RESULTS AND DISCUSSION	41
3.3.1. <i>Structural characterization</i>	41
3.3.2. <i>Cell activity</i>	44
3.3.3. <i>Oxygen control</i>	45
3.3.4. <i>Evaluation of drugs/nanoagents uptake in living cells</i>	46
3.3.5. <i>Quantification of radiation effect on cell survival</i>	47
3.4. CONCLUSION.....	49
4. ACKNOWLEDGEMENTS	50
5. SUPPLEMENTARY MATERIALS	50
5.1. SEGMENTATION AND ANALYSIS OF NUCLEI.....	50
5.2. UPTAKE CALCULATION.....	52
5.3. CLONOGENIC ASSAY	52

1. INTRODUCTION

The previous chapter introduced the need to evaluate the effect of treatments with 3D cell models. In view of the strengths and weaknesses of each model presented in the previous section, a set of specifications regarding our experimental constraints has been established (Figure 2.1).

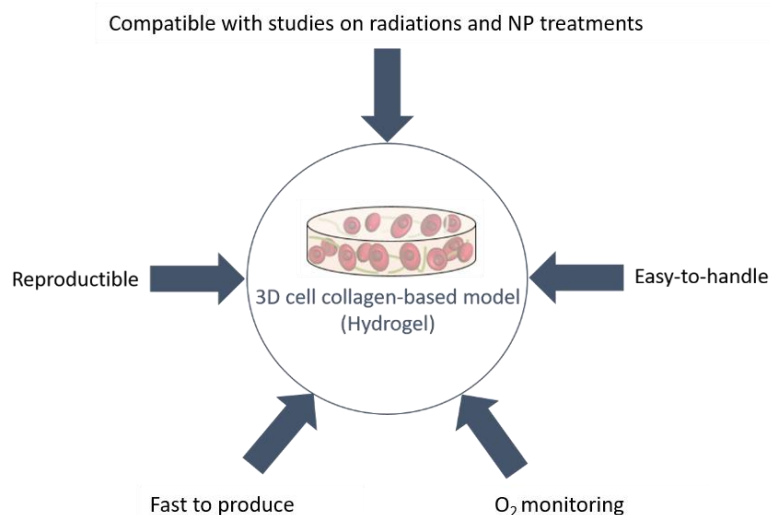


Figure 2.1 - Set of specifications for the 3D cell model optimized for the present studies

First, the degree of complexity must be acceptable. In addition, microscopy, toxicity and irradiations experiments must be possible. Moreover, as for irradiation experiments, we irradiate each sample with a different radiation dose, the reproducibility in the creation process appears as a key parameter to be sure that the differences observed are treatment effects and not due to inter-sample variability.

In addition, as we carry out ions beam irradiations at the NIRS in Chiba, the creation of the samples must be fast (<1 week of preparation) and adaptable worldwide from universal equipments. Hydrogels seem to meet all these criteria.

As presented in the previous chapter, the main criticisms associated with this type of model were a batch-to-batch variability, low mechanical properties and limited gradient reproduction. To overcome these limitations, we have chosen a 3D cell collagen-based model. This system is commercially available (patented by Lonza™ company). The manufacturing process, based on a system of absorbers, seems to us to partially address the problem relative to mechanical stress. All the experiments of a same experiment will be carried out using the same batch of collagen to avoid variability. Finally, a hypoxic chamber will be used to monitor the oxygen concentration in the sample.

This chapter - copy of the paper recently published in *Frontiers*- includes a presentation of the production and optimization protocol of the 3D cellular model, and a characterization of its properties. It is compared to the monolayer cultures traditionally used in the evaluation of treatments.

2. ABSTRACT

2D cell cultures are commonly used to rapidly evaluate the therapeutic potential of various treatments on living cells. However, the effects of the extracellular matrix (ECM) including the 3D arrangement of cells and the complex physiology of native environment are missing, which makes these models far from *in vivo* conditions. 3D cell models have emerged in preclinical studies to simulate the impact of the ECM and partially bridge the gap between monolayer cultures and *in vivo* tissues.

To date, the difficulty to handle the existing 3D models, the cost of their production and their poor reproducibility have hindered their use. Here, we present a reproducible and commercially available “3D cell collagen-based model” (3D-CCM) that allows to study the influence of the matrix on nanoagent uptake and radiation effects. The cell density in these samples is homogeneous. The oxygen concentration in the 3D-CCM is tunable, which opens the opportunity to investigate hypoxic effects. In addition, thanks to the intrinsic properties of the collagen, the second harmonic imaging microscopy may be used to probe the whole volume and visualize living cells in real-time. Thus, the architecture and composition of 3D-CCMs as well as the impact of various therapeutic strategies on cells embedded in the ECM is observed directly. Moreover, the disaggregation of the collagen matrix allows recovering of cells without damaging them. It is a major advantage that makes possible single cell analysis and quantification of treatment effects using clonogenic assay. In this work, 3D-CCMs were used to evaluate the correlative efficacies of nanodrug exposure and medical radiation on cells contained in a tumor like sample. A comparison with monolayer cell cultures was performed showing the advantageous outcome and the higher potential of 3D-CCMs. This cheap and easy to handle approach is more ethical than *in vivo* experiments, thus, giving a fast evaluation of cellular responses to various treatments.

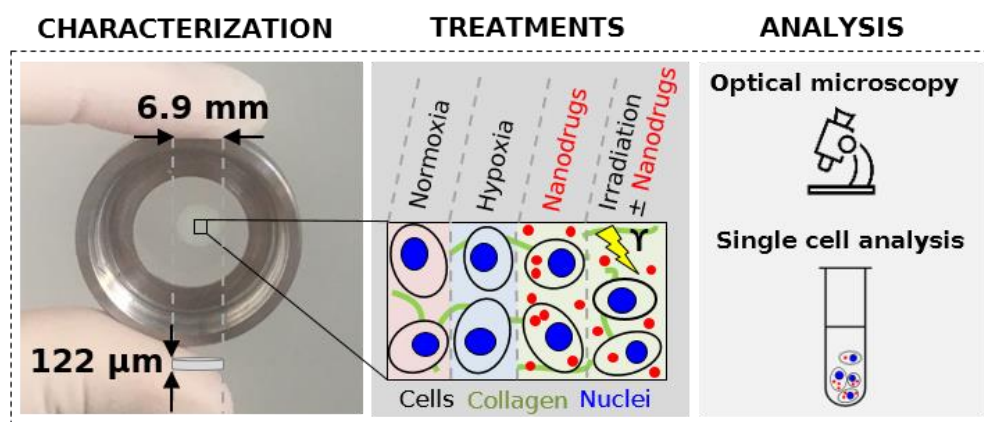


Figure 2.2 – Graphical abstract: 3D cell collagen-based model with tunable environment conditions (oxygen concentration, nanodrug exposure, radiations)

3. CORPUS

3.1. Introduction

In vitro cell models are commonly used to study the cause and progression of diseases, to predict treatment effectiveness and to analyze drug-induced toxicities (Bell et al., 2016; Magdeldin et al., 2014; Rayner et al., 2019). Monolayer cultures have led to numerous advances even if success at the bench does not always translate into success at the bedside. Despite their accessibility and low cost, the current 2D models do not faithfully mimic *in vivo* tissue conditions (Achilli et al., 2012; Lazzari et al., 2017). Simple spatial organization appears to be a major drawback: the predominance of the cell-surface attachment allows the cells to spread which modifies their morphology and behavior (Eke and Cordes, 2011). In addition, in 2D cultures, cells are bathed in a standard cell culture medium whose composition differs from that of the cellular microenvironment. *In vivo*, cells are surrounded by a natural structure, the extracellular matrix (ECM), which acts as a structural and biochemical support. The ECM, which is primarily composed of water, proteins and polysaccharides, provides a mechanical framework that influences cell shape, stiffness and adhesion (Ghosh et al., 2007; Pedersen and Swartz, 2005; Qiu et al., 2017). The ECM also permits communication between cells via the transmission of biochemical signals and plays a crucial role in the regulation of numerous cell functions such as proliferation, differentiation and gene expression (Even-Ram and Yamada, 2005; Walker et al., 2018). These essential communication pathways involving the ECM-cell and cell-cell interactions cannot be reproduced in 2D cultures. Finally, in 2D monolayers cells have direct access to molecular oxygen. In this case, mass transport and diffusion phenomena are too simplistic and not representative of the various conditions encountered in the cytoarchitecture of native tissues.

In this perspective, 3D cell models have been developed to overcome the limitations of the current 2D models. Even if all aspects of the microenvironment cannot be fully captured such as vascularization and circulation processes, reticuloendothelial and hepatic uptakes or local immune repose, *in vitro* 3D models recreate numerous features of living cells. The presence of an ECM makes the models more architecturally and physiologically relevant and allows a more realistic evaluation of the cell response (Achilli et al., 2012; Benien and Swami, 2014; Costa et al., 2016; Cui et al., 2017; Lazzari et al., 2017; Nath and Devi, 2016; Ryu et al., 2019). For instance, when cells are irradiated in 2D and 3D models, substantial differences in the DNA damage response are observed (Sedelnikova et al., 2007; Storch et al., 2010; Suzuki et al., 2010; Zhao et al., 2015), specifically in cell cycle arrest (Topsch et al., 2007; Walenta and Mueller-Klieser, 2016) and repair kinetics (Acheva et al., 2014; Asaithamby et al., 2011).

In the field of nanotoxicity, Belli and coworkers (Belli et al., 2017b) showed that monolayer cultures are not fully suitable to study the NP internalization because the membrane area in contact with NPs is smaller than for 3D cells. The adhesion of the cells to the plastic substrate induces a reduction of the exposure area. In 3D, the surface of interaction is higher because only the parts of cells contact cannot be exposed to NPs. Moreover, in the absence of ECM, NPs interact directly with the cell membrane, which may modify their uptake. So, 3D-CCMs better reproduce the microenvironment of NPs interacting with cells. Finally, drastic modifications in cytoskeletal arrangement and cell membrane tension were observed in cells cultured in 2D models. This effect, avoided in the case of 3D samples, strongly influences internalization pathways (Storch et al., 2010).

There is therefore an undeniable interest to model nanoagents diffusion in the presence of the ECM to better predict *in vivo* therapeutics behavior (Anderson et al., 2006; Gomez-Roman et al., 2016; Leeman et al., 2002). Currently, two types of 3D cellular models have emerged: (i) scaffold-based

3D models (*i.e.*, hydrogels) and (ii) non-scaffold-based 3D models (*i.e.*, spheroids) (Chaicharoenaudomrung et al., 2019; Ferreira et al., 2018; Lazzari et al., 2017). In spheroids, ECM is produced after a period of culture maintenance, whilst scaffold-based 3D models dispose of a pre-existing matrix (Caliari and Burdick, 2016; Costa et al., 2016; Ferreira et al., 2018). In this study, collagen was used as matrix because of its biomimetic properties. Biocompatible, biodegradable and non-toxic, it provides a native viscoelastic environment for embedded cells, mimicking physiological conditions (Antoine et al., 2014; Caliari and Burdick, 2016; Catoira et al., 2019; Curtin et al., 2018; Dong and Lv, 2016). The hydrogels produced are less fragile and easier to manipulate than conventional spheroids (Achilli et al., 2012; Lin and Chang, 2008; Vadivelu et al., 2017). In the present work, the robustness and the preparation reproducibility of commercial 3D cell collagen-based models (3D-CCMs) were assessed. In this purpose, the structure and the size of the samples were characterized as well as the viability and the metabolic activity of the cells. By tuning the oxygen concentration in the environment, we probed the capacity of the sample to mimic hypoxia tissues, such as found in highly lethal and radioresistant tumors (Hirayama et al., 2005; Jiang et al., 2011; Wang et al., 2019). Finally, the performance of 3D-CCM as a tissue-mimicking model was probed by studying the cell uptake and toxicity of Gd-based NPs as well as NPs impact on radiation effects on HeLa cells.

3.2. Material and Methods

3.2.1. Sample preparation

This 3D model was first implemented using HeLa human cervical adenocarcinoma cells (ATCC[®] CCL-2TM) and most of the experiments were performed with this immortalized cell line. For comparison, primary dermal fibroblasts (ATCC[®] PCS-201-010TM) (human fibroblasts derived from the foreskin of male African newborn with spindle-shaped morphology) were used for 3D-CCM characterization and evaluation of the reproducibility. All the cells were purchased in 2016 from ATCC[®] (ATCC France, Molsheim, France). Several ampoules containing cells at early passage were then generated and frozen to have a stock. HeLa cells were used until passage 25 and fibroblasts until passage 15 before returning to stock.

a. Cell culture

Adherent cells were cultured in monolayer in complete medium composed of Dulbecco's Modified Eagle Medium supplemented with 10% fetal bovine serum, 1% penicillin and 1% streptomycin (Life Technologies[™]). The cells were plated in T-75 flasks and maintained in an incubator at 37°C and 5% CO₂. Once cells were confluent, they were harvested using trypsin. Some cells were seeded on a plastic substrate and maintained in monolayer conditions for experimental use in 2D models. The remainder of the cells was collected to prepare 3D-CCMs according to the protocol described below.

b. 3D-CCM production

3D-CCM was produced using a RAFT[™] kit (Lonza[®]) according to the protocol distributed by the manufacturer (Lonza, 2016).

First, the HeLa cell suspension obtained from the cell culture was centrifuged at 20°C for 7 min at 1100 rpm and resuspended to obtain an appropriate concentration of 2.4-2.6 x 10⁷ cells/ml, as determined by a Luna (Logos Biosystems[®]) automated cell counter.

This cell solution was homogeneously mixed with 10X Modified Eagle Medium, neutralizing solution and 2 mg/ml rat-tail type I collagen solution (diluted in 0.6% acetic acid) to obtain a mixture of cells embedded in collagen in the liquid phase with a dilution rate of 4.2%.

During this process, all liquids were maintained at 4°C and kept on ice to prevent unwanted polymerization. To reduce uncertainty and batch-to-batch variability, all samples used in the same experiment were prepared from the same solution.

A volume of 320 µl from this solution was dispensed into each well of a 96-well culture plate to seed around ~350 000 cells per 3D-CCMs. After 15 min in the incubator, RAFT™ absorbers were finally placed at room temperature on top of each well for 15 min to obtain the hydrogels.

Then, 200 µl of fresh complete medium was added to each well after collagen gel formation and 3D-CCMs were maintained in the incubator during 12 to 36 h prior to the experiment performed.

For model characterization purposes, 3D-CCMs were also prepared with human primary dermal fibroblasts following exactly the same process. These samples were prepared with a cell suspension at a concentration of 5.3×10^6 cells/ml to obtain 72 000 cells per 3D-CCM.

The production of this model is a rapid process (requiring approximately two hours) and a simple procedure that can be developed in conventional biology laboratories.

3.2.2. Microscopy methods

Structural characterization of 3D-CCMs was performed using complementary microscopy techniques. Fluorescence techniques (confocal and multiphoton microscopy) were used to image 3D-CCM, while transmission images allowed the visualization of cell morphology on living samples.

a. Confocal microscopy

Confocal images of 3D-CCMs were acquired with a LEICA SP5 confocal system. Cell nuclei and the plasma membrane were stained for 30 min with a 1 µmol/L Hoechst 33342 solution (exc: 350 nm/em: 461 nm) (Thermo Fisher Scientific®) and Cell Mask™ Deep Red Actin tracking Stain (Invitrogen™) respectively. Data acquisition was performed with a scan speed of 400 Hz. Field of view (FOV) and pixel sizes used were reported in the legend of the figures. For each sample, transmission images were captured together with the fluorescent images.

b. Multiphoton microscopy

Multiphoton microscopy was the method used to characterize the model structure. This technique has an improved penetration depth within scattering samples relative to confocal microscopy. Thus, 3D images may be recorded along the full depth of the sample. Moreover, multiphoton microscopy provides complementary modes of contrast, notably SHG, which allows specific imaging of fibrillary collagen without any labeling. The combination of SHG and 2PEF thus enables the simultaneous detection of the collagen of the 3D sample and the cell nuclei, without any cross-talk, which results in the availability of multimodal z-stacks for further analysis (Strupler, 2008).

Sequential 3D acquisitions were performed with a commercial multiphoton microscope (TriM Scope II, LaVision BioTec) equipped with two ultrafast oscillators (Mai Tai HP DeepSee, $\lambda = 690-1040$ nm,

Spectra Physics and Insight DeepSee, $\lambda = 690\text{-}1300$ nm, Spectra Physics) and a low magnification and high NA microscope objective (25x 1.05NA, XLPLN25XWMP2, Olympus).

Collagen was imaged using second harmonic imaging microscopy derived from a nonlinear optic effect termed second harmonic generation (SHG). The signal is generated by a beam of the Insight DeepSee laser set at $\lambda = 1150$ nm. The SHG scattered light centered approximately 575 nm was detected by a photomultiplier tube placed in transmission (H7422-40, Hamamatsu) and separated from the laser light by a dichroic mirror (Di02-R635, Semrock) and an interference filter (FF02-575-25, Semrock).

Cell nuclei were mapped by two-photon excitation microscopy. Two-photon fluorescence (2PEF) was generated by the fluorophore Hoescht 33342 when irradiated by the laser beam from the MaiTai set at $\lambda = 830$ nm after 30 min of staining with a $1 \mu\text{mol/L}$ Hoescht 33342 solution (Thermo Fisher Scientific®). The signals were collected in epidetection mode by a photomultiplier tube (H6780-01, Hamamatsu) and separated from the laser light by a dichroic mirror (T695lpxr, Chroma) and an interference filter (FF01-450-70 or FF01-460-80, Semrock). Data acquisition was performed on a $350 \mu\text{m}$ square field of view with a pixel size of $0.192 \mu\text{m}$ and an acquisition frequency of 400 Hz. Images were captured with a z-step of $1 \mu\text{m}$.

c. Image processing

Two parameters were investigated to determine the reproducibility of the production method: sample thickness and cell distribution. The volume and shape of 3D models are known to be sources of variability that can lead to different treatment responses (Zanoni et al., 2016). Thus, size uniformity is a key parameter that was evaluated from sample thickness measurements. This parameter was calculated from the acquired SHG stacks according to the determination of a z-range containing a detectable collagen signal.

In parallel, we developed a Python code (V. 3.7) to analyze the cell distribution inside 3D-CCMs. Our program is open-access, available online on Zenodo (DOI: 10.5281/zenodo.3814365) and described in detail in the Supplementary Materials. Briefly, each 2PEF image stacks were thresholded to create binary images. The small areas ($< 3 \text{ pixel} \times 3 \text{ pixel}$) were removed from the binary image and all cell nuclei contained in the stack were detected and isolated. Their three-dimensional position was determined using a centroid function. Finally, the minimum distance between two nuclei was calculated for the entire population of nuclei contained within 3D-CCMs.

3.2.3. Cell activity in 3D-CCM

a. Cell viability

The viability was evaluated 28h after sample creation to determine the fate of cells embedded in the matrix. To extract cells from 3D-CCMs, samples were washed with 1X PBS and disaggregated in 1 mg/ml collagenase purchased from *Clostridium histolyticum* (Sigma-Aldrich®). After 30 min at 37°C , the collagenase was inactivated with complete medium and ethylenediaminetetraacetic acid solution (EDTA, Sigma-Aldrich®). Cells were stained with trypan blue and counted with a Luna automatic cell counter (Logos Biosystems®) which provides total, live and dead cells numbers, and so the cell viability. Viability study was performed 28 h after the 3D-CCM creation.

b. Cell plating efficiency

Cell plating efficiency (PE) was determined for each type of culture. For the 3D culturing, this was performed after cells recovering according to the protocol described in paragraph a. In both cases, cells were plated in 100 mm diameter Petri dishes (Thermo Fisher) to obtain a density of 100 surviving cells per dish. The PE determined were $37\% \pm 11\%$ (n=8) for the cells extracted from the 3D cell culture and $61\% \pm 3\%$ (n=2) for the cells from the monolayer culture.

c. Cell proliferation assay

The metabolic activity of the cells was examined using a MTT (3-(4,5-dimethylthiazol-2-yl)-2,5-diphenyltetrazolium bromide) assay. In this goal, 3D-CCMs were prepared to obtain ~50 000 cells/sample. 3D-CCMs were successively exposed in a 96-well plate to 125 μ l of tetrazolium dye MTT 3-(4,5-dimethylthiazol-2-yl)-2,5-diphenyltetrazolium bromide and incubated at 37°C for 4 h. Then, 125 μ l of lysis buffer were added to dissolve the formazan crystals. Cellular viability and proliferation were measured at three time points after the sample creation: 12 h (Day 0), 33 h (Day 1) and 57 h (Day 2). Absorbance, proportional to the number of living and metabolically active cells, was quantified using a Glomax[®] Microplate reader (Promega[®]) (absorbance 560nm) and compared to the absorbance of a negative control treated with 200 μ l of a 500 μ mol/L toxic solution of menadione for 4h.

3.2.4. Oxygen tunability in 3D-CCM

The oxygen concentration in 3D-CCMs was tuned using the hypoxia workstation Hypoxylab[™] (Oxford Optronix[®]) where the concentration in oxygen (pO₂) and in carbon dioxide (pCO₂), as well as the temperature and the humidity can be set. Before adding the cell models, each well of a 96-well plate was filled with 320 μ l of supplemented medium and maintained in the hypoxic workstation overnight to reach the level of the chosen O₂ pressure. 3D-CCMs were then transferred to the wells inside the hypoxic device. The pO₂ in 3D-CCMs was measured using the *in situ* sensor Oxylite[™] (Oxford Optronix[®]), which provides real-time information. A minimum of ten samples was considered for each measurement. A comparison with 2D was performed by measuring the pO₂ value inside 5 flasks of monolayer cultures with 3 measurements for each. For each value, the conversion from mmHg to %O₂ was carried out according to the Eq 12:

$$\%O_2 = \frac{[\text{mmHg } O_2]}{[\text{atmospheric pressure in mmHg}]/100} \quad \text{Eq. 12}$$

3.2.5. Nanoagent monitoring in 3D-CCM

3D-CCMs were used to study the migration, uptake and toxicity of nanoagents. Gd-based NPs called AGuIX[®], which are currently being tested in the clinic and were provided by NH TherAguix (Lyon, France) were considered here. AGuIX[®], composed of a polysiloxane matrix and Gd chelates, have a hydrodynamic diameter of 5 nm and a negative surface charge (Lux et al., 2018). They can be tagged with a Cyanine 5.5 fluorescent marker (AGuIX[®]-Cy5.5) for microscopy experiments (Bridot et al., 2007; Louis et al., 2005). In this study, all the concentrations of AGuIX[®] are expressed in the concentration of Gd³⁺, *i.e.*, 1 mmol/L of Gd, which corresponds to 0.1 mmol/L of NPs.

a. Internalization monitoring

The localization of nanoagents in 3D-CCMs was monitored by confocal microscopy according to the methodology described in section a. From this perspective, the samples were prepared according to the protocol described in section 3.2.1. Briefly, 240 μ l of 1 mmol/L AGuIX[®]-Cy5.5 was used to expose ~350 000 HeLa cells/sample to the agents over 4 h. NPs emission was detected on a 655-740 nm spectral range upon excitation at 633 nm.

b. Uptake monitoring

The mass of Gd contained in the samples was determined at the Ultra Trace Analyses Aquitaine (UT2A) Technological Center, Pau, France, using an Agilent 7800 ICP-MS (Agilent Technologies[®]). The objective was to determine the relative amount of AGuIX[®] that was internalized by the cells and the amount of AGuIX[®] that was trapped in the collagen. In this goal, six samples containing cells and collagen (3D-CCMs) were prepared. All samples were incubated in 240 μ l of 1 mmol/L AGuIX[®] solution for 4 h. The composition of the collagen-based model allowed for sample disaggregation according to the protocol given in section 3.2.3, aa, in order to extract the cells and make a dosage of the Gd contained inside. Details of the uptake calculation are given in Supplementary Material section 5.2.

3.2.6. Cell response to radiation treatment in 3D-CCM

3D-CCMs were used to perform a clonogenic assay to evaluate treatment-induced cell death. However, sample disaggregation methodology could also be used to predict the efficacy of chemotherapy (Alberts, 1980; Liu et al., 2020), drugs (Law et al., 2020) or photothermal therapy (Zhang et al., 2019). Specifically, we investigated in this work the effect of AGuIX[®] on cellular damage induced by gamma irradiation.

Sample preparation. For each irradiation experiment, fourteen 3D samples were prepared 36 h before irradiation according to the protocol described in section b. AGuIX[®] were added to 3D-CCMs 18 h before irradiation at a concentration of 0.5 mmol/L in Gd. This concentration is known to be non-toxic to the cells (Lux et al., 2011; Porcel et al., 2014).

Irradiation. Irradiation was performed under atmospheric conditions with a 662 keV Cesium (¹³⁷Cs) gamma source located at Institut Curie, Orsay (GSR-D1, RadeXp).

Clonogenic assay. Samples were then disaggregated according to the protocol given in section 3.2.6. For each irradiation dose, three Petri dishes were prepared. Cells were then incubated for 15 days before fixation and staining in a solution of 50% methanol/50% methylene blue. Colonies consisting of at least 50 cells were counted. The survival fractions (SFs) were determined as the number of colonies counted divided by the product of the plating efficiency (PE) with the cell seeding.

Statistical analysis. A statistical analysis of the colony formation assay results was performed with the software package CFAssay for R (R Core Team, R: A Language and Environment for Statistical Computing, 2014). The F-test was performed based on the maximum likelihood (ML) method, which was described in 2015 by Braselmann and colleagues (Braselmann et al., 2015). The complete statistical analysis is provided in the Supplementary Materials, section 5.3.

3.3. Results and discussion

3.3.1. Structural characterization

a. Sample thickness

3D-CCMs produced in 96-well plates have uniform radial size of 6.9 mm corresponding to the well diameter. However, due to the vertical compression exerted by the absorbers during the production process (see section b), a variability in the z direction was expected.

The sample thickness was measured using the SHG collagen signal of each sample stack. The average thickness obtained on seven samples was $122 \mu\text{m} \pm 4 \mu\text{m}$, as shown in Figure 2.3 - (A) Thickness of 3D-CCMs composed of HeLa cells (n=7), (B) Comparison of the coefficient of variation (CV) obtained from the 3D-CCM thickness measurements (blue dashed line) with the CVs reported in the literature for spheroids of uniform sizes obtained by different methods: pellet culture (in pink), microwell arrays (in green), microfluidic devices (in red), hanging drop method (in black) or other (in yellow). The use of variation bars instead of square points illustrates the dependency of the CV to different parameters (cell seeding density, size of the well). The coefficient of variation (CV) (%), defined as the standard deviation divided by the mean height, was equal to 3.2%. This parameter was directly used to characterize the reproducibility of the sample preparation and compared with the values of the literature. A quantitative comparison of CV obtained with 3D-CCMs and the ones reported in different studies is illustrated in Figure 2.3 - (A) Thickness of 3D-CCMs composed of HeLa cells (n=7), (B) Comparison of the coefficient of variation (CV) obtained from the 3D-CCM thickness measurements (blue dashed line) with the CVs reported in the literature for spheroids of uniform sizes obtained by different methods: pellet culture (in pink), microwell arrays (in green), microfluidic devices (in red), hanging drop method (in black) or other (in yellow). The use of variation bars instead of square points illustrates the dependency of the CV to different parameters (cell seeding density, size of the well) (Chen et al., 2016; Gong et al., 2015; Kang et al., 2015; Kwak et al., 2018; Sarkar et al., 2018; Shi et al., 2018; Thakuri et al., 2019; Zaroni et al., 2016).

Among the methods used to produce spheroids, three of them resulted in spheroid size uniformity: the pellet culture method, the hanging drop method and the spheroid preparation using microfluidic devices (Achilli et al., 2012; Benien and Swami, 2014; Cui et al., 2017; Lin and Chang, 2008). Zaroni and colleagues estimated the equivalent mean diameter of many of these spheroids and their associated standard deviations (Zaroni et al., 2016). The pellet culture method gives the best results in terms of size uniformity. With a spheroid diameter of $880 \mu\text{m}$, the standard deviation of $21 \mu\text{m}$ leads to a CV of 2.4%. However, this approach is often neglected because its yield is low, the shear stress induces damage and the spheroids are difficult to manipulate (Achilli et al., 2012; Lazzari et al., 2017; Lin and Chang, 2008). With the hanging drop method, the variability is much higher than the one obtained for 3D-CCM: the standard deviation is $95 \mu\text{m}$ for a diameter of $359 \mu\text{m}$ (CV=26.5%) (Zaroni et al., 2016). The use of patterned surfaces and microfluidics systems is an attractive strategy despite the tedious transfer of the created samples and the cost of the equipment (Lazzari et al., 2017). The samples generated in a controlled environment, present a uniform size which depends on the size of the wells (Kang et al., 2015; Lee et al., 2018) or on the initial cell seeding density (Chen et al., 2016; Gong et al., 2015; Kwak et al., 2018; Sarkar et al., 2018). The CV depends on these parameters as illustrated in Figure 2.3B.

For a concentration similar to ours (i.e 1×10^6 cells/ml), Kwak and coworkers obtained a CV of 22% (Kwak et al., 2018). So, the 3D-CCM CV is one of the lowest, which shows that the model is one of the most reproducible systems.

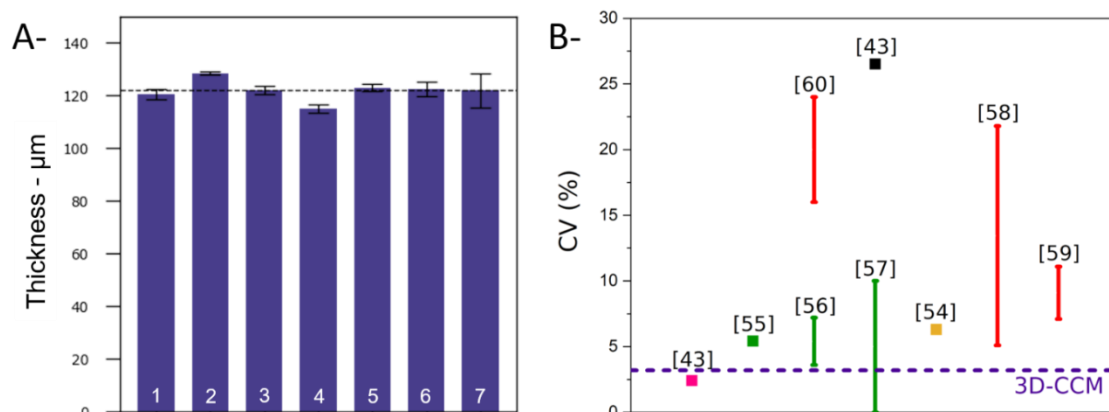


Figure 2.3 - **(A)** Thickness of 3D-CCMs composed of HeLa cells ($n=7$), **(B)** Comparison of the coefficient of variation (CV) obtained from the 3D-CCM thickness measurements (blue dashed line) with the CVs reported in the literature for spheroids of uniform sizes obtained by different methods: pellet culture (in pink), microwell arrays (in green), microfluidic devices (in red), hanging drop method (in black) or other (in yellow). The use of variation bars instead of square points illustrates the dependency of the CV to different parameters (cell seeding density, size of the well). References given in the figure correspond to : [43] (Zanoni et al., 2016), [54] (Shi et al., 2018), [55] (Thakuri et al., 2019), [56] (Kang et al., 2015), [57] (Gong et al., 2015), [58] (Kwak et al., 2018), [59] (Sarkar et al., 2018) and [60] (Chen et al., 2016).

b. Cell morphology and distribution in 3D-CCM

The impact of cell morphology on the cell culture is shown in Figure 2.4 with HeLa cells cultivated in 2D (Figure A) and in 3D-CCM (Figure B). In the 3D model, the size of the cell was found smaller and its shape more spherical than in 2D cultures (Belli et al., 2017b). The cell morphology in 3D-CCMs represents better the morphology of cells in tissues (Le et al., 2016). This effect of the culture conditions on the cell shape is explained by the presence of ECM, which exerts constraints on the cytoplasm, influences cell spreading and regulates tissue organization and cell fate (Muncie and Weaver, 2019). A cytoskeletal modification is induced in 2D cultures due to substrate adhesion. Note that a modification of morphology may induce a loss of polarity, which, in turn, may impact growth factor receptors and proliferation pathways (Belli et al., 2017b; Duval et al., 2017; Yamada and Cukierman, 2007).

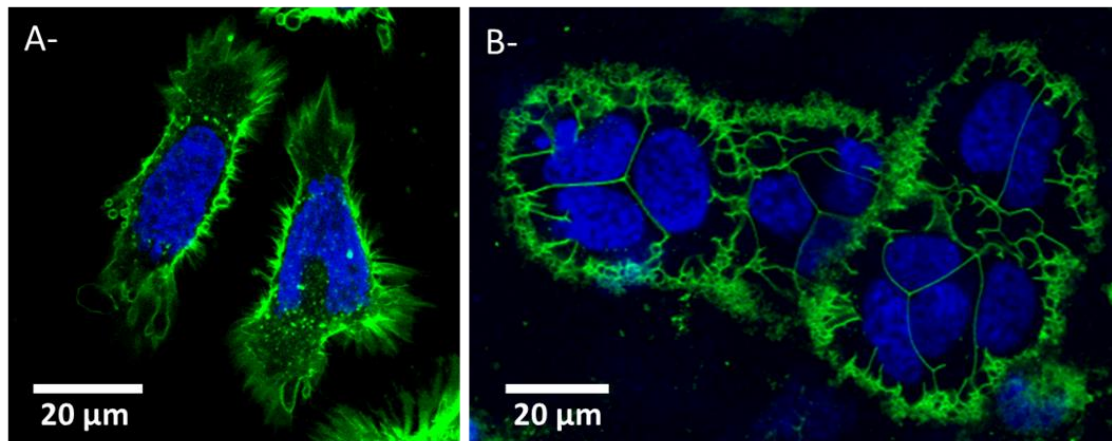


Figure 2.4 - HeLa cells morphology in **(A)** 2D culture and **(B)** 3D cell collagen-based model. Nuclei and plasma membrane are stained in blue and green respectively. Images (A) and (B) were obtained by confocal microscopy (Respective FOV of $82\ \mu\text{m} \times 84\ \mu\text{m}$ and $123\ \mu\text{m} \times 83\ \mu\text{m}$ and respective pixel size side of $0.186\ \mu\text{m}$ or $0.312\ \mu\text{m}$).

The characterization of the cell distribution on the sample is also a key issue to reproduce at best the spatial organization of cells in tissues. For HeLa cells, the concentration of $2.4\text{-}2.6 \times 10^7$ cells/ml (see section b) was optimal to get a tight and homogeneous cell distribution. For comparison, we investigated the cell distribution with fibroblasts. In the latter case, a lower cell density was used to compensate the size difference between the two types of cells. As shown in the 2PEF/SHG images, HeLa and fibroblasts cells presented the same homogeneous cell distribution in 3D-CCM. The images obtained with HeLa are shown only Figure 2.5(A). The number of nuclei obtained in each case, extracted from SHG/2PEF stack measurements, is plotted in Figure 2.5(B) and Figure 2.5(C).

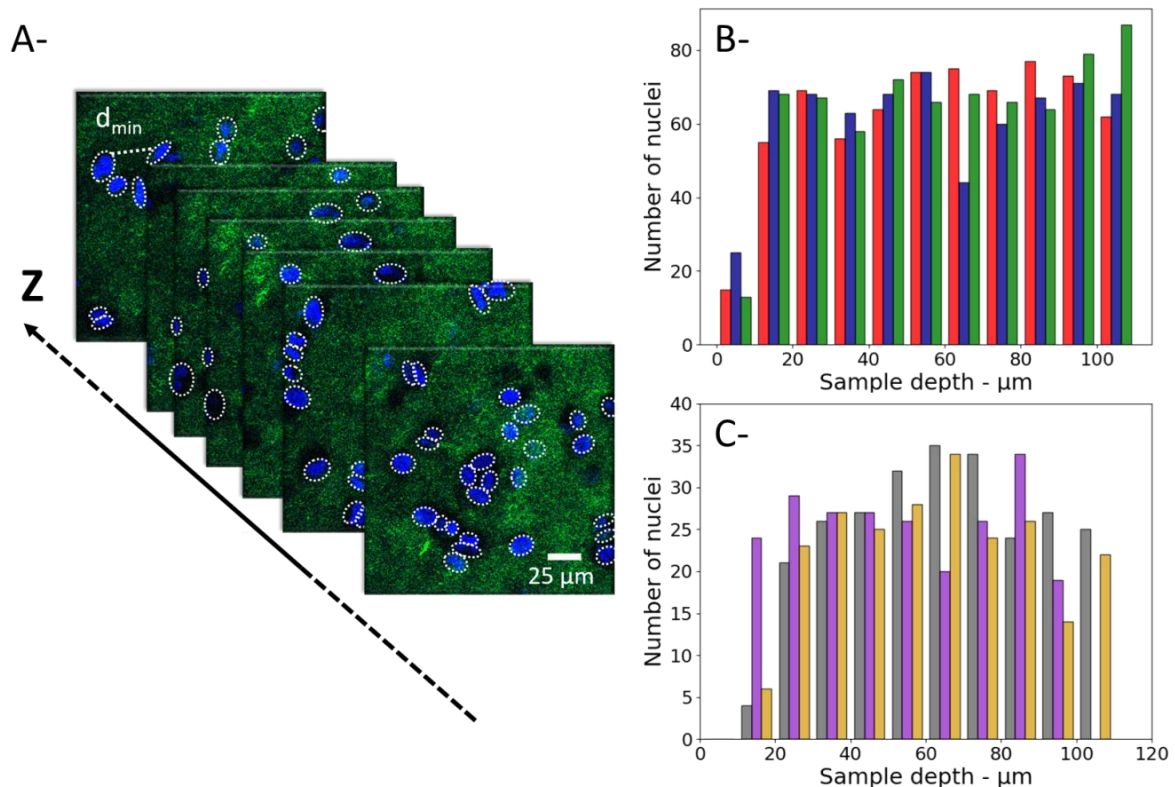


Figure 2.5 - **(A)** 2PEF/SHG images of HeLa nuclei (in blue) embedded in the fibrillary collagen matrix (in green) (FOV of 350 μm x 350 μm , pixel size of 0.192 μm side), **(B)** Number of nuclei as a function of depth for HeLa in 3D-CCMs (n=3, sample 1 in red, sample 2 in blue, sample 3 in green), **(C)** Number of nuclei as a function of depth for fibroblasts in 3D-CCMs (n=3, sample 1 in grey, sample 2 in purple, sample 3 in yellow)

These data show that the cells were evenly distributed along the z-axis and did not fall in the bottom of the sample despite gravity. As expected, more nuclei were found with HeLa cells because of the higher density used in this experiment.

The minimum distance between two nuclei was calculated to characterize the cell distribution in the 3D model (x-y-z directions). The median values of the minimum distances obtained from three different samples are reported in the Figure 2.6. These values vary from 14.3 μm to 15.3 μm with a standard deviation of 0.5 μm (~3.3%) for HeLa, and from 21.5 μm to 23.0 μm with a standard deviation of 0.8 μm (~3.7%) for the fibroblasts.

These values are consistent with that reported in the literature. Internuclear distances of 4 - 30 μm are reported for the tibialis anterior muscle in mice (Stroud et al., 2017). Another study based on hematoxylin and eosin (H&E)-stained images of mouse brain showed that the internuclear distance is lower than 25 μm (Li et al., 2018). In 2017, Yi and coworkers (Yi et al., 2017) reported a method of automatic extraction of cell nuclei from H&E-stained images of human lung tumors in which the order of magnitude of the nucleus-nucleus distance is approximately 10 μm . This distance distribution between nuclei shows that cells are homogeneously distributed in 3D-CCMs, thus faithfully mimicking the distribution of cells in tissues.

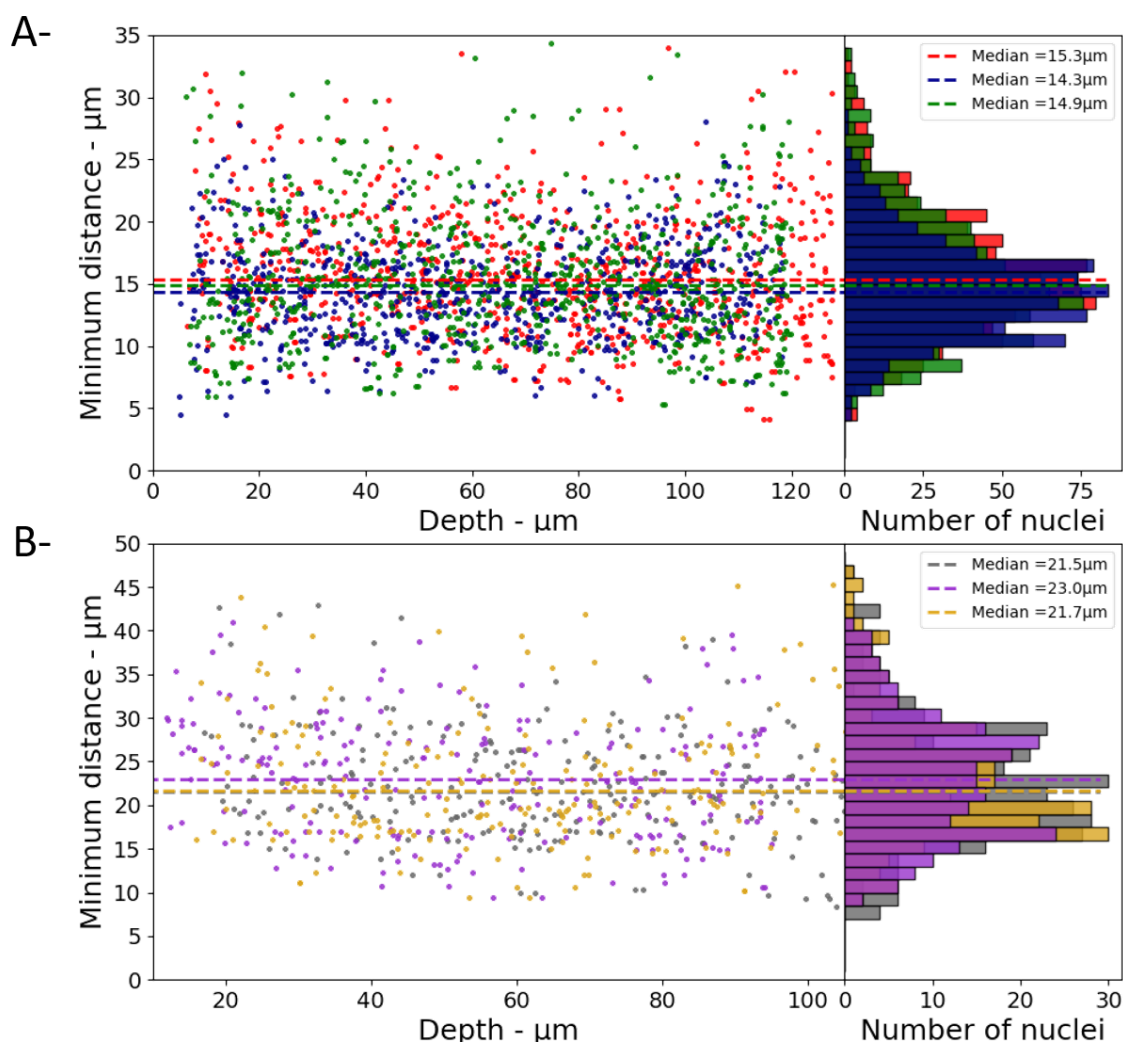


Figure 2.6 - Minimum distance between two nuclei as a function of depth for 3D-CCMs composed of **(A)** HeLa cells **(B)** Fibroblasts (n=3)

3.3.2. Cell activity

As shown in Figure 2.7, a viability higher than 90%, with an average value close to 93%, was observed for all the samples. It indicates that cells stayed alive in 3D cultures for several days. This is confirmed, for instance, by the cell division process observed in the confocal image (Figure 2.4) acquired 48h after the sample preparation.

In parallel, a MTT assay was performed to assess the mitochondrial activity of the cells embedded in the collagen matrix as function of the time after the 3D-CCMs creation. As illustrated in Figure 2.7, the results (in green) were compared to a negative control (in red) composed of dead cells. A strong mitochondrial activity was observed. It proves that the cell metabolism is not impacted even after 57 hours in 3D-CCM. The activity increase attests of the ability of the cells to proliferate. Between the first and the second day (i.e. 11h), the cellular metabolic activity increased by more than 30%. Between the 2nd and the 3rd day, it remained stable, which reflects a slow-down of the cell proliferation. This finding agrees with the literature where a reduced proliferation is observed for a variety of cell lines in 3D cultures (Adcock, 2015; Maria et al., 2011).

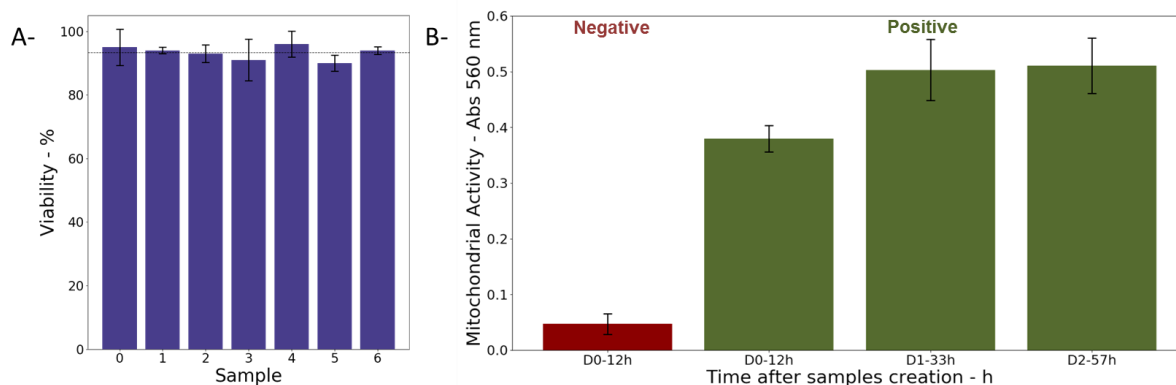


Figure 2.7 - **(A)** Cell viability in 3D-CCMs measured 28 h after model creation. **(B)** Evolution of the mitochondrial activity in 3D-CCMs (in green) quantified by MTT assay as function of the time in the sample. The negative control is shown (in red)

3.3.3. Oxygen control

The oxygen concentration in 3D-CCMs was tuned so as to mimic various tissue environments. In 2D samples, the cells are typically maintained in incubators to reproduce normoxic conditions in a controlled atmosphere of 37°C, 5% CO₂, and 21%-160 mmHg O₂.

In this condition, pO₂ is close to 143 mmHg ± 2 mmHg (19.4% ± 0.2%). In healthy tissues, pO₂ is of the order of 50 mmHg (Wion et al., 2008). In 3D-CCMs, pO₂ measured after one night in the incubator (37°C, 5% CO₂, 21% O₂) is 112 mmHg ± 12 mmHg (14.7% ± 1.5%).

This value is close to pO₂ observed in physiological conditions (i.e. 100 mmHg (13.5%) in body lung alveoli (McKeown, 2014)). The pO₂ depletion observed in 3D cultures is attributed to the O₂ consumption by the cells and not to reduced oxygen diffusion in the matrix (Cheema et al., 2012; Ehsan and George, 2013; Sarem et al., 2019).

Moreover, pO₂ was determined using T-25 flasks for 2D samples and 96 wells plates for 3D-CCMs. Differences of depth from the medium surface, medium volume and cell density are expected to affect pO₂ (Oze et al., 2012; Place et al., 2017; Zhang et al., 2016).

We investigated the oxygen control in 3D-CCMs incubated in different atmospheres. Exposure of 3D samples to a controlled atmosphere containing 18 mmHg of oxygen (2.3%) allowed to artificially reproduce the oxygenation conditions in tumors. We also found that pO₂ increased with the time of exposure of 3D-CCM to hypoxic conditions. pO₂ varied from 0.6 ± 0.3 mmHg after 1 h exposure, to 1.3 ± 1.4 mmHg after 3 h and to 5.6 ± 2.3 mmHg after 5 h. Values below 8 mmHg (1%) are associated to a “pathological hypoxia” (McKeown, 2014). Figure 2.8 summarizes the pO₂ values measured in 2D and 3D cultures in Hela cells exposed to different oxygen conditions (normoxic and hypoxic). They are compared to values reported in the literature for various tissues.

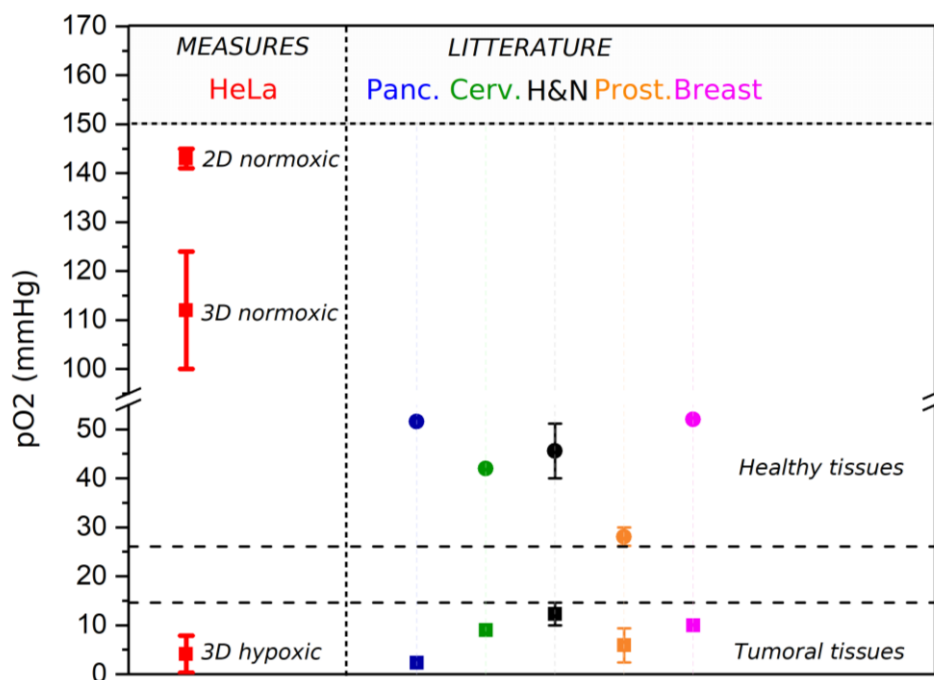


Figure 2.8 - pO₂ measured in 3D and 2D samples (red bold bar) (n=10). It is compared to pO₂ reported in the literature (McKeown, 2014) for tumoral (square) and healthy tissues (circle), such as pancreas (blue), cervix (green), head & neck (black), prostate (orange) and breast (pink). For the values reported from literature, an error bar was represented when several studies were considered.

This experiment demonstrated that 3D-CCM is fully adapted to study the impact of treatments on cells growing in hypoxic tissues such as tumors.

3.3.4. Evaluation of drugs/nanoagents uptake in living cells

The cellular uptake of AGuIX[®] in Hela cells embedded in 3D-CCMs was followed using confocal microscopy (Figure 2.9). The images show the NPs infiltration in the collagen matrix (Figure 2.9B) and cells (Figure 2.9C) after incubation with 0.5 mmol/L AGuIX[®] for 18 h. We observe that the NPs are homogeneously distributed in the collagen matrix. Although the collagen is a natural barrier that hampers the transport of nanoagents (Belli et al., 2017a) and limits the internalization of nano-objects (Costa et al., 2016; Fallica et al., 2012), we found AGuIX[®] aggregates in cells, in the cytoplasm exclusively. No NPs were observed in the nucleus, as already reported in 2D cultures (Figure 2.9A) (Porcel et al., 2014; Štefančíková et al., 2014).

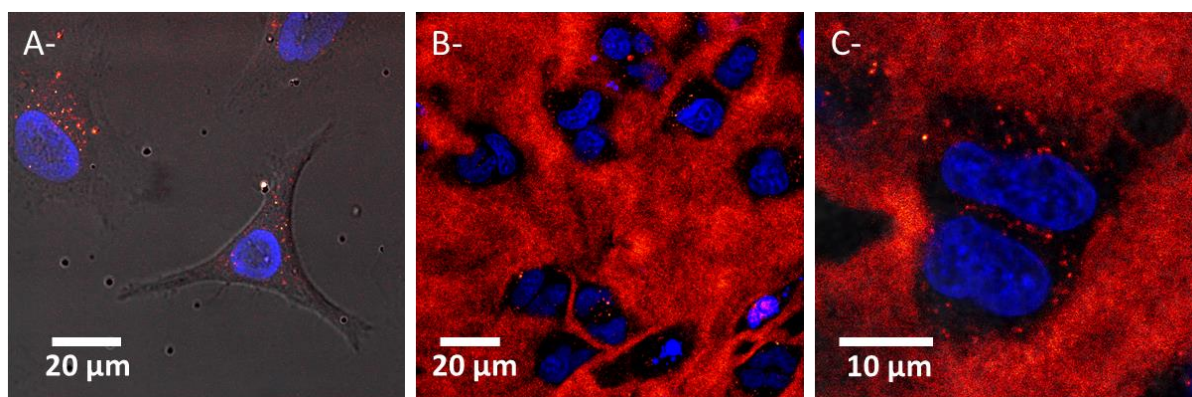
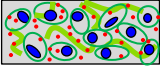
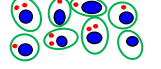


Figure 2.9 - Confocal microscopy images of HeLa cells exposed to AGuIX[®] in **(A)** a 2D culture (FOV of 110 µm x 101 µm, pixel size of 0.229 µm side) and **(B,C)** 3D-CCMs (FOV of 140 µm x 140 µm and 41 µm x 41µm, pixel size of 0.273 µm and 0.080 µm side). Each image results from superimposition of the transmission and fluorescence images. Nuclei and NPs are labelled in blue and red respectively. The black holes correspond to cells (absence of collagen).

The quantification of nanoagents internalized in cells and trapped in the collagen was performed by ICP-MS. In this perspective, 3D-CCMs were disaggregated. The results are presented in Table 2. Quantification of AGuIX[®] determined by ICP-MS. This measurement indicates that, in these conditions of incubation (see 3.2.5), 1.2×10^{13} NPs penetrated in 3D-CCMs, from which 5.9×10^{11} were internalized in the cells (20 times less). It corresponds to internalizations close to 0.1% of NPs in 3D-CCMs and 0.004% in the cells. This result is in agreement with the microscopy observations presented above.

Table 2. Quantification of AGuIX[®] determined by ICP-MS.

	COLLAGEN + CELLS 	CELLS 
Mass of Gd (µg)/sample	0.031 ± 0.005	0.002 ± 0.001
NPs (#)/sample	$1.2 \text{ E}+13$	$5.9 \text{ E}+11$
Concentration of Gd per cell (pmol/L per cell)	-	0.056
Uptake/sample (%)	0.1	0.004

This experiment confirms that 3D-CCM is suitable for investigating nanoagents uptake in tissue-mimicking samples. In particular, it demonstrates that, at even low amounts, AGuIX[®] diffuses through the collagen and is partially engulfed in cells embedded in the matrix.

3.3.5. Quantification of radiation effect on cell survival

The robustness of 3D-CCMs to study external treatments effects on cells was evaluated by investigating the effects of gamma rays on cell survival and, also, the influence of nanoagents on the radiotoxicity. In this perspective, the samples were disaggregated after the irradiation to proceed with clonogenic assay analysis. This method is the gold standard of radiobiology to quantify

the effect of radiation on cell death and proliferative loss. The survival curves are presented in Figure 2.10.

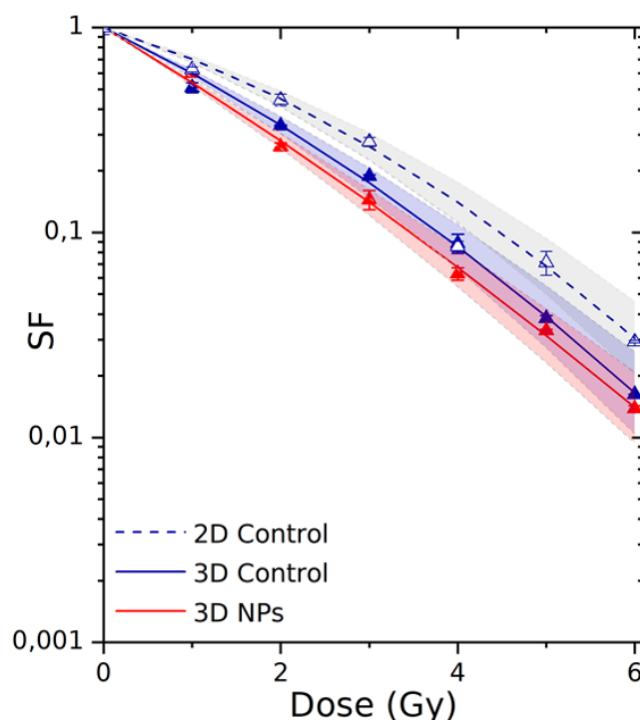


Figure 2.10 - Survival fractions of HeLa cells irradiated in 2D culture (dashed curve/empty triangles) and in 3D-CCMs (solid curve/solid triangles). The influence of AGuIX[®] on radiotoxicity was investigated using 3D-CCMs (red curve). The theoretical uncertainties (area) were determined according to the standard deviations of the α and β parameters. F-statistical tests, based on the maximum likelihood method (see details in Supplementary Materials, 5.3), were performed to compare 2D and 3D models, and, models with or without AGuIX[®]. The differences were significant with a p value of 1.099×10^{-7} ($p < 0.05$) and 0.03 ($p < 0.05$)

The cell response function was simulated using a linear quadratic law, where α is associated with the contribution of the directly lethal lesions induced in the cell and β with the accumulation of additive sublethal lesions (Tubiana et al., 1986). The parameters of the theoretical fits are given in Table 3.

Table 3. Calculated radiobiological coefficients.

$SF(D) = e^{-(\alpha D + \beta D^2)}$	α (Gy^{-1})	β (Gy^{-2})	α/β (Gy)	R^2	SER _{2Gy} (%)	DEF _{10%}
Control 2D	0.31 ± 0.03	0.05 ± 0.01	7	0.99	N.A	N.A
Control 3D	0.48 ± 0.03	0.03 ± 0.01	16	> 0.99	N.A	N.A
AGuIX [®] 3D	0.60 ± 0.03	0.02 ± 0.01	30	> 0.99	16	1.09

a. Comparison of the results obtained in 2D and 3D models

The 2D culture is the primary reference model used in radiobiology. Thus, we first compared the results obtained in 2D culture and 3D-CCM. The experimental data have been adjusted with a linear

quadratic model. The survival fraction (SF) of the cells irradiated in 2D cultures decreased exponentially with increasing irradiation doses, which corresponds to previous studies (Porcel et al., 2014; Štefančíková et al., 2014). We show here that a similar trend is observed for cells irradiated in 3D-CCMs. α is close to 0.48 Gy^{-1} for the 3D culture and 0.31 Gy^{-1} for the 2D culture. It demonstrates that the directly lethal damage induced by radiation are more important for cells embedded in 3D-CCM. On the contrary, the β value is constant (0.05 Gy^{-2}) in the two cases. In total, the α/β ratio, a parameter that is representative of the cell radiosensitivity, is about two times higher for cells in collagen.

This result is different from other studies where cells in 3D models (spheroids for instance) generally present a higher resistance to radiations (Doctor et al., 2020). Contrary, it is consistent with results published on the irradiation of cervical carcinoma cells incorporated in hydrogels based on collagen I, where the effect of radiation was found higher in 3D than in 2D models (Topsch et al., 2007; Walenta and Mueller-Klieser, 2016). This observation can be attributed to difference in cell cycle between 2D and 3D cultures. In 3D cultures in particular, the radiosensitivity of cells is higher because the cells stay in a prolonged arrest in the G2/M-phase, the most sensitive to radiations. In addition, the doubling time of cells in 3D samples (61.2 h) is three times higher than the doubling time cells in 2D monolayers (17.3 h). Thus, the number of colonies counted in the clonogenic assay (min 50 cells) may be underestimated for the 3D cultures.

b. Application of 3D-CCM to the evaluation of NPs induced amplification of radiation effects

3D-CCM was used to evaluate the influence of nanoagents on radiation effects. We investigated the response of the HeLa cells treated with AGuIX[®] and by radiation. As shown in Figure 2.10 - Survival fractions of HeLa cells irradiated in 2D culture (dashed curve/empty triangles) and in 3D-CCMs (solid curve/solid triangles). The influence of AGuIX[®] on radiotoxicity was investigated using 3D-CCMs (red curve). The theoretical uncertainties (area) were determined according to the standard deviations of the α and β parameters. F-statistical tests, based on the maximum likelihood method (see details in Supplementary Materials, 5.3), were performed to compare 2D and 3D models, and models with or without AGuIX[®]. The differences were significant with a p value of $1.099 \text{ e-}07$ ($p < 0.05$) and 0.03 ($p < 0.05$), the decrease in cell survival was stronger in the presence of AGuIX[®]. It demonstrates that the exposure to NPs of cells embedded in 3D-CCMs amplifies efficiently radiation effects.

The amplification efficiency of NPs is commonly quantified using two parameters, namely the radiation Sensitizer Enhancement Ratio (SER) and the Dose Enhancement Factor (DEF). Their calculation is detailed in the Supplementary Materials. As reported in Table 3, the survival fraction at 2 Gy was reduced by 16% for cells incubated with AGuIX[®] in 3D-CCMs. Interestingly, the induction of directly lethal damage (α value) increased in the presence of NPs.

These results demonstrate, for the first time in a tissue-like model, that AGuIX[®] improve the quality of radiotherapy treatments.

3.4. Conclusion

This work demonstrates the advantage of the 3D cytoarchitecture and collagen-based cell model to investigate the impact of various cell treatments. The production of 3D-CCMs, mimicking the microenvironment of cells in tissues, requires minimal material. It is a rapid and robust method which is adaptable to several cell lines.

We found that the preparation of the samples is highly reproducible. The size of the models is constant and the distribution of cells is homogeneous. Thanks to the optical properties of the collagen matrix, label free multiphotonic microscopy can be used to characterize the samples and monitor the internalization of agents (such as Gd-based NPs) in living cells. Another major advantage of the model is that the oxygen concentration may be tuned so as to reflect various architectures and physiologies of tissues

Many tests, frequently used with monolayer cultures, remain directly applicable to the 3D cultures such as metabolic activity assays (MTT). Furthermore, the cells are easily and rapidly recovered by disaggregation of 3D-CCMs. Thus, the impact of various treatments on cells may be evaluated using single cell experiments. As an example, we successfully addressed the toxicity of external agents (Gadolinium-based) and the effect of radiation treatment on cancer cells in this tissue-like sample.

In summary, 3D-CCM is an advantageous *in vitro* model that may be applied to rapidly assess the effect of novel therapies in conditions more realistic than 2D cell cultures. This promising model brings *in vitro* experiments one stage closer to the *in vivo* application, without ethical and financial constraints of animal experiments.

4. ACKNOWLEDGEMENTS

The authors want to thank the Centre de Photonique pour la Biologie et les Matériaux (CPBM) (<https://www.pluginlabs-universiteparisclay.fr/fr/entity/917033-lumat-fr-2764-centre-de-photonique-biomedicale-cpbm>) at ISMO and particularly Ludivine Houël-Renault for the confocal microscope facilities and biological advices. In addition, Multiphoton imaging was performed at the Polytechnique bioimaging facility with financial support from Région Ile-de-France and Agence Nationale de la Recherche (contracts ANR-11-EQPX-0029 Morphoscope2 and ANR-10-INBS-04 France Biolmaging).

5. SUPPLEMENTARY MATERIALS

5.1. Segmentation and analysis of nuclei

The analysis was performed using Python 3.7, whose code and data are available online on Zenodo (DOI: 10.5281/zenodo.3814365). Cell nuclei were distinguished using a threshold method. Due to absorption and scattering, the excitation intensity decreases with depth. Thus, stack images present different intensity statistics. This variation was considered with an adaptive threshold t , which linearly varies with the σ standard deviation of individual image stacks ($t = a \cdot \sigma + b$) (Figure 2.11). The slope of this linear threshold was approximately 1 and its intercept was taken around the median value of the global image.

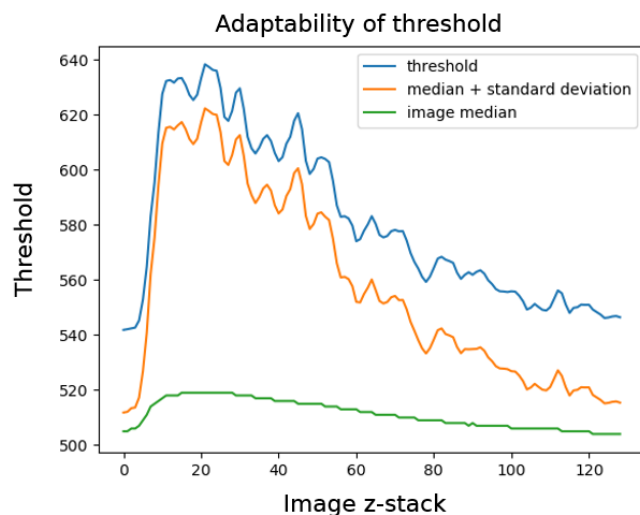


Figure 2.11 - Varying the threshold with imaging depth. Green, orange and blue curves respectively indicate the median of the image at each stack, the sum of the median and the standard deviation, and the adaptive threshold. In this example, the threshold was $1.0 \cdot \text{std_dev} + 535$.

Before application of the threshold, each stack was smoothed by a local median filter. Once the 3D binary image was generated with this adaptive threshold, a binary opening operation was performed to erase small erroneous spots and to maintain wide cell-related parts. Then, the `measure.label` function from `skimage` distinguished individual nuclei in three dimensions, based on the binary image (Figure 2.12).

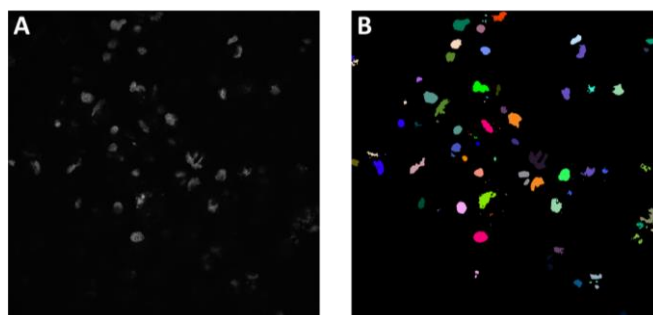


Figure 2.12 - Example of the clustering of individual cells in 2D: **(A)** Cell image at a fixed stack, **(B)** Resulting clustering image where each color indicates a different cell

For each nuclei cluster, we then extracted the size, centroid and global intensity parameters. The distance between each nucleus centroid was calculated to extract the nucleus-nucleus minimum distance using the nearest neighbor python algorithm. The global workflow is described in Figure 2.13.

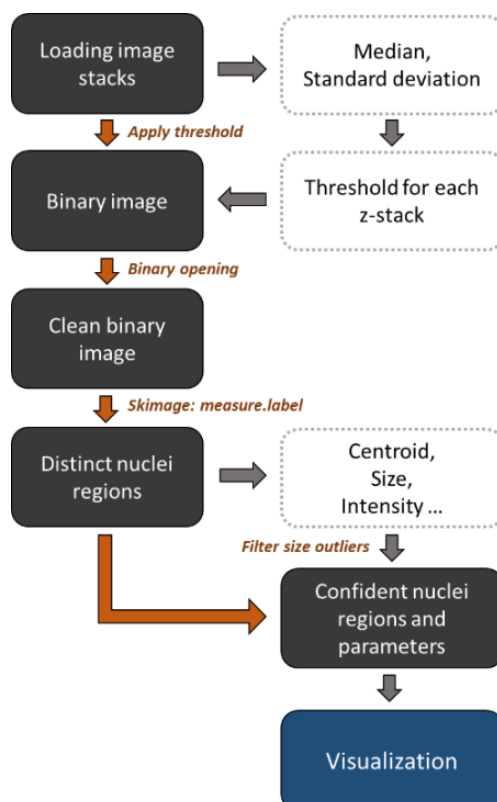


Figure 2.13 - Global Python code workflow. The adaptive threshold is applied to generate a 3D binary image. This image is cleaned via an opening, and parameters are extracted for individual regions. After a final filtering of outliers, plots and histograms are generated.

5.2. Uptake calculation

The number of NPs per sample was calculated from the mass value using the Eq. 13:

$$\frac{\text{NPs}}{\text{sample}} = \frac{m_{\text{Gd}} \cdot N_{\text{A}}}{n \cdot M_{\text{Gd}} \cdot (\text{atoms}_{\text{Gd}}/\text{NP})} \quad \text{Eq. 13}$$

where m_{Gd} is the mass of Gd in μg determined after ICP-MS, n is the number of samples ($n=3$ because we prepared 3 samples per condition (see section 3.2.5)), N_{A} is Avogadro's number equal to $6.02 \times 10^{23} \text{ mol}^{-1}$, M_{Gd} is the Gd molar mass equal to $157.25 \text{ g} \cdot \text{mol}^{-1}$, and $(\text{atoms}_{\text{Gd}}/\text{NP})$ represents the number of Gd atoms per NP, i.e., 10 for the AGuIX[®].

To calculate the uptake, we determined N_{NPs} , the quantity of NPs available during the 4 h of incubation given by the equation Eq. 14:

$$N_{\text{NPs}} = \frac{C_{\text{incub}} \cdot V_{\text{incub}} \cdot N_{\text{A}}}{(\text{atoms}_{\text{Gd}}/\text{NP})} \quad \text{Eq. 14}$$

where C_{incub} is the incubation concentration of NPs equal to $1 \cdot 10^{-3} \text{ mol} \cdot \text{L}^{-1}$ (see section 3.2.5) and V_{incub} is the incubation volume, i.e., 240 μl according to the protocol given in section 3.2.5. The uptake is determined by the ratio of Eq. 13/Eq. 14.

5.3. Clonogenic assay

Statistical test. A test for the comparison of cell survival curves was performed using the package CFAssay implemented in R software. Colony numbers are discrete values following the Poisson distribution. The maximum-likelihood (ML) method was chosen and the R-function glm (generalized linear model) was used. The workflow of this open access package is divided into three steps: (1) data input and double-check, (2) separate calculation of cell survival curves for each of the two conditions, (3) comparison test of the curves for the two experiments. (Brasemann, 2019; Brasemann et al., 2015)

First, the survival curves of the two conditions (with and without NPs) were independently plotted using the *cellsurvLQfit* function, and plating efficiencies were fitted as intercepts. The ML method gives the α and β values (that we compared with those given by Origin) and the dispersion parameter (d.p) (see Figure 2.14 - Survival curves and radiobiological coefficients determined from the CFAssay program (R software).

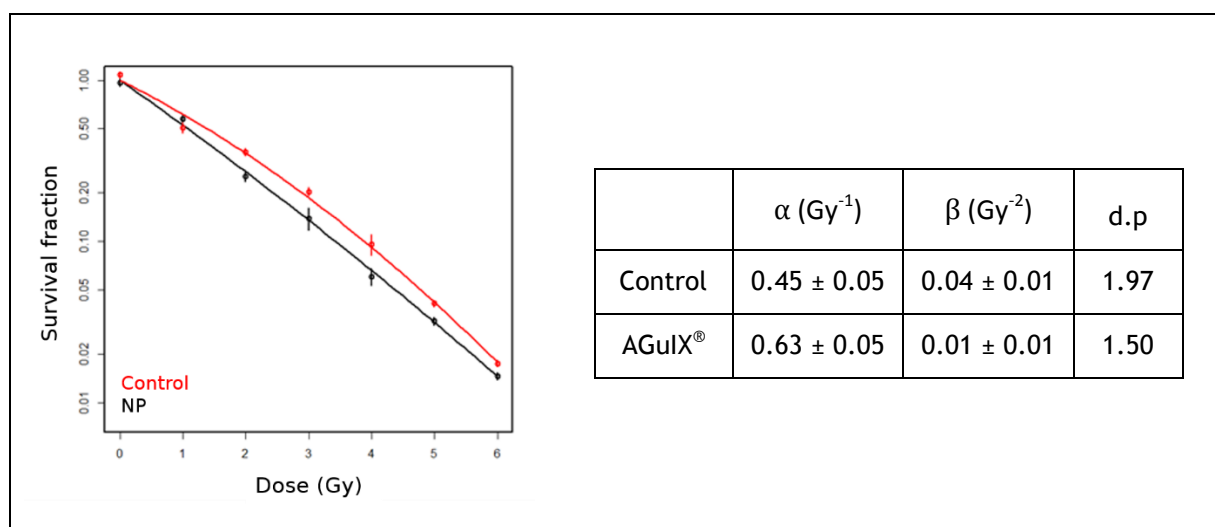


Figure 2.14 – Survival curves and radiobiological coefficients determined from the CFAssay program (R software) rather than Origin program (Table 3)

The dispersion parameter was compared with the value of 9.00, which corresponds to 3 Poisson standard deviations, and shows low variability in the data. The function *cellsurvLQdiff* was used to compare the control and the AGuIX® fits using the ANOVA F-test. This statistical test is composed of two models. Model 1 corresponds to the null hypothesis, which is the hypothesis to reject (*i.e.*, “There is no difference between the two fits”). The curve is fitted to the total cell survival. Parameters α and β are independent of the two curves for 2D and 3D, while for model 2, the curves are fitted separately. The F value obtained after the F-test was 3.93 with a p value of 0.030 ($p > 0.05$). This p-value, which is the probability that the difference between the residual data scatter of model 1 compared with that of model 2 occurs by chance, indicates a significant difference.

Efficiency. The efficiency of AGuIX® to amplify gamma radiation was calculated using two indicators obtained from the survival curves. The radiation sensitizer enhancement ratio (SER) is indicative of the radiation effect induced by the presence of AGuIX®. This parameter is defined at a dose point, specifically 2 Gy, which is the reference dose/fraction in conventional radiotherapy treatments.

$$\text{SER}_D(\%) = \frac{\text{SF}_D^c - \text{SF}_D^N}{\text{SF}_D^c} \quad \text{Eq. 15}$$

where SF_D^c and SF_D^N are the survival fractions at the D dose for the control sample and the sample incubated with AGuIX[®].

The dose enhancement factor (DEF) is the ratio between the radiation dose needed to achieve a certain survival fraction in the control, D_{SF}^c and the radiation dose needed to obtain the same biological effect in the presence of AGuIX[®], $D_{\text{SF}}^{\text{NP}}$. This indicator is commonly calculated for 10% of SF.

$$\text{DEF}_{\text{SF}} = \frac{D_{\text{SF}}^c}{D_{\text{SF}}^{\text{NP}}} \quad \text{Eq. 16}$$

The content of this chapter will be submitted in the journal *Theranostics* as follow:

Maury P., Darricau A., Shahin M., Chargari C., Ammari S., Bockel S., Mondini M., Rouyar-Nicolas A., Lux F., Tillement O., Lacombe S., Deutsch E., Robert C., Porcel E, Treatment of locally advanced cervical cancer using Gadolinium nanoparticles: MR quantification and in vitro insights based on the NANOCOL clinical trial, (in submission)

CHAPTER 3. EVALUATION OF TREATMENT COMBINING AGUIX AND RADIOTHERAPY



La Nuit, Aristide Maillol, 1909, Jardin des tuileries, Paris

“Tous les dragons de notre vie sont peut-être des princesses qui attendent de nous voir beaux et courageux ”

Rainer Maria Rilke –
Lettres à un jeune poète, 1929

Contents

1. INTRODUCTION	57
2. ABSTRACT	58
3. CORPUS	58
3.1. INTRODUCTION	58
3.2. MATERIALS AND METHODS.....	59
3.2.1. <i>Workflow of the present study</i>	59
3.2.2. <i>Nanoparticle quantification in the patients</i>	60
3.2.3. <i>Preparation and characterization of 3D-CCMs</i>	62
3.2.4. <i>Irradiation protocols of the 3D-CCMs</i>	62
3.2.5. <i>Clonogenic assay</i>	63
3.3. RESULTS	64
3.3.1. <i>Calibration curve of T_1 as a function of AGuIX[®] concentration</i>	64
3.3.2. <i>Determination of AGuIX[®] concentrations used in clinic</i>	64
3.3.3. <i>Preparation of AGuIX[®] loaded 3D HeLa cells models</i>	68
3.3.4. <i>Evaluation of the AGuIX[®] effect on the radiotoxicity</i>	69
3.4. DISCUSSION	71
3.5. CONCLUSION.....	72

1. INTRODUCTION

As shown in the previous chapter, 3D-CCM is a reliable and reproducible tool. The present chapter illustrates an application of the 3D-CCM in a clinical context. The framework of this study is a phase 1 clinical trial combining radiations to Gadolinium-based NPs (AGuIX® NPs), applied to patients with locally advanced cervical cancer (LACC).

Briefly, these NPs are composed of ten gadolinium cyclic chelates covalently grafted on an inorganic polysiloxane matrix. As shown in the previous chapter, AGuIX® NPs increase the interaction cross-section due to their high-Z material composition. It results in a local increase of the dose deposition in the vicinity of the NPs. In addition, the gadolinium is a contrast agent for MRI. MRI is the modality of reference for soft tissue visualization and allows to capture in a non-irradiating way micro-scale tumor features and functional properties of tissues with high spatial resolution. The high longitudinal relaxativity of AGuIX® allows for better contrast properties than gadolinium chelates currently used in clinic (Detappe, 2017). MR images and in particular T2-weighted sequences are usually merged to CT scan for radiotherapy treatment planning of cervical cancers.

This work aims at providing the inputs required in the Treatment Planning Systems (TPS) to take into account the biological effects induced by the NPs. In this perspective, a calibration methodology was developed to determine the AGuIX® concentration at the voxel scale based on patient' MRIs.

The 3D-CCMs were used to quantify the biological effect of the combined treatments. As presented in Figure 3.1, these data will be implemented in the TPS to take into account the presence of NPs as proposed by two groups (Brüningk et al., 2020; van Leeuwen et al., 2017).

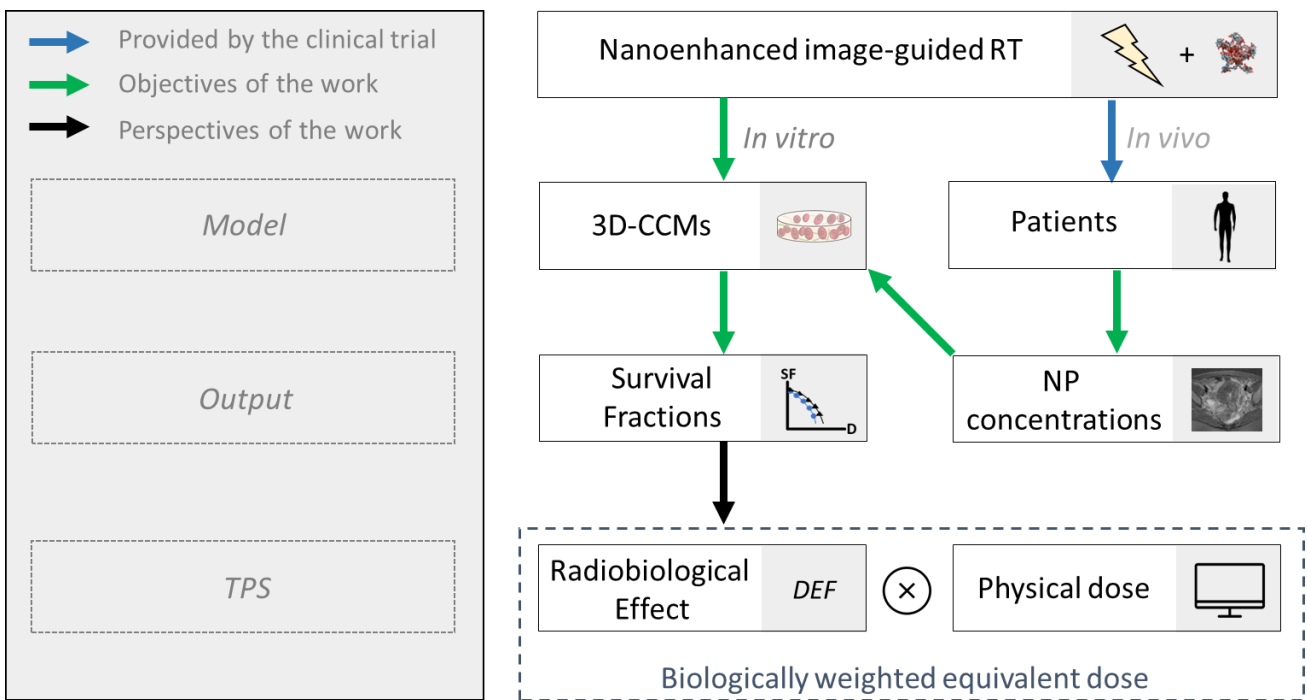


Figure 3.1 - Contribution of the study in the framework of nanoenhanced image-guided RT

2. ABSTRACT

The present study reports about MRI tumor diagnostic in a phase 1 clinical trial of treatments combining radiations and Gd-based NPs (AGuIX[®]) applied to patients with locally advanced cervical cancer. It includes a method to quantify the nanoparticle uptake in patient tumors after intravenous injection using MR images. For this purpose, a calibration curve was established, which gives the T₁ absolute signal as a function of the AGuIX[®] concentration in tumor.

In a second step, the influence of AGuIX[®] on the treatment effect was investigated using a 3D cell collagen-based model, which recapitulate the structural architecture and microenvironmental features of tumor, in particular by the presence of an extracellular matrix. The capacity of these nanoagents to amplify the effects produced by a medical radiotherapy beam (6MV) or a brachytherapy source (¹⁹²Ir) was then evaluated. We found that the AGuIX[®] enhance the effects of the X-rays by ~15% at 1.8 Gy and those of the brachytherapy by ~30% at 5.25 Gy.

To continue the translation to the clinic of NPs-based radiotherapy, the development of new software tools able to calculate the dose in presence of NPs is needed. This work aims to provide the inputs required in the treatment planning system (TPS) to take into account the biological effect of the NPs on radiation dose distribution.

3. CORPUS

3.1. Introduction

Cervical cancer remains a major cause of mortality among women worldwide, with a 5-year overall survival ranging from 93% to 15%, according to the International Federation of Gynecology and Obstetrics (FIGO) stage (Kawamoto and Macura, 2016). Cisplatin-based concomitant chemoradiation followed by uterovaginal brachytherapy is the standard of care for locally advanced cervical cancer (LACC) (Haie-Meder et al., 2005; Mittal et al., 2018). Despite the dose escalation permitted by the recent implementation of image-guided treatments, the risk of local relapse is still significant (Castelnu-Marchand et al., 2015).

The administration of sub-10nm theranostic nanoagents able to accumulate in the tumor via enhanced permeability and retention (EPR) effect has been shown to offer new perspectives in cancer diagnosis and therapy (Lacombe et al., 2017; Popović et al., 2010).

In this context, sub-5nm diameter AGuIX[®] (NH TherAguiX, Lyon, France) based on Gd chelates have been developed. On the one hand, AGuIX[®] act as contrast agents and improve MRI tumor diagnosis. On the other hand, thanks to their high Z materials composition, they increase locally the energy deposited by the incident radiation (Hubbell, 1999). As a consequence, the emission of short-range electrons enhances the water radical production and the formation of radical oxygen species (ROS) in nanovolumes (Lux et al., 2018) which are responsible for cell death (Kuncic and Lacombe, 2018). Thus, in the presence of NPs, a better therapeutic index is achieved increasing the local tumor control without majoring toxicities to healthy tissues (Tran et al., 2016).

Since their development about ten years ago, these Gd-based nanoagents led to convincing preclinical results (Bort et al., 2020). The first evaluation of the theranostic properties of AGuIX[®] in clinic was conducted in a phase 1 clinical trial involving 15 patients with multiple brain metastases (Verry et al., 2020b).

If the clinical benefits of the treatment are still being assessed, the MRIs of patient brains clearly confirmed accumulation and retention of the NPs in the tumors (Bort et al., 2020). A second clinical trial named NANOCOL started at Gustave Roussy in 2018 for patients suffering of LACC (NCT03308604). The treatment protocol is described in Figure 3.2 Figure 3.2 - Overview of the NANOCOL protocol (“AGuIX Gadolinium-based Nanoparticles in Combination With Chemoradiation and Brachytherapy (NANOCOL),” n.d.).

The first step consists in treating the tumor by external beam therapy (EBT) using a modulated intensity technique delivering 45 Gy in 5 weeks (1.8 Gy per fraction). Intravenous cisplatin 40 mg/m² is weekly administered, in concomitance with the EBT (5 cycles in total). An integrated boost of 55-57.5 Gy is added for patients with a macroscopic lymph node. In a second step, a treatment by image-guided brachytherapy of 15 Gy is applied.

During the treatment, patients undergo three AGuIX[®] intravenous injections at D₀ and D₁₁ of the EBT and at D₀ of the brachytherapy session. The first dose level is 30 mg/kg body weight. Acquisitions of MR images are performed at four time points including the beginning of the treatment, before any NPs injections (MRI 1) and after each NP injection (MRI 2, 3 and 4).

A weekly biological monitoring is carried out during the treatment course and a clinical follow-up is planned 6 weeks after the end of the treatment.

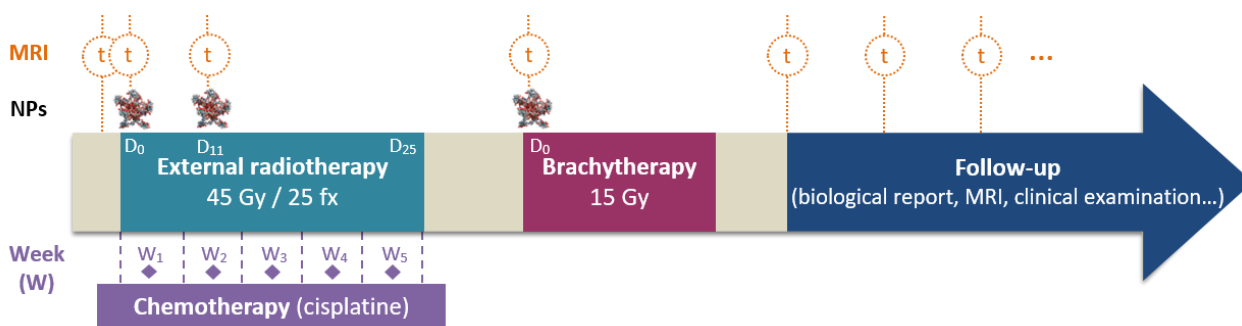


Figure 3.2 - Overview of the NANOCOL protocol

Safety and tolerability of escalating doses of AGuIX[®] used in combination with radiation and cisplatin are currently being evaluated (Lux et al., 2018). However, the quantity of NPs localized in the tumor after intravenous injections and the evaluation of the effect of NPs on radiation treatments are missing. Therefore, the present work aims at developing a method to determine the AGuIX[®] concentration in the tumor based on MR images of patients and evaluating the impact of AGuIX[®] on radiation effects using a 3D cell collagen-based model (3D-CCM) treated in the same conditions than in clinic.

3.2. Materials and methods

3.2.1. Workflow of the present study

The workflow of this work is represented in Figure 3.3. Figure 3.3 - Workflow of the present study

In a first step, an MR phantom was developed (step 1) to perform T₁ measurements in the presence of NPs. This phantom was used to establish the calibration curve of T₁ absolute signal as a function of the NPs concentration (step 2). From the patients' MR images (and T₁ values), mean concentrations of AGuIX[®] in the Gross Tumor Volume (GTV) were determined (step 3) using the calibration. In the next step (step 4), 3D-CCMs were prepared so that the quantity of AGuIX[®] in the model correspond to the NP concentration found

in the tumors of patients. 3D-CCMs were then irradiated with the conditions used in the clinical EBT and brachytherapy (step 5). The biological effect of the AGuIX[®] was evaluated using clonogenic assay to establish survival curves (step 6).

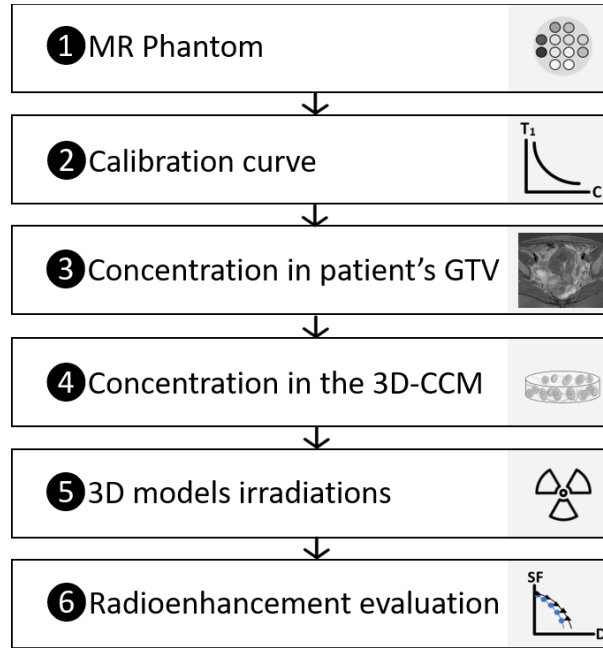


Figure 3.3 - Workflow of the present study: from the patient MRI to the AGuIX[®] effect

3.2.2. Nanoparticle quantification in the patients

Our study is based on the MRI obtained for the 4 recruited patients of the trial. The first three were injected with 30 mg/kg of NPs while the 4th received a higher dose of 50 mg/kg. The MR acquisitions were performed using a 1.5 T MR scanner (Optima MR450w 1.5 T GE MR scanner, General Electric, Boston, MA, USA).

Each serie was composed at least of:

(i) a Variable Flip Angle (VFA) sequence allowing the determination voxel by voxel of the T_1 values based on the linear regression of Eq. 17 (Cheng and Wright, 2006):

$$\frac{S(\alpha)}{\sin(\alpha)} = e^{\frac{-TR}{T_1}} \frac{S(\alpha)}{\tan(\alpha)} + M_0(1 - e^{\frac{-TR}{T_1}}) \quad \text{Eq. 17}$$

where the MR signal S was acquired for different flip angles $\alpha = 2, 3, 5, 7, 15, 20, 35^\circ$; a field of view (FOV) = 240 mm; fixed values of Repetition Time (TR) / Echo Time (TE) = 8.2 / 4.2 ms; a pixel spacing of 1.0 mm x 1.0 mm and a slice thickness of 5 mm.

(ii) a T_2 -weighted anatomical sequence (T_2 Propeller performed) with TR / TE = 11472.3 / 78.4 msec; a pixel spacing of 0.7 mm x 0.7 mm and a slice thickness of 3 mm.

a. Calibration curve

The calibration curve was built using the Eurospin TO5 phantom (Eurospin TO5, Diagnostic Sonar, Livingston, Scotland) composed of 10 syringes filled with 5 ml of AGuIX[®] solution. Assuming that the patients are mainly composed of water, the calibration was performed diluting NPs in water. The concentrations in Gd, [Gd³⁺], were chosen as follows: 1 mM; 0.75 mM; 0.5 mM; 0.25 mM; 0.15 mM; 0.1 mM; 0.05 mM; 0.015 mM; 0.005 mM and 0 mM. These concentrations were validated by an ICP-MS quantification of the Gd amount in the AGuIX[®] mother solution. Note that all the concentration of the paper will be expressed in Gd concentration (1 mmol/L of Gd is approximately equal to 0.1 mmol/L of AGuIX[®]).

VFA acquisitions of the phantom were performed using the same acquisition parameters as detailed above. The Olea Sphere[®] software version 3.0 (Olea Sphere, Olea Medical, La Ciotat, France) was used to deduce T₁ maps. For each syringe, 4 circular 2D region of interest (ROI) of 191.6 mm² each were drawn. Mean values of T₁ and their standard deviations were extracted from each ROI. Experimental points were modelled by a theoretical fit using a least squares method.

A mean value of the AGuIX[®] relaxativity, r₁, calculated using the Eq. 18 (Fries et al., 2014), was obtained using the data (concentration [Gd³⁺] and T₁) obtained for each insert containing a NP concentration between 0.05mM and 1mM.

$$r_1 = \frac{\Delta(1/T_1)}{[Gd^{3+}]} = \frac{1}{[Gd^{3+}]} \left(\frac{1}{T_{1,post}} - \frac{1}{T_{1,pre}} \right) \quad \text{Eq. 18}$$

b. Determination of the NP concentration

The first images of the patients were acquired before the injection of the AGuIX[®] to determine the baseline T₁ in the GTV (GTV MR 1). The three other MR sequences were acquired after AGuIX[®] injection at D₀ and D₁₁ after the start of the radiotherapy treatment (GTV MR 2 and GTV MR 3) and the first day of the brachytherapy treatment (GTV MR 4).

On each patient's MRI series, a physician defined the GTV. Contours were delineated on the T₂-weighted sequence; then reported on the T₁ maps. For each MRI time point, mean T₁ and its associated standard deviation was extracted to determine the absolute T₁ signal evolution during the treatment course.

Mean concentrations of AGuIX[®] in the GTV (GTV MR 2 and 3) were deduced using the calibration curve and were corrected by subtracting the AGuIX[®] concentration evaluated on baseline images (GTV MR 1). Following method exposed above, biodistribution was investigated for each patient. In this goal, mean AGuIX[®] concentrations were determined in the bladder and in a circular ROI located in healthy fat tissues in the vicinity of the tumor volume. However, the quantification of the AGuIX[®] amount at time point 4 was not performed because of the presence of an inflated balloon urinary catheter placed in the patient's bladder during brachytherapy.

The mean NPs concentrations in the GTV obtained using the calibration curve (Method 1) were compared with an analytical method reported by Verry and coworkers (Method 2) (Verry et al., 2016). This latter gives the mean concentration of Gd³⁺ in the GTV (in mM) function to the relaxation times (in ms) before (T_{1,pré}) and after (T_{1,post}) AGuIX[®] injection. r₁ is the relaxivity per Gd³⁺ of AGuIX[®] at 1.5 T (equal to 11.4 mM⁻¹.s⁻¹) (Fries et al., 2015). The equation is provided in Eq. 19.

$$[Gd^{3+}] = \frac{1000}{r_1} \left(\frac{1}{T_{1,post}} - \frac{1}{T_{1,pré}} \right) \quad \text{Eq. 19}$$

Then, the distributions of the T_1 values of the patients' GTV were established. The 95th percentile (highest 5% AGuIX[®] concentrations of the GTV) were determined using the calibration curve. These maximal concentrations, corrected of the T_1 tissues baseline, were considered to further evaluate the radioenhancement effect due to the NPs.

3.2.3. Preparation and characterization of 3D-CCMs

a. Production of 3D-CCMs

3D-CCMs were prepared from HeLa cervical cancer cells cultured in a monolayer in complete medium composed of Dulbecco's Modified Eagle Medium supplemented with 10% fetal bovine serum, 1% penicillin and 1% streptomycin (Life Technologies[™]). The samples were produced in a 96 wells plate using a RAFT[™] kit (Lonza[®]) according to the protocol presented in our previous study (Maury et al., n.d.). Each 3D-CCM was a cylinder of 6.9 mm thickness and $122 \mu\text{m} \pm 4 \mu\text{m}$ diameter where $\sim 350\,000$ HeLa cells were embedded in a collagen I matrix. To reduce uncertainty and batch-to-batch variability, all samples of the same experiment were prepared from the same solution.

b. AGuIX[®] exposure

3D-CCMs were incubated with 240 μL of AGuIX[®]. Two conditions of NPs incubation were selected (0.5 mmol/L - 4h and 0.5 mmol/L - 24h) as leading to the closest to the maximal concentrations measured in the patients' tumors. Two different dosages were performed (i) in the whole samples (3D-CCMs) composed of cells embedded in collagen (ii) in the cells extracted from the 3D-CCMs after digestion of the collagen matrix. Analyses were performed at the Ultra Trace Analyses Aquitaine (UT2A) Technological Center, Pau, France, using an Agilent 7800 ICP-MS technology (Agilent Technologies[®]).

Finally, AGuIX[®] were localized in the 3D-CCMs using a LEICA SP5 confocal microscopy. In this aim, AGuIX[®] were labeled with Cy5.5 fluorescent tag (exc: 633 nm/em: 655-740 nm) and cell nuclei were stained for 30 minutes with a 1 $\mu\text{mol/L}$ Hoescht 33342 solution (exc: 350 nm/em: 461 nm) (Thermo Fisher Scientific[®]).

3.2.4. Irradiation protocols of the 3D-CCMs

3D-CCMs were irradiated in a phantom reproducing the patient geometry as represented in Figure 3.4. The phantom was composed of 15 cm water equivalent plates of 30 cm x 30 cm, in which is placed a 1.5 cm thick bolus of density 1.05 (Bolusil[®], Kerjean Biotechnologies) containing the plastic tubes with the 3D-CCMs samples to irradiate. The phantom was scanned with the clinical protocol used for pelvis treatment (120 kV, pixel spacing of 1 mm x 1 mm, slice thickness of 2 mm) using a Siemens Sensation Open Syngo 2014A CT scanner (Siemens, Munich, Germany).

The EBT dose distribution planning was realized with the Raystation v.6 Treatment Planning System (TPS) (Raysearch Laboratories, Stockholm, Sweden). Irradiation doses from 1 to 6 Gy (1 Gy step) were delivered by a Novalis TX (Varian, Palo Alto, CA, USA) linear accelerator, using a 6 MV Volumetric Modulated Arc Therapy (VMAT). Each plan was composed of a single arc. Irradiation delivery was optimized to make dose as homogeneous as possible in the tube containing the sample. At least 95% of the prescribed dose was delivered to 95% of the volume.

Brachytherapy treatment planning was prepared using the Oncentra Brachytherapy version 4.6 TPS (Elekta, Stockholm, Sweden). Considering the irradiation time needed in brachytherapy (up to 240 s to deliver 1 Gy depending on the source activity) the effect of NP was investigated at 24h incubation time only.

Irradiations from 1.25 to 5 Gy (step of 1.25 Gy) were performed using a MicroSelectron Digital projector (microSelectron Digital, Stockholm, Sweden) loaded with an ^{192}Ir source ($E = 316 \text{ keV}$, 80%), whose reference air kerma rate was between 29.408 and 16.380 $\text{mGy}\cdot\text{m}^2/\text{h}$ depending on the experiment date. Two catheters including each 15 source positions were used to obtain a homogenous dose in the sample. High Dose Rate (HDR) brachytherapy was preferred to make irradiation times compatible with cell lifetime.

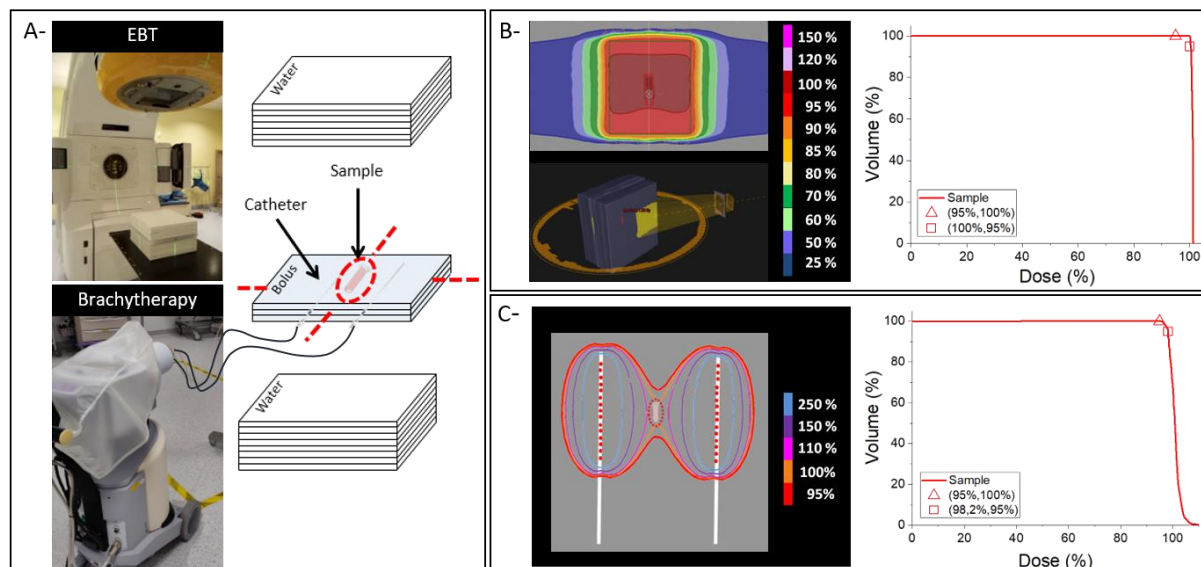


Figure 3.4 - **(A)** Experimental setups for EBT (upper image) and HDR (lower image) showing the irradiation of the 3D-CCM by these two modalities (sample surrounded by red dotted line). The sample was placed in a bolus and centered in the phantom using positioning lasers (red dotted lines). Dose distributions and dose volume histograms (DVH) for **(B)** EBT and **(C)** HDR. Irradiation of the 3D-CCM was performed delivering at least 95% of the prescribed dose to 99% of the sample

3.2.5. Clonogenic assay

After treatment, the cells were recovered to evaluate the survival fractions (SFs) using a clonogenic assay. The 3D-CCMs were disaggregated in 1 mg/mL collagenase from *Clostridium histolyticum* (Sigma-Aldrich[®]) following the protocol given in 3.2.3. For each irradiation dose (see 3.2.4), cells were plated in triplicate into 100 mm diameter Petri dishes (Thermo Fisher) at a density of 100 surviving cells per dish. After 15 days of incubation, cells were fixed and stained with 1% crystal violet in 10% ethanol dye solution. The SFs were determined as the number of counted colonies divided by the number of seeded cells. The results were normalized with SF at 0 Gy. The cell response as a function of radiation doses was simulated using the linear quadratic model (LQ) (Eq. 20):

$$\text{SF}(D) = e^{-(\alpha D + \beta D^2)} \quad \text{Eq. 20}$$

where the parameter α is attributed to the induction of directly lethal damages and β to the additive sub-lethal lesions leading to cell death.

A statistical analysis of the clonogenic assay results was performed with the CFAssay package included in the R software (R Core Team (2020), R: A Language and Environment for Statistical Computing, R Foundation for Statistical Computing, Vienna, Austria, <https://www.R-project.org>). The F-test based on the maximum likelihood (ML) method was performed to compare the cell survival curves in the presence of NPs with the control one and conclude about the significance of the results (Brasemann, 2019). The efficiency of AGuIX[®] was quantified by two parameters, namely the radiation Sensitizer Enhancement Ratio (SER) and the Dose Enhancement Factor (DEF). The SER, defined at a dose point D , reflects the radioamplification

effect due to the presence of NPs while the DEF evaluates the dose reduction leading to the same survival fraction with NPs than without.

3.3. Results

3.3.1. Calibration curve of T_1 as function of AGuIX[®] concentration

The Figure 3.5 Figure 3.5 - Calibration curve presents the calibration curve of the measured T_1 (called 'y') as a function of the NP concentration (called 'x'). The equation of the plot is given in equation 21. y is expressed in ms, x in mM.

$$y = \frac{1}{0.0112x + 9.7264 \cdot 10^{-4}} \quad \text{Eq. 21}$$

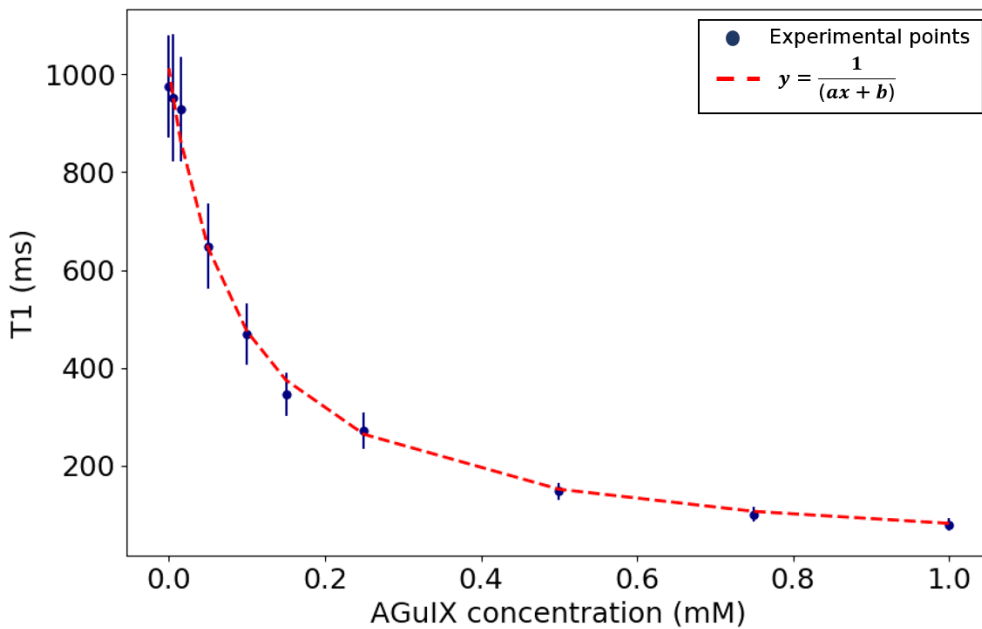


Figure 3.5 - Calibration curve of T_1 measured with the VFA sequence as a function of the AGuIX[®] concentration in the phantom syringes. Experimental points are represented in black and the fit corresponds to the red dotted line.

3.3.2. Determination of AGuIX[®] concentrations used in clinic

Figure 3.6 illustrates T2-PROPELLER sequences corresponding to Patient 4 before and after NP injection obtained the first day of radiotherapy treatment course.

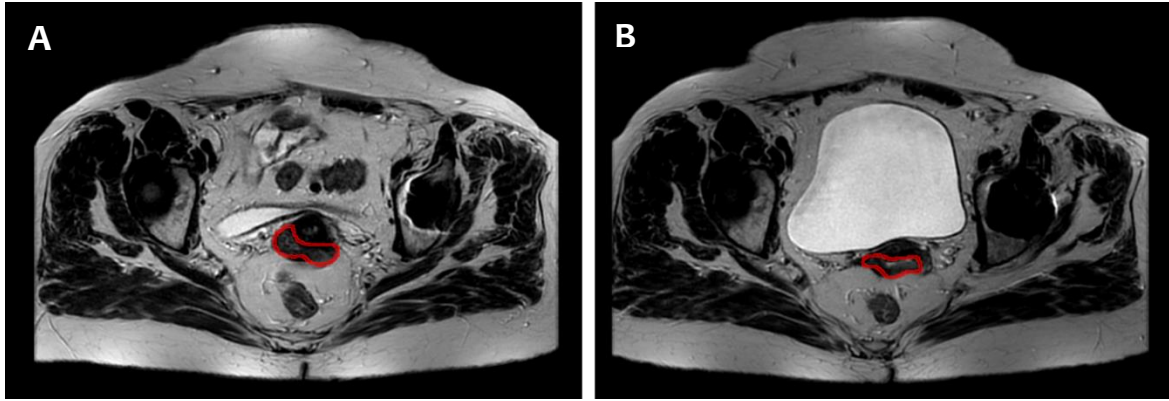


Figure 3.6 - MR images (T2-PROPELLER) of the GTV (red line) of Patient 4 acquired **(A)** without injection of AGuIX[®] (at D₀ of the treatment-P4/T1) and **(B)** after 30 mg/kg AGuIX[®] injection (at D₀ of the radiotherapy-P4/T2)

For each patient, mean absolute T₁ was determined in the GTV as well as in healthy fat tissues close to the GTV and in bladder, as shown in Figure 3.7.

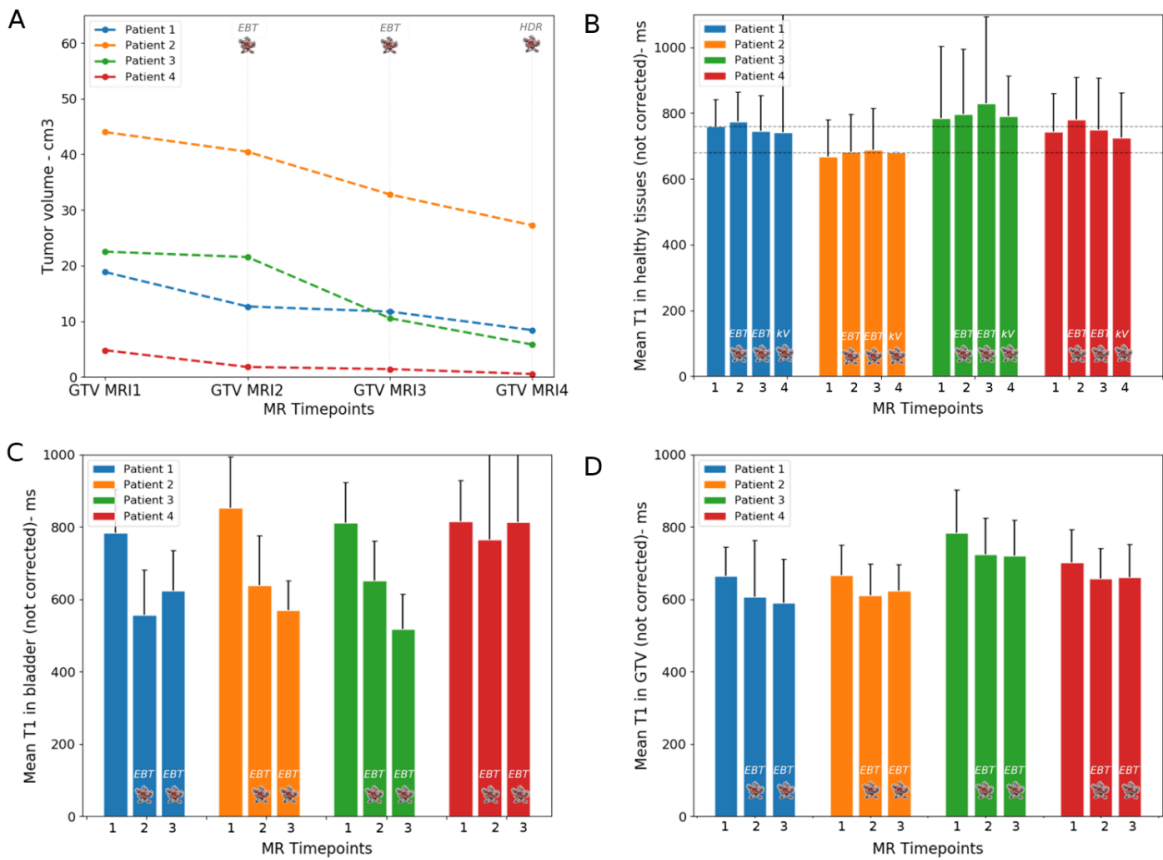


Figure 3.7 - Evolution of the tumor volume (reductions of 53%, 37%, 75% and 91% between MRI 1 and 4 for the patients 1, 2, 3 and 4 respectively) **(A)** and T₁ value in healthy fat tissues **(B)**, in the bladder **(C)** and in the GTV **(D)**, at each time point, for the 4 patients included in the clinical trial (blue, orange, green and red). Patients 1, 2, 3 have received an injection of 30 mg/kg while a dose of 50 mg/kg was delivered to patient 4.

A significant reduction of the tumor volume was observed during treatment course (Figure 3.7A). For patients 3 and 4, decreases of 75% and 91% were observed between start of the EBT treatment and the first brachytherapy session leading to volumes inferior to 10 cm^3 before brachytherapy. This tumor reduction makes it difficult to analyze NPs uptake in the GTV at time point 4. The tumor size is expected to affect the AGuIX[®] concentration in the GTV, so the values from MRI 4 were disregarded and the mean absolute T_1 signals determined after EBT only were plotted.

The Figure 3.7B presents the variation of the mean T_1 value measured in the peritumoral fat tissues on each MRI. The evolution of the mean T_1 was almost constant, with a value around 680 ms for patient 2 and 770 ms for patient 1, 3, 4. For each patient, the difference between the mean T_1 value obtained after AGuIX[®] injection (MR 2, 3, 4) and the value evaluated without NP (MRI 1) was around 2 to 3%. It indicates that the mean NP concentration in healthy tissues was lower than $3.1 \pm 42 \text{ } \mu\text{mol/L}$ for the entire duration of the treatment.

Figure 3.7C shows that, for each patient, a decrease in the T_1 value was observed in the bladder at the MR 2 and MR 3 time points. Table 5 shows that a mean NP concentration between 0 and $62 \text{ } \mu\text{mol/L}$ was found in the bladder.

Figure 3.7D presents the mean T_1 signal obtained in patients' GTV at time points 1, 2 and 3. For each patient, a decrease in the mean T_1 value was observed on MRI 2 and 3 compared to MRI 1. As expected, the mean T_1 value obtained in the GTV MRI 1 was not equal to 0. Measurements taken in the cervix on the MRI 1 (without NPs injection) showed that the organ's T_1 ($T_{1, \text{cervix}, \text{MRI } 1} = 709 \pm 57 \text{ ms}$) was not equal to T_1 measured in water with the VFA sequence ($T_{1, \text{wVFA}} = 970 \pm 105 \text{ ms}$), leading to a relative difference of 37%. The Table 4 presents the translation of mean T_1 values into mean NP concentrations corrected of this tissues baseline. A significant uptake of AGuIX[®] between 8.4 (Patient 4, MR 2) and $16.0 \text{ } \mu\text{mol/L}$ (Patient 1, MR 3) was found in the GTV (Table 4, column 2, Method 1).

All tumors have internalized NPs, however an inter-patients variation was noticed, with a difference between the mean NP concentrations in the GTV which can reach 31% at the MR 2 time point and 53% at the MR 3 time point.

For a same patient, the mean T_1 measured in GTV after the two AGuIX[®] injections performed during the EBT (GTV MRI 2 and GTV MRI 3) was relatively stable (Figure 3.7D). Indeed, the mean NP concentrations in the tumor at MRI 2 and MRI 3 do not differ by more than $3 \text{ } \mu\text{mol/L}$, suggesting, for each patient, a comparable accumulation of AGuIX[®] in the GTV at D_0 and D_{11} .

For comparison, the mean NP concentration obtained in the patients' GTV calculated using the analytical method is given in Table 4, column 3 (Method 2). The relative differences between the values obtained by the two methods are reported in column 4. A good agreement, lower than 2%, was observed. Besides, AGuIX[®] relaxativity value, r_1 , calculated from the calibration curve data was found equal to $11.3 \pm 0.7 \text{ mM}^{-1} \cdot \text{s}^{-1}$, in accordance with the value of $11.4 \text{ mM}^{-1} \cdot \text{s}^{-1}$ defined in a previous study (Fries et al., 2015).

Table 4. Mean AGuIX[®] concentration in patients' GTV corrected of the baselines. The values were determined from MRI 2 and 3 (performed during EBT, after NP injection) according to the two different methods. Relative difference is reported (column 4)

GTV		Mean concentrations corrected of the concentration tissues baseline (µmol/L)		Difference (%)
Timepoint	Patient	Method 1	Method 2	
MRI 2	1	12.4 ± 53.2	12.2 ± 52.3	-0
	2	12.0 ± 21.0	11.8 ± 36.9	2
	3	9.2 ± 33.8	9.0 ± 33.2	2
	4	8.6 ± 33.2	8.4 ± 32.6	2
MRI 3	1	16.3 ± 46.0	15.9 ± 45.2	-0
	2	9.1 ± 33.1	8.9 ± 32.5	2
	3	9.8 ± 33.6	9.6 ± 33.0	2
	4	7.7 ± 34.4	7.5 ± 33.8	2

Table 5. Mean AGuIX[®] concentration in patients' bladder corrected of the baselines. The values were determined from MRI 2 and 3 (performed during EBT, after NP injection) according to the two different methods. Relative difference is reported (column 4)

Bladder		Mean concentrations corrected of the concentration tissues baseline (µmol/L)		Difference (%)
Timepoint	Patient	Method 1	Method 2	
MRI 2	1	45.6 ± 174.7	44.7 ± 171.7	2
	2	34.7 ± 46.9	34.0 ± 46.0	2
	3	26.7 ± 37.9	26.1 ± 37.2	2
	4	7.0 ± 60.0	6.9 ± 58.9	2
MRI 3	1	28.7 ± 42.3	28.1 ± 41.6	2
	2	51.3 ± 39.5	50.3 ± 38.8	2
	3	61.7 ± 47.3	60.4 ± 46.5	2
	4	0.3 ± 46.3	0.3 ± 45.5	2

The maximum concentrations calculated in the GTV from the T₁ distribution are presented in Figure 3.8B. These concentrations range from 63 (Patient n°2, MRI 3) to 128 µmol/L (Patient n°1, MRI 2).

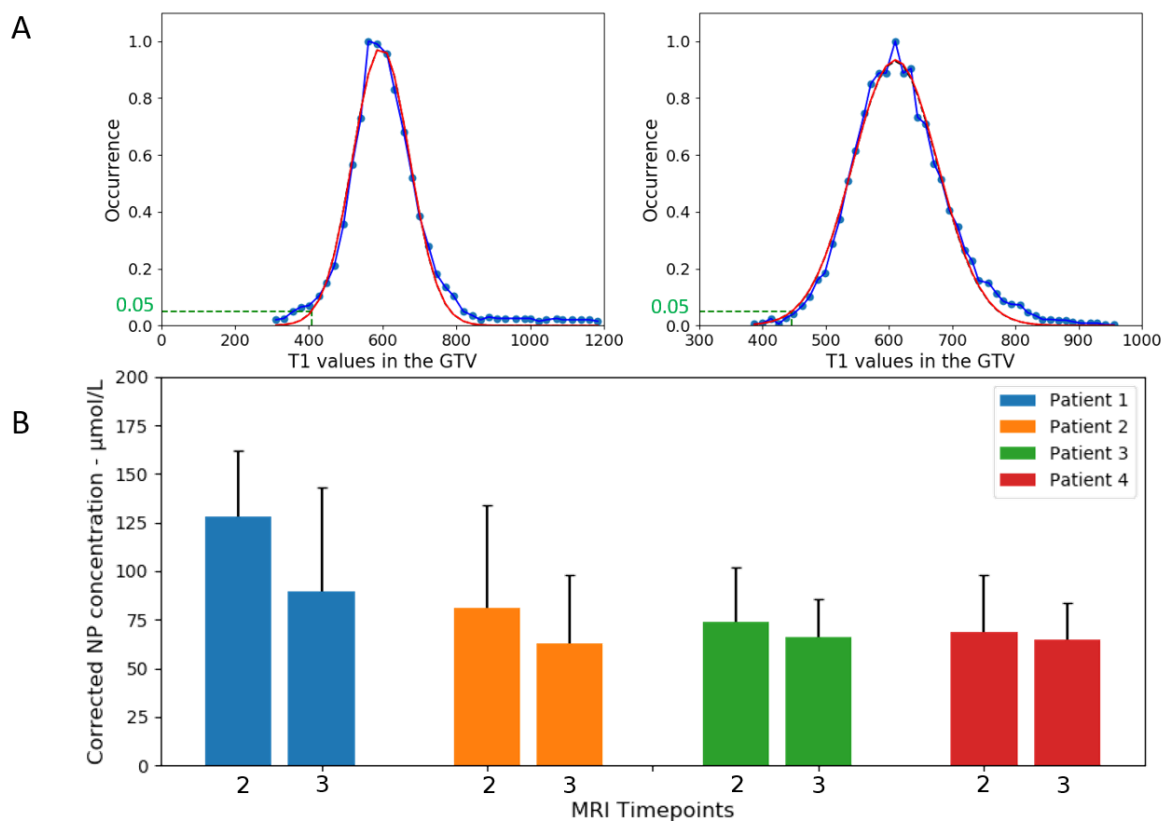


Figure 3.8 - **(A)** Gaussian distributions of T₁ values measured in the GTV for the Patient 2 at the time points MR 2 and MR 3. **(B)** Maximum AGuIX[®] concentrations in patient's GTV

A quantification of the amount of AGuIX[®] internalized in the tumor was successfully performed and shows that the uptake in the GTV is significant.

3.3.3. Preparation of AGuIX[®] loaded 3D HeLa cells models

To rapidly evaluate the effect of NPs on radiotoxicity, 3D-CCMs were developed to reproduce at best the cell environment of tumor loaded with AGuIX[®]. The two incubation conditions (0.5 mmol/L for 4 or 24h) were used to reproduce the 5% maximum AGuIX[®] concentrations found in the patient's GTV.

Confocal microscopy images presented in

Figure 3.9 A illustrate the NP distribution in a 3D-CCM. This experiment shows that AGuIX[®] penetrate and diffuse homogeneously in collagen I. This indicates that the nanoagents are able to travel through the extracellular matrix, a major finding that explains distribution of AGuIX[®] into tumor volumes as shown before. The cell nuclei are labeled in blue and the black zones delineate the cell cytoplasm. AGuIX[®] penetrate as aggregates inside the cells, in the cytoplasm exclusively, as shown before for 2D cell cultures (Porcel et al., 2014; Štefančíková et al., 2014).

The total amount of AGuIX[®] contained in the sample and in cells, determined by ICP-MS, is reported in the table of Figure 3.9 B.

The AGuIX[®] concentration in the 3D-CCM is close to 135-170 $\mu\text{mol/L}$ which corresponds to $\sim 4\text{E}+13$ NPs per sample. The AGuIX[®] concentration internalized in cells is below 500 nmol/L , corresponding to $\sim 1\text{E}+7$ NPs per cell.

The amount of NPs in the 3D-CCM varies as a function of the incubation time. An increase of 25% was found in the 3D-CCM for an incubation varying from 4 to 24 h. In the same time, an increase of approximately 130% was observed for the quantity of Gd in the cells. Thus, increasing the incubation time strongly improves the migration of NPs in the matrix before to reach the cells.

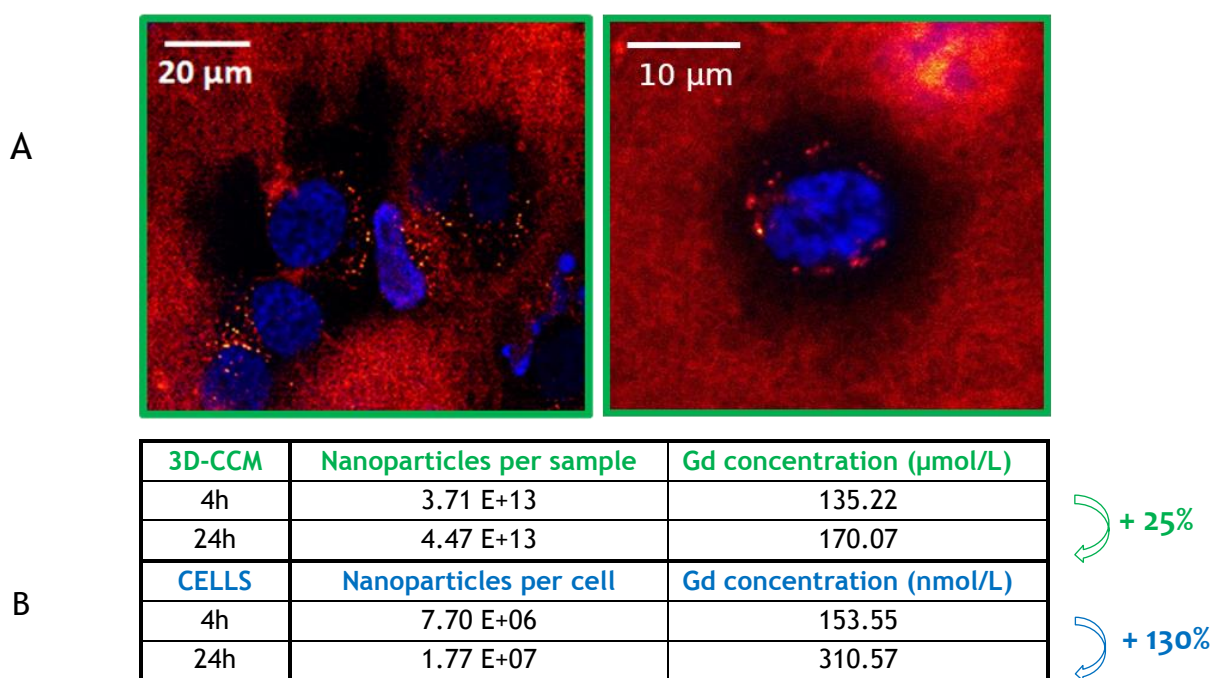


Figure 3.9 - **(A)** Confocal images of 3D-CCMs treated with 0.5 mmol/L AGuIX[®] for 24 h. Cells are identified as black holes in the collagen matrix, their nuclei are labeled in blue and AGuIX[®] in red. **(B)** ICP-MS dosages of Gd in the samples (in green) or in cells extracted from the samples (in blue) for the two incubation times (4h or 24h).

3.3.4. Evaluation of the AGuIX[®] effect on the radiotoxicity

The effect of AGuIX[®] at concentrations in the sample as used in clinic, was evaluated by clonogenic assay (see Section 3.2.5). The survival curves of HeLa cells extracted from 3D-CCM after incubation or not with AGuIX[®] and treatment by two different irradiation conditions (see Section Irradiation protocols of the 3D-CCMs 3.2.3, b), are presented in Figure 3.10.

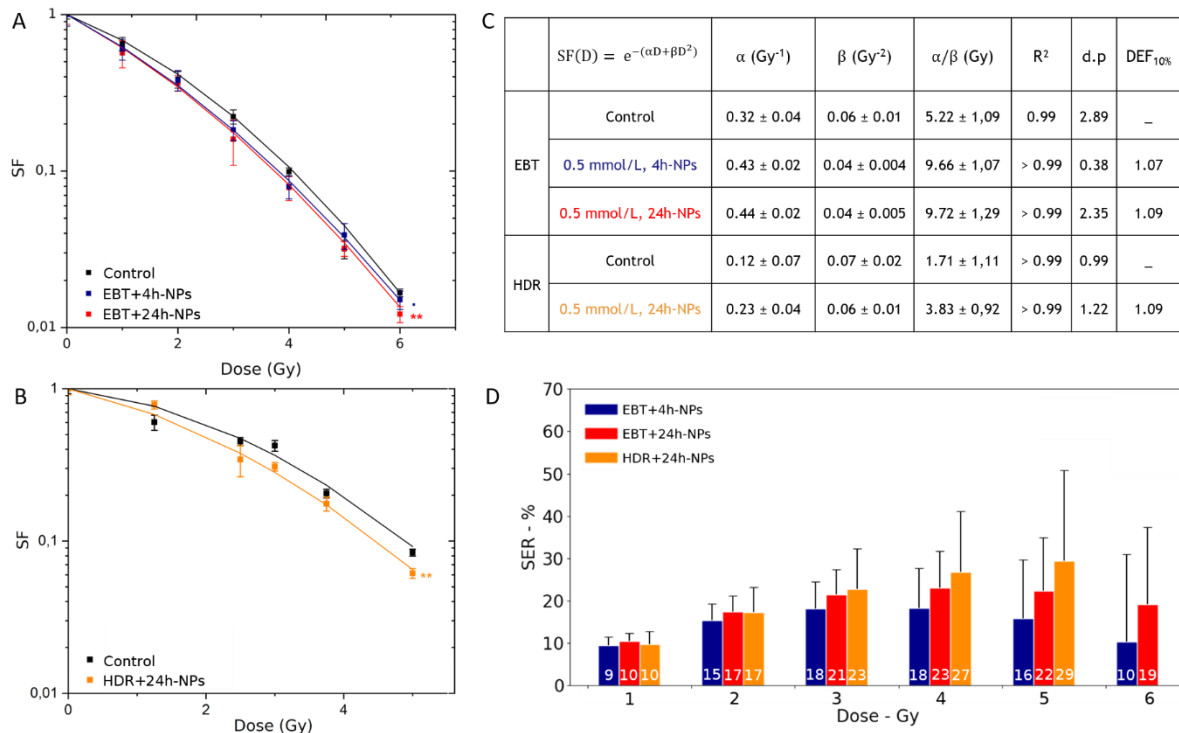


Figure 3.10 - Survival curves obtained after irradiation of HeLa cells in 3D-CCM treated by **(A)** EBT **(B)** HDR with and without NPs. Results of the F-test were $F=3.003$ (p value of 0.08) for MV+4h NPs, $F=6.42$ (p value of 0.007) for MV+24h-NPs and $F=9.16$ (p value of for 0.001) kV+24h NPs. **(C)** Radiobiological parameters extracted from the LQ model fit and DEF value. **(D)** Evaluation of the combined treatments (SER values) for the three irradiation conditions.

a. Effect on EBT radiation

The cell survival curve shows a linear quadratic dose-dependent decrease of the survival fraction (see Figure 3.10). The presence of NPs induces an amplification of cell killing for the two conditions of incubation with higher significance for the 24h incubation (p value of 0.007 rather than 0.08). In the presence of NPs, the α value increases by 30% while β tends to decrease, showing an amplification of the directly lethal damage specifically.

At 1.8 Gy, which is the dose per fraction delivered during the MV-treatment in clinic, the AGuIX[®] enhanced the effect of radiations by 14% and 16% for the 4h and 24h conditions respectively. A stronger effect is observed at 4 Gy with SERs of 18.3 and 23.0% for the respective conditions.

In summary, compared to radiotherapy alone, the addition of AGuIX[®] allows to obtain a cell survival of 10% with a radiation dose reduced by 9% (for 24h incubation).

b. Effect of NPs on brachytherapy

As for EBT, the cell survival curve shows a linear quadratic dose-dependent decrease of the survival fraction and an enhancement effect of the brachytherapy treatment is observed in the presence of AGuIX[®] (F value of 9.16 - p value of 0.001). As for EBT, we note a tendency of α value to increase (from 0.12 to 0.23) while β is constant (around 0.06-0.07). For doses of 1 and 2 Gy, SER values are equal to those obtained with EBT, 10 and 17% respectively. The values increase with the irradiation dose. For a dose of

5.25 Gy, which is a dose per fraction commonly delivered in HDR brachytherapy, the enhancement can reach 30%. Under the same incubation conditions (0.5 mmol/L for 24 h), from 3 Gy onwards, the effects obtained in brachytherapy are greater than those obtained in EBT (+4% at 4 Gy, +7% at 5 Gy). The alpha value is lower in brachytherapy than in EBT (0.23 instead of 0.44) but the beta is higher (0.06 instead of 0.04), suggesting that the difference of effects observed is caused by a higher accumulation of sublethal damage.

3.4. Discussion

This paper presents a quantification method of magnetic AGuIX[®] in patient's GTV based on T₁ mapping of MRI diagnostics and a method to evaluate the effect of the NPs on the radiation efficacy.

We found that, after NP injections mean AGuIX[®] concentrations in the patient's GTV are comprised between 7.6 and 16.0 μmol/L. A significant quantity of NPs was found in the bladder (up to almost 4 times higher than in the GTV) suggesting an excretion of nanoagents by the urine and a passage in the systemic circulation, as previously reported (Bort et al., 2020; Lux et al., 2018). After NP injection, no significant increase in the mean NP concentration was observed in healthy peripheral tissues. These findings supports that AGuIX[®] is deposited in the tumor exclusively, without any leakage in the surrounding tissues.

Our results are in line with a recent study performed on patients' brain metastasis, where the mean AGuIX[®] in the tumor was found between 8 and 63 μmol/L after NP injection of 100 mg/kg (Verry et al., 2020b). Our values are also in agreement with the mean NP concentrations of 13 μmol/L obtained by Verry and workers in rat glioma 24h after AGuIX[®] injection. Note that Verry and coworkers determined the mean AGuIX[®] concentrations in the GTV using an analytical method. We attempted to use the same method to determine the NPs concentrations from the patients' MR images.

An agreement better than 2% was found, validating our method and values of AGuIX[®] concentrations.

The calibration curve method is more fastidious than the analytical method but it is more universal. It can be applied if the theoretical value of relaxativity r_1 is not tabulated. Indeed, the value of r_1 is defined for each contrast agent and depends on the physicochemical properties of the compound and of the magnetic fields of the MRI instrument (Fries et al., 2014). However, the measurements performed to establish the calibration curve allowed us to verify that the value of relaxativity obtained in this work is close to the theoretical one (Fries et al., 2015, 2014).

In a second part, we demonstrated that 3D-CCM can be used to study the diffusion and effect of NPs in a tumor-like environment using concentrations close to the maximum ones found in clinic. This experiment shows that AGuIX[®] enter and diffuse in the collagen I and penetrate in cells with concentrations 1000 times lower than in the matrix.

The effect of AGuIX[®] on the radiotoxicity of two types of radiations, EBT and brachytherapy, was evaluated with this model. Radiobiological parameters that we have extracted from the survival curves are in agreement with other studies on cervical cancer tumors (Chow et al., 2019). From experimental data obtained after EBT, Chapman and Nahum reported α values of $0.35 \pm 0.21 \text{ Gy}^{-1}$ ($0.32 \pm 0.04 \text{ Gy}^{-1}$ in our study) and β value of 0.06 Gy^{-2} ($0.06 \pm 0.01 \text{ Gy}^{-2}$) (Chapman and Nahum, 2015; West et al., 1993). The radiobiological data presented in this paper for brachytherapy ($\alpha = 0.12 \pm 0.07 \text{ Gy}^{-1}$ and $\beta = 0.07 \pm 0.02$) also corroborate the results reported by Roberts and coworkers ($\alpha = 0.13 \pm 0.07 \text{ Gy}^{-1}$) after brachytherapy trials for stage I and II cervix carcinoma (Rangarajan et al., 2004). For both EBT and brachytherapy, we observe a larger contribution of the α parameter (i.e. complex lethal damage).

Despite the low NP concentration in cells (150-300 nmol/L), a significant enhancement of radiation effects was observed for EBT and brachytherapy. EBT irradiation of the 3D-CCMs leading to a SER at 2 Gy of 15-17%

is in agreement with previously published results after ^{137}Cs irradiation (662 keV) where a SER of 16% was obtained (Maury et al, 2019). The statistical tests highlight that the 24h AGuIX® incubation condition leads to a significant effect. In addition, a significant radioenhancement effect, which increase with the irradiation dose, was observed also in brachytherapy in presence of NPs. For a dose of 5.25 Gy, used in the schema of the HDR treatments, a radioenhancement of 30% was observed (Albuquerque et al., 2019). As expected, a greater or equal SER was systematically observed for the ^{192}Ir irradiation compared to the 6 MV. This is attributed to the contribution of photoelectric process which is higher for the keV range incident energy of the brachytherapy. **Erreur ! Source du renvoi introuvable.**

Thus, we demonstrated that there is a great interest of injecting NPs both during radio and brachytherapy treatments. Besides, due to a long retention time, it has been shown that AGuIX® are still detectable in pancreatic, lung and breast tumors 24h after intravenous injection (Lux et al., 2018). This ensures a radioenhancement effect of the NPs during the treatment (at least at D0/D1 and D11/D12 of the EBT and at D0/D1 of the brachytherapy).

In a study published last year, Sisin et al (Sisin et al., 2019) reported the potential of bismuth oxide NPs used as radiosensitizers in combination with cisplatin during brachytherapy treatments. They obtained a SER between 1.67-0.77 with 2D cell monolayers (to be compared to 1.22 in the present study with HeLa cells cultured in 3D). They suggested a synergic effect between cisplatin and Bismuth NPs, which - if verified for AGuIX®, could be of great interest because the standard of care for cervix cancer includes 5 cures of cisplatin (see Figure 3.2 - Overview of the NANOCOL)

3.5. Conclusion

In this paper, we reported a robust method based on T1-mapping from VFA sequences allowing an evaluation of the concentration of NPs accumulated in the GTV of patients treated for a cervix cancer in the NANOCOL clinical trial. MR signal enhancement in presence of NPs was observed in the tumor specifically. Mean AGuIX® concentration inside was determined and validated thanks to an independent method of quantification. In radiotherapy as in brachytherapy, we demonstrated that a very low quantity of AGuIX® in the tumoral cells (150-300 nmol/L in the tumoral cells, resulting from a local concentration of 100-150 $\mu\text{mol/L}$ in 3D-CCM after sample incubation with 500 $\mu\text{mol/L}$ NP concentration) was sufficient to induce a significant radiosensitizing effect (15-17% at 2 Gy). Thus, the accurate delineation of target volumes made possible by a strong MR contrast and promising radiobiological responses obtained in the presence of NPs promote a strategy of dose escalation by boosting or dose painting, allowing adaptable and personalized treatments. Even if follow-up studies are still expected to prove the clinical outcomes on patients, this work constitutes an additional step toward the development of a nanoenhanced image-guided radiotherapy. As a perspective, new technologies coupling an MRI with a Linac will provide daily treatment guidance, enabling adaptive radiotherapy, i.e. treatment plan personalization based on MR images and NP concentration of the day.

The content of this chapter is in preparation for a publication in the journal Science Translational Medicine as follow:

Maury P., Porcel E., Hirayama R., Li X., Mahou P., Schanne-Klein M-C., Gref R., Lacombe S., Synergistic effect of Gemcitabin-loaded metal organic nanoparticles with hadrontherapy

CHAPTER 4. EVALUATION OF GEM-LOADED NANOMOFs COMBINED WITH HADRONTHERAPY



“Impose ta chance, serre ton bonheur et va vers ton risque. A te regarder, ils s’habitueront”

René Char –
Rougeur des matinaux, 1948

Les champs du hameau d'Umezawa dans la province de Sagami,
Hokusai, 1829-1833, Bibliothèque Nationale de France

Content

1. INTRODUCTION	75
2. CORPUS	76
2.1. INTRODUCTION	76
2.2. MATERIALS	77
2.2.1. <i>NanoMOFs Synthesis and Gemcitabin incorporation</i>	77
2.2.2. <i>Cell cultures</i>	78
2.3. METHODS.....	78
2.3.1. <i>Characterization of the nanoMOFs toxicity</i>	78
2.3.2. <i>Characterization of the nanoMOFs localization by fluorescence microscopy</i>	79
2.3.3. <i>Quantification of the nanoMOFs in the samples</i>	79
2.3.4. <i>Irradiation experiments</i>	80
2.4. RESULTS	82
2.4.1. <i>Toxicity of nanoagents</i>	83
2.4.2. <i>Localization of nanoMOFs</i>	83
2.4.3. <i>Quantification of nanoMOFs</i>	84
2.4.4. <i>Impact of nanoMOFs, Gemcitabin and Gem-loaded nanoMOFs on radiation effects: comparison of normoxic and hypoxic conditions (in 2D cell cultures)</i>	85
2.4.5. <i>Impact of nanoMOFs, Gemcitabin and Gem-loaded nanoMOFs on radiation effects: impact of the matrix (3D cell cultures)</i>	89
2.5. DISCUSSION	91
2.5.1. <i>Molecular processes induced by irradiation</i>	91
2.5.2. <i>Mechanisms induced in presence of Gemcitabin</i>	92
2.6. CONCLUSIONS	94
3. SUPPLEMENTARY DATA	95
3.1. DEPENDANCE OF THE LET	96
3.2. SUMMARY OF THE RADIOBIOLOGICAL VALUES.....	96

1. INTRODUCTION

In the previous chapter, the 3D-CCMs were applied to help improve the treatment based on radiotherapy combined with AGulX[®], currently evaluated in clinic.

In this chapter, the same preclinical model was used to probe a highly innovative strategy: the association of new nanoagents, the Gemcitabin-loaded nanoMOFs, with particle beam radiation. The aim was to evaluate the potential of these nanoagents developed in our laboratory by Ruxandra Gref.

In this drug development process, 3D cellular models reproducing the structural architecture and microenvironmental features of tumors, have rapidly emerged as relevant *in vitro* platform for new therapies screening. The presence of the ECM allows a more realistic evaluation of the cell response to both irradiation and nanoagents exposure.

2. CORPUS

2.1. Introduction

The combination of chemotherapy with radiations treatments, called chemoradiation, is the standard of care for many solid cancers (Pauwels et al., 2003; Song et al., 2017). In comparison with other therapeutic alternatives, this strategy exhibits clinical benefits, such as organ preservation and tumoral control (Seiwert et al., 2007). The cytotoxic effects induced by the drug and the radiation together, produced at the tumor site, increase the therapeutic ratio (Seiwert et al., 2007). In addition, the spatial cooperation between the locoregional action of the radiotherapy and the systemic properties of the chemotherapy reduces the risk of metastasis (Gordon Steel and Peckham, 1979). The synergistic effects reported by the different studies are mainly attributed to the sensitization effects of cells by the antitumor agent. Gemcitabin (Gem) is an efficient radiosensitizer already used in clinic which exerts its cytotoxic effect by targeting DNA (Carmichael et al., 1995). The anticancer nucleoside analog Gem is a prodrug which needs to be converted by cellular kinases into the pharmacologically active triphosphate form. However, in some cases, this intracellular conversion is not efficient leading to drug resistance and systemic toxicity. The direct administration of the phosphorylated form of Gem is hampered by its poor stability in biological media, low intracellular penetration and low tissue specificity (Bouffard et al., 1993).

A promising approach was recently proposed by Gref and coworkers to improve the stability and the tumor transportation of Gem to the tumor. It consists in encapsulating the active form of Gem, Gem-monophosphate (GemMP) in highly porous hybrid metal-organic nanoparticles (nanoMOFs) (Rodriguez-Ruiz et al., 2015). These biodegradable (Li et al., 2017) and biocompatible (Baati et al., 2013) nanoparticles protect the drug against degradation and significantly improve drug delivery in tumor cells. As a major advantage, the iron-based composition of the nanoMOFs allows them to act as enhancers of radiation effects (X. Li et al., 2020a). Besides, these paramagnetic nanoparticles may be used as contrast agents monitored by MRI (Horcajada et al., 2010).

The group already reported the efficiency of GemMP-loaded nanoMOFs to improve the effect of radiations. Experiments were conducted with 2D cell cultures HeLa cancer cells in normoxic conditions. An 80% increase of cell killing was observed when gamma radiation (Cs-137, energy = 662 keV (γ)) was used (X. Li et al., 2020a). This increase was among the strongest ever reported for tumor treatment with gamma irradiation and nanoparticles.

However, gamma rays are not used in external radiotherapy. Based on our strong proof of concept, this work aims to go steps beyond by addressing the important challenge to investigate the potential of GemMP-loaded nanoMOFs with a medically relevant radiation modality and a cell environment better representative of the tumor reality than monolayer normoxic cultures.

In tumors, cells interact with and through an extracellular matrix (ECM), which acts as a structural and biochemical support. It was shown that this natural barrier limits the penetration and the accumulation of nanoagents in solid tumors after extravasation from the blood vessels and, also, it may influence the cell response to irradiation (Jain, 1997). Thus, the ECM often compromises the antitumor efficiency of the treatments (Magzoub et al., 2008; Minchinton and Tannock, 2006; Pratiwi et al., 2021; Steichen et al., 2013; Tchoryk et al., 2019b).

In addition, most of radioresistant tumors are hypoxic (oxygen concentration below 1%) (McKeown, 2014). This specificity is associated to poor treatment outcomes, high probability of relapse and increased risks of metastases (Brown and Wilson, 2004; Vaupel and Mayer, 2007). Thus, oxygen concentration in monolayer cultures was monitored to work in challenging hypoxic conditions and a realistic 3D tumor model was proposed to mimic the tumor environment.

In the present work, the properties of GemMP-loaded nanoMOFs were evaluated using an advanced treatment modality, the particle therapy (also called hadrontherapy). This technique, based on the use of high energy charged particles (carbon or helium ions of MeV/amu), allows to enhance tumor targeting and local control compared to conventional radiotherapy. The advantage of ions compared to photons stems from their property to deposit their maximum energy at the end of the track (Bragg peak). In operating conditions, the Bragg peak is widened to create a spread-out Bragg peak (SOBP) which covers the total volume of the tumor (Durante et al., 2017). As a result, the damage induced behind the tumor is close to zero and the surrounding healthy tissues can be spared (Porcel et al., 2014) (see supplementary section, Figure 1). Compared to photons, charged particle beams also have a higher biological effectiveness. They induce more complex DNA damages, result in multiple damage sites or clustered DNA lesions, which increases cell killing in the tumor (Durante et al., 2017; Durante and Cucinotta, 2008; Hagiwara et al., 2019, 2017; Lorat et al., 2015; Sage and Shikazono, 2017). These advantageous properties are exploited in the present work by proposing a combination of this type of beams with GemMP-loaded nanoMOFs.

The effect of GemMP-loaded nanoMOFs was measured *in vitro* in different conditions of oxygen concentration and cell environment. First, the impact of oxygen on GemMP-loaded nanoMOFs effects was evaluated on 2D HeLa cell cultures (normoxic and hypoxic conditions). Then, a comparison of the effects produced on cells in 2D cultures or embedded in a collagen I matrix was conducted. This *in vitro* model, newly developed in the field of radiation studies, mimics the influence of a microenvironment and disrupts the cells' response both to nanoagents and irradiation (Goodman et al., 2007; Magzoub et al., 2008; Minchinton and Tannock, 2006; Netti et al., 2000; Steichen et al., 2013; Tchoryk et al., 2019b). Thus, the influence of these two factors, ECM and oxygen concentration were investigated.

2.2. Materials

2.2.1. NanoMOFs Synthesis and Gemcitabin incorporation

Synthesis of iron trimesate MIL-100(Fe) nanoMOFs (MIL stands for Material of Institute Lavoisier) is performed by microwave-assisted solvent-free “green” hydrothermal techniques as previously described (X. Li et al., 2020). Briefly, a mixture of iron chloride (8.97 mmol) and trimesic acid (4.02 mmol) in 20 mL of deionized water was placed in Pyrex reactors and heated for 6 min at 130 °C under stirring. The applied power was 1600 Watts (Mars-5, CEM, US). The reactors were cooled in ice bath and the synthesized nanoMOFs were recovered by centrifugation (10000 g, 15 minutes) and were purified by washing with absolute EtOH six times to remove the residual non-reacted trimesic acid. The nanoMOFs were stored in EtOH until final use. Their average hydrodynamic mean diameter was 220 ± 25 nm and 200 ± 64 nm, determined according to dynamic light scattering (DLS) (Nano-ZS, Zetasizer Nano series, Malvern Instruments, UK) or NP tracking analysis (NTA) (Nanosight, Malvern Instruments, UK) respectively. The BET (Brunauer-Emmett-Teller) surface area reached 1680 ± 90 m²/g and the nanoMOFs possessed a crystalline structure in agreement with previous studies.

GemMP was loaded in nanoMOFs at GemMP:nanoMOFs weight ratio of 1:10. GemMP was quantified by HPLC (Agilent 1100, USA) using a previously described method (X. Li et al., 2020).

Encapsulation efficacy (EE) was calculated as:

$$EE (\%) = \frac{\text{Encapsulated Drug (mg)}}{\text{Initial Drug (mg)}} \times 100 \quad \text{Eq. 22}$$

where “encapsulated drug” represents the amount (mg) of drug incorporated in the nanoMOFs and “initial drug” represents the amount (mg) of drug used in the preparation procedure. The drug loading (DL) was calculated as.

$$DL (\%) = \frac{\text{Encapsulated Drug (mg)}}{\text{Initial Drug (mg)}} \times 100 \quad \text{Eq. 23}$$

Mother solutions of 2 mg/mL of nanoMOFs and 100 µg/mL of Gemcitabin were used for toxicity, quantification and irradiation experiments. For microscopy studies, the nanoMOFs (0.5 mg/mL) were labelled with the fluorescent tags Rhodamine B or Alexa 568. A two steps procedure was used: (i) the nanoMOFs were incubated overnight with the fluorescent dye (weight ratio of 1:10) and (ii) the free fluorophores were eliminated by successive water washing.

2.2.2. Cell cultures

The experiments were performed with the human cervical adenocarcinoma cell line (HeLa), purchased from ATCC[®] in 2016 (ATCC France, Molsheim, France) or RIKEN BRC in 2015 (RIKEN BRC Japan, Tsukuba-shi, Japan). Cells were cultivated in Dulbecco's Modified Eagle Medium (DMEM) or Minimum Essential Medium Eagle (E-MEM) supplemented with 10% heat-inactivated foetal bovine serum (FBS), 1% penicillin/streptomycin (P/S) and 1% L-glutamine (Life Technologies).

2D experiments were performed from monolayer cultures of HeLa cultured in flasks while 3D-CCMs were prepared by embedding ~350 000 HeLa cells in a collagen I matrix using a commercially available system (RAFT[™] 3D cell culture kit, Lonza, Basel, Switzerland).

As detailed in a previous study (Maury et al., n.d.), 3D-CCMs were prepared by mixing a cell suspension of 2.4-2.6 cells/mL with 10X MEM, neutralizing solution and 2mg/mL rat-tail type I collagen solution. 320 µL of the final solution were dispensed in each 96 well plate and kept in the incubator for 15 min. RAFT[™] absorbers were finally disposed on top of each well for 15 min.

2.3. Methods

2.3.1. Characterization of the nanoMOFs toxicity

In a previous study performed on monolayer cultures (X. Li et al., 2020), it was shown that a concentration of 17 µg/ml unloaded nanoMOFs was not toxic for cells incubated for 6h (>95% cell viability). As expected, the Gem, used free or incorporated in the nanoMOFs, induced a cytotoxic effect killing 50% of cells at concentration of 1.7 µg/ml.

On this basis, the same concentration of nanoMOFs (17 µg/mL) was chosen in the present study but concentration of GemMP was lowered to 0.85 µg/ml to reduce its toxicity.

Monolayer cells were incubated with these concentrations for 6h while 3D-CCMs were incubated during 18h to allow homogeneous migration of the agents in the matrix. 2D toxicity studies were performed using a clonogenic assay (see section 2.3.4 for detailed protocol). For the cells embedded in the 3D-CCMs, the toxicity of GemMP-loaded nanoMOFs used at the same concentration than in the experiments with 2D cultures (i.e. 17 µg/mL of nanoMOFs loaded with 0.85 µg/mL of GemMP) were determined using MTT test.

In this purpose, 3D-CCMs were exposed to 125 µL of tetrazolium dye MTT 3-(4,5-dimethylthiazol-2-yl)-2,5-diphenyltetrazolium bromide in a 96-well plate at 37°C for 4 h. Then, 125 µL of lysis buffer was added to dissolve the formazan crystals. The proportion of living and metabolically active cells, was quantified from the absorbance measured with a Glomax[®] Microplate reader (Promega[®]) (absorbance 560 nm). A sample consisting of 3D-CCM incubated with a volume of water equivalent to the volume of GemMP-loaded

nanoMOFs was used as positive control. A sample composed of 3D-CCM treated for 4h with 200 μL of menadione (500 $\mu\text{mol/L}$) was used as negative control.

2.3.2. Characterization of the nanoMOFs localization by fluorescence microscopy

The localization of the nanoagents in cells was characterized using two techniques, namely confocal microscopy and multiphotons microscopy for the 2D and 3D samples, respectively.

a. Confocal microscopy protocol (for the 2D cultures)

Monolayer living cells incubated with nanoMOFs labelled with Rhodamine for 6h were imaged on sterile glass slides using a LEICA SP5 confocal system according to the protocol described in our previous study (X. Li et al., 2020). Briefly, the images were acquired at 514 nm excitation wavelength, in the 560 to 600 nm range of emission. During the acquisition, the temperature was kept at 37°C and the CO₂ was regulated at 5%.

b. Multiphoton microscopy protocol (for the 3D samples)

Multiphoton microscopy (2PEF) was used to study the nanoMOFs migration in 3D-CCMs. 3D-CCMs were incubated with nanoMOFs-Alexa 568 in the conditions specified above (i.e. 17 $\mu\text{g/mL}$ nanoMOFs concentration, 18h incubation time). After PBS washing, nuclei were stained for 20 min with 1 $\mu\text{mol/L}$ Hoescht 33342 solution. Multimodal z-stacks images were recorded with a commercial multiphoton microscope (TriM Scope II, LaVision BioTec) allowing sequential 3D acquisitions.

Collagen of the 3D-CCMs was imaged without any labelling using a nonlinear optic effect which is the second harmonic generation (SHG). This signal was generated by a beam of the Insight DeepSee laser set at $\lambda = 1140$ nm. The SHG scattered light centered approximately 560 nm was detected by a photomultiplier tube placed in transmission (H7422-40, Hamamatsu) and separated from the laser light by a dichroic mirror (Di02-R635, Semrock) and an interference filter (FF02-575-25, Semrock). Cell nuclei and nanoMOFs were imaged by 2PEF. After excitation by a laser beam at $\lambda = 830$ nm, the signal of the nuclei or nanoMOFs were respectively collected in epidetection mode by a photomultiplier tube (H6780-01 Hamamatsu) and separated from the laser light by a dichroic mirror (T695lpxr, Chroma) and an interference filter (FF01-450-70/FF01-466-40 (nuclei) or FF01-607-70 (nanoMOFs) - Semrock). Data acquisition was performed on a 350 μm square field of view with a pixel size of 0.192 μm and an acquisition frequency of 400 Hz. Images were captured with a z-step of 1 μm .

2.3.3. Quantification of the nanoMOFs in the samples

A method to quantify the nanoMOFs concentration in cells of 2D cultures is described elsewhere (X. Li et al., 2020a). Briefly, the intracellular amount of nanoMOFs was determined using a method based on iron staining with potassium ferrocyanide (Wuttke et al., 2015). Although reliable, this method is time-consuming as it requires the establishment of a calibration curve.

The quantification of the nanoMOFs concentrations contained in (i) entire 3D-CCM and (ii) in the cells extracted from the 3D-CCM, was performed by faster method, the Inductively Coupled Plasma-Mass Spectroscopy (ICP-MS) (UT2A - Technological Center, Pau, France). To collect the cells from the 3D-CCMs, an addition step of enzymatic degradation with 1 mg/ml collagenase from *Clostridium histolyticum* (Sigma-Aldrich©) was needed (Maury et al., 2019).

2.3.4. Irradiation experiments

a. Preparation of 2D samples to study the influence of oxygen influence on irradiation effects

Approximately 200 000 cells per sample were prepared onto 3.8 cm glass dishes 24h prior to irradiation. The cells were incubated 6h before irradiation with the agents at respective concentrations in the solution (17 µg/mL nanoMOFs, 0.85 µg/mL GemMP and 17 µg/mL of nanoMOFs containing 0.85 µg/mL of Gemcitabin). After 5h, the volume of the medium was reduced from 3 ml down to 0.9 mL. For the experiments performed with hypoxic conditions (setup environment composed of 0.5% O₂, 95% N₂ and 5% CO₂), the samples were disposed 1h prior to irradiation in a gas chamber flushed with a mixture of N₂/CO₂/air of 950/50/25 mL/min respectively to reach the required oxygen concentration. For normoxic conditions, the dishes were placed in the radiation chamber under atmospheric conditions (20% O₂, 78% N₂) 30 min before irradiation.

b. Preparation of 3D samples to study the influence of the matrix on irradiation

3D-CCMs were prepared in 96 wells plates 24h before irradiation (see 2.2.2) 18h before irradiation, 3D-CCMs were put in contact with solution of free drug or nanoMOF formulation containing equivalent amounts of GemMP and empty nanoMOFs as controls. Incubation concentrations were the same as for 2D experiments (i.e. 17 µg/mL nanoMOFs, 0.85 µg/ml GemMP and 17 µg/mL of nanoMOFs containing 0.85 µg/mL of GemMP). Samples were incubated at 37°C until irradiation. Just before irradiation, these solutions were replaced by fresh cell culture medium. After irradiation, the cells were extracted from the 3D-CCM matrix using 1 mg/mL collagenase as indicated in a previous study (Maury et al., 2019).

c. Irradiations

The irradiations were performed using passive beam delivery systems at HIMAC (Heavy Ion Medical Accelerator in Chiba) in Chiba, Japan (Porcel et al., 2014) (Porcel et al., 2014). Two 10 cm diameter beams of different LET were used: a beam of carbon ions C⁶⁺ (primary energy = 290 MeV/u, LET = approximately 50 keV/µm) and a beam of helium ions He²⁺ (primary energy = 150 MeV/u, LET = approximately 12 keV/µm). Dishes were irradiated vertically and one by one, at the center of a 6 cm-SOBP with a dose rate of approximately 3 Gy/min.

d. Analysis by clonogenic assay

The effects of radiation combined with nanoagents was analyzed by clonogenic assay as described elsewhere (Tubiana et al., 1986). Briefly, harvested cells were seeded in Petri dishes to determine the ability of cells to proliferate and form colonies. For each condition, cell survival curves were established and simulated with a linear-quadratic model (LQ) as commonly used (Tubiana et al., 1986).

e. Statistical tests and quantitative parameters of analysis

Statistical test

Statistical tests were performed using the CFAssay package included in the R software (R Core Team (2020), R: A Language and Environment for Statistical Computing, R Foundation for Statistical Computing, Vienna, Austria, <https://www.R-project.org>) (Brasemann, 2019; Brasemann et al., 2015). These F-tests, based on

a maximum likelihood (ML) method, allow to conclude about the significance of the difference observed (i) between the cell survival curve of the control and those obtained in the presence of nanoagent (nanoMOFs, Gem or Gem-loaded nanoMOFs) (ii) between the curves with nanoMOFs alone or loaded with Gem. Statistical analysis was applied from the experimental points and significance of the p values was indicated on the survival curve as follows: 0 ‘****’, 0.001 ‘***’, 0.01 ‘**’, 0.05 ‘.’, 0.1 ‘ ‘, 1.

Quantitative parameters for analysis

Efficiencies of combined strategies were quantified using the radiation Sensitizing Enhancement Ratio (SER)(Eq. 24). This parameter is defined at a specific dose point and is indicative of the radiation effect induced by the presence of nanoagents.

$$SER_D(\%) = \frac{SF_D^c - SF_D^N}{SF_D^c} \quad \text{Eq. 24}$$

where SF_D^c and SF_D^N are the survival fractions at the D dose for the control sample and the sample incubated with nanoagents.

In the first part of the work that deals with oxygen influence on the combination effect, hypoxia induced radioresistance was quantified by the oxygen enhancement ratio (OER). It is defined by the Eq. 25 as the ratio between the dose of radiation needed when oxygen concentration is reduced (i.e. $D_{\text{hypoxic}}^{SF_0}$, here with $pO_2=0.5\%$) and the radiation dose required in fully oxygenated conditions (i.e. $D_{\text{normoxic}}^{SF_0}$, with $pO_2=20\%$) to produce the same level of biological effect (here $SF=10\%$). OER is related to indirect effects and thus to the quality of the beam (LET dependency).

$$OER = \frac{D_{\text{hypoxic}}^{SF_0}}{D_{\text{normoxic}}^{SF_0}} \quad \text{Eq. 25}$$

Isobologram analysis

In addition, to characterize the effects produced by the combination of the radiations with Gem-loaded nanoMOFs, an isologram analysis was performed using the software CompuSyn (Chou and Martin, 2005). This method, introduced by Chou-Talalay (Chou, 2010; Chou and Talalay, 1984; Leonard et al., 1996) is based on a combination index (CI) approach. The value of the CI, calculated according to the theorem defines antagonism ($CI>1.0$), additive effect ($CI=1.0$) or synergism ($CI<1.0$) (Huang et al., 2019)(Eq. 26).

$$CI = \frac{(D)_1}{(D_x)_1} + \frac{(D)_2}{(D_x)_2} \quad \text{Eq. 26}$$

$(D_x)_1$ and $(D_x)_2$ are the doses for radiations (1) and Gem-loaded nanoMOFs (2) used alone that give a fraction affected (F_a) of x% while D_1 and D_2 are the doses used in combination that reproduce this same cytotoxic effect. Values of $(D_x)_1$ and $(D_x)_2$ are extracted from the median-effect equation of Chou (Eq.27).

$$D_x = D_m \cdot \left(\frac{F_a}{1-F_a} \right)^{\frac{1}{m}} \quad \text{Eq. 27}$$

Where D_m is the median-effect dose.

D_m (more precisely $-m \cdot \log(D_m)$) is obtained from the intercept of the dose effect plot (linearization of the $Dx = D_m \cdot \left(\frac{F_a}{1-F_a}\right)^{\frac{1}{m}}$ which is $y = \log\left(\frac{F_a}{1-F_a}\right)$ function to $x = m \cdot \log(D)$). m is the slope (kinetic order) of the curve.

In this study, the cell fractions affected by increasing doses of (i) nanoagents alone (ii) radiation alone and (iii) nanoagents combined with radiation were implemented in the program. Consequently, calculated values of the different parameters required for analysis were provided by the software and plots were automatically generated, allowing a simple graphical interpretation.

2.4. Results

2.4.1. NanoMOFs synthesis and characterization, GemMP incorporation

The nanoMOFs possess a porous structure with oxocentered Fe(III) trimers connected by trimesate (1,3,5-benzene tricarboxylate) linkers (Figure 4.1)

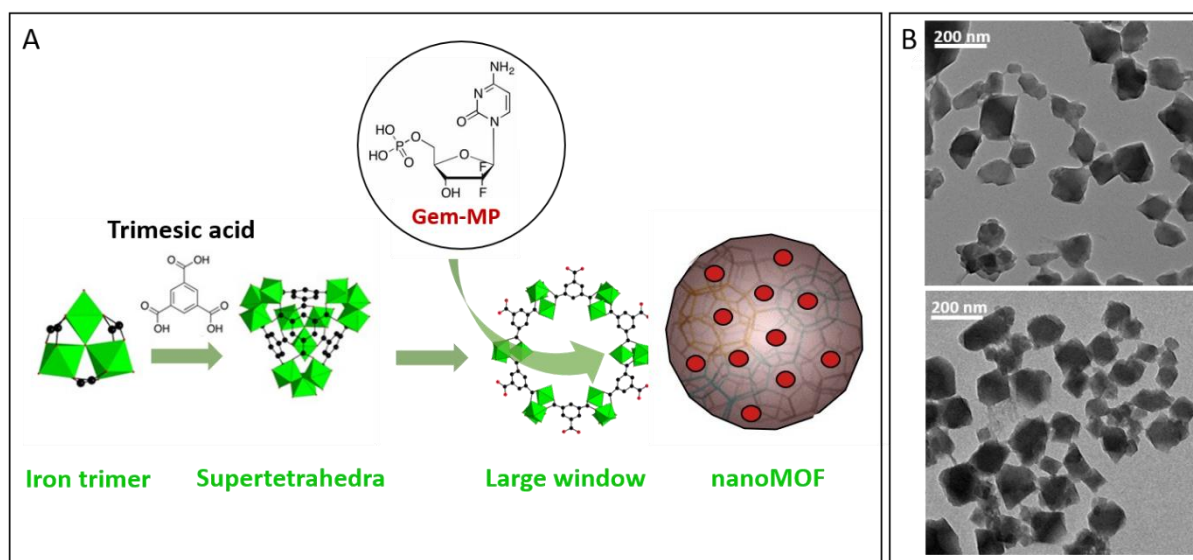


Figure 4.1- (A) Schematic representation of the nanoMOF assembly from iron trimers and trimesate organic linkers, forming supertetrahedra that further assemble into porous nanoparticles. The anticancer drug GemMP can cross the large windows of around 9Å and fill the nanoMOF pores by interacting with the iron sites. (B) Typical TEM images of nanoMOFs empty (upper) and loaded with 5% GemMP (lower).

The nanoMOFs present an homogenous size, with mean hydrodynamic diameters of 220 ± 25 nm, BET surface area of 1680 ± 90 m²/g. GemMP was incorporated by coordination with the accessible unsaturated sites of Fe trimers, EE close to 100%, DL of 10 wt% ensuring a loading of these frameworks without size modification (220 ± 25 nm & 226 ± 28 nm before and after GemMP encapsulation). Encapsulated drug is released to the target by progressive degradation of nanoMOFs by the phosphates contained in the biological medium, where a strong coordination is created with the phosphate groups of GemMP (X. Li et al., 2020a; Rodriguez-Ruiz et al., 2015). By using tritiated GemMP it was demonstrated that it could not penetrate inside PANC-1 cancer cells, in reason of its hydrophilic character (Rodriguez-Ruiz et al., 2015). Indeed, less than 0.7% of the free drug was found inside the cells after 5h incubation, whereas more than 6% of the nanoMOF-incorporated drug was in the cells after only 1h incubation. However, 5h after incubation with the cells, the drug amount was reduced to 3.3% and it was hypothesized that at longer incubation times, the released drug can be substantially effluxed out. In a nutshell these studies

highlighted that : i) GemMP is unable to bypass cell membranes; ii) nanoMOFs carry the drug efficiently inside cancer cells; iii) the released drug inside the cells might be effluxed out.

2.4.2. Toxicity of nanoagents

a. Toxicities for cells cultivated in 2D monolayers

In presence of nanoMOFs (17 $\mu\text{g}/\text{mL}$), the toxicity is not significant ($> 95\%$ cell viability). On the other hand, as shown in the Table 6, the toxicities of GemMP free or GemMP incorporated in nanoMOFs were found very similar for equivalent concentrations. In particular, an equivalent GemMP concentration of ~ 1.7 $\mu\text{g}/\text{mL}$ leads to cytotoxic effect killing around 50-55%. These results agree with our previous experiments (X. Li et al., 2020). A lower equivalent GemMP concentration (i.e. 0.42 $\mu\text{g}/\text{mL}$) reduces cytotoxicity by about 30%.

Then, an intermediate equivalent GemMP concentration of ~ 0.85 $\mu\text{g}/\text{mL}$ leads to cytotoxicity of 26% for the free GemMP and 22% for GemMP-loaded nanoMOFs. It is this concentration (~ 0.85 $\mu\text{g}/\text{mL}$) that we chose for the irradiation study to reduce the drug's toxicity while maintaining a significant effect on cells.

Table 6. Comparison of the survival fractions obtained in presence of Gem free or 5% Gem loaded nanoMOFs.

Concentration in Gem	SF for Gem free	SF for 5% Gem-loaded nanoMOFs
0.42 $\mu\text{g}/\text{ml}$	83% \pm 15%	85% \pm 8%
0.83 $\mu\text{g}/\text{ml}$	74% \pm 15%	78% \pm 8%
1.70 $\mu\text{g}/\text{ml}$	50% \pm 7%	55% \pm 4%

b. Toxicities in cells embedded in 3D-CCMs

Results of the MTT assay performed on 3D-CCM with these conditions (0.85 $\mu\text{g}/\text{mL}$ of GemMP in 17 $\mu\text{g}/\text{mL}$ of nanoMOFs) are presented in Figure 4.2 - **(A)** Localisation of 17 $\mu\text{g}/\text{mL}$ nanoMOFs incubated a- in monolayer cultures for 6h or b-c-d- in 3D-CCMs for 18h. NanoMOFs are labelled in red, collagen is green and nuclei are blue. b- and c- images represent the same area in the sample : b is the merged image (SHG+2PEF) while c represents the nanoparticle channel in 2PEF exclusively An acquisition in the z-depth of the area framed in orange was performed. Images extracted from the stack are given in d-. SHG images were captured with a pixel size of 0.192 μm , an acquisition frequency of 400 Hz and a z-step of 1 μm . **(B)** Evaluation of the cytotoxicity of nanoMOFs loaded with Gemcitabin based on the mitochondrial activity measurement of cells contained in 3D-CCM (in black) compared to positive (green) and negative (red) controls. **(C)** Quantification of nanoMOFs amount in 3D-CCM and cells after an incubation of the samples with 17 $\mu\text{g}/\text{mL}$ nanoMOFs for 18h. Mitochondrial activity of cells incubated with GemMP-loaded nanoMOFs (in black) was found identical to that of the control cells (in green). Results are significantly differ from the negative control (in red) and show that the drug-loaded nanoMOFs are not toxic for cells cultured in 3D.

2.4.3. Localization of nanoMOFs

In order to avoid interfering with the entrapped GemMP drug, nanoMOFs were surface-labelled with rhodamine B as previously described (X. Li et al., 2020). The label was not detached under incubation in cell culture media

a. Localisation in cells cultivated in 2D monolayer

Confocal images of nanoMOFs surface-labelled with rhodamine B internalized in 2D cells are presented in Figure 4.2 - (A) Localisation of 17 $\mu\text{g}/\text{ml}$ nanoMOFs incubated a- in monolayer cultures for 6h or b-c-d- in 3D-CCMs for 18h. NanoMOFs are labelled in red, collagen is green and nuclei are blue. b- and c- images represent the same area in the sample : b is the merged image (SHG+2PEF) while c represents the nanoparticle channel in 2PEF exclusively An acquisition in the z-depth of the area framed in orange was performed. Images extracted from the stack are given in d-. SHG images were captured with a pixel size of 0.192 μm , an acquisition frequency of 400 Hz and a z-step of 1 μm . (B) Evaluation of the cytotoxicity of nanoMOFs loaded with Gemcitabin based on the mitochondrial activity measurement of cells contained in 3D-CCM (in black) compared to positive (green) and negative (red) controls. (C) Quantification of nanoMOFs amount in 3D-CCM and cells after an incubation of the samples with 17 $\mu\text{g}/\text{ml}$ nanoMOFs for 18h. NanoMOFs were found in the cytoplasm exclusively and not in the nuclei. This result is in line with our previous observation (X. Li et al., 2020).

b. Localisation in cells embedded in 3D-CCMs

SHG microscopy images of nanoMOFs internalized in 3D-CCMs are presented in Figure 3. For the first time, we observed that nanoMOFs can penetrate through the collagen of 3D-CCM. After 18h, they have infiltrated the entire sample depth and are homogeneously distributed in the matrix. The nanoMOFs signal in the matrix is much weaker than in the cells (where the nanoMOFs were internalized in aggregates). It explains that we don't distinguish nanoMOFs in the matrix on the merged images b and d.

As demonstrated in the case of 2D monolayers, the nanoMOFs penetrate in the cells and localize in the cytoplasm but not in the nuclei (X. Li et al., 2020a). Besides, the images show the presence of nanoparticles clusters in the cytoplasm, suggesting internalisation in the cells by endocytic process. This internalization pathway is frequently reported for nanoparticles of this size (~200 nm) (Foroozandeh and Aziz, 2018; Manzanares and Ceña, 2020).

2.4.4. Quantification of nanoMOFs

The quantification of nanoMOFs in 2D monolayers cultures was performed in a previous study (X. Li et al., 2020a). In this work, we quantified nanoMOFs in 3D-CCMs.

The ICP-MS results show that the natural concentration of iron is close to 0.09 μg in a 3D-CCM composed of 295 680 cells. The amount of iron contained in 3D-CCM after 18h incubation with nanoMOFs was almost 5 times higher than in the control (i.e. 0.42 μg of iron for 3D-CCMs containing 295 680 cells embedded in collagen). It indicates that 0.33 μg of iron penetrated into 3D-CCM, which corresponds to 1.70 μg nanoMOFs. As the sample was incubated with 240 μl of 17 $\mu\text{g}/\text{mL}$ nanoMOFs, after 18h the uptake of nanoMOFs in the 3D-CCM was 42%.

The mean quantity of iron found per cell (after disaggregation of 3D-CCM) was close to 0.37 pg (corresponding to 1.92 pg nanoMOFs). Thus, 0.57 μg of nanoMOFs were uptaken by the cells in 3D-CCM namely 14% of the nanoagents available during incubation. Regarding the uptake in cells and in the sample, it clearly appears that most of the nanoMOFs were trapped in the collagen matrix. However, the quantity found in cells which represents 1/3 of the nanoagents contained in the sample confirms microscopy results, proving the ability of nanoMOFs to pass through the matrix and reach cells (Figure 4.2 - (A) Localisation of 17 $\mu\text{g}/\text{ml}$ nanoMOFs incubated a- in monolayer cultures for 6h or b-c-d- in 3D-CCMs for 18h. NanoMOFs are labelled in red, collagen is green and nuclei are blue. b- and c- images represent the same area in the sample : b is the merged image (SHG+2PEF) while c represents the nanoparticle channel in 2PEF exclusively An acquisition in the z-depth of the area framed in orange was performed. Images extracted from the stack

are given in d-. SHG images were captured with a pixel size of $0.192\ \mu\text{m}$, an acquisition frequency of 400 Hz and a z-step of $1\ \mu\text{m}$. **(B)** Evaluation of the cytotoxicity of nanoMOFs loaded with Gemcitabin based on the mitochondrial activity measurement of cells contained in 3D-CCM (in black) compared to positive (green) and negative (red) controls. **(C)** Quantification of nanoMOFs amount in 3D-CCM and cells after an incubation of the samples with $17\ \mu\text{g}/\text{ml}$ nanoMOFs for 18h.

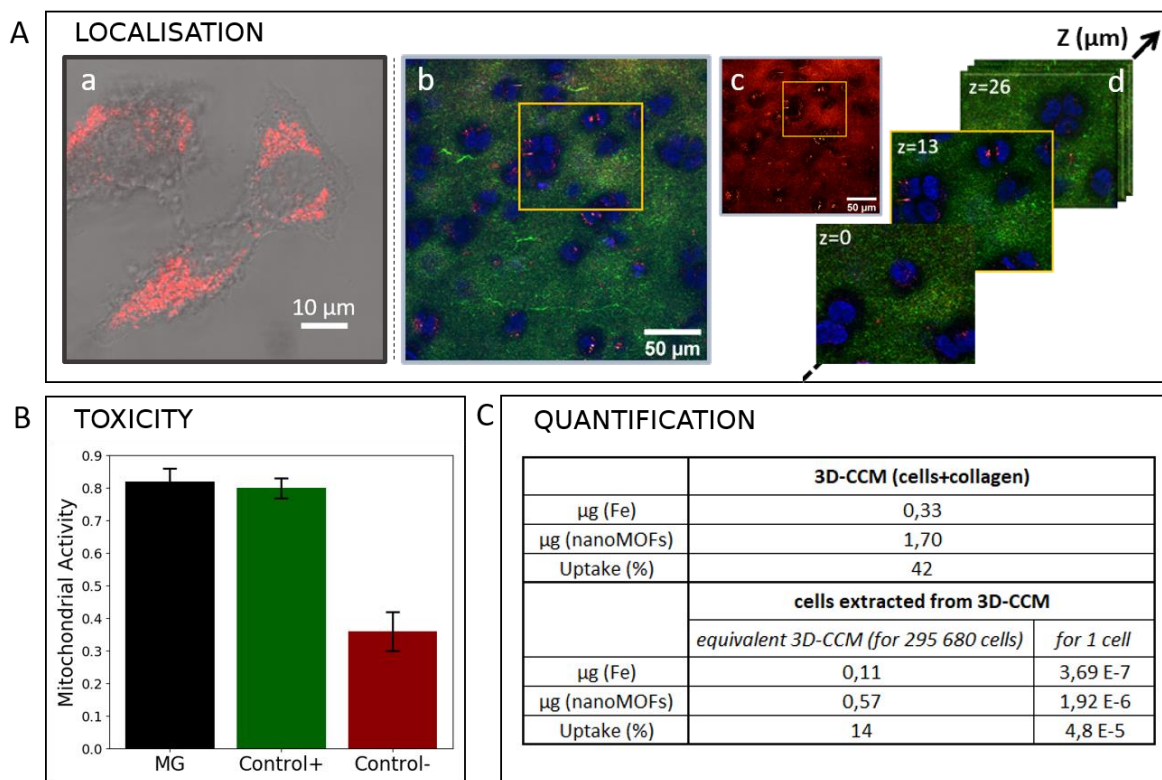


Figure 4.2 – **(A)** Localisation of $17\ \mu\text{g}/\text{ml}$ nanoMOFs incubated a- in monolayer cultures for 6h or b-c-d- in 3D-CCMs for 18h. NanoMOFs are labelled in red, collagen is green and nuclei are blue. b- and c- images represent the same area in the sample : b is the merged image (SHG+2PEF) while c represents the nanoparticle channel in 2PEF exclusively An acquisition in the z-depth of the area framed in orange was performed. Images extracted from the stack are given in d-. SHG images were captured with a pixel size of $0.192\ \mu\text{m}$, an acquisition frequency of 400 Hz and a z-step of $1\ \mu\text{m}$. **(B)** Evaluation of the cytotoxicity of nanoMOFs loaded with Gemcitabin based on the mitochondrial activity measurement of cells contained in 3D-CCM (in black) compared to positive (green) and negative (red) controls. **(C)** Quantification of nanoMOFs amount in 3D-CCM and cells after an incubation of the samples with $17\ \mu\text{g}/\text{ml}$ nanoMOFs for 18h

2.4.5. Impact of nanoMOFs, Gemcitabin and Gem-loaded nanoMOFs on radiation effects: comparison of normoxic and hypoxic conditions (in 2D cell cultures)

a. Carbon ion irradiation

The survival curves obtained by the exposition of monolayer culture with 290 MeV carbon ions (6 cm SOBP) beam (LET = $50\ \text{keV}/\mu\text{m}$) are presented in Figure 4.3A.

Both under normoxic ($p\text{O}_2 = 20\%$) and hypoxic conditions ($p\text{O}_2 = 0.5\%$), the results were constant with and without nanoMOFs. These nanoagents are not radio-enhancer. Contrary to what was observed with γ -irradiation (X. Li et al., 2020a). On the other hand, the cell response to irradiation was strongly affected when cells were incubated with GemMP or GemMP-loaded nanoMOFs.

The survival curves presented in Figure 4.3 show that the carbon irradiation was amplified when combined with a radiosensitizer (GemMP or GemMP-loaded nanoMOFs). The same efficiency was observed for the two oxygenation conditions. SER values are reported in the histograms of Figure 4.3B for the different irradiation conditions. The presence of GemMP (free or loaded in nanoMOFs) increases the carbon radiation effect by ~50% at 2 Gy, both in hypoxic and normoxic conditions. The amplification efficiency increases with the irradiation dose. However, the encapsulation of GemMP in nanoMOFs doesn't play a major role on its amplification property (difference not significant between the two curves, GemMP and GemMP-loaded nanoMOFs).

In addition, for a same agent (GemMP in red or GemMP-loaded nanoMOFs in black), the comparison between normoxic and hypoxic conditions demonstrates that the SER does not depend on the oxygenation conditions when radiosensitizer was used. The oxygen concentration at the time of irradiation does not seem to influence the effectiveness of the combination. A decrease of the OER values was observed in the presence of drug. While a value of 1.4 was calculated for the control, the OER decreases to 1.3 for GemMP and 1.2 for GemMP-loaded nanoMOFs. To understand the origin of the radiosensitizing effect observed in presence of drug, radiobiological parameters values extracted from the survival curves were reported in a table Figure 4.3C. For Gem free or Gem-loaded MOFs, increases of α and β values were observed regardless the oxygen concentration meaning that their presence induces both an amplification of directly lethal damage and sublethal lesions.

To investigate the nature of the effects produced by the combination of carbon irradiation with these nanoagents a median-effect plot Figure 4.3C was built using the methodology provided in the section e. This graphical analysis allows to obtain the doses of treatment (irradiation, GemMP or MG) which gives alone a SF of 50%. D_m values were reported in the table and used for the CI calculations. For GemMP and GemMP-loaded nanoMOFs, CI were systematically lower or equal to 1. This analysis, performed for normoxic conditions, shows that the combination leads to synergistic effects (i) whatever the dose of irradiation when GemMP-loaded nanoMOFs were used (ii) for doses superior to 1 Gy in presence of free GemMP. As the effects produced in hypoxic conditions are similar to the normoxic ones, it seems reasonable to assume that synergism is also verified when oxygenation concentration is reduced to 0.5%.

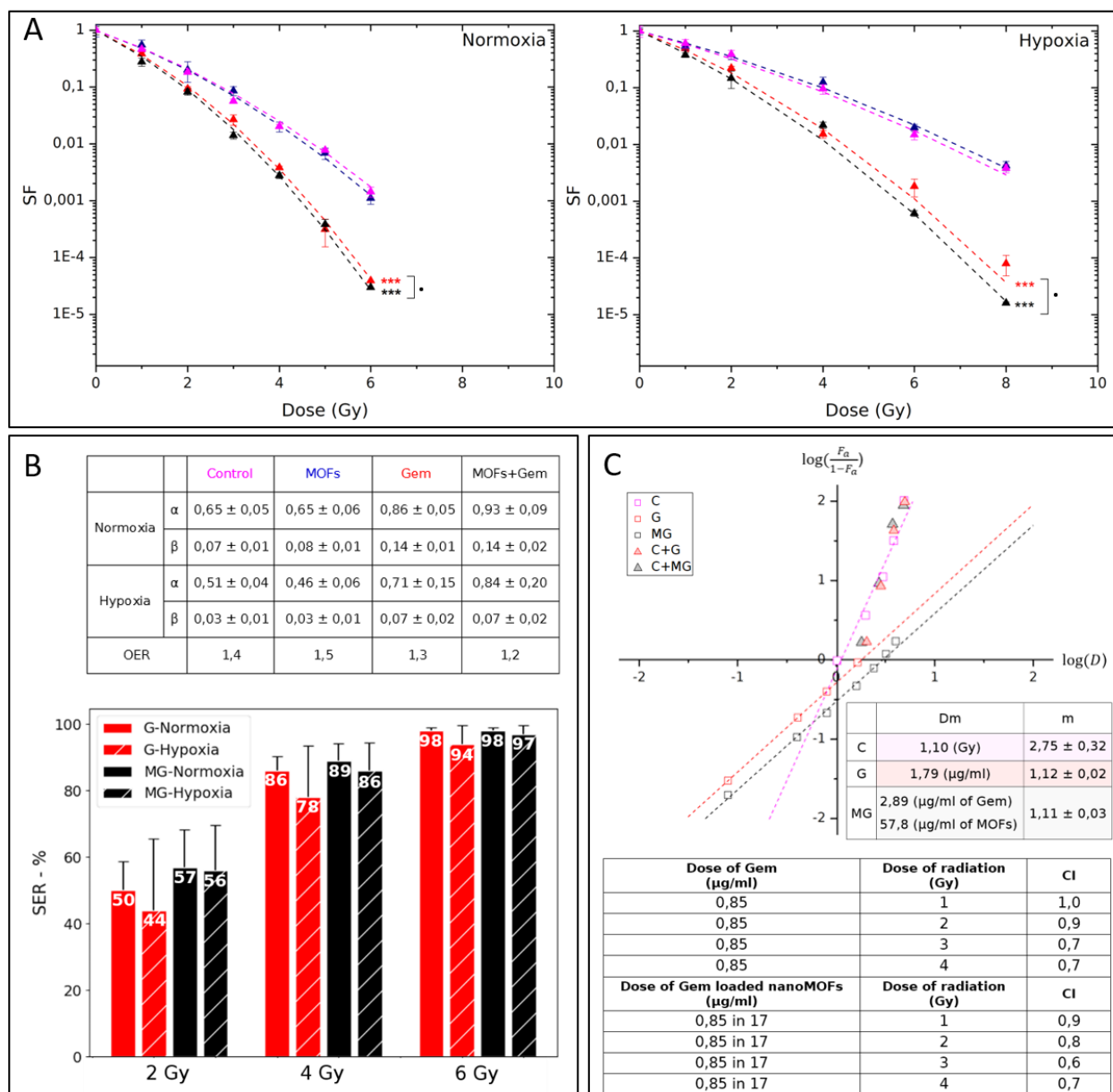


Figure 4.3 – **(A)** Survival curves obtained with carbon ion irradiation in normoxic (left) and hypoxic (right) conditions. The control is labelled in pink and the response of the cells incubated with nanoMOFs, free Gem or GemMP-loaded nanoMOFs is represented in blue, red or black respectively. The p values between the control and the SF curves with GemMP or GemMP-loaded nanoMOFs is < 0.001 (***). The p value between the curve of the GemMP and the curve of the GemMP-loaded nanoMOFs is < 0.1 (.). **(B)** Analysis parameters extracted from the survival curves. Top: Radiobiological parameters values (α in Gy^{-1} and β in Gy^{-2}). Below: Quantification of the radiosensitizing effect induced by the presence of free GemMP (G) or GemMP-loaded nanoMOFs (MG), in normoxic (smooth) and hypoxic (hatching) conditions. SER values were calculated for irradiation doses of 2, 4 and 6 Gy.

(C) Isobologram analysis performed in normoxic conditions and graphical representation giving the values of D_m for carbon irradiation (C), GemMP (G) and GemMP-loaded nanoMOFs (MG) taken alone. Combination Index values are reported showing additive ($\text{CI}=1.0$) or synergistic effect ($\text{CI}<1.0$)

b. Helium ion irradiation

The survival curves obtained by the exposition of monolayer culture with 150 MeV helium ions (6 cm SOBP) beam (LET=12 keV/ μm) are presented in Figure 4.4 - (A) Survival curves obtained with helium ions irradiation in normoxic (left) and hypoxic (right) conditions. Control is labelled in pink and the response of the cells incubated with nanoMOFs, free Gem or Gem-loaded nanoMOFs is blue, red or black respectively. The p values between the control and the SF curves with GemMP or GemMP-loaded nanoMOF are < 0.001 (***) . The p value between the curves with GemMP and GemMP-loaded nanoMOFs is < 0.05 (*) for normoxic and < 0.1 (.) for hypoxic conditions. (B) Analysis parameters extracted from the survival curves. Top: Radiobiological parameters values (α in Gy^{-1} and β in Gy^{-2}). Below: Quantification of the radiosensitizing effect induced by the presence of free Gem or Gem-loaded nanoMOFs, in normoxic (smooth) and hypoxic (hatching) conditions. SER values were calculated for irradiation doses of 2, 4 and 6 Gy and DEF for a survival fraction of 10%. (C) Isobologram analysis for normoxic conditions and graphical representation giving the values of Dm. Combination Index values are reported showing additive (CI=1.0) or synergistic effect (CI<1.0).

Similarly to carbon ions irradiation, nanoMOFs are not radio-enhancer. However, the high potential of GemMP to sensitize cells was demonstrated once again, even when the cells were hypoxic (Figure 4.4). (A) Survival curves obtained with helium ions irradiation in normoxic (left) and hypoxic (right) conditions. Control is labelled in pink and the response of the cells incubated with nanoMOFs, free Gem or Gem-loaded nanoMOFs is blue, red or black respectively. The p values between the control and the SF curves with GemMP or GemMP-loaded nanoMOF are < 0.001 (***) . The p value between the curves with GemMP and GemMP-loaded nanoMOFs is < 0.05 (*) for normoxic and < 0.1 (.) for hypoxic conditions. (B) Analysis parameters extracted from the survival curves. Top: Radiobiological parameters values (α in Gy^{-1} and β in Gy^{-2}). Below: Quantification of the radiosensitizing effect induced by the presence of free Gem or Gem-loaded nanoMOFs, in normoxic (smooth) and hypoxic (hatching) conditions. SER values were calculated for irradiation doses of 2, 4 and 6 Gy and DEF for a survival fraction of 10%. (C) Isobologram analysis for normoxic conditions and graphical representation giving the values of Dm. Combination Index values are reported showing additive (CI=1.0) or synergistic effect (CI<1.0). A). the SERs obtained in the presence of nanoMOFs tend to be higher than those obtained with free Gem but statistical tests show that encapsulation does not bring really significant interest (Figure 4.4 B). Radioenhancement effects reported with helium irradiation are a bit lower than for carbon but Gem-loaded nanoMOFs continues to induce considerable effects whatever the oxygenation conditions: + ~45% at 2 Gy, ~ 82% at 4 Gy and ~ 95% at 6 Gy.

As previously observed, the tendency of the OER to decrease reveals that the presence of drug allows a reduction of the oxygen influence on the treatment effectiveness. Interestingly, isobologram analysis (Figure 4.4 C) that when the LET of the beam is lower, the irradiation dose needed to reach synergistic effects is higher (2 Gy rather than 1 Gy for the Gem and 1 Gy at least for Gem loaded nanoMOFs).

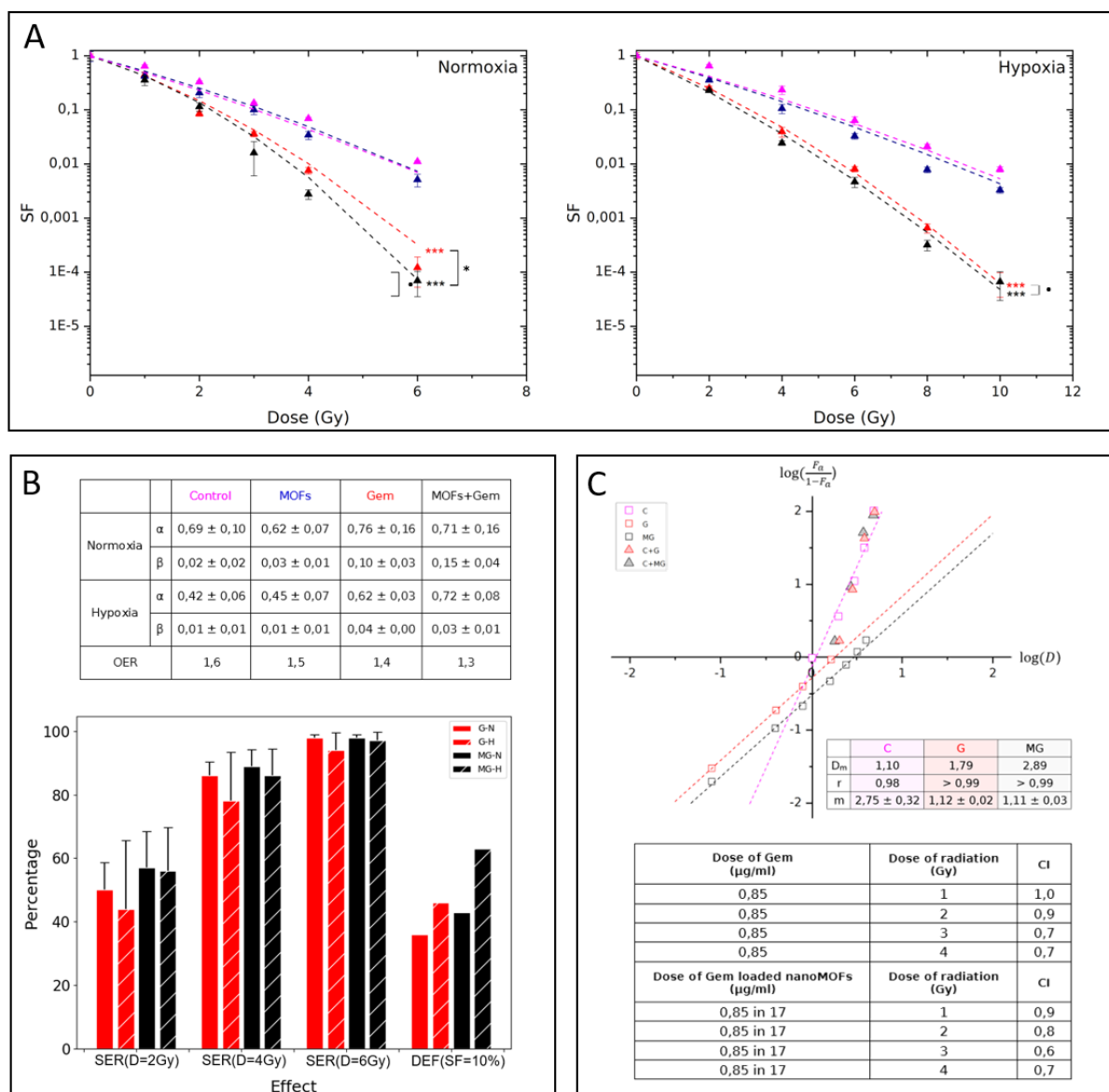


Figure 4.4 – **(A)** Survival curves obtained with helium ions irradiation in normoxic (left) and hypoxic (right) conditions. Control is labelled in pink and the response of the cells incubated with nanoMOFs, free Gem or Gem-loaded nanoMOFs is blue, red or black respectively. The p values between the control and the SF curves with GemMP or GemMP-loaded nanoMOF are < 0.001 (***). The p value between the curves with GemMP and GemMP-loaded nanoMOFs is < 0.05 (*) for normoxic and < 0.1 (.) for hypoxic conditions. **(B)** Analysis parameters extracted from the survival curves. Top: Radiobiological parameters values (α in Gy^{-1} and β in Gy^{-2}). Below: Quantification of the radiosensitizing effect induced by the presence of free Gem or Gem-loaded nanoMOFs, in normoxic (smooth) and hypoxic (hatching) conditions. SER values were calculated for irradiation doses of 2, 4 and 6 Gy and DEF for a survival fraction of 10%. **(C)** Isobologram analysis for normoxic conditions and graphical representation giving the values of D_m . Combination Index values are reported showing additive (CI=1.0) or synergistic effect (CI<1.0)

2.4.6. Impact of nanoMOFs, GemMP and GemMP-loaded nanoMOFs on radiation effects: impact of the matrix (3D cell cultures)

The presence of a cell microenvironment can also affect the diffusion of nanoagents in tissues and thus their impact. The proposed combined strategy has therefore been tested on 3D-CCMs.

Irradiations were performed on the 3D-CCMs with Carbon and Helium ions beams (in normoxic conditions).

Survival curves presented in Figure 4.5 show that for a same condition (control, GemMP, nanoMOFs or GemMP-loaded nanoMOFs), the cell survival was systematically lower in the case of carbon rather than helium irradiation, confirming an influence of the beam LET on radiotoxicity.

In line with the 2D experiments, the presence of nanoMOFs doesn't impact radiation effects for the two irradiation beams. The values of α and β reported in Figure 4.5B are not significantly different for the nanoMOFs and the control.

In the presence of a matrix, GemMP (free or encapsulated) exhibits strong radiosensitizing behaviour. Interestingly, for the two irradiation beams, the survival curves obtained with free GemMP (red) and GemMP-loaded nanoMOFs (black) are significantly different (p values of $1e-4$ (carbon) and $3e-4$ (helium)). It indicates that the effect of GemMP when it is encapsulated, is higher than for the GemMP free. This result is different from the one observed with monolayer cultures (see sections 2.4.5, parts a and b). As represented in Figure 4.5 C, for an irradiation dose of 2 Gy, the SER values obtained with GemMP-loaded nanoMOFs were 3 times higher than with GemMP free (from 17% to 59% with carbon ions; from 15 to 42% with helium ions).

Then, as presented in the Figure 4.5 B, the presence of GemMP-loaded nanoMOFs is associated to an increase of the α value compared to the control ($\times 2$ for carbon, $\times 1.6$ for helium). Contrary to the 2D case the β value remains relatively stable. Thus, the presence of GemMP-loaded nanoMOFs in 3D-CCM induces an increase of the directly lethal damage.

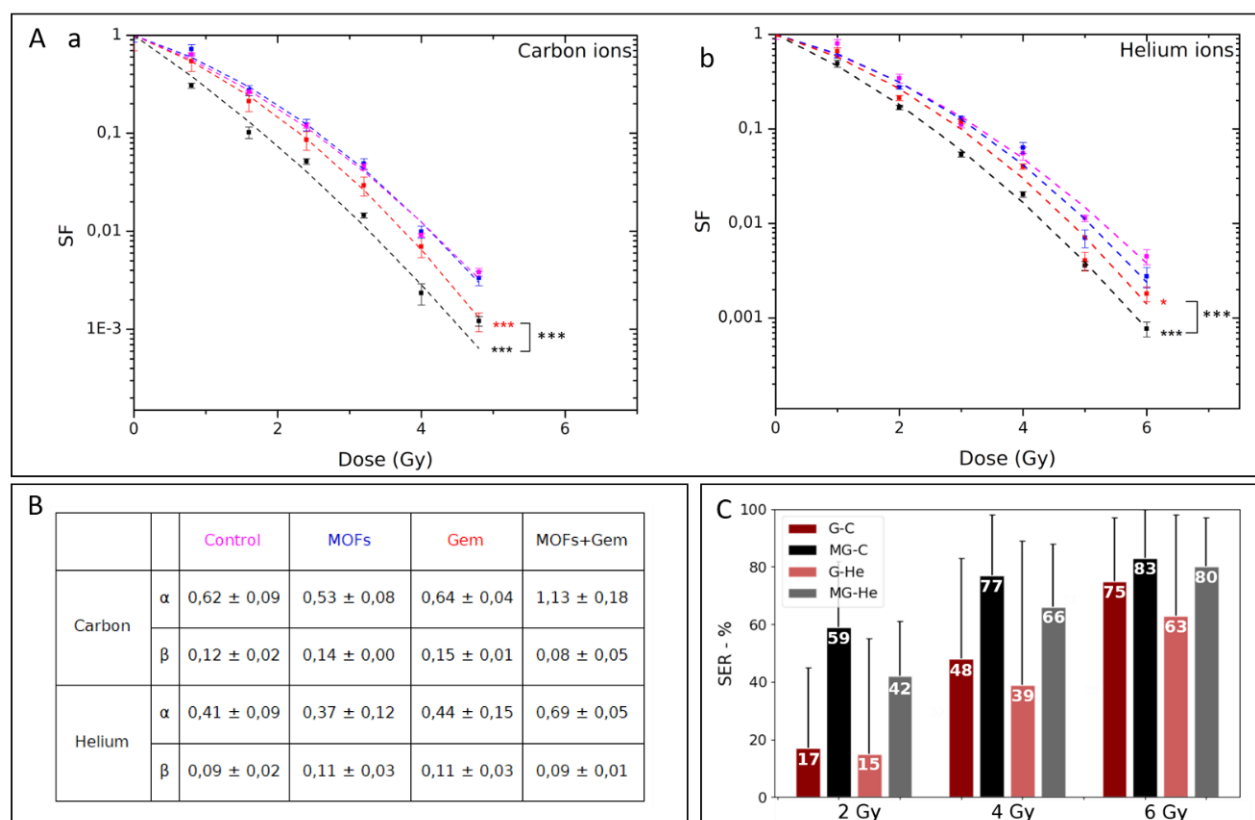


Figure 4.5 - **(A)** Survival fractions of Hela cells extracted from 3D-CCMs irradiated with carbon ions (left) and helium ions (right), in the presence of nanoMOFs (blue), free GemMP (red) and GemMP loaded nanoMOFs (black). p values between the control curve and the curves established in the presence of GemMP or GemMP loaded nanoMOFs were $2e-4$ (***) and $4e-10$ (***) for carbon ions irradiation and (*) and (***) with helium ions irradiation. The p values between the two curves in the presence of Gem

(GemMP and GemMP loaded nanoMOFs) is <0.001 (***) **(B)** Radiobiological parameters (α in Gy^{-1} and β in Gy^{-2}). **(C)** Quantification of the enhancement effects (SER) of carbon ions (black and dark red) and helium ions (gray and light red) beams induced by the presence of Gem (red) or Gem-loaded nanoMOFs (black and gray).

2.5. Discussion

This study evaluates the efficiency of a strategy based on the use of GemMP-loaded nanoMOFs. Due to accessible unsaturated metal sites of Fe trimers, a strong coordination is created with the phosphate groups of GemMP, ensuring a loading of these frameworks without size modification. Encapsulated GemMP is then released to the target after a progressive degradation of nanoMOFs by the phosphates contained in the biological medium. We showed that these nanoparticles are able to penetrate cancer cells both in monolayer cultures but also in cells embedded in collagen matrix. Clusters of nanoMOFs are found in the cytoplasm, suggesting internalisation in the cells by endocytic process. This internalization pathway is frequently reported for nanoparticles of this size (~200 nm) (Foroozandeh and Aziz, 2018; Manzanares and Ceña, 2020). Numerous functions of the nanoparticles are expected to influence cellular uptake and penetration in tumor such as size, surface charge, surface properties, shape, chemical composition (Pratiwi et al., 2021; Tchoryk et al., 2019b). In particular, for pH ~ 7, the nanoMOFs exhibit a negative zeta potential (X. Li et al., 2020b). The surface charge of the nanoMOFs could have hindered their diffusion by inducing repulsive electrostatic forces with the cell surface or the ECM (Meng et al., 2016). However, nanoMOFs succeeded in penetrating through the matrix. These results are of great interest for a potential future clinical application, limiting the risk of poor in vivo penetration which often results in poor performance of therapies (Magzoub et al., 2008; Minchinton and Tannock, 2006).

In this perspective, the first objective of this study was to investigate the effect of oxygen on the efficacy of the ion beams to kill cancer cells in the presence of GemMP-loaded nanoMOFs. For this, irradiations were performed with carbon and helium ions beams in two oxygenation conditions ($p\text{O}_2 = 0.5\%$ and $p\text{O}_2=20\%$). Thus, will be discussed in the following section: (i) the effects of oxygen on irradiation alone (performed on monolayer cells in the absence of nanoagents) (ii) the effects of oxygen and beam type on the radioenhancement effect induced when GemMP-loaded nanoMOFs were used.

The second objective was to study the efficacy of GemMP-loaded nanoMOFs to kill cancer cells embedded inside a more realistic 3D model comprising an extracellular matrix.

2.5.1. Molecular processes induced by irradiation

a. Oxygen effect on irradiation

The interaction of radiation with biological medium (mainly composed of water molecules) leads to the production of OH^\bullet , H^\bullet , H^+ and secondary electrons along the track (Baldacchino and Katsumura, 2010). Due to its high reaction rate, damage are commonly attributed to the hydroxyl radical, OH^\bullet , which induce formation of unstable species in DNA (DNA^\bullet) and in the cytoplasm (R^\bullet) (Chapman et al., 1973). In addition, reactions of OH^\bullet clusters or electrons spurs with biomolecules can also lead to complex lesions (DNA: and R:) (Bolsa Ferruz, 2017). In normoxic conditions, the molecular oxygen O_2 can scavenge reducing primary species to form superoxide radicals $\text{O}_2^{\bullet-}$ known to be very reactive towards biological components (DNA^\bullet and R^\bullet), causing many toxicities (Baldacchino et al., 2019b).

In addition, O_2 can directly react with DNA^\bullet and R^\bullet and fix radicals defects by the formation of oxidized molecules species (ROO^\bullet and DNA-OO^\bullet), making the cell damages permanent and non-reparable (Scifoni et al., 2013; Sonntag, 1987). When O_2 concentration is reduced (hypoxic conditions), the probability to fix the

damage on biomolecules decreases, and the competitive interaction of biomolecule radicals with radical-reducing species results in “chemical repair” (Furusawa et al., 2000).

These oxygen effects are observable on the control curves obtained with monolayer cultures under carbon and helium irradiation depending on the O_2 concentration tuned in cells. OER values (see section 2.3.4, part e) obtained for the controls irradiated in carbon (Figure A) or helium (Figure B) are in agreement with the data obtained by Monte Carlo studies (Figure C). With a $pO_2=0.5\%$, similar to our experimental conditions, OER for carbon (LET ~ 50 keV/ μ m) and helium (LET ~ 12 keV/ μ m) irradiations calculated by simulations were 1.6 and 1.7 close to our values of 1.4 ± 0.02 and 1.6 ± 0.01 . Moreover, under the same conditions of oxygenation, previous irradiations performed to HIMAC with carbon ions had led to an OER value of 1.3 (1.4 in this study), showing the reliability of the data that we obtained (Scifoni et al., 2013).

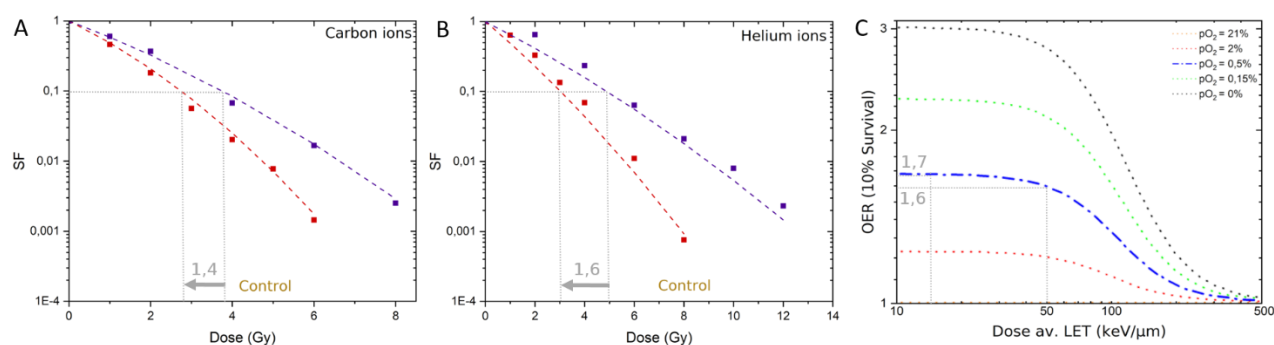


Figure 4.6 – Survival curves for controls and cells treated by **(A)** carbon ions and **(B)** helium ions using monolayer cultures under normoxic ($pO_2=20\%$, in red) and hypoxic ($pO_2=0.5\%$, in blue) conditions. **(C)** OER reported by Scifoni et al (Scifoni et al., 2013).

b. Radiations LET effect

As expected, we observed that the cell survival was systematically lower after carbon (50 keV/ μ m) than helium irradiation (12 keV/ μ m) (data shown in the Supplementary). In this study, a LET effect was observed on the cell survival curves of the controls whatever the experimental conditions (2D normoxic, 2D hypoxic, 3D). This can be explained by the ionizing density and therefore the localized energy deposition produced by high LET beams. On the one hand, they induce more complex DNA damage. On the other hand, they can also generate clusters of multiple DNA lesions (Sage and Shikazono, 2017).

c. Effect of the LET on the OER

Interestingly, this hypoxia induced radioresistance quantified by the OER depends on the radiation type: OER for helium (1.6) is higher than for carbon (1.4) (Figure 5C). When LET increases too much, the oxygen fixation mechanisms plays a minor role (OER tends to 1) because of the presence of too severe damage that the cells cannot repair (Hirayama et al., 2009). In addition, the track density effect induces a drop in the yields of the radicals generated since they recombine into molecular species (LaVerne, 2000). Thus, the component of indirect damage is drastically reduced, as well as the consequent dependence on oxygen concentration (Scifoni et al., 2013). From a medical point of view, it is therefore interesting to treat hypoxic tumors with heavy ion beams such as carbon ions in order to exploit the relative biological effectiveness and the OER of carbon ions. However, helium beams ions allow to reduce the dose deposition distal to the tumor compared to carbon ions and also open up new perspectives for online monitoring (Mazzucconi et al., 2018; Volz et al., 2020). Mixed treatment plans based on the combined use of carbon and helium ions appear particularly promising (Graeff et al., 2018).

d. Benefits of Gem encapsulation/ 2D vs 3D effects

While the radiosensitization experiments carried out in 2D showed similar efficiencies between the free GemMP and the GemMP encapsulated in nanoMOFs, a major difference was observed in 3D. When MOFs were loaded, a significantly higher radiosensitivity was observed. In the presence of extracellular matrix, mass transport and diffusion phenomena are more complex than with 2D cells. Collagen hampers the diffusion of nanoagents and encapsulation of the drug becomes of great interest to better transport the Gem to the cells. The encapsulation of the GemMP in the nanoMOFs allows to increase the cell penetration. The free GemMP is a hydrophilic molecule that struggles to cross the cell barrier, especially when interactions occur between the drug and the extracellular matrix. For this reason, our study focuses more on the combination of radiation with GemMP-loaded nanoMOFs.

During the transition from 2D to 3D, the incubation concentration was kept constant but the incubation time was increased (from 6h to 18h) to allow time for the nanoparticles to penetrate through the matrix. Whereas previous study has shown that monolayer cells incubated with $17\mu\text{g}/\text{mL}$ during 6h internalized around $8\text{ pg nanoMOFs}/\text{cell}$ (corresponding to $1.5\text{ pg Fe}/\text{cell}$ (X. Li et al., 2020)), a lower quantity was found in the 3D-CCMs ($0.4\text{ pg Fe}/\text{cell}$). However, this low uptake is sufficient to induce considerable radioamplifier effects, as described in the section 2.4.5.

2.5.2. Mechanisms induced in presence of GemMP

a. Reduction of oxygen effect

The presence of GemMP-loaded nanoMOFs during irradiation produce additional cell lethal damages to that described below. In this paper, we have demonstrated that synergistic effects can be observed when the drug is combined with hadrons beams. Whatever the oxygenation conditions, the radiosensitizing effect at 2 Gy exceeds 40% with 150MeV- He^{2+} and 50% with 290MeV-C^{6+} beams.

For carbon and helium ions, the lack of oxygen effect was reduced with presence of GemMP-loaded nanoMOFs. Comparison between Figure 4.6 and 4.7 highlights a reduction of the OER from 1.4 ± 0.02 to 1.2 ± 0.02 for carbon and 1.6 ± 0.01 to 1.3 ± 0.02 for helium, making of GemMP loaded nanoMOFs an excellent candidate to eradicate hypoxic tumors.

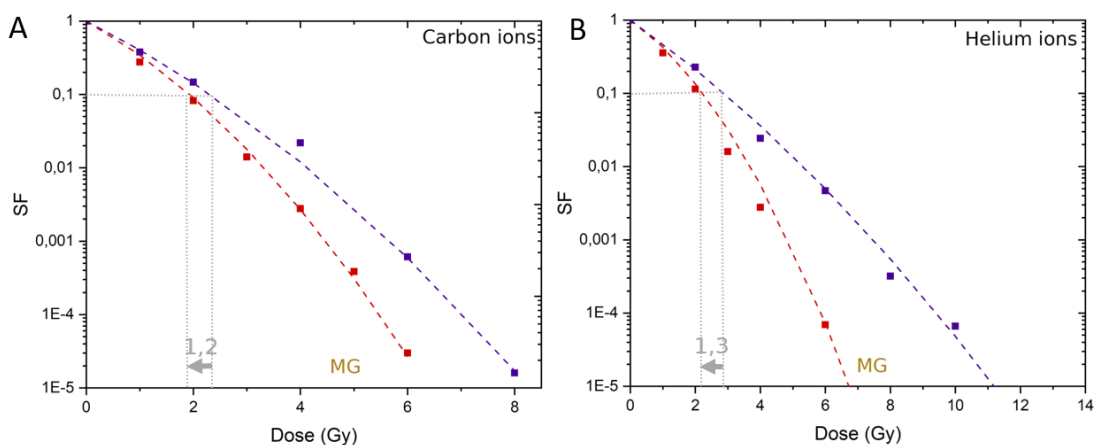


Figure 4.7 – Survival curves for controls and cells treated by **(A)** carbon ions and **(B)** helium ions using monolayer cultures incubated with Gem-loaded nanoMOFs (0.85 µg/ml in 17 µg/ml) under normoxic ($pO_2=20\%$, in red) and hypoxic ($pO_2=0.5\%$, in blue) conditions.

b. Combination efficiencies depending on the beam

As expected and introduced in section 2.4.5, a LET effect on the survival of cells incubated with GemMP-loaded nanoMOFs was observed whatever the experimental conditions (data shown in the Supplementary). The combination with carbon ions is the most lethal, at least 30% more efficient at 2 Gy than helium ions. However, the effects produced with a combination based on helium beam remain considerable. Allowing online monitoring, helium ions induce a strong radiosensitizing effect which make the clinical use of mixed treatment plans particularly appropriate.

c. Mechanisms of nanoMOFs effects

As observed in the tables of section 2.4.5 (a and b) and summarized in Supplementary, section 3.3, the addition of Gem-loaded nanoMOFs induce a significant increase of the α values (average amplification of the α value of 1.6). An increase of the β can be observed, but only when the irradiation is performed on normoxic 2D cells (carbon or helium ions). This illustrates that in the presence of Gem, directly lethal DNA damages are multiplied. An increase of sublethal lesions may occur, partly attributed to oxygen effect and damage fixation described above. This confirms the high radiosensitizing potential of the GemMP that targets DNA. Several mechanisms of action reported in the literature could be involved: (i) inhibitions of DNA synthesis and post radiation damage repair (ii) incorporation into DNA as fraudulent base making the defect significantly more difficult to repair (iii) interference in the cell cycle imposing a block in the most radiosensible phase (Herscher et al., 1999; Seiwert et al., 2007; Shewach and Lawrence, 1996).

2.6. Conclusions

The therapeutic strategy proposed in this study aims at combining hadrontherapy and chemotherapy to fight cancer. Synergistic effects between ions irradiation with GemMP-loaded nanoMOFs were demonstrated using monolayer cancerous cells. Higher efficiency was obtained when carbon was used rather than helium ions beams, highlighting a TEL effect on the radioamplifier potential of the combination. However, high radiosensitizing properties of the GemMP-loaded nanoMOFs were observed whatever the oxygenation conditions of the cells. In the presence of the drug, directly lethal damage to DNA were drastically increased, leading to significantly higher cytotoxicity even in hypoxic environment.

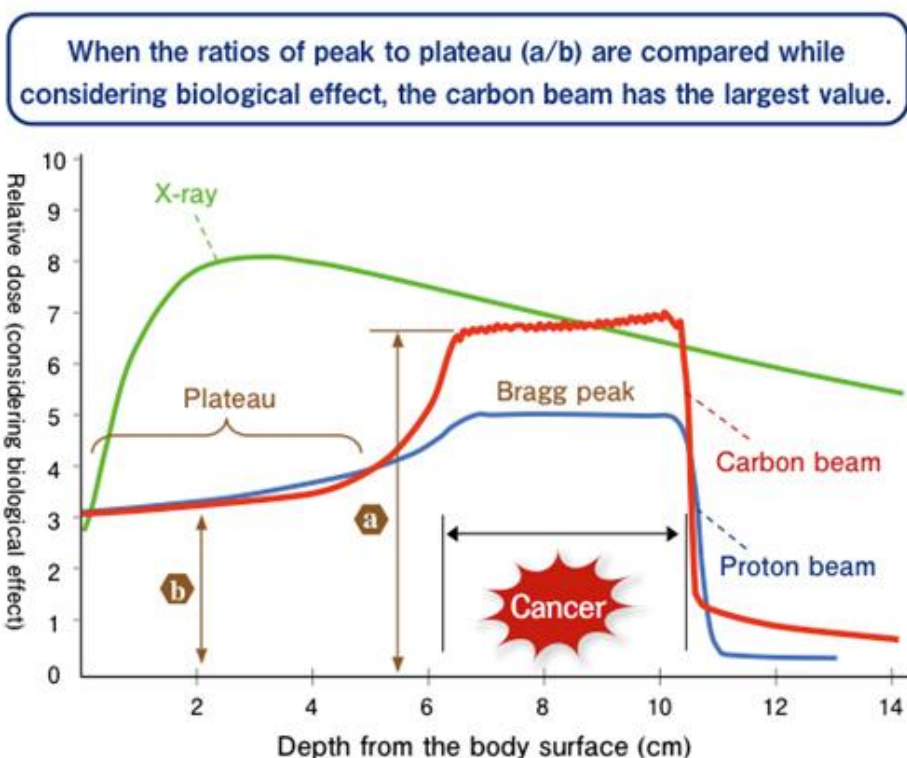
In addition, 3D cell models, more representative of the tissues reality than 2D cell cultures, were introduced to study the nanoagents diffusion through the extracellular matrix and evaluate the combination effectiveness in the presence of a microenvironment. For this, non-toxic concentrations of GemMP-loaded nanoMOFs were used. First, as illustrated by the fluorescence microscopy results, we demonstrated that nanoMOFs were able to penetrate through the ECM to reach the cells. Then, ICP MS analyses showed that a very small amount of nanoMOFs (in the order of pg/cell in iron) was sufficient to induce a considerable radioamplifying effect.

While the experiments performed with monolayer cultures did not show any benefit in the GemMP encapsulation, the results of the 3D-CCMs irradiations demonstrated that the benefits of loading drug becomes undeniable in presence of a matrix in which 42% of the drug nanocarriers efficiently diffused. Improving the drug delivery, GemMP-loaded nanoMOFs led to greater effects than free GemMP. Although no amplifying effect of nanoMOFs alone was observed, this type of hybrid material acts as an efficient nanocarrier (entrapping the drug with almost 100% efficiency) endowed with intrinsic properties as contrast

agent. The theranostic properties of the versatile GemMP-loaded nanoMOFs make them a promising candidate to eradicate tumoral cells. Finally, the synergistic effects observed between chemotherapy and hadrontherapy and the reduction of the oxygen effect that occur in the presence of the drug open up new perspectives. In particular, this promising multimodal approach could be a potential solution for the treatments of hypoxic tumors that still remain therapeutic failures.

3. Supplementary data

3.1. Hadrontherapy



3.2. Dependence of the LET

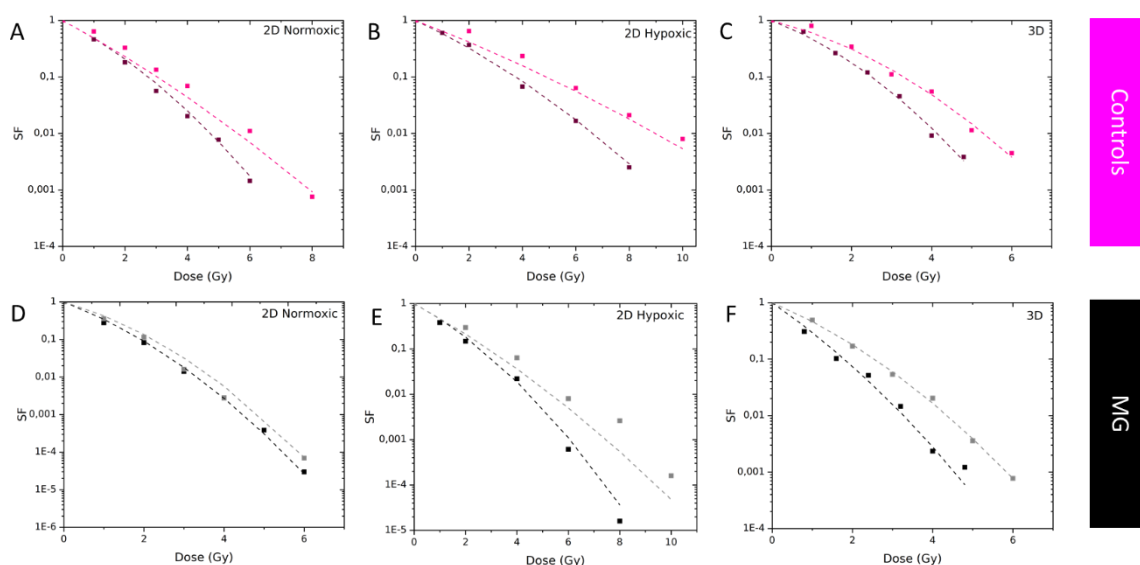


Figure 4.8 - Survival curves for the controls (from A to C) and for cells incubated with Gem-loaded nanoMOFs (from D to E) and treated by carbon ions (dark purple and black curves) and helium ions (light pink and grey curves). Three experimental conditions are presented: irradiations of monolayer cells in normoxia (A-D), irradiation of monolayer cells in hypoxia (B-E) and irradiation of 3D-CCMs (C-F)

3.3. Summary of the radiobiological values

Beam	Experimental conditions	α_C (Gy ⁻¹)	α_{MG} (Gy ⁻¹)	β_C (Gy ⁻²)	β_{MG} (Gy ⁻²)
Carbon	2D, pO ₂ = 20%	0.65 ± 0.05	0.93 ± 0.09	0.07 ± 0.01	0.14 ± 0.02
	2D, pO ₂ = 0.5%	0.51 ± 0.04	0.84 ± 0.20	0.03 ± 0.01	0.07 ± 0.02
	3D, pO ₂ ~ 14.5%	0.62 ± 0.09	1.13 ± 0.18	0.12 ± 0.02	0.08 ± 0.05
Helium	2D, pO ₂ = 20%	0.69 ± 0.10	0.71 ± 0.16	0.02 ± 0.02	0.15 ± 0.04
	2D, pO ₂ = 0.5%	0.42 ± 0.06	0.72 ± 0.08	0.01 ± 0.01	0.03 ± 0.01
	3D, pO ₂ ~ 14.5%	0.41 ± 0.09	0.69 ± 0.05	0.09 ± 0.02	0.09 ± 0.01

Table 7. Radiobiological values extracted from the cell survival curves for the control (C) and Gem loaded nanoMOFs (MG) depending on the experimental conditions (beam, cell cytoarchitecture, oxygenation conditions). The values in bold are those for the difference between the control and MG are significant taking into account the standard deviation of each of the parameters

CHAPTER 5. CONCLUSIONS & PERSPECTIVES



Arbre de vie, Kenya, Yann Arthus-Bertrand, 2007

“Tout ce que tu feras sera dérisoire, mais il est essentiel que tu le fasses”

Gandhi – Philosophe indien
(1869-1948)

Content

1. GENERAL CONCLUSIONS	100
2. PERSPECTIVES	101

1. GENERAL CONCLUSIONS

The aim of my PhD thesis was to evaluate the efficacy of innovative strategies based on NP to treat cancer. The first consists in the association of photons with Gd-based NPs, a protocol which is currently evaluated in clinic. The second is based on the combination of newly developed nanoagents composed of nanoMOFs loaded with drugs - the Gemcitabin - with particle beam radiation (hadrontherapy).

For this purpose, a 3D cellular model, commercialized by Lonza[®], has been optimized for the purpose of these studies. This collagen-based hydrogel contains an extracellular matrix, which is a key parameter to reproduce the microenvironment of cells in tumor and the cell-cell and cell-matrix interactions. Its method of preparation has been established to ensure reproducibility of the size and cell distribution. As a result, it was found that the coefficient of variation between 3D-CCMs is 3.2% only. Moreover, the intercellular distance of 15 μm fitted with the spatial organization of cells in tumors. Easy-to-handle, it was proved to be compatible with microscopy observations, allowing the observation of the NP migration in the extracellular matrix and internalization in cells. In addition, this 3D model allowed the recovery of the cells to measure cell survival after treatments. Last but not least, the oxygen concentration in the 3D-CCMs was successfully monitored, enabling the reproduction of hypoxic conditions as encountered in radioresistant tumors.

The efficacy of treatments combining Gd nanoparticles (AGuiX[®]) with radio- (6 MV-X rays) or brachy- (380 keV- γ rays) photon beams has been successfully evaluated. In the framework of the first-in-man NANOCOL clinical trial, a method to quantify in-vivo the NP uptake in patients' tumors using MRI T1 mapping has been developed. Based on the images of four patients included in the clinical trial, 3D models mimicking the observed NP concentrations were produced. The results show that, even if a low quantity of AGuIX[®] was observed in tumor cells (150-300 $\mu\text{mol/L}$), significant enhancement effects (~15% for 1.8 Gy of X-rays and ~30% for 5.25 Gy of brachytherapy) were achieved.

The quantification of NPs in tumours using MRI and the results of radiation effects are important prerequisites to establish new dosimetric approaches and simulate dose distributions in the presence of NPs. Although the clinical benefits on patients are still being assessed, this work provides an additional building block for the clinic translation of nanoenhanced radiations treatments, opening new perspectives in the development of adaptive and personalized treatments. This case study demonstrated the relevance of 3D-CCM to be used as a new approach to consolidate clinical studies.

3D-CCMs were also successfully used to evaluate the potential of new therapeutics in the early stage of their development. A major output of my work was to evaluate the combination associating Gemcitabin-loaded nanoMOFs with hadrontherapy. This work highlighted the huge potential of these agents to enhance radiation effects, namely ~55% for carbon ions and ~45% for helium ions at 2 Gy, both under normoxic and hypoxic conditions. Thanks to the 3D-CCMs models, it was established that the nanoMOFs penetrate in the extracellular matrix and accumulate in the cells. This important finding validates the ability of the agents to migrate in the tumor after extravation from blood vessel, an important property to ensure the best antitumor efficacy. We have also demonstrated that, in the presence of the ECM, the effect of the encapsulated Gemcitabin was higher than for the free agent. These experiments confirm the key role of the nanocages in reducing interactions between the molecule and the ECM. Finally, the model can act as a filter to eliminate inefficient agents before launching tests based on complex and expensive systems (such as small animals).

Finally, my work demonstrated that NP effects and combined treatments may be rapidly characterized and quantified using the 3D model specially optimized for the purpose. This tool and related protocol may be used to either accompany a clinical trial in predicting the effect of treatments on patients, or contribute to the development of new agents and innovative combinations with alternative radiations such as ions. It thus contributes to prepare the clinical translation of nanoenhanced radiation treatments.

2. PERSPECTIVES

During my PhD work, the efficacy of treatments combining radiations to nanoparticles has been evaluated using different cell models (2D/3D), irradiation beams (γ -rays, X-rays, C^{6+} , He^{2+}), nanoparticles (Gd, nanoMOFs) and oxygenation conditions (hypoxic, normoxic). These experiments and associated outputs (DEF, SER) have contributed to feed a database that can be exploited in two different ways for biological effects prediction of new molecules/experimental conditions (Figure 5.1).

In a more conventional way, experimental observations can be used to adapt the Nanoparticle-Local Effect Model (LEM) approach proposed by Lin et al. in 2015 to take into account (1) the real geometry of cells, (2) the NP-internalization way, (3) the NP concentration inside the cell, (4) the oxygenation degree. This perspective is in accordance with a previous work already performed in collaboration with IGR during the IRS NanoTheRad in which a realistic cell model has been developed based on the GATE/Geant4 simulation tool. On this topic, a challenge will be to model chemical species production in presence of NP and to introduce oxygen concentration as an input parameter.

In parallel, new tools of prediction such as artificial intelligence develop rapidly. In this perspective, the data obtained in this work will be used as inputs for the development of regression machine learning models whose aim to determine biological enhancing factors. Complementary data will be needed to feed the database with other variables such as the beam parameters (type, energy, LET...), the nanoagents properties (type, size, cell uptake) and the characteristics of the biological target (cell line, oxygen concentration).

These perspectives are of foremost importance to accurately account for the NP effects in dose calculations of on-going clinical trials.

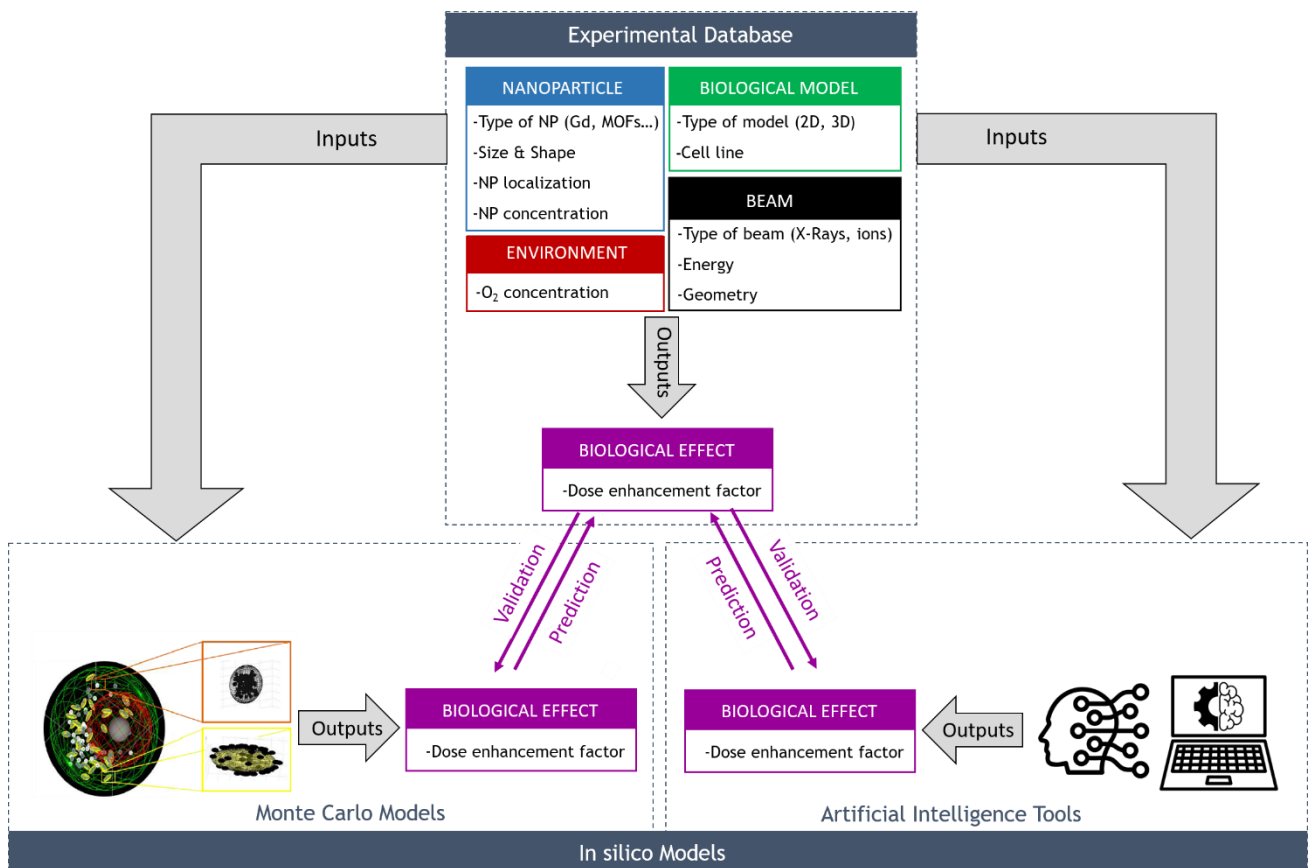


Figure 5.1 – Perspectives: simulation, prediction, validation.

LIST OF REFERENCES

- Acheva, A., Ghita, M., Patel, G., Prise, K.M., Schettino, G., 2014. Mechanisms of DNA damage response to targeted irradiation in organotypic 3D skin cultures. *PLoS One* 9, 1–13. <https://doi.org/10.1371/journal.pone.0086092>
- Achilli, T., Meyer, J., Morgan, J.R., 2012. Advances in the formation, use and understanding of multi-cellular spheroids. *Expert Opin. Biol. Ther.* 12, 1347–1360. <https://doi.org/10.1517/14712598.2012.707181>
- Adcock, A.F., 2015. Three-Dimensional (3D) Cell Cultures in Cell-based Assays for in-vitro Evaluation of Anticancer Drugs. *J. Anal. Bioanal. Tech.* 06. <https://doi.org/10.4172/2155-9872.1000249>
- Agents, P., Extracellular, D., Cells, E.C., Kolosnjaj-tabi, J., Kralj, S., Griseti, E., Nemec, S., Golzio, M., Rols, M., n.d. Magnetic Silica-Coated Iron Oxide Nanochains as.
- AGuIX Gadolinium-based Nanoparticles in Combination With Chemoradiation and Brachytherapy (NANOCOL) [WWW Document], n.d. URL <https://clinicaltrials.gov/ct2/show/NCT03308604>
- Al Zaki, A., Joh, D., Cheng, Z., De Barros, A.L.B., Kao, G., Dorsey, J., Tsourkas, A., 2014. Gold-loaded polymeric micelles for computed tomography-guided radiation therapy treatment and radiosensitization. *ACS Nano* 8, 104–112. <https://doi.org/10.1021/nn405701q>
- Alberts, D., 1980. In vitro clonogenic assay for predicting response of ovarian cancer to chemotherapy. *Lancet* 316, 340–342. [https://doi.org/10.1016/S0140-6736\(80\)90340-2](https://doi.org/10.1016/S0140-6736(80)90340-2)
- Albuquerque, K., Hrycushko, B.A., Harkenrider, M.M., Mayadev, J., Klopp, A., Beriwal, S., Petereit, D.G., Scanderbeg, D.J., Yashar, C., 2019. Compendium of fractionation choices for gynecologic HDR brachytherapy—An American Brachytherapy Society Task Group Report. *Brachytherapy* 18, 429–436. <https://doi.org/10.1016/j.brachy.2019.02.008>
- Anderson, A.R.A., Weaver, A.M., Cummings, P.T., Quaranta, V., 2006. Tumor Morphology and Phenotypic Evolution Driven by Selective Pressure from the Microenvironment. *Cell* 127, 905–915. <https://doi.org/10.1016/j.cell.2006.09.042>
- Antoine, E.E., Vlachos, P.P., Rylander, M.N., 2014. Review of collagen i hydrogels for bioengineered tissue microenvironments: Characterization of mechanics, structure, and transport. *Tissue Eng. - Part B Rev.* 20, 683–696. <https://doi.org/10.1089/ten.teb.2014.0086>
- Asaithamby, A., Hu, B., Delgado, O., Ding, L.H., Story, M.D., Minna, J.D., Shay, J.W., Chen, D.J., 2011. Irreparable complex DNA double-strand breaks induce chromosome breakage in organotypic three-dimensional human lung epithelial cell culture. *Nucleic Acids Res.* 39, 5474–5488. <https://doi.org/10.1093/nar/gkr149>
- Baati, T., Njim, L., Neffati, F., Kerkeni, A., Bouttemi, M., Gref, R., Najjar, M.F., Zakhama, A., Couvreur, P., Serre, C., Horcajada, P., 2013. In depth analysis of the in vivo toxicity of nanoparticles of porous iron(III) metal–organic frameworks. *Chem. Sci.* 4, 1597–1607. <https://doi.org/10.1039/c3sc22116d>
- Baldacchino, G., Brun, E., Denden, I., Bouhadoun, S., Roux, R., Khodja, H., 2019a. Importance of radiolytic reactions during high LET irradiation modalities : LET effect , role of O₂ and radiosensitization by nanoparticles. *Cancer Nanotechnol.* 1–21. <https://doi.org/10.1186/s12645-019-0047-y>
- Baldacchino, G., Brun, E., Denden, I., Bouhadoun, S., Roux, R., Khodja, H., Sicard-Roselli, C., 2019b. Importance of radiolytic reactions during high-LET irradiation modalities: LET effect, role of O₂ and radiosensitization by nanoparticles. *Cancer Nanotechnol.* 10. <https://doi.org/10.1186/s12645-019->

0047-y

- Baldacchino, G., Katsumura, Y., 2010. Chemical processes in heavy ions track, in: *Recent Trends in Radiation Chemistry*. pp. 231–254.
- Becher, O.J., Holland, E.C., 2006. Genetically engineered models have advantages over xenografts for preclinical studies. *Cancer Res.* 66, 3355–3358. <https://doi.org/10.1158/0008-5472.CAN-05-3827>
- Bell, C.C., Hendriks, D.F.G., Moro, S.M.L., Ellis, E., Walsh, J., Renblom, A., Fredriksson Puigvert, L., Dankers, A.C.A., Jacobs, F., Snoeys, J., Sison-Young, R.L., Jenkins, R.E., Nordling, Å., Mkrтчian, S., Park, B.K., Kitteringham, N.R., Goldring, C.E.P., Lauschke, V.M., Ingelman-Sundberg, M., 2016. Characterization of primary human hepatocyte spheroids as a model system for drug-induced liver injury, liver function and disease. *Sci. Rep.* 6, 1–13. <https://doi.org/10.1038/srep25187>
- Belli, V., Guarnieri, D., Biondi, M., della Sala, F., Netti, P.A., 2017a. Dynamics of nanoparticle diffusion and uptake in three-dimensional cell cultures. *Colloids Surfaces B Biointerfaces* 149, 7–15. <https://doi.org/10.1016/j.colsurfb.2016.09.046>
- Belli, V., Guarnieri, D., Biondi, M., Della Sala, F., Netti, P.A., 2017b. Dynamics of nanoparticle diffusion and uptake in three-dimensional cell cultures. *Colloids Surf. B. Biointerfaces* 149, 7–15. <https://doi.org/10.1016/j.colsurfb.2016.09.046>
- Benien, P., Swami, A., 2014. 3D tumor models: history, advances and future perspectives. *Future Oncol.* 10, 1311–27. <https://doi.org/10.2217/fon.13.274>
- Berger, M.J., Inokuti, M., Andersen, H.H., Bichsel, H., Powers, D., Seltzer, S. M., Thwaites, D., Watt, D.E., 1993. Report 49. *J. Int. Comm. Radiat. Units Meas.* os25, NP-NP. <https://doi.org/10.1093/jicru/os25.2.Report49>
- Boghaert, E.R., Lu, X., Hessler, P.E., McGonigal, T.P., Oleksijew, A., Mitten, M.J., Foster-Duke, K., Hickson, J.A., Santo, V.E., Brito, C., Uziel, T., Vaidya, K.S., 2017. The Volume of Three-Dimensional Cultures of Cancer Cells In Vitro Influences Transcriptional Profile Differences and Similarities with Monolayer Cultures and Xenografted Tumors. *Neoplasia (United States)* 19, 695–706. <https://doi.org/10.1016/j.neo.2017.06.004>
- Bolsa Ferruz, M., 2017. Oxygen effect in medical ion beam radiation combined with nanoparticles. Université Paris Saclay (COMUE).
- Bonvalot, S., Le Pechoux, C., De Baere, T., Kantor, G., Buy, X., Stoeckle, E., Terrier, P., Sargos, P., Coindre, J.M., Lassau, N., Sarkouh, R.A., Dimitriu, M., Borghi, E., Levy, L., Deutsch, E., Soria, J.C., 2017. First-in-human study testing a new radioenhancer using nanoparticles (NBTXR3) activated by radiation therapy in patients with locally advanced soft tissue sarcomas. *Clin. Cancer Res.* 23, 908–917. <https://doi.org/10.1158/1078-0432.CCR-16-1297>
- Bonvalot, S., Rutkowski, P.L., Thariat, J., Carrère, S., Ducassou, A., Sunyach, M.P., Agoston, P., Hong, A., Mervoyer, A., Rastrelli, M., Moreno, V., Li, R.K., Tiangco, B., Herraiez, A.C., Gronchi, A., Mangel, L., Sy-Ortin, T., Hohenberger, P., de Baère, T., Le Cesne, A., Helfre, S., Saada-Bouزيد, E., Borkowska, A., Anghel, R., Co, A., Gebhart, M., Kantor, G., Montero, A., Loong, H.H., Vergés, R., Lapeire, L., Dema, S., Kacso, G., Austen, L., Moureau-Zabotto, L., Servois, V., Wardelmann, E., Terrier, P., Lazar, A.J., Bovée, J.V.M.G., Le Pechoux, C., Papai, Z., 2019. NBTXR3, a first-in-class radioenhancer hafnium oxide nanoparticle, plus radiotherapy versus radiotherapy alone in patients with locally advanced soft-tissue sarcoma (Act.In.Sarc): a multicentre, phase 2–3, randomised, controlled trial. *Lancet Oncol.* 20, 1148–1159. [https://doi.org/10.1016/S1470-2045\(19\)30326-2](https://doi.org/10.1016/S1470-2045(19)30326-2)
- Bort, G., Lux, F., Dufort, S., Crémillieux, Y., Verry, C., Tillement, O., 2020. EPR-mediated tumor targeting

- using ultrasmall-hybrid nanoparticles: From animal to human with theranostic AGuiX nanoparticles. *Theranostics* 10, 1319–1331. <https://doi.org/10.7150/thno.37543>
- Bouffard, D.Y., Laliberté, J., Momparler, R.L., 1993. Kinetic studies on 2',2'-difluorodeoxycytidine (gemcitabine) with purified human deoxycytidine kinase and cytidine deaminase. *Biochem. Pharmacol.* 45, 1857–1861. [https://doi.org/10.1016/0006-2952\(93\)90444-2](https://doi.org/10.1016/0006-2952(93)90444-2)
- Brancato, V., Oliveira, J.M., Correlo, V.M., Reis, R.L., Kundu, S.C., 2020. Could 3D models of cancer enhance drug screening?, *Biomaterials.* Elsevier Ltd. <https://doi.org/10.1016/j.biomaterials.2019.119744>
- Braselmann, H., 2019. CFAssay: Statistical analysis for the Colony Formation Assay [WWW Document]. <https://doi.org/10.18129/B9.bioc.CFAssay>
- Braselmann, H., Michna, A., Heß, J., Unger, K., 2015. CFAssay : statistical analysis of the colony formation assay. *Radiat. Oncol.* 1–6. <https://doi.org/10.1186/s13014-015-0529-y>
- Bray, F., Ferlay, J., Soerjomataram, I., Siegel, R.L., Torre, L.A., Jemal, A., 2018. Global cancer statistics 2018: GLOBOCAN estimates of incidence and mortality worldwide for 36 cancers in 185 countries. *CA. Cancer J. Clin.* 68, 394–424. <https://doi.org/10.3322/caac.21492>
- Bridot, J.-L., Faure, A.-C., Laurent, S., Rivière, C., Billotey, C., Hiba, B., Janier, M., Josserand, V., Coll, J.-L., Elst, L. Vander, Muller, R., Roux, S., Perriat, P., Tillement, O., 2007. Hybrid gadolinium oxide nanoparticles: multimodal contrast agents for in vivo imaging. *J. Am. Chem. Soc.* 129, 5076–84. <https://doi.org/10.1021/ja068356j>
- Brown, J.M., Wilson, W.R., 2004. Exploiting tumour hypoxia in cancer treatment. *Nat. Rev. Cancer* 4, 437–447. <https://doi.org/10.1038/nrc1367>
- Brüningk, S.C., Rivens, I., Box, C., Oelfke, U., ter Haar, G., 2020. 3D tumour spheroids for the prediction of the effects of radiation and hyperthermia treatments. *Sci. Rep.* 10, 1–13. <https://doi.org/10.1038/s41598-020-58569-4>
- Butterworth, K., McMahon, S., Taggart, L., Prise, K., 2013. Radiosensitization by gold nanoparticles: effective at megavoltage energies and potential role of oxidative stress. *Transl. Cancer Res.* 2. <https://doi.org/10.3978/j.issn.2218-676X.2013.08.03>
- Caliari, S.R., Burdick, J.A., 2016. A practical guide to hydrogels for cell culture. *Nat. Methods* 13, 405–14. <https://doi.org/10.1038/nmeth.3839>
- Carmichael, J., Possinger, K., Phillip, P., Beykirch, M., Kerr, H., Walling, J., Harris, A.L., 1995. Advanced breast cancer: A phase II trial with gemcitabine. *J. Clin. Oncol.* 13, 2731–2736. <https://doi.org/10.1200/JCO.1995.13.11.2731>
- Castelnu-Marchand, P., Chargari, C., Maroun, P., Dumas, I., Del Campo, E.R., Cao, K., Petit, C., Martinetti, F., Tafo-Guemnie, A., Lefkopoulos, D., Morice, P., Haie-Meder, C., Mazon, R., 2015. Clinical outcomes of definitive chemoradiation followed by intracavitary pulsed-dose rate image-guided adaptive brachytherapy in locally advanced cervical cancer. *Gynecol. Oncol.* 139, 288–294. <https://doi.org/10.1016/j.ygyno.2015.09.008>
- Catoira, M.C., Fusaro, L., Di Francesco, D., Ramella, M., Boccafoschi, F., 2019. Overview of natural hydrogels for regenerative medicine applications. *J. Mater. Sci. Mater. Med.* 30. <https://doi.org/10.1007/s10856-019-6318-7>
- Chaicharoenadomrung, N., Kunhorm, P., Noisa, P., 2019. Three-dimensional cell culture systems as an in

- vitro platform for cancer and stem cell modeling. *World J. Stem Cells* 11, 1065–1083. <https://doi.org/10.4252/wjsc.v11.i12.1065>
- Chapman, J., Reuvers, A., Borsa, J., Greenstock, C., 1973. Chemical radioprotection and radiosensitization of mammalian cells growing in vitro. *Radiat. Res.* 56, 291–306.
- Chapman, J.D., Nahum, A.E., 2015. *Radiotherapy Treatment Planning: Linear-Quadratic Radiobiology*.
- Cheema, U., Rong, Z., Kirresh, O., MacRobert, A.J., Vadgama, P., Brown, R.A., 2012. Oxygen diffusion through collagen scaffolds at defined densities: implications for cell survival in tissue models. *J. Tissue Eng. Regen. Med.* 6, 77–84. <https://doi.org/10.1002/term.402>
- Chen, K., Wu, M., Guo, F., Li, P., Chan, C.Y., Mao, Z., Li, S., Ren, L., Zhang, R., Huang, T.J., 2016. Rapid formation of size-controllable multicellular spheroids via 3D acoustic tweezers. *Lab Chip* 16, 2636–2643. <https://doi.org/10.1039/C6LC00444J>
- Chen, L., Xiao, Z., Meng, Y., Zhao, Y., Han, J., Su, G., Chen, B., Dai, J., 2012. The enhancement of cancer stem cell properties of MCF-7 cells in 3D collagen scaffolds for modeling of cancer and anti-cancer drugs. *Biomaterials* 33, 1437–1444. <https://doi.org/10.1016/j.biomaterials.2011.10.056>
- Cheng, H.L.M., Wright, G.A., 2006. Rapid high-resolution T1 mapping by variable flip angles: Accurate and precise measurements in the presence of radiofrequency field inhomogeneity. *Magn. Reson. Med.* 55, 566–574. <https://doi.org/10.1002/mrm.20791>
- Chou, T.C., 2010. Drug combination studies and their synergy quantification using the chou-talalay method. *Cancer Res.* 70, 440–446. <https://doi.org/10.1158/0008-5472.CAN-09-1947>
- Chou, T.C., Martin, N., 2005. *PC Software and User's Guide: A Computer Program for Quantitation of Synergism and Antagonism in Drug Combinations, and the Determination of IC50 and ED50 and LD50 Values*. ComboSyn Inc.
- Chou, T.C., Talalay, P., 1984. Quantitative analysis of dose-effect relationships: the combined effects of multiple drugs or enzyme inhibitors. *Adv. Enzyme Regul.* 22, 27–55. [https://doi.org/10.1016/0065-2571\(84\)90007-4](https://doi.org/10.1016/0065-2571(84)90007-4)
- Chow, B., Warkentin, B., Menon, G., 2019. Radiobiological dose calculation parameters for cervix cancer brachytherapy: A systematic review. *Brachytherapy* 18, 546–558. <https://doi.org/10.1016/j.brachy.2019.02.007>
- Costa, E.C., Moreira, A.F., de Melo-Diogo, D., Gaspar, V.M., Carvalho, M.P., Correia, I.J., 2016. 3D tumor spheroids: an overview on the tools and techniques used for their analysis. *Biotechnol. Adv.* 34, 1427–1441. <https://doi.org/10.1016/j.biotechadv.2016.11.002>
- Cui, X., Hartanto, Y., Zhang, H., 2017. Advances in multicellular spheroids formation. *J. R. Soc. Interface* 14, 20160877. <https://doi.org/10.1098/rsif.2016.0877>
- Curtin, C., Nolan, J.C., Conlon, R., Deneweth, L., Gallagher, C., Tan, Y.J., Cavanagh, B.L., Asraf, A.Z., Harvey, H., Miller-Delaney, S., Shohet, J., Bray, I., O'Brien, F.J., Stallings, R.L., Piskareva, O., 2018. A physiologically relevant 3D collagen-based scaffold-neuroblastoma cell system exhibits chemosensitivity similar to orthotopic xenograft models. *Acta Biomater.* 70, 84–97. <https://doi.org/10.1016/j.actbio.2018.02.004>
- Darrigues, E., Nima, Z.A., Griffin, R.J., Anderson, J.M., Biris, A.S., Rodriguez, A., 2020. 3D cultures for modeling nanomaterial-based photothermal therapy. *Nanoscale Horizons* 5, 400–430. <https://doi.org/10.1039/c9nh00628a>

- Detappe, A., 2017. AGuIX, a theranostic nanoparticle to improve image-guided radiation therapy : a proof of concept in pancreatic cancer. Université de Lyon.
- Detappe, A., 2017. AGuIX, a theranostic nanoparticle to improve image-guided radiation therapy : a proof of concept in pancreatic cancer. Université de Lyon.
- Detappe, A., Thomas, E., Tibbitt, M.W., Kunjachan, S., Zavidij, O., Parnandi, N., Reznichenko, E., Lux, F., Tillement, O., Berbeco, R., 2017. Ultrasmall Silica-Based Bismuth Gadolinium Nanoparticles for Dual Magnetic Resonance–Computed Tomography Image Guided Radiation Therapy. *Nano Lett.* 17, 1733–1740. <https://doi.org/10.1021/acs.nanolett.6b05055>
- Doctor, A., Seifert, V., Ullrich, M., Hauser, S., Pietzsch, J., 2020. Three-dimensional cell culture systems in radiopharmaceutical cancer research. *Cancers (Basel)*. 12, 1–28. <https://doi.org/10.3390/cancers12102765>
- Dong, C., Lv, Y., 2016. Application of Collagen Scaffold in Tissue Engineering: Recent Advances and New Perspectives. *Polymers (Basel)*. 8, 42. <https://doi.org/10.3390/polym8020042>
- Dufort, S., Le Duc, G., Salomé, M., Bentivegna, V., Sancey, L., Bräuer-Krisch, E., Requardt, H., Lux, F., Coll, J.L., Perriat, P., Roux, S., Tillement, O., 2016. The High Radiosensitizing Efficiency of a Trace of Gadolinium-Based Nanoparticles in Tumors. *Sci. Rep.* 6, 1–8. <https://doi.org/10.1038/srep29678>
- Durante, M., Cucinotta, F., 2008. Heavy ion carcinogenesis and human space exploration. *Nat. Rev. Cancer* 8, 465–472. <https://doi.org/10.1038/nrc2391>
- Durante, M., Orecchia, R., Loeffler, J.S., 2017. Charged-particle therapy in cancer: Clinical uses and future perspectives. *Nat. Rev. Clin. Oncol.* 14, 483–495. <https://doi.org/10.1038/nrclinonc.2017.30>
- Duval, K., Grover, H., Han, L.H., Mou, Y., Pegoraro, A.F., Fredberg, J., Chen, Z., 2017. Modeling physiological events in 2D vs. 3D cell culture. *Physiology* 32, 266–277. <https://doi.org/10.1152/physiol.00036.2016>
- Ehsan, S.M., George, S.C., 2013. Nonsteady state oxygen transport in engineered tissue: Implications for design. *Tissue Eng. - Part A* 19, 1433–1442. <https://doi.org/10.1089/ten.tea.2012.0587>
- Eke, I., Cordes, N., 2011. Radiobiology goes 3D: How ECM and cell morphology impact on cell survival after irradiation. *Radiother. Oncol.* 99, 271–278. <https://doi.org/10.1016/j.radonc.2011.06.007>
- European commission, n.d. Cancer, research and innovation [WWW Document]. URL https://ec.europa.eu/info/research-and-innovation/research-area/health-research-and-innovation/cancer_en
- Even-Ram, S., Yamada, K.M., 2005. Cell migration in 3D matrix. *Curr. Opin. Cell Biol.* 17, 524–532. <https://doi.org/10.1016/j.ceb.2005.08.015>
- Fallica, B., Maffei, J.S., Villa, S., Makin, G., Zaman, M., 2012. Alteration of Cellular Behavior and Response to PI3K Pathway Inhibition by Culture in 3D Collagen Gels. *PLoS One* 7, 1–11. <https://doi.org/10.1371/journal.pone.0048024>
- Fang, Y., Eglén, R.M., 2017. Three-Dimensional Cell Cultures in Drug Discovery and Development. *SLAS Discov.* 22, 456–472. <https://doi.org/10.1177/1087057117696795>
- Ferreira, L.P., Gaspar, V.M., Mano, J.F., 2018. Design of spherically structured 3D in vitro tumor models - Advances and prospects. *Acta Biomater.* 75, 11–34. <https://doi.org/10.1016/j.actbio.2018.05.034>
- Foroozandeh, P., Aziz, A.A., 2018. Insight into Cellular Uptake and Intracellular Trafficking of

Nanoparticles. *Nanoscale Res. Lett.* 13. <https://doi.org/10.1186/s11671-018-2728-6>

- Fries, P., Morelli, J.N., Lux, F., Tillement, O., Schneider, G., Buecker, A., 2014. The issues and tentative solutions for contrast-enhanced magnetic resonance imaging at ultra-high field strength. *Wiley Interdiscip. Rev. Nanomedicine Nanobiotechnology* 6, 559–573. <https://doi.org/10.1002/wnan.1291>
- Fries, P., Morr, D., Müller, A., Lux, F., Tillement, O., Massmann, A., Seidel, R., Schäfer, T., Menger, M.D., Schneider, G., Buecker, A., 2015. Evaluation of a Gadolinium-Based Nanoparticle (AGuIX) for Contrast-Enhanced MRI of the Liver in a Rat Model of Hepatic Colorectal Cancer Metastases at 94 Tesla. *RoFo Fortschritte auf dem Gebiet der Röntgenstrahlen und der Bildgeb. Verfahren* 187, 1108–1115. <https://doi.org/10.1055/s-0035-1553500>
- Furusawa, Y., Fukutsu, K., Aoki, M., Itsukaichi, H., Eguchi-Kasai, K., Ohara, H., Yatagai, F., Kanai, T., Ando, K., 2000. Inactivation of aerobic and hypoxic cells from three different cell lines by accelerated ^3He -, ^{12}C - and ^{20}Ne -ion beams. *Radiat. Res.* 154, 485–496. [https://doi.org/10.1667/0033-7587\(2000\)154\[0485:IOAAHC\]2.0.CO;2](https://doi.org/10.1667/0033-7587(2000)154[0485:IOAAHC]2.0.CO;2)
- Gautier Defossez Sandra Le Guyader-Peyrou Zoé Uhry Pascale Grosclaude Marc Colonna Emmanuelle Dantony Patricia Delafosse Florence Molinié Anne-Sophie Woronoff Anne-Marie Bouvier Laurent Remontet Nadine Bossard Alain Monnereau, A., 2018. Estimations nationales de l'incidence et de la mortalité par cancer en Étude à partir des registres des cancers du réseau Francim Synthèse.
- Gazis, E., 2019. The Ionizing Radiation Interaction with Matter, the X-ray Computed Tomography Imaging, the Nuclear Medicine SPECT, PET and PET-CT Tomography Imaging. <https://doi.org/10.5772/intechopen.84356>
- Gervais, B., Beuve, M., Olivera, G.H., Galassi, M.E., Rivarola, R.D., 2005. Production of HO_2 and O_2 by multiple ionization in water radiolysis by swift carbon ions. *Chem. Phys. Lett.* 410, 330–334. <https://doi.org/10.1016/j.cplett.2005.05.057>
- Ghosh, K., Pan, Z., Guan, E., Ge, S., Liu, Y., Nakamura, T., Ren, X.-D., Rafailovich, M., Clark, R.A.F., 2007. Cell adaptation to a physiologically relevant ECM mimic with different viscoelastic properties. *Biomaterials* 28, 671–679. <https://doi.org/10.1016/j.biomaterials.2006.09.038>
- Gomez-Roman, N., Stevenson, K., Gilmour, L., Hamilton, G., Chalmers, A.J., 2016. A novel 3D human glioblastoma cell culture system for modeling drug and radiation responses. *Neuro. Oncol.* 19, now164. <https://doi.org/10.1093/neuonc/now164>
- Gong, X., Lin, C., Cheng, J., Su, J., Zhao, H., Liu, T., Wen, X., Zhao, P., 2015. Generation of Multicellular Tumor Spheroids with Microwell-Based Agarose Scaffolds for Drug Testing. *PLoS One* 10, e0130348. <https://doi.org/10.1371/journal.pone.0130348>
- Goodman, T.T., Olive, P.L., Pun, S.H., 2007. Increased nanoparticle penetration in collagenase-treated multicellular spheroids. *Int. J. Nanomedicine* 2, 265–74.
- Gordon Steel, G., Peckham, M.J., 1979. Exploitable mechanisms in combined radiotherapy-chemotherapy: The concept of additivity. *Int. J. Radiat. Oncol. Biol. Phys.* 5, 85–91. [https://doi.org/10.1016/0360-3016\(79\)90044-0](https://doi.org/10.1016/0360-3016(79)90044-0)
- Graeff, C., Weber, U., Schuy, C., Saito, N., Volz, L., Piersimoni, P., Seco, J., Kraemer, M., 2018. [OA027] Helium as a range probe in carbon ion therapy. *Phys. Medica* 52, 11. <https://doi.org/10.1016/j.ejmp.2018.06.099>
- Hagiwara, Y., Niimi, A., Isono, M., Yamauchi, M., Yasuhara, T., Limsirichaikul, S., Oike, T., Sato, H., Held, K., Nakano, T., Shibata, A., 2017. 3D-structured illumination microscopy reveals clustered DNA double-

strand break formation in widespread γ H2AX foci after high LET heavy-ion particle radiation. *Oncotarget* 8, 109370–109381. <https://doi.org/10.18632/oncotarget.22679>

Hagiwara, Y., Oike, T., Niimi, A., Yamauchi, M., Sato, H., Limsirichaikul, S., Held, K., Nakano, T., Shibata, A., 2019. Clustered DNA double-strand break formation and the repair pathway following heavy-ion irradiation. *J. Radiat. Res.* 60, 69–79. <https://doi.org/10.1093/jrr/rry096>

Haie-Meder, C., Pötter, R., Van Limbergen, E., Briot, E., De Brabandere, M., Dimopoulos, J., Dumas, I., Hellebust, T.P., Kirisits, C., Lang, S., Muschitz, S., Nevinson, J., Nulens, A., Petrow, P., Wachter-Gerstner, N., 2005. Recommendations from Gynaecological (GYN) GEC-ESTRO Working Group (I): Concepts and terms in 3D image based 3D treatment planning in cervix cancer brachytherapy with emphasis on MRI assessment of GTV and CTV. *Radiother. Oncol.* 74, 235–245. <https://doi.org/10.1016/j.radonc.2004.12.015>

Hainfeld, J.F., Slatkin, D.N., Smilowitz, H.M., 2004. The use of gold nanoparticles to enhance radiotherapy in mice. *Phys. Med. Biol.* 49. <https://doi.org/10.1088/0031-9155/49/18/N03>

Hainfeld, J.F., Smilowitz, H.M., O'connor, M.J., Dilmanian, F.A., Slatkin, D.N., 2013. Gold nanoparticle imaging and radiotherapy of brain tumors in mice. *Nanomedicine* 8, 1601–1609. <https://doi.org/10.2217/nnm.12.165>

Halfter, K., Hoffmann, O., Ditsch, N., Ahne, M., Arnold, F., Paepke, S., Grab, D., Bauerfeind, I., Mayer, B., 2016. Testing chemotherapy efficacy in HER2 negative breast cancer using patient-derived spheroids. *J. Transl. Med.* 14, 1–14. <https://doi.org/10.1186/s12967-016-0855-3>

Haume, K., de Vera, P., Verkhovtsev, A., Surdutovich, E., Mason, N., Solov'yov, A., 2018. Transport of secondary electrons through coatings of ion-irradiated metallic nanoparticles. *Eur. Phys. J. D* 72. <https://doi.org/10.1140/epjd/e2018-90050-x>

Herscher, L.L., Cook, J.A., Pacelli, R., Pass, H.I., Russo, A., Mitchell, J.B., 1999. Principles of chemoradiation: theoretical and practical considerations. *Oncology (Williston Park)*. 13, 11–22.

Hirayama, R., Furusawa, Y., Fukawa, T., Ando, K., 2005. Repair kinetics of DNA-DSB induced by X-rays or carbon ions under oxic and hypoxic conditions. *J. Radiat. Res.* 46, 325–32. <https://doi.org/10.1269/jrr.46.325>

Hirayama, R., Ito, A., Tomita, M., Tsukada, T., Yatagai, F., Noguchi, M., Matsumoto, Y., Kase, Y., Ando, K., Okayasu, R., Furusawa, Y., 2009. Contributions of Direct and Indirect Actions in Cell Killing by High-LET Radiations. *Radiat. Res.* 171, 212–218. <https://doi.org/10.1667/RR1490.1>

Horcajada, P., Chalati, T., Serre, C., Gillet, B., Sebrie, C., Baati, T., Eubank, J.F., Heurtaux, D., Clayette, P., Kreuz, C., Chang, J.S., Hwang, Y.K., Marsaud, V., Bories, P.N., Cynober, L., Gil, S., Férey, G., Couvreur, P., Gref, R., 2010. Porous metal-organic-framework nanoscale carriers as a potential platform for drug delivery and imaging. *Nat. Mater.* 9, 172–178. <https://doi.org/10.1038/nmat2608>

Horsman, M.R., Overgaard, J., 2016. The impact of hypoxia and its modification of the outcome of radiotherapy. *J. Radiat. Res.* 57, i90–i98. <https://doi.org/10.1093/jrr/rrw007>

Huang, R.Y., Pei, L., Liu, Q., Chen, S., Dou, H., Shu, G., Yuan, Z.X., Lin, J., Peng, G., Zhang, W., Fu, H., 2019. Isobologram analysis: A comprehensive review of methodology and current research. *Front. Pharmacol.* 10, 1–12. <https://doi.org/10.3389/fphar.2019.01222>

Hubbell, J.H., 1999. Review of photon interaction cross section data in the medical and biological context. *Phys. Med. Biol.* 44. <https://doi.org/10.1088/0031-9155/44/1/001>

- Hubbell, J.H., 1971. PHOTON CROSS SECTION COMPILATION ACTIVITY IN THE U. S. IN THE RANGE 1 keV TO 100 GeV. *Le J. Phys. Colloq.* 32, C4-14-C4-20. <https://doi.org/10.1051/jphyscol:1971403>
- ICRU, 2005. Stopping of ions heavier than helium. *J. Int. Comm. Radiat. Units Meas.* 5, 0–0. <https://doi.org/10.1093/jicru/ndi001>
- Inca [WWW Document], n.d. URL <http://lesdonnees.e-cancer.fr/Themes/Soins/La-radiotherapie>
- Ingber, D.E., 2018. Developmentally inspired human ‘organs on chips.’ *Dev.* 145, 10–13. <https://doi.org/10.1242/dev.156125>
- Ivošev, V., Sánchez, G.J., Stefancikova, L., Haidar, D.A., González Vargas, C.R., Yang, X., Bazzi, R., Porcel, E., Roux, S., Lacombe, S., 2020. Uptake and excretion dynamics of gold nanoparticles in cancer cells and fibroblasts. *Nanotechnology* 31, 135102. <https://doi.org/10.1088/1361-6528/ab5d82>
- Jain, R.K., 1997. Delivery of molecular and cellular medicine to solid tumors. *Adv. Drug Deliv. Rev.* 26, 71–90. [https://doi.org/10.1016/S0169-409X\(97\)00027-6](https://doi.org/10.1016/S0169-409X(97)00027-6)
- Jeon, J., Cheong, J.H., 2019. Clinical implementation of precision medicine in gastric cancer. *J. Gastric Cancer* 19, 235–253. <https://doi.org/10.5230/jgc.2019.19.e25>
- Jiang, J., Tang, Y., Liang, X., 2011. EMT: A new vision of hypoxia promoting cancer progression. *Cancer Biol. Ther.* 11, 714–723. <https://doi.org/10.4161/cbt.11.8.15274>
- Joiner, M., Van der Kogel, A., 2016. *Basic clinical radiobiology*. CRC Press.
- Joiner, M., Van der Kogel, A., 2009. *Basic clinical radiobiology*. HodderArnoldLondon.
- Jung, J., Seol, H.S., Chang, S., 2018. The generation and application of patient-derived xenograft model for cancer research. *Cancer Res. Treat.* 50, 1–10. <https://doi.org/10.4143/crt.2017.307>
- Kang, A., Seo, H.I., Chung, B.G., Lee, S.-H., 2015. Concave microwell array-mediated three-dimensional tumor model for screening anticancer drug-loaded nanoparticles. *Nanomedicine* 11, 1153–61. <https://doi.org/10.1016/j.nano.2015.02.009>
- Kawamoto, S., Macura, K.J., 2016. *Genitourinary Imaging: Case reviews series*.
- Khaitan, D., Dwarakanath, B.S., 2006. Multicellular spheroids as an in vitro model in experimental oncology: Applications in translational medicine. *Expert Opin. Drug Discov.* 1, 663–675. <https://doi.org/10.1517/17460441.1.7.663>
- Khan, F.. and G.J.P., 2014. *Khan’s The Physics of Radiation Therapy*, 5th editio. ed.
- Kim, J.-K., Seo, S.-J., Kim, H.-T., Kim, K.-H., Chung, M.-H., Kim, K.-R., Ye, S.-J., 2012. Enhanced proton treatment in mouse tumors through proton irradiated nanoradiator effects on metallic nanoparticles. *Phys. Med. Biol.* 57, 8309–8323. <https://doi.org/10.1088/0031-9155/57/24/8309>
- Kim, S., Choung, S., Sun, R.X., Ung, N., Hashemi, N., Fong, E.J., Lau, R., Spiller, E., Gasho, J., Foo, J., Mumenthaler, S.M., 2020. Comparison of Cell and Organoid-Level Analysis of Patient-Derived 3D Organoids to Evaluate Tumor Cell Growth Dynamics and Drug Response. *SLAS Discov.* 25, 744–754. <https://doi.org/10.1177/2472555220915827>
- Klein, O., Nishina, Y., 1929. Über die Streuung von Strahlung durch freie Elektronen nach der neuen relativistischen Quantendynamik von Dirac. *Zeitschrift für Phys.* 52, 853–868. <https://doi.org/10.1007/BF01366453>

- Kotb, S., Detappe, A., Lux, F., Appaix, F., Barbier, E.L., Tran, V.L., Plissonneau, M., Gehan, H., Lefranc, F., Rodriguez-Lafrasse, C., Verry, C., Berbeco, R., Tillement, O., Sancey, L., 2016. Gadolinium-based nanoparticles and radiation therapy for multiple brain melanoma metastases: Proof of concept before phase I trial. *Theranostics* 6, 418–427. <https://doi.org/10.7150/thno.14018>
- Krause, M.O., 1979. Atomic radiative and radiation less yields for K and L shells. *J. Phys. Chem. Ref. Data* 8.2.
- Kuncic, Z., Lacombe, S., 2018. Nanoparticle radio-enhancement: principles, progress and application to cancer treatment. *Phys. Med. Biol.* 63, 02TR01. <https://doi.org/10.1088/1361-6560/aa99ce>
- Kwak, B., Lee, Y., Lee, J., Lee, S., Lim, J., 2018. Mass fabrication of uniform sized 3D tumor spheroid using high-throughput microfluidic system. *J. Control. Release* 275, 201–207. <https://doi.org/10.1016/j.jconrel.2018.02.029>
- Kwatra, D., Venugopal, A., Anant, S., 2013. Nanoparticles in radiation therapy: A summary of various approaches to enhance radiosensitization in cancer. *Transl. Cancer Res.* 2, 330–342. <https://doi.org/10.3978/j.issn.2218-676X.2013.08.06>
- Lacombe, S., Porcel, E., Scifoni, E., 2017. Particle therapy and nanomedicine: state of art and research perspectives. *Cancer Nanotechnol.* 8, 9. <https://doi.org/10.1186/s12645-017-0029-x>
- Lammers, T., Hennink, W.E., Storm, G., 2008. Tumour-targeted nanomedicines: Principles and practice. *Br. J. Cancer* 99, 392–397. <https://doi.org/10.1038/sj.bjc.6604483>
- Lancaster, M.A., Knoblich, J.A., 2014. Organogenesis in a dish: Modeling development and disease using organoid technologies. *Science* (80-.). 345. <https://doi.org/10.1126/science.1247125>
- Langhans, S.A., 2018. Three-dimensional in vitro cell culture models in drug discovery and drug repositioning. *Front. Pharmacol.* 9, 1–14. <https://doi.org/10.3389/fphar.2018.00006>
- Laura Harkness-Brennan, 2018. Radiation interactions with matter. Morgan & Claypool Publishers.
- LaVerne, J., 2000. Track effects of heavy ions in liquid water. *Radiat. Res.* 153, 487–496.
- Law, S., Leung, A.W., Xu, C., 2020. Folic acid-modified celastrol nanoparticles: synthesis, characterization, anticancer activity in 2D and 3D breast cancer models. *Artif. Cells, Nanomedicine Biotechnol.* 48, 542–559. <https://doi.org/10.1080/21691401.2020.1725025>
- Lazzari, G., Couvreur, P., Mura, S., 2017. Multicellular tumor spheroids: a relevant 3D model for the in vitro preclinical investigation of polymer nanomedicines. *Polym. Chem.* 8, 4947–4969. <https://doi.org/10.1039/C7PY00559H>
- Le Duc, G., Miladi, I., Alric, C., Mowat, P., Bräuer-Krisch, E., Bouchet, A., Khalil, E., Billotey, C., Janier, M., Lux, F., Epicier, T., Perriat, P., Roux, S., Tillement, O., 2011. Toward an image-guided microbeam radiation therapy using gadolinium-based nanoparticles. *ACS Nano* 5, 9566–9574. <https://doi.org/10.1021/nn202797h>
- Le, V.M., Lang, M.D., Shi, W. Bin, Liu, J.W., 2016. A collagen-based multicellular tumor spheroid model for evaluation of the efficiency of nanoparticle drug delivery. *Artif. Cells, Nanomedicine Biotechnol.* 44, 540–544. <https://doi.org/10.3109/21691401.2014.968820>
- Lee, J.M., Park, D.Y., Yang, L., Kim, E.-J., Ahrberg, C.D., Lee, K.-B., Chung, B.G., 2018. Generation of uniform-sized multicellular tumor spheroids using hydrogel microwells for advanced drug screening. *Sci. Rep.* 8, 17145. <https://doi.org/10.1038/s41598-018-35216-7>

- Leeman, M.F., McKay, J.A., Murray, G.I., 2002. Matrix metalloproteinase 13 activity is associated with poor prognosis in colorectal cancer. *J. Clin. Pathol.* 55, 758–762. <https://doi.org/10.1136/jcp.55.10.758>
- Leonard, C.E., Chan, D.C., Chou, T.C., Kumar, R., Bunn, P.A., 1996. Paclitaxel enhances in vitro radiosensitivity of squamous carcinoma cell lines of the head and neck. *Cancer Res.* 56, 5198–5204.
- Li, W.B., Belchior, A., Beuve, M., Chen, Y.Z., Di Maria, S., Friedland, W., Gervais, B., Heide, B., Hocine, N., Ipatov, A., Klapproth, A.P., Li, C.Y., Li, J.L., Multhoff, G., Poignant, F., Qiu, R., Rabus, H., Rudek, B., Schuemann, J., Stangl, S., Testa, E., Villagrasa, C., Xie, W.Z., Zhang, Y.B., 2020. Intercomparison of dose enhancement ratio and secondary electron spectra for gold nanoparticles irradiated by X-rays calculated using multiple Monte Carlo simulation codes. *Phys. Medica* 69, 147–163. <https://doi.org/10.1016/j.ejmp.2019.12.011>
- Li, X., Lachmanski, L., Safi, S., Sene, S., Serre, C., Grenèche, J.M., Zhang, J., Gref, R., 2017. New insights into the degradation mechanism of metal-organic frameworks drug carriers. *Sci. Rep.* 7, 1–11. <https://doi.org/10.1038/s41598-017-13323-1>
- Li, X., Porcel, E., Menendez-Miranda, M., Qiu, J., Yang, X., Serre, C., Pastor, A., Desmaële, D., Lacombe, S., Gref, R., 2020a. Highly Porous Hybrid Metal–Organic Nanoparticles Loaded with Gemcitabine Monophosphate: a Multimodal Approach to Improve Chemo- and Radiotherapy. *ChemMedChem* 15, 274–283. <https://doi.org/10.1002/cmdc.201900596>
- Li, X., Salzano, G., Qiu, J., Menard, M., Berg, K., Theodossiou, T., Ladavière, C., Gref, R., 2020b. Drug-Loaded Lipid-Coated Hybrid Organic-Inorganic “Stealth” Nanoparticles for Cancer Therapy. *Front. Bioeng. Biotechnol.* 8, 1–12. <https://doi.org/10.3389/fbioe.2020.01027>
- Li, Y., Li, N., Yu, X., Huang, K., Zheng, T., Cheng, X., Zeng, S., Liu, X., 2018. Hematoxylin and eosin staining of intact tissues via delipidation and ultrasound. *Sci. Rep.* 8, 1–8. <https://doi.org/10.1038/s41598-018-30755-5>
- Lin, R.-Z., Chang, H.-Y., 2008. Recent advances in three-dimensional multicellular spheroid culture for biomedical research. *Biotechnol. J.* 3, 1172–1184. <https://doi.org/10.1002/biot.200700228>
- Lin, R.Z., Chou, L.F., Chien, C.C.M., Chang, H.Y., 2006. Dynamic analysis of hepatoma spheroid formation: Roles of E-cadherin and β 1-integrin. *Cell Tissue Res.* 324, 411–422. <https://doi.org/10.1007/s00441-005-0148-2>
- Liu, N., Ji, J., Qiu, H., Shao, Z., Wen, X., Chen, A., Yao, S., Zhang, X., Yao, H., Zhang, L., 2020. Improving radio-chemotherapy efficacy of prostate cancer by co-delivering docetaxel and dbait with biodegradable nanoparticles. *Artif. Cells, Nanomedicine Biotechnol.* 48, 305–314. <https://doi.org/10.1080/21691401.2019.1703726>
- Lonza, 2016. RAFT™ 3D Cell Culture Kit Protocol [WWW Document]. URL https://bioscience.lonza.com/lonza_bs/CH/en/download/product/asset/30053
- Lorat, Y., Brunner, C., Schanz, S., Jakob, B., Taucher-Scholz, G., Rube, C., 2015. Nanoscale analysis of clustered DNA damage after high-LET irradiation by quantitative electron microscopy - The heavy burden to repair. *DNA Repair (Amst.)* 28, 93–106. <https://doi.org/10.1016/j.dnarep.2015.01.007>
- Louis, C., Bazzi, R., Marquette, C.A., Bridot, J.-L., Roux, S., Ledoux, G., Mercier, B., Blum, L., Perriat, P., Tillement, O., 2005. Nanosized Hybrid Particles with Double Luminescence for Biological Labeling. *Chem. Mater.* 17, 1673–1682. <https://doi.org/10.1021/cm0480162>
- Luchette, M., Korideck, H., Makrigiorgos, M., Tillement, O., Berbeco, R., 2014. Radiation dose enhancement of gadolinium-based AGuIX nanoparticles on HeLa cells. *Nanomedicine*

Nanotechnology, *Biol. Med.* 10, 1751–1755. <https://doi.org/10.1016/j.nano.2014.06.004>

- Lux, F., Detappe, A., Dufort, S., Sancey, L., Louis, C., Carme, S., Tillement, O., 2015. Nanoparticules ultrafines en radiothérapie: le cas des AGuIX. *Cancer/Radiothérapie* 19, 508–514. <https://doi.org/10.1016/j.canrad.2015.05.019>
- Lux, F., Mignot, A., Mowat, P., Louis, C., Dufort, S., Bernhard, C., Denat, F., Boschetti, F., Brunet, C., Antoine, R., Dugourd, P., Laurent, S., Elst, L. Vander, Muller, R., Sancey, L., Josserand, V., Coll, J.L., Stupar, V., Barbier, E., Rémy, C., Broisat, A., Ghezzi, C., Le Duc, G., Roux, S., Perriat, P., Tillement, O., 2011. Ultrasmall rigid particles as multimodal probes for medical applications. *Angew. Chemie - Int. Ed.* 50, 12299–12303. <https://doi.org/10.1002/anie.201104104>
- Lux, F., Tran, V.L., Thomas, E., Dufort, S., Rossetti, F., Martini, M., Truillet, C., Doussineau, T., Bort, G., Denat, F., Boschetti, F., Angelovski, G., Detappe, A., Crémillieux, Y., Mignet, N., Doan, B.-T., Larrat, B., Meriaux, S., Barbier, E., Roux, S., Fries, P., Müller, A., Abadjian, M.-C., Anderson, C., Canet-Soulas, E., Bouziotis, P., Barberi-Heyob, M., Frochot, C., Verry, C., Balosso, J., Evans, M., Sidi-Boumedine, J., Janier, M., Butterworth, K., McMahon, S., Prise, K., Aloy, M.-T., Ardail, D., Rodriguez-Lafrasse, C., Porcel, E., Lacombe, S., Berbeco, R., Allouch, A., Perfettini, J.-L., Chargari, C., Deutsch, E., Le Duc, G., Tillement, O., 2018. AGuIX® from bench to bedside-Transfer of an ultrasmall theranostic gadolinium-based nanoparticle to clinical medicine. *Br. J. Radiol.* 20180365. <https://doi.org/10.1259/bjr.20180365>
- Lv, D., Hu, Z., Lu, L., Lu, H., Xu, X., 2017. Three-dimensional cell culture: A powerful tool in tumor research and drug discovery. *Oncol. Lett.* 14, 6999–7010. <https://doi.org/10.3892/ol.2017.7134>
- Ma, J., Wang, Y., Liu, J., 2018. Bioprinting of 3D tissues/organs combined with microfluidics. *RSC Adv.* 8, 21712–21727. <https://doi.org/10.1039/c8ra03022g>
- Magdeldin, T., López-Dávila, V., Villemant, C., Cameron, G., Drake, R., Cheema, U., Loizidou, M., 2014. The efficacy of cetuximab in a tissue-engineered three-dimensional in vitro model of colorectal cancer. *J. Tissue Eng.* 5. <https://doi.org/10.1177/2041731414544183>
- Magzoub, M., Jin, S., Verkman, A.S., 2008. Enhanced macromolecule diffusion deep in tumors after enzymatic digestion of extracellular matrix collagen and its associated proteoglycan decorin. *FASEB J.* 22, 276–284. <https://doi.org/10.1096/fj.07-9150com>
- Manzanares, D., Ceña, V., 2020. Endocytosis: The nanoparticle and submicron nanocompounds gateway into the cell. *Pharmaceutics* 12, 1–22. <https://doi.org/10.3390/pharmaceutics12040371>
- Mapanao, A.K., Santi, M., Voliani, V., 2021. Combined chemo-photothermal treatment of three-dimensional head and neck squamous cell carcinomas by gold nano-architectures. *J. Colloid Interface Sci.* 582, 1003–1011. <https://doi.org/10.1016/j.jcis.2020.08.059>
- Maria, O.M., Maria, O., Liu, Y., Komarova, S. V., Tran, S.D., 2011. Matrigel improves functional properties of human submandibular salivary gland cell line. *Int. J. Biochem. Cell Biol.* 43, 622–631. <https://doi.org/10.1016/j.biocel.2011.01.001>
- Marples, B., 2015. Radiobiology of Particulate Irradiation, *ASTRO Annu. ed.*
- Matsumura, Y., Maeda, H., 1986. A New Concept for Macromolecular Therapeutics in Cancer Chemotherapy: Mechanism of Tumor-tropic Accumulation of Proteins and the Antitumor Agent Smancs. *Cancer Res.* 46, 6387–6392.
- Maury, P., Porcel, E., Mau, A., Lux, F., Tillement, O., Mahou, P., Schanne-Klein, M.-C., Lacombe, S., n.d. Rapid evaluation of novel therapeutic strategies using a 3D collagen-based tissue-like model. *Front. Bioeng. Biotechnol.* <https://doi.org/10.3389/fbioe.2021.574035>

- Maury, T., Morales Serrano, S., Loubet, P., Sonnemann, G., Colombo, C., Innocenti, L., 2019. Space debris through the prism of the environmental performance of space systems: the case of Sentinel-3 redesigned mission, in: First International Orbital Debris Conference. NASA, Houston, TX, United States.
- Mazzucconi, D., Agosteo, S., Ferrarini, M., Fontana, L., Lante, V., Pullia, M., Savazzi, S., 2018. Mixed particle beam for simultaneous treatment and online range verification in carbon ion therapy: Proof-of-concept study. *Med. Phys.* 45, 5234–5243. <https://doi.org/10.1002/mp.13219>
- McCabe-Lankford, E.E., Brown, T.L., Levi-Polyachenko, N.H., 2018. Assessing fluorescence detection and effective photothermal therapy of near-infrared polymer nanoparticles using alginate tissue phantoms. *Lasers Surg. Med.* 50, 1040–1049. <https://doi.org/10.1002/lsm.22955>
- McKeown, S.R., 2014. Defining normoxia, physoxia and hypoxia in tumours—implications for treatment response. *Br. J. Radiol.* 87, 20130676. <https://doi.org/10.1259/bjr.20130676>
- McMahon, S.J., Hyland, W.B., Muir, M.F., Coulter, J.A., Jain, S., Butterworth, K.T., Schettino, G., Dickson, G.R., Hounsell, A.R., O’Sullivan, J.M., Prise, K.M., Hirst, D.G., Currell, F.J., 2011. Biological consequences of nanoscale energy deposition near irradiated heavy atom nanoparticles. *Sci. Rep.* 1, 1–10. <https://doi.org/10.1038/srep00018>
- Mehnaz, Yang, L.H., Zou, Y.B., Da, B., Mao, S.F., Ding, Z.J., 2019. A comparative study on monte carlo simulations of electron emission from liquid water. *arXiv* 1–25.
- Meng, W., Garnett, M.C., Walker, D.A., Parker, T.L., 2016. Penetration and intracellular uptake of poly(glycerol-adipate) nanoparticles into three-dimensional brain tumour cell culture models. *Exp. Biol. Med.* 241, 466–477. <https://doi.org/10.1177/1535370215610441>
- Migdal, C., Serres, M., 2011. Espèces réactives de l’oxygène et stress oxydant. *Médecine/Sciences* 27, 405–412. <https://doi.org/10.1051/medsci/2011274405>
- Miladi, I., Aloy, M.T., Armandy, E., Mowat, P., Kryza, D., Magné, N., Tillement, O., Lux, F., Billotey, C., Janier, M., Rodriguez-Lafrasse, C., 2015. Combining ultrasmall gadolinium-based nanoparticles with photon irradiation overcomes radioresistance of head and neck squamous cell carcinoma. *Nanomedicine Nanotechnology, Biol. Med.* 11, 247–257. <https://doi.org/10.1016/j.nano.2014.06.013>
- Minchinton, A.I., Tannock, I.F., 2006. Drug penetration in solid tumours. *Nat. Rev. Cancer* 6, 583–592. <https://doi.org/10.1038/nrc1893>
- Mirbagheri, M., Adibnia, V., Hughes, B.R., Waldman, S.D., Banquy, X., Hwang, D.K., 2019. Advanced cell culture platforms: a growing quest for emulating natural tissues. *Mater. Horizons* 6, 45–71. <https://doi.org/10.1039/c8mh00803e>
- Mittal, P., Chopra, S., Pant, S., Mahantshetty, U., Engineer, R., Ghosh, J., Gupta, S., Ghadi, Y., Menachery, S., Swamidas, J., Gurram, L., Shrivastava, S.K., 2018. Standard Chemoradiation and Conventional Brachytherapy for Locally Advanced Cervical Cancer: Is It Still Applicable in the Era of Magnetic Resonance–Based Brachytherapy? *J. Glob. Oncol.* 1–9. <https://doi.org/10.1200/jgo.18.00028>
- Mohammad-Hadi, L., MacRobert, A.J., Loizidou, M., Yaghini, E., 2018. Photodynamic therapy in 3D cancer models and the utilisation of nanodelivery systems. *Nanoscale* 10, 1570–1581. <https://doi.org/10.1039/c7nr07739d>
- Mowat, P., Mignot, A., Rima, W., Lux, F., Tillement, O., Roulin, C., Dutreix, M., Bechet, D., Huger, S., Humbert, L., Barberi-Heyob, M., Aloy, M.T., Armandy, E., Rodriguez-Lafrasse, C., Le Duc, G., Roux, S., Perriat, P., 2011. In vitro radiosensitizing effects of ultrasmall gadolinium based particles on tumour

- cells. *J. Nanosci. Nanotechnol.* 11, 7833–7839. <https://doi.org/10.1166/jnn.2011.4725>
- Muncie, J., Weaver, V., 2019. The Physical and Biochemical Properties of the Extracellular Matrix Regulate Cell Fate. *Curr Top Dev Biol* 1–30. <https://doi.org/10.1016/bs.ctdb.2018.02.002>
- Murphy, S. V., Atala, A., 2014. 3D bioprinting of tissues and organs. *Nat. Biotechnol.* 32, 773–785. <https://doi.org/10.1038/nbt.2958>
- Nath, S., Devi, G.R., 2016. Three-dimensional culture systems in cancer research: Focus on tumor spheroid model. *Pharmacol. Ther.* 163, 94–108. <https://doi.org/10.1016/j.pharmthera.2016.03.013>
- Netti, P.A., Berk, D.A., Swartz, M.A., Grodzinsky, A.J., Jain, R.K., 2000. Role of extracellular matrix assembly in interstitial transport in solid tumors. *Cancer Res.* 60, 2497–2503.
- Neuer, A.L., Gerken, L.R.H., Keevend, K., Gogos, A., Herrmann, I.K., 2020. Uptake, distribution and radio-enhancement effects of gold nanoparticles in tumor microtissues. *Nanoscale Adv.* 2, 2992–3001. <https://doi.org/10.1039/d0na00256a>
- Oze, H., Hirao, M., Ebina, K., Shi, K., Kawato, Y., Kaneshiro, S., Yoshikawa, H., Hashimoto, J., 2012. Impact of medium volume and oxygen concentration in the incubator on pericellular oxygen concentration and differentiation of murine chondrogenic cell culture. *Vitr. Cell. Dev. Biol. - Anim.* 48, 123–130. <https://doi.org/10.1007/s11626-011-9479-3>
- Pauwels, B., Korst, A.E.C., De Pooter, C.M.J., Lambrechts, H.A.J., Pattyn, G.G.O., Lardon, F., Vermorken, J.B., 2003. The radiosensitising effect of gemcitabine and the influence of the rescue agent amifostine in vitro. *Eur. J. Cancer* 39, 838–846. [https://doi.org/10.1016/S0959-8049\(03\)00002-9](https://doi.org/10.1016/S0959-8049(03)00002-9)
- Pedersen, J.A., Swartz, M.A., 2005. Mechanobiology in the Third Dimension 33, 1469–1490. <https://doi.org/10.1007/s10439-005-8159-4>
- Pinto, B., Henriques, A.C., Silva, P.M.A., Bousbaa, H., 2020. Three-dimensional spheroids as in vitro preclinical models for cancer research. *Pharmaceutics* 12, 1–38. <https://doi.org/10.3390/pharmaceutics12121186>
- Place, T.L., Domann, F.E., Case, A.J., 2017. Limitations of oxygen delivery to cells in culture: An underappreciated problem in basic and translational research. *Free Radic. Biol. Med.* 113, 311–322. <https://doi.org/10.1016/j.freeradbiomed.2017.10.003>
- Poignant, F., Monini, C., Testa, É., Beuve, M., 2020. Influence of gold nanoparticles embedded in water on nanodosimetry for keV photon irradiation. *Med. Phys.* <https://doi.org/10.1002/mp.14576>
- Popović, Z., Liu, W., Chauhan, V.P., Lee, J., Wong, C., Greytak, A.B., Insin, N., Nocera, D.G., Fukumura, D., Jain, R.K., Bawendi, M.G., 2010. A Nanoparticle Size Series for In Vivo Fluorescence Imaging. *Angew. Chemie Int. Ed.* 49, 8649–8652. <https://doi.org/10.1002/anie.201003142>
- Porcel, E., Liehn, S., Remita, H., Usami, N., Kobayashi, K., Furusawa, Y., Sech, C. Le, Lacombe, S., 2010. Platinum nanoparticles: a promising material for future cancer therapy? *Nanotechnology* 21, 085103. <https://doi.org/10.1088/0957-4484/21/8/085103>
- Porcel, E., Tillement, O., Lux, F., Mowat, P., Usami, N., Kobayashi, K., Furusawa, Y., Le Sech, C., Li, S., Lacombe, S., 2014. Gadolinium-based nanoparticles to improve the hadrontherapy performances. *Nanomedicine Nanotechnology, Biol. Med.* 10, 1601–1608. <https://doi.org/10.1016/j.nano.2014.05.005>
- Pratiwi, F.W., Peng, C., Wu, S., Kuo, C.W., Mou, C., Tung, Y., Chen, P., 2021. Evaluation of Nanoparticle Penetration in the Tumor Spheroid Using Two-Photon Microscopy 1–14.

- Qiu, Y., Ning, D., Zhang, P., Curly, S., Qiao, Y., Ma, L., Su, M., 2017. Three-dimensional microtissues as an in vitro model for personalized radiation therapy. *Analyst* 142, 3605–3612. <https://doi.org/10.1039/c7an00794a>
- Quan, Y., Sun, M., Tan, Z., Eijkel, J.C.T., Van Den Berg, A., Van Der Meer, A., Xie, Y., 2020. Organ-on-a-chip: The next generation platform for risk assessment of radiobiology. *RSC Adv.* 10, 39521–39530. <https://doi.org/10.1039/d0ra05173j>
- Ramani, S., Crawford, S.E., Blutt, S.E., Estes, M.K., 2018. Human organoid cultures: transformative new tools for human virus studies. *Curr. Opin. Virol.* 29, 79–86. <https://doi.org/10.1016/j.coviro.2018.04.001>
- Rangarajan, A., Hong, S.J., Gifford, A., Weinberg, R.A., 2004. Species- and cell type-specific requirements for cellular transformation. *Cancer Cell* 6, 171–183. <https://doi.org/10.1016/j.ccr.2004.07.009>
- Rayner, R.E., Makena, P., Prasad, G.L., Cormet-Boyaka, E., 2019. Optimization of Normal Human Bronchial Epithelial (NHBE) Cell 3D Cultures for in vitro Lung Model Studies. *Sci. Rep.* 9, 2–11. <https://doi.org/10.1038/s41598-018-36735-z>
- Richmond, A., Yingjun, S., 2008. Mouse xenograft models vs GEM models for human cancer therapeutics. *DMM Dis. Model. Mech.* 1, 78–82. <https://doi.org/10.1242/dmm.000976>
- Robertson, F.L., Marqués-Torrejón, M.A., Morrison, G.M., Pollard, S.M., 2019. Experimental models and tools to tackle glioblastoma. *DMM Dis. Model. Mech.* 12. <https://doi.org/10.1242/dmm.040386>
- Robley Evan, 1956. The atomic nucleus. McGraw Hill B. Co. 2, 11S-12S. <https://doi.org/10.1002/aic.690020327>
- Rodriguez-Ruiz, V., Maksimenko, A., Anand, R., Monti, S., Agostoni, V., Couvreur, P., Lampropoulou, M., Yannakopoulou, K., Gref, R., 2015. Efficient “green” encapsulation of a highly hydrophilic anticancer drug in metal–organic framework nanoparticles. *J. Drug Target.* 23, 759–767. <https://doi.org/10.3109/1061186X.2015.1073294>
- Rodriguez, H., Akman, S.A., 1998. Mapping oxidative DNA damage at nucleotide level. *Free Radic. Res.* 29, 499–510. <https://doi.org/10.1080/10715769800300551>
- Roy, P., Canet-Jourdan, C., Annereau, M., Zajac, O., Gelli, M., Broutin, S., Mercier, L., Paci, A., Lemare, F., Ducreux, M., Elias, D., Malka, D., Boige, V., Goéré, D., Jaulin, F., 2017. Organoids as preclinical models to improve intraperitoneal chemotherapy effectiveness for colorectal cancer patients with peritoneal metastases: Preclinical models to improve HIPEC. *Int. J. Pharm.* 531, 143–152. <https://doi.org/10.1016/j.ijpharm.2017.07.084>
- Ryu, N.-E., Lee, S.-H., Park, H., 2019. Spheroid Culture System Methods and Applications for Mesenchymal Stem Cells. *Cells* 8, 1620. <https://doi.org/10.3390/cells8121620>
- Sage, E., Shikazono, N., 2017. Radiation-induced clustered DNA lesions: Repair and mutagenesis. *Free Radic. Biol. Med.* 107, 125–135. <https://doi.org/10.1016/j.freeradbiomed.2016.12.008>
- Saha, G.B., 2013. *Physics and Radiobiology of Nuclear Medicine*. Springer New York, New York, NY. <https://doi.org/10.1007/978-1-4614-4012-3>
- Sánchez, G., Maury, P., Stefancikova, L., Champion, O., Laurent, G., Chateau, A., Hoch, F., Boschetti, F., Denat, F., Pinel, S., Devy, J., Porcel, E., Lacombe, S., Bazzi, R., Roux, S., 2019. Fluorescent radiosensitizing gold nanoparticles. *Int. J. Mol. Sci.* 20. <https://doi.org/10.3390/ijms20184618>

- Sarem, M., Otto, O., Tanaka, S., Shastri, V.P., 2019. Cell number in mesenchymal stem cell aggregates dictates cell stiffness and chondrogenesis. *Stem Cell Res. Ther.* 10, 1–18. <https://doi.org/10.1186/s13287-018-1103-y>
- Sarkar, S., Peng, C.-C., Kuo, C.W., Chueh, D.-Y., Wu, H.-M., Liu, Y.-H., Chen, P., Tung, Y.-C., 2018. Study of oxygen tension variation within live tumor spheroids using microfluidic devices and multi-photon laser scanning microscopy. *RSC Adv.* 8, 30320–30329. <https://doi.org/10.1039/C8RA05505J>
- Scher, N., Bonvalot, S., Le Tourneau, C., Chajon, E., Verry, C., Thariat, J., Calugaru, V., 2020. Review of clinical applications of radiation-enhancing nanoparticles. *Biotechnol. Reports* 28, e00548. <https://doi.org/10.1016/j.btre.2020.e00548>
- Schlathölter, T., Eustache, P., Porcel, E., Salado, D., Stefancikova, L., Tillement, O., Lux, F., Mowat, P., Biegun, A.K., Van Goethem, M., Remita, H., Lacombe, S., 2016. Improving proton therapy by metal-containing nanoparticles: Nanoscale insights. *Int. J. Nanomedicine* 11, 1549–1556. <https://doi.org/10.2147/IJN.S99410>
- Schneider, T., 2020. Advancing the generation of proton minibeam for radiation therapy. Université Paris-Saclay,.
- Schuemann, J., Berbeco, R., Chithrani, D.B., Cho, S.H., Kumar, R., McMahon, S.J., Sridhar, S., Krishnan, S., 2016. Roadmap to clinical use of gold nanoparticles for radiation sensitization. *Int. J. Radiat. Oncol. Biol. Phys.* 94, 189–205. <https://doi.org/10.1016/j.ijrobp.2015.09.032>
- Schuemann, J., McNamara, A.L., Ramos-Méndez, J., Perl, J., Held, K.D., Paganetti, H., Incerti, S., Faddegon, B., 2019. TOPAS-nBio: An Extension to the TOPAS Simulation Toolkit for Cellular and Sub-cellular Radiobiology. *Radiat. Res.* 191, 125–138. <https://doi.org/10.1667/RR15226.1>
- Scifoni, E., Tinganelli, W., Weyrather, W.K., Durante, M., Maier, A., Krämer, M., 2013. Including oxygen enhancement ratio in ion beam treatment planning: Model implementation and experimental verification. *Phys. Med. Biol.* 58, 3871–3895. <https://doi.org/10.1088/0031-9155/58/11/3871>
- Sedelnikova, O.A., Nakamura, A., Kovalchuk, O., Koturbash, I., Mitchell, S.A., Marino, S.A., Brenner, D.J., Bonner, W.M., 2007. DNA double-strand breaks form in bystander cells after microbeam irradiation of three-dimensional human tissue models. *Cancer Res.* 67, 4295–4302. <https://doi.org/10.1158/0008-5472.CAN-06-4442>
- Seiwert, T.Y., Salama, J.K., Vokes, E.E., 2007. The concurrent chemoradiation paradigm - General principles. *Nat. Clin. Pract. Oncol.* 4, 86–100. <https://doi.org/10.1038/nconco0714>
- Seltzer, S.M., Bartlett, D.T., Burns, D.T., Dietze, G., Menzel, H.-G., Paretzke, H.G., Wambersie, A., 2011. The International Commission on Radiation Units and Measurements. *J. ICRU* 11, NP.1-NP. <https://doi.org/10.1093/jicru/ndro11>
- Shewach, D.S., Lawrence, T.S., 1996. Gemcitabine and radiosensitization in human tumor cells. *Invest. New Drugs* 14, 257–263. <https://doi.org/10.1007/BF00194528>
- Shi, W., Kwon, J., Huang, Y., Tan, J., Uhl, C.G., He, R., Zhou, C., Liu, Y., 2018. Facile Tumor Spheroids Formation in Large Quantity with Controllable Size and High Uniformity. *Sci. Rep.* 8, 1–9. <https://doi.org/10.1038/s41598-018-25203-3>
- Shield, K., Ackland, M.L., Ahmed, N., Rice, G.E., 2009. Multicellular spheroids in ovarian cancer metastases: Biology and pathology. *Gynecol. Oncol.* 113, 143–148. <https://doi.org/10.1016/j.ygyno.2008.11.032>

- Simpson, W.C., Orlando, T.M., Parenteau, L., Nagesha, K., Sanche, L., 1998. Dissociative electron attachment in nanoscale ice films: Thickness and charge trapping effects. *J. Chem. Phys.* 108, 5027–5034. <https://doi.org/10.1063/1.475924>
- Siolas, D., Hannon, G.J., 2013. Patient-Derived Tumor Xenografts: Transforming Clinical Samples into Mouse Models. *Cancer Res.* 73, 5315–5319. <https://doi.org/10.1158/0008-5472.CAN-13-1069>
- Sisin, N.N.T., Razak, K.A., Abidin, S.Z., Mat, N.F.C., Abdullah, R., Rashid, R.A., Khairil, M.A., Anuar, Hamizah, N., Zainudin, M., Tagiling, N., Nawati, N.M., Rahman, W.N., 2019. Radiosensitization Effects by Bismuth Oxide Nanoparticles in Combination with Cisplatin for High Dose Rate Brachytherapy. *Int. J. Nanomedicine* 14, 9941–9954. <https://doi.org/10.2147/IJN.S228919>
- Song, G., Cheng, L., Chao, Y., Yang, K., Liu, Z., 2017. Emerging Nanotechnology and Advanced Materials for Cancer Radiation Therapy. *Adv. Mater.* 29, 1–26. <https://doi.org/10.1002/adma.201700996>
- Sonntag, C., 1987. *The chemical basis of radiation biology.*
- Štefančíková, L., Porcel, E., Eustache, P., Li, S., Salado, D., Marco, S., Guerquin-Kern, J.-L., Réfrégiers, M., Tillement, O., Lux, F., Lacombe, S., 2014. Cell localisation of gadolinium-based nanoparticles and related radiosensitising efficacy in glioblastoma cells. *Cancer Nanotechnol.* 5, 6. <https://doi.org/10.1186/s12645-014-0006-6>
- Steichen, S.D., Caldorera-Moore, M., Peppas, N.A., 2013. A review of current nanoparticle and targeting moieties for the delivery of cancer therapeutics. *Eur. J. Pharm. Sci.* 48, 416–427. <https://doi.org/10.1016/j.ejps.2012.12.006>
- Storch, K., Eke, I., Borgmann, K., Krause, M., Richter, C., Becker, K., Schröck, E., Cordes, N., 2010. Three-dimensional cell growth confers radioresistance by chromatin density modification. *Cancer Res.* 70, 3925–3934. <https://doi.org/10.1158/0008-5472.CAN-09-3848>
- Stroud, M.J., Feng, W., Zhang, J., Veevers, J., Fang, X., Gerace, L., Chen, J., 2017. Nesprin 1 α 2 is essential for mouse postnatal viability and nuclear positioning in skeletal muscle. *J. Cell Biol.* 216, 1915–1924. <https://doi.org/10.1083/jcb.201612128>
- Strupler, M., 2008. *Imagerie du collagène par microscopie multiphotonique.* Ecole Polytechnique X.
- Stumpf, V., Gokhberg, K., Cederbaum, L.S., 2016. The role of metal ions in X-ray-induced photochemistry. *Nat. Chem.* 8, 237–241. <https://doi.org/10.1038/nchem.2429>
- Surdutovich, E., Solov'yov, A. V., 2017. Multiscale Physics of Ion-Beam Cancer Therapy, in: *Nanoscale Insights into Ion-Beam Cancer Therapy.* Springer International Publishing, Cham, pp. 1–60. https://doi.org/10.1007/978-3-319-43030-0_1
- Sutherland RM, McCredie JA, I.W., 1971. Growth of multicell spheroids in tissue culture as a model of nodular carcinomas. *J Natl Cancer Inst.*
- Suzuki, K., Nakashima, M., Yamashita, S., 2010. Dynamics of Ionizing Radiation-Induced DNA Damage Response in Reconstituted Three-Dimensional Human Skin Tissue. *Radiat. Res.* 174, 415–423. <https://doi.org/10.1667/rr2007.1>
- Taggart, L.E., McMahon, S.J., Currell, F.J., Prise, K.M., Butterworth, K.T., 2014. The role of mitochondrial function in gold nanoparticle mediated radiosensitisation. *Cancer Nanotechnol.* 5, 1–12. <https://doi.org/10.1186/s12645-014-0005-7>
- Tchoryk, A., Taresco, V., Argent, R.H., Ashford, M., Gellert, P.R., Stolnik, S., Grabowska, A., Garnett, M.C.,

- 2019a. Penetration and Uptake of Nanoparticles in 3D Tumor Spheroids. *Bioconj. Chem.* 30, 1371–1384. <https://doi.org/10.1021/acs.bioconjchem.9b00136>
- Tchoryk, A., Taresco, V., Argent, R.H., Ashford, M., Gellert, P.R., Stolnik, S., Grabowska, A., Garnett, M.C., 2019b. Penetration and uptake of nanoparticles in 3D tumor spheroids. *Bioconj. Chem.* 30, 1371–1384. <https://doi.org/10.1021/acs.bioconjchem.9b00136>
- Thakuri, P.S., Gupta, M., Plaster, M., Tavana, H., 2019. Quantitative Size-Based Analysis of Tumor Spheroids and Responses to Therapeutics. *Assay Drug Dev. Technol.* 17, 140–149. <https://doi.org/10.1089/adt.2018.895>
- Thariat, J., Habrand, J., Lesueur, P., Chaikh, A., Kammerer, E., Lecomte, D., Batalla, A., Balosso, J., Tessonnier, T., 2018. Apports de la protonthérapie à la radiothérapie d'aujourd'hui, pourquoi, comment ? *Bull. Cancer* 105, 315–326. <https://doi.org/10.1016/j.bulcan.2017.12.004>
- Topsch, J., Scholz, M., Mueller-Klieser, W., 2007. Radiobiological Characterization of Human Tumor Cell Multilayers after Conventional and Particle Irradiation. *Radiat. Res.* 167, 645–654. <https://doi.org/10.1667/RR0775.1>
- Torchilin, V.P., 2012. Multifunctional nanocarriers. *Adv. Drug Deliv. Rev.* 64, 302–315. <https://doi.org/10.1016/j.addr.2012.09.031>
- Tran, H.N., Karamitros, M., Ivanchenko, V.N., Guatelli, S., McKinnon, S., Murakami, K., Sasaki, T., Okada, S., Bordage, M.C., Francis, Z., El Bitar, Z., Bernal, M.A., Shin, J.I., Lee, S.B., Barberet, P., Tran, T.T., Brown, J.M.C., Nhan Hao, T. V., Incerti, S., 2016. Geant4 Monte Carlo simulation of absorbed dose and radiolysis yields enhancement from a gold nanoparticle under MeV proton irradiation. *Nucl. Instruments Methods Phys. Res. Sect. B Beam Interact. with Mater. Atoms* 373, 126–139. <https://doi.org/10.1016/j.nimb.2016.01.017>
- Tubiana, M., Dutreix, J., Wambersie, A., 1986. *Radiobiologie*.
- Usami, N., Furusawa, Y., Kobayashi, K., Frohlich, H., Lacombe, S., Le Sech, C., 2005. Fast He²⁺ ion irradiation of DNA loaded with platinum-containing molecules. *Int. J. Radiat. Biol.* 81, 515–522. <https://doi.org/10.1080/09553000500304318>
- Usami, N., Furusawa, Y., Kobayashi, K., Lacombe, S., Reynaud-Angelin, A., Sage, E., Wu, T., Croisy, A., Guerquin-Kern, J.L., Le Sech, C., 2008. Mammalian cells loaded with platinum-containing molecules are sensitized to fast atomic ions. *Int. J. Radiat. Biol.* 84, 603–611. <https://doi.org/10.1080/09553000802199846>
- Vadivelu, R., Kamble, H., Shiddiky, M., Nguyen, N.-T., 2017. Microfluidic Technology for the Generation of Cell Spheroids and Their Applications. *Micromachines* 8, 94. <https://doi.org/10.3390/mi8040094>
- van Leeuwen, C.M., Crezee, J., Oei, A.L., Franken, N.A.P., Stalpers, L.J.A., Bel, A., Kok, H.P., 2017. 3D radiobiological evaluation of combined radiotherapy and hyperthermia treatments. *Int. J. Hyperth.* 33, 160–169. <https://doi.org/10.1080/02656736.2016.1241431>
- Vandamme, T., 2014. Use of rodents as models of human diseases. *J. Pharm. Bioallied Sci.* 6, 2–9. <https://doi.org/10.4103/0975-7406.124301>
- Vaupel, P., Mayer, A., 2007. Hypoxia in cancer: Significance and impact on clinical outcome. *Cancer Metastasis Rev.* 26, 225–239. <https://doi.org/10.1007/s10555-007-9055-1>
- Verkhovtsev, A. V., Korol, A. V., Solov'yov, A. V., 2015a. Electron production by sensitizing gold nanoparticles irradiated by fast ions. *J. Phys. Chem. C* 119, 11000–11013.

<https://doi.org/10.1021/jp511419n>

- Verkhovtsev, A. V., Korol, A. V., Solov'Yov, A. V., 2015b. Revealing the mechanism of the low-energy electron yield enhancement from sensitizing nanoparticles. *Phys. Rev. Lett.* 114, 1–6. <https://doi.org/10.1103/PhysRevLett.114.063401>
- Verry, C., Dufort, S., Barbier, E.L., Montigon, O., Peoc'H, M., Chartier, P., Lux, F., Balosso, J., Tillement, O., Sancey, L., Le Duc, G., 2016. MRI-guided clinical 6-MV radiosensitization of glioma using a unique gadolinium-based nanoparticles injection. *Nanomedicine* 11, 2405–2417. <https://doi.org/10.2217/nnm-2016-0203>
- Verry, C., Dufort, S., Lemasson, B., Grand, S., Pietras, J., Troprès, I., Crémillieux, Y., Lux, F., Mériaux, S., Larrat, B., Balosso, J., Le Duc, G., Barbier, E.L., Tillement, O., 2020a. Targeting brain metastases with ultrasmall theranostic nanoparticles, a first-in-human trial from an MRI perspective. *Sci. Adv.* 6. <https://doi.org/10.1126/sciadv.aay5279>
- Verry, C., Dufort, S., Lemasson, B., Grand, S., Pietras, J., Troprès, I., Crémillieux, Y., Lux, F., Mériaux, S., Larrat, B., Balosso, J., Le Duc, G., Barbier, E.L., Tillement, O., 2020b. Targeting brain metastases with ultrasmall theranostic nanoparticles, a first-in-human trial from an MRI perspective. *Sci. Adv.* 6, eaay5279. <https://doi.org/10.1126/sciadv.aay5279>
- Vigier, S., Fülöp, T., 2016. Exploring the Extracellular Matrix to Create Biomaterials, in: *Composition and Function of the Extracellular Matrix in the Human Body*. InTech. <https://doi.org/10.5772/62979>
- Vijayavenkataraman, S., Yan, W.C., Lu, W.F., Wang, C.H., Fuh, J.Y.H., 2018. 3D bioprinting of tissues and organs for regenerative medicine. *Adv. Drug Deliv. Rev.* 132, 296–332. <https://doi.org/10.1016/j.addr.2018.07.004>
- Vilotte, F., Jumeau, R., Bourhis, J., 2019. High Z nanoparticles and radiotherapy: a critical view. *Lancet Oncol.* 20, e557. [https://doi.org/10.1016/S1470-2045\(19\)30579-0](https://doi.org/10.1016/S1470-2045(19)30579-0)
- Volz, L., Kelleter, L., Brons, S., Burigo, L., Graeff, C., Niebuhr, N.I., Radogna, R., Scheloske, S., Schömers, C., Jolly, S., Seco, J., 2020. Experimental exploration of a mixed helium/carbon beam for online treatment monitoring in carbon ion beam therapy. *Phys. Med. Biol.* 65, 055002. <https://doi.org/10.1088/1361-6560/ab6e52>
- Walenta, S., Mueller-Klieser, W., 2016. Differential Superiority of Heavy Charged-Particle Irradiation to X-Rays: Studies on Biological Effectiveness and Side Effect Mechanisms in Multicellular Tumor and Normal Tissue Models. *Front. Oncol.* 6, 30. <https://doi.org/10.3389/fonc.2016.00030>
- Walker, C., Mojares, E., Del Río Hernández, A., 2018. Role of extracellular matrix in development and cancer progression, *International Journal of Molecular Sciences*. <https://doi.org/10.3390/ijms19103028>
- Wälzlein, C., Scifoni, E., Krämer, M., Durante, M., 2014. Simulations of dose enhancement for heavy atom nanoparticles irradiated by protons. *Phys. Med. Biol.* 59, 1441–1458. <https://doi.org/10.1088/0031-9155/59/6/1441>
- Wang, H., Jiang, H., Van De Gucht, M., De Ridder, M., 2019. Hypoxic radioresistance: Can ROS be the key to overcome it? *Cancers (Basel)*. 11. <https://doi.org/10.3390/cancers11010112>
- West, C.M.L., Davidson, S.E., Roberts, S.A., Hunter, R.D., 1993. Intrinsic radiosensitivity and prediction of patient response to radiotherapy for carcinoma of the cervix. *Br. J. Cancer* 68, 819–823. <https://doi.org/10.1038/bjc.1993.434>

- Wion, D., Dematteis, M., Nissou, M.-F., Cretallaz, C., Berger, F., Issartel, J.-P., 2008. Pression partielle en oxygène et culture de cellules cancéreuses. *Médecine/Sciences* 24, 1093–1095. <https://doi.org/10.1051/medsci/200824121093>
- Wu, Q., Liu, J., Wang, X., Feng, L., Wu, J., Zhu, X., Wen, W., Gong, X., 2020. Organ-on-a-chip: Recent breakthroughs and future prospects. *Biomed. Eng. Online* 19, 1–19. <https://doi.org/10.1186/s12938-020-0752-0>
- Wuttke, S., Braig, S., Preiß, T., Zimpel, A., Sicklinger, J., Bellomo, C., Rädler, J.O., Vollmar, A.M., Bein, T., 2015. MOF nanoparticles coated by lipid bilayers and their uptake by cancer cells. *Chem. Commun.* 51, 15752–15755. <https://doi.org/10.1039/c5cc06767g>
- Yamada, K.M., Cukierman, E., 2007. Modeling Tissue Morphogenesis and Cancer in 3D. *Cell* 130, 601–610. <https://doi.org/10.1016/j.cell.2007.08.006>
- Yang, B., Liu, H., Yang, H., Chen, W., Wu, Jingban, Feng, X., Tong, R., Yu, H., Chen, Y., Lv, Z., Sun, W., He, B., Wu, Jian, Yu, G., Mao, Z., Zheng, S., 2019. Combinatorial photochemotherapy on liver cancer stem cells with organoplatinum(II) metallacage-based nanoparticles. *J. Mater. Chem. B* 7, 6476–6487. <https://doi.org/10.1039/c9tb01299k>
- Yi, F., Huang, J., Yang, L., Xie, Y., Xiao, G., 2017. Automatic extraction of cell nuclei from H&E-stained histopathological images. *J. Med. Imaging* 4, 027502. <https://doi.org/10.1117/1.JMI.4.2.027502>
- Zanoni, M., Piccinini, F., Arienti, C., Zamagni, A., Santi, S., Polico, R., Bevilacqua, A., Tesei, A., 2016. 3D tumor spheroid models for in vitro therapeutic screening: a systematic approach to enhance the biological relevance of data obtained. *Sci. Rep.* 6, 19103. <https://doi.org/10.1038/srep19103>
- Zhang, F., Han, X., Hu, Y., Wang, S., Liu, S., Pan, X., Wang, H., Ma, J., Wang, W., Li, S., Wu, Q., Shen, H., Yu, X., Yuan, Q., Liu, H., 2019. Interventional Photothermal Therapy Enhanced Brachytherapy: A New Strategy to Fight Deep Pancreatic Cancer. *Adv. Sci.* 6. <https://doi.org/10.1002/adv.201801507>
- Zhang, K., Zhao, T., Huang, X., He, Y., Zhou, Y., Wu, L., Wu, K., Fan, M., Zhu, L., 2016. Dissolved oxygen concentration in the medium during cell culture: Defects and improvements. *Cell Biol. Int.* 40, 354–360. <https://doi.org/10.1002/cbin.10570>
- Zhao, Y., Zhong, R., Sun, L., Jia, J., Ma, S., Liu, X., 2015. Ionizing radiation-induced adaptive response in fibroblasts under both monolayer and 3-dimensional conditions. *PLoS One* 10, 1–13. <https://doi.org/10.1371/journal.pone.0121289>
- Zietarska, M., Maugard, C.M., Filali-Mouhim, A., Alam-Fahmy, M., Tonin, P.N., Provencher, D.M., Mes-Masson, A.-M., 2007. Molecular description of a 3D in vitro model for the study of epithelial ovarian cancer (EOC). *Mol. Carcinog.* 46, 872–885. <https://doi.org/10.1002/mc.20315>

SUPPLEMENTARY SECTION

1. Supplementary informations

Different techniques to generate spheroids are currently available. The 4 main methods (to which we referred in Chapter II) are presented here:

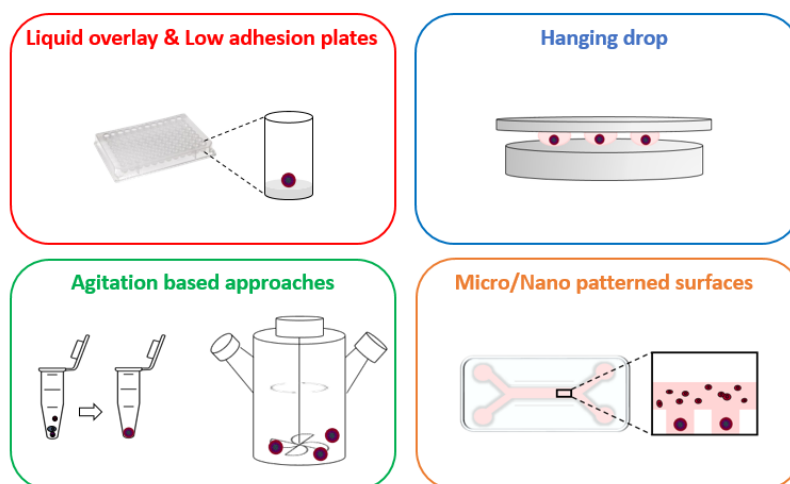


Figure 1.1 - Preclinical model: from bench to bedside

1.1. Liquid overlay & Low adhesion plates

The first technic is based on the use of surface covered with a thin film of inert substrates preventing cell attachment and promoting self-aggregation of cells into spheroids (Fang and Eglén, 2017; Nath and Devi, 2016). However, the size of formed spheroids was variable (Lin and Chang, 2008). Recently, ultralow attachment plates which contain individual wells with a layer of hydrophilic polymer on their surface have been proposed (Chaicharoenaudomrung et al., 2019). The key advantage of this approach is to form, propagate, and assay the spheroids within the same plate.

1.2. Hanging drop method

This method uses the surface tension to hang a droplet of cell suspension on the underside of a culture dish lid (Lazzari et al., 2017). Rapid aggregation is induced by the gravity which drive cell accumulation at the tip of the drop. Spheroids created present a uniform-size but this method has many disadvantages including a limited volume that does not provide enough nutrient for a long-term culture and a risky sample transfer (Nath and Devi, 2016).

1.3. Agitation-based approaches

The third approach uses a bioreactor (e.g., spinner flask, rotational culture systems, microgravity bioreactor) to drive cells to self-aggregate into spheroids under dynamic culture condition avoiding their attachment to the container wall (Fang and Eglén, 2017). This method allows a large-scale production and a long-term culture but the spheroids created lack of uniformity in size and number of cells. In addition their transfer into different supports are mandatory before any further assay (Lazzari et al., 2017; Nath and Devi, 2016).

The pellet culture method uses centrifugal force to concentrate cells to the bottom of the tube (Achilli et al., 2012; Ryu et al., 2019). Aggregation is induced by the contact of the single cells at the bottom of the tube. This method is simple and rapid to perform, can create large diameter spheroids but the shear stress from centrifugation that can damage cells (Achilli et al., 2012).

1.4. Micro-/nano patterned surfaces

The fourth approach is to use micro-/nano-patterned surfaces as the scaffolds to control cell adhesion and migration. This method uses nanoscale scaffolds imprinted onto a flat substrate for the selection of appropriate patterns and adhesive properties for a variety of cell type (Fang and Eglén, 2017). Arrays of microwells or microfluidics systems containing various micro-sized chambers can also be used (Lazzari et al., 2017). These systems allow a creation of samples of homogenous shape, size and cell composition. However, the retrieve of the sample is difficult. This micro/nano technologies require also specific setups and device fabrication, which are expensive equipments (Benien and Swami, 2014; Lazzari et al., 2017).

2. Supplementary results

During my PhD work, additional results were obtained. In particular, the efficacy of a treatment combining Gd nanoparticles with a carbon ions beam was evaluated. We found that the presence of AGuIX® enhance the effects of carbon ions of 15% at 2 Gy.

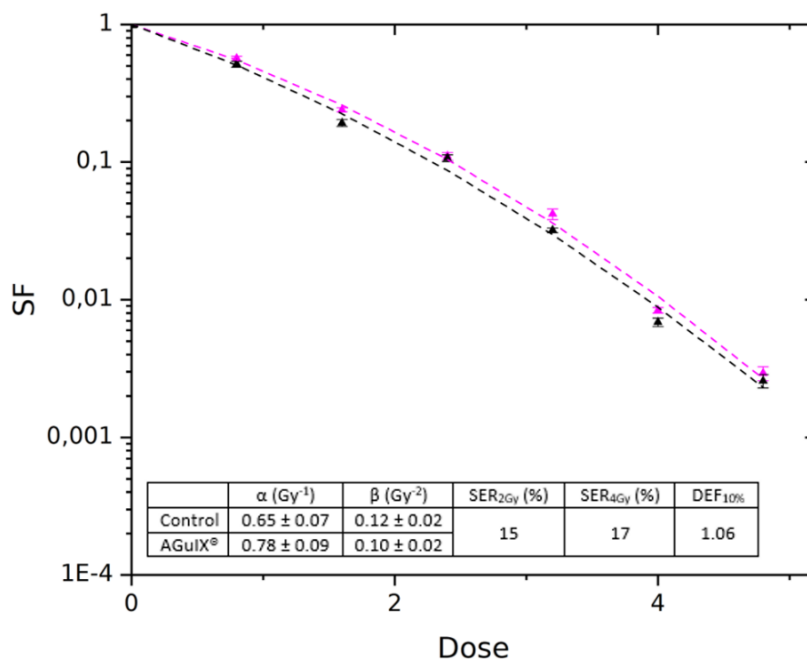


Figure 6.1 - Survival curves obtained after irradiation of cells in 3D-CCM treated by 290 MeV C⁶⁺ with (black) or without (pink) AGuIX® NPs (incubation of 3D-CCM at 0.5 mmol/L for 18h)

Based on this proof of concept on 3D model and in line with the promising preclinical and clinical results obtained in France with AGuIX® NPs (biodistribution, toxicity, pharmacokinetics), in vivo experiments on xenografts mice had to be carried out. This work was the subject of a JSPS Grant (Summer Program 2020), cancelled due to COVID crisis.

3. Published papers



Article

Fluorescent Radiosensitizing Gold Nanoparticles

Gloria Jiménez Sánchez ¹, Pauline Maury ², Lenka Stefancikova ², Océane Champion ³,
Gautier Laurent ¹ , Alicia Chateau ⁴, Farhan Bouraleh Hoch ¹, Frédéric Boschetti ⁵,
Franck Denat ⁶ , Sophie Pinel ⁴, Jérôme Devy ³ , Erika Porcel ² , Sandrine Lacombe ² ,
Rana Bazzi ¹ and Stéphane Roux ^{1,*}

¹ Institut Univers, Temps-fréquence, Interfaces, Nanostructures, Atmosphère et environnement, Molécules (UTINAM), UMR 6213 CNRS-UBFC, Université Bourgogne Franche-Comté, 25030 Besançon CEDEX, France; gloria.jimenez.sanch@gmail.com (G.J.S.); gautier.laurent0@gmail.com (G.L.); youyin_08@hotmail.com (F.B.H.); rana.bazzi@univ-fcomte.fr (R.B.)

² Institut des Sciences Moléculaires d'Orsay, UMR 8214 CNRS-UPS, Université Paris-Sud, 91405 Orsay CEDEX, France; pauline.maury@u-psud.fr (P.M.); llanayau@gmail.com (L.S.); erika.porcel@u-psud.fr (E.P.); sandrine.lacombe@u-psud.fr (S.L.)

³ Matrice Extracellulaire et Dynamique Cellulaire, MEDyC, UMR 7369 CNRS-URCA, Université de Reims Champagne-Ardenne, 51687 Reims CEDEX 2, France; Oceane.Campion@mrsolutions.com (O.C.); jerome.devy@univ-reims.fr (J.D.)

⁴ Centre de Recherche en Automatique de Nancy, Département Biologie, Signaux et Systèmes en Cancérologie et Neurosciences, UMR 7039 CNRS-UL, Université de Lorraine, 54505 Vandœuvre-lès-Nancy, France; alicia.chateau@univ-lorraine.fr (A.C.); sophie.pinel@univ-lorraine.fr (S.P.)

⁵ CheMatech, 21000 Dijon, France; fboschetti@chematech-mdt.com

⁶ Institut de Chimie Moléculaire de l'Université de Bourgogne (ICMUB), UMR 6302 CNRS-UBFC, Université Bourgogne Franche-Comté, 21078 Dijon CEDEX, France; franck.denat@u-bourgogne.fr

* Correspondence: stephane.roux@univ-fcomte.fr; Tel.: +33-381-666-299

Received: 31 August 2019; Accepted: 16 September 2019; Published: 18 September 2019



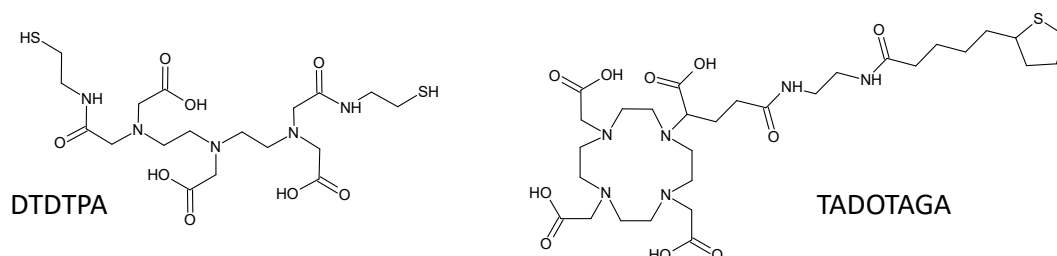
Abstract: Ultrasmall polyaminocarboxylate-coated gold nanoparticles (NPs), Au@DTDTPA and Au@TADOTAGA, that have been recently developed exhibit a promising potential for image-guided radiotherapy. In order to render the radiosensitizing effect of these gold nanoparticles even more efficient, the study of their localization in cells is required to better understand the relation between the radiosensitizing properties of the agents and their localization in cells and in tumors. To achieve this goal, post-functionalization of Au@DTDTPA nanoparticles by near-infrared (NIR) organic dyes (aminated derivative of cyanine 5, Cy5-NH₂) was performed. The immobilization of organic Cy5-NH₂ dyes onto the gold nanoparticles confers to these radiosensitizers fluorescence properties which can be exploited for monitoring their internalization in cancerous cells, for determining their localization in cells by fluorescence microscopy (a common and powerful imaging tool in biology), and for following up on their accumulation in tumors after intravenous injection.

Keywords: gold nanoparticles; radiosensitization; fluorescence imaging

1. Introduction

Among the numerous biomedical applications with gold nanoparticles (NPs) under consideration, the use as radiosensitizing agents for image-guided radiotherapy appears very promising, in particular in the case of ultrasmall gold nanoparticles (core diameter <3 nm) [1–6]. Radiotherapy, which is one of the three main treatments of cancer (applied alone or in combination with surgery and/or chemotherapy), consists of the eradication of cancerous cells using ionizing radiation (X- or γ -ray). Although it is commonly applied to treat a large range of cancers, radiotherapy is limited by a lack of selectivity that results from a behavior of normal and cancerous cells that is too similar when

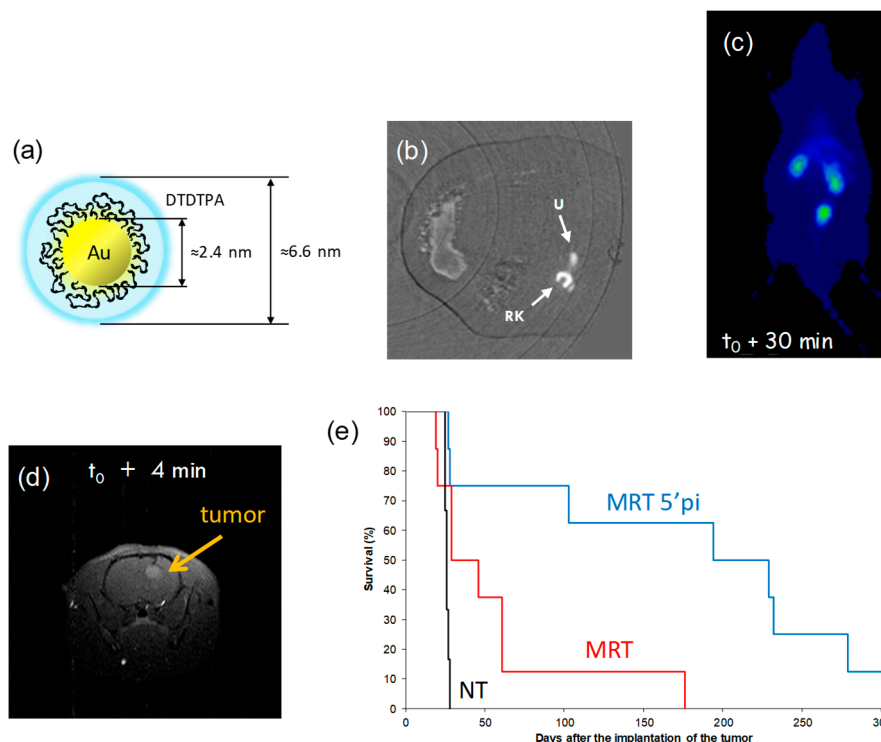
they are exposed to ionizing radiation. The chemical composition of normal and cancerous cells is too close to generate a difference in the X-ray absorption. In order to improve selectivity of the radiotherapy to be used, and therefore its efficacy, it has been proposed to exploit the local dose-enhancement induced by the interaction between nanoparticles containing elements with a high atomic number (Z) and the X-ray photons [1–6]. Nanoparticles are more suited than molecules because the biodistribution of nanoparticles is better controlled and each nanoparticle contains a larger amount of high- Z elements than molecules do ($10\text{--}10^6$ vs. <10) [7–14]. As a result, the accumulation of the radiosensitizing nanoparticles in the tumor should favor the absorption of the ionizing radiation in a solid tumor. Such a preferential absorption will induce a cascade of physical and chemical reactions, which leads to a localized production of highly reactive species (radicals) [7,9]. The latter can generate lethal damage to cells. Such a strategy has been recently proven to be efficient for inhibiting tumor growth and sparing surrounding healthy tissues when irradiation was performed after the administration of gold-, platinum-, gadolinium-, or bismuth-based nanoparticles [4–6,10,11,15–21]. McMahon et al. demonstrated that ultrasmall gold nanoparticles are more efficient than large nanoparticles for enhancing the dose effect [7]. This conclusion is very interesting since nanoparticles with a hydrodynamic diameter of <10 nm can be removed from the body by renal clearance, which is a prerequisite to the in vivo application of non-biodegradable nanoparticles (such as gold nanoparticles) [22,23]. Besides the radiosensitizing effect, the ability to absorb X-ray photons can be exploited for monitoring the accumulation of the nanoparticles and therefore guiding the therapy [1–3]. The most opportune moment for inducing the irradiation can indeed be determined on the basis of data collected by X-ray imaging. However, X-ray imaging is probably not the most appropriate imaging modality for guiding radiotherapy owing to its low sensitivity and ionizing character. In order to overcome the limitations of X-ray imaging, gadolinium, indium, or technetium chelate-coated gold nanoparticles (Au@DTDTPA and Au@TADOTAGA) have been developed [24–30]. These nanoparticles are composed of an ultrasmall gold core (2 to 3 nm) encapsulated in a shell of linear (DTDTPA) or macrocyclic (TADOTAGA) polyaminocarboxylate ligands (Scheme 1).



Scheme 1. General structures of dithiolated derivative of diethylenetriaminepentaacetic acid (DTDTPA) and 1,4,7,10-tetraazacyclododecane-1-glutaric acid-4,7,10-triacetic acid functionalized by thioctic acid (TADOTAGA).

These ligands are dithiolated derivatives of diethylenetriaminepentaacetic acid (DTPA) and 1,4,7,10-tetraazacyclododecane-1,4,7,10-tetraacetic acid (DOTA) chelators that are well known for their ability to form highly stable complexes with gadolinium and indium ions [31]. As a result, Au@DTDTPA and Au@TADOTAGA nanoparticles behave as positive contrast agents for magnetic resonance imaging (MRI) and as radiotracers for nuclear imaging (planar scintigraphy and single-photon emission computed tomography (SPECT)) when they are labeled by gadolinium and technetium ions, respectively (Scheme 2) [25–29]. The data collected from SPECT (highly sensitive) and MRI (high spatial resolution) showed that these nanoparticles freely circulate after intravenous injection (i.e., no accumulation in healthy tissue) and are relatively quickly cleared renally and that a small fraction of them is temporary retained in the solid tumor [28,29]. On the basis of the images, a temporal window for the radiotherapeutic treatment was determined for an optimal exploitation of the radiosensitizing effect of the gold nanoparticles present in the solid tumor. When rats bearing a 9L gliosarcoma (9LGS,

a brain tumor) in the right hemisphere of the brain are irradiated 5–10 min after intravenous injection of Au@DTDTPA(Gd) or Au@TADOTAGA(Gd), the life span of these diseased animals is increased by a factor 5 in comparison to non-treated animals and by a factor 2 in comparison to animals treated only by radiotherapy (Scheme 2) [28,29].



Scheme 2. Illustration of Au@DTDTPA nanoparticles, properties, and applications. (a) Schematic representation of Au@DTDTPA nanoparticles. Behavior of Au@DTDTPA nanoparticles after intravenous injection into rats without a tumor (b,c) and with 9L gliosarcoma in the brain (d) as (b) contrast agent for X-ray imaging, (c) radiotracer for scintigraphy (after immobilization of ^{99m}Tc ions in the organic DTDTPA shell), (d) positive contrast agent for MRI (after immobilization of gadolinium ions in the organic DTDTPA shell), and (e) efficient radiosensitizer for improving the survival of 9L gliosarcoma-bearing rats (tumor in the right hemisphere of the brain). NT, no treatment (no nanoparticle, no irradiation); MRT, only radiotherapy; MRT 5'pi, radiotherapy 5 min after intravenous injection of Au@DTDTPA(Gd) nanoparticles.

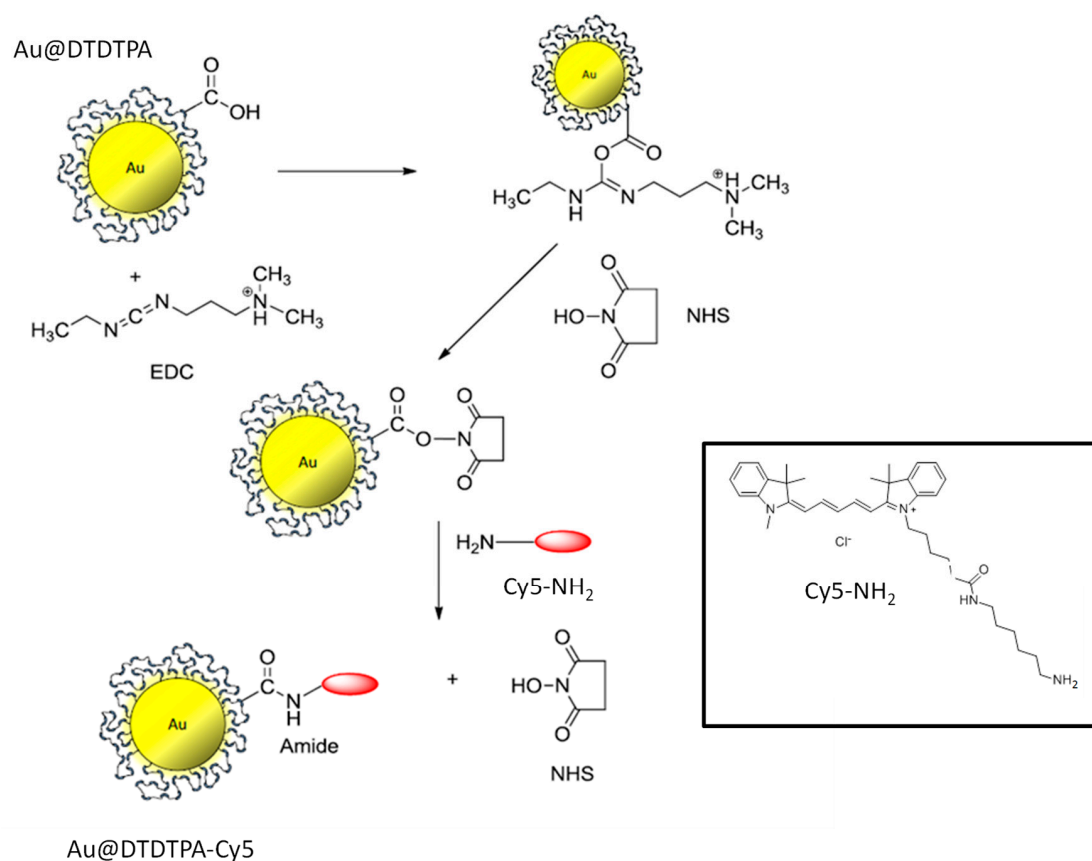
Although X-ray imaging, MRI, and SPECT are powerful imaging modalities which provide complementary meaningful information on the distribution of these gold nanoparticles *in vivo*, they are not suited for cell imaging. However, an improvement of the radiosensitizing efficiency of Au@DTDTPA nanoparticles requires a better comprehension of the impact of gold nanoparticles on cells when treated by radiation. This implies collecting information on the localization of the nanoparticles in the cells. This can be achieved by using fluorescence imaging. In this perspective, the functionalization of Au@DTDTPA nanoparticles by the aminated derivative of cyanine-5 (Cy5-NH₂), which is a near-infrared (NIR) organic dye, is a crucial issue since the immobilization of fluorescent molecules onto gold nanoparticles will allow a visualization by fluorescence microscopy (a common and efficient technique for imaging cells) and also *in vivo* follow-up by fluorescence imaging (a powerful tool for preclinical studies) [32].

In this manuscript, we report on the modification of the radiosensitizing gold nanoparticles (Au@DTDTPA) with aminated NIR organic dyes (Cy5-NH₂) and on their follow-up both in cells and in a living organism by fluorescence imaging.

2. Results and Discussion

2.1. Synthesis of Fluorescent Gold Nanoparticles

Since each DTDTPA contains three carboxylic acid groups, the latter can be used as a grafting site for the covalent immobilization of the aminated derivative of Cy5 (Cy5-NH₂). The functionalization of Au@DTDTPA nanoparticles by Cy5-NH₂ was therefore based on the formation of amide bonds, which results from the condensation between carboxylic acid and amine functions (Scheme 3).



Scheme 3. Functionalization of Au@DTDTPA with Cy5-NH₂.

This reaction performed in aqueous media was promoted by *N*-(3-Dimethylaminopropyl)-*N'*-ethylcarbodiimide (EDC) and *N*-hydroxysuccinimide (NHS) [33]. After purification of the colloid by dialysis against an acid aqueous solution, transmission electron microscopy (TEM) experiments show that the reaction with Cy5-NH₂ does not induce, as expected, any change in the morphology and core diameter of the Au@DTDTPA nanoparticles (Figure 1).

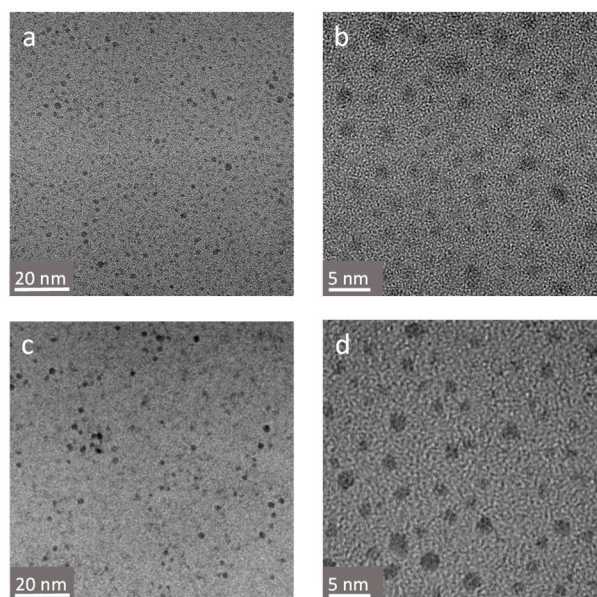


Figure 1. Transmission electron micrographs at different magnifications of (a,b) Au@DTDTPA and (c,d) Au@DTDTPA-Cy5 nanoparticles.

Before and after the reaction, the core diameter was in the range of 2 to 3 nm. Despite the variation of pH imposed by the NHS ester chemistry (pH 5 for the activation step of COOH moieties and pH 7.5 for the grafting of Cy5-NH₂), no agglomeration was observed. Such a behavior confirms the great colloidal stability of Au@DTDTPA nanoparticles for pH >3, which is mainly ensured by the electrostatic repulsion between charged nanoparticles. Au@DTDTPA nanoparticles exhibit a global positive charge for pH <3 and are negatively charged for pH >3 as reflected by the evolution of zeta potential as a function of pH (Figure 2). The pH dependent-charge of Au@DTDTPA nanoparticles can be explained by the nature of DTDTPA ligands anchored onto the gold core. DTDTPA is a polyaminocarboxylate derivative bearing three carboxylic acid (COOH/COO⁻) and three tertiary amine (R₁R₂R₃NH⁺/R₁R₂R₃N) groups. At low pH, the global positive charge of Au@DTDTPA nanoparticles stems from the predominance of protonated groups (COOH and R₁R₂R₃NH⁺), whereas the negative charge of Au@DTDTPA nanoparticles observed for pH >3 is the consequence of the release of protons from the COOH and R₁R₂R₃NH⁺ groups which yields COO⁻ and R₁R₂R₃N. After reaction with Cy5-NH₂, the evolution of zeta potential as a function of pH is similar to the one observed for non-functionalized Au@DTDTPA nanoparticles (Figure 2). However, the point of zero charge (pzc) is shifted to higher pH after the grafting reaction (from 2.3 to 4, Figure 2).

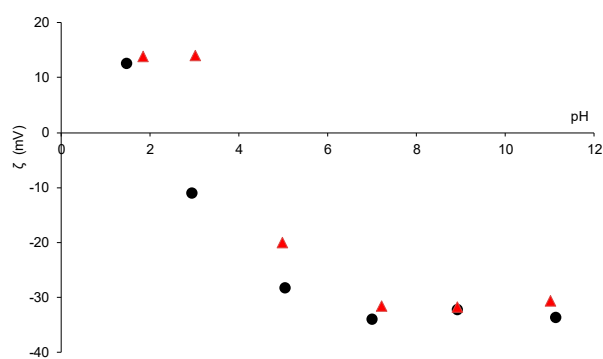


Figure 2. Zeta potential of Au@DTDTPA (black circles) and Au@DTDTPA-Cy5 (red triangles) as a function of pH.

This shift can be attributed to the grafting of the NIR organic dyes which provide additional positive charges to the nanoparticles (Scheme 3). Despite the pzc shift, the great colloidal stability of Au@DTDTPA nanoparticles is preserved after the reaction with Cy5-NH₂ in a large range around the physiological pH as reflected by the strongly negative values of zeta potential for pH >5. Another difference is revealed by UV-visible and luminescence spectra (Figures 3 and 4). UV-visible spectra provide useful information on the size, the polydispersity, and the colloidal stability of gold nanoparticles. Gold nanoparticles with a core size larger than 5 nm are characterized by a strong absorption band assigned to the plasmon resonance phenomenon [34].

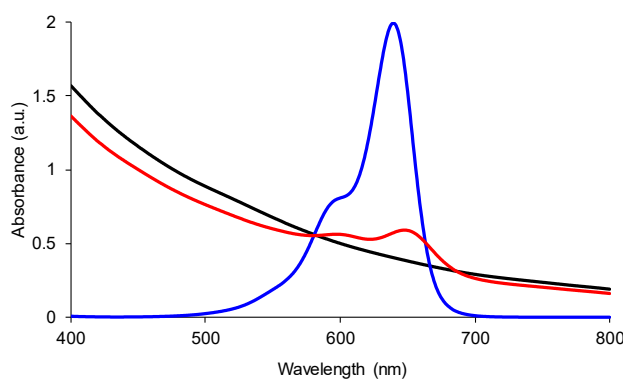


Figure 3. UV-visible spectra of aqueous suspensions containing Au@DTDTPA (black curve) and Au@DTDTPA-Cy5 (red curve) and of aqueous solution of Cy5-NH₂ (blue curve).

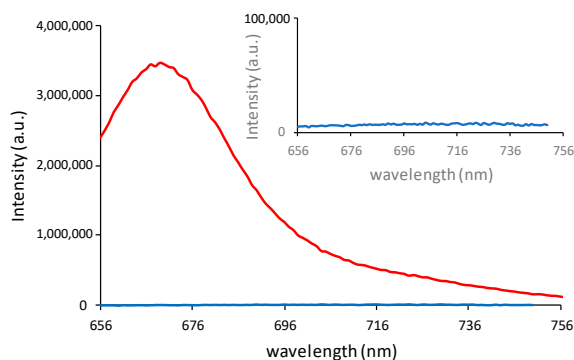


Figure 4. Emission spectra of aqueous suspensions containing Au@DTDTPA (blue curve) and Au@DTDTPA-Cy5 (red curve) ($\lambda_{exc} = 646$ nm). Inset: emission spectrum of the aqueous suspension containing Au@DTDTPA.

The position and the shape of the plasmon band depend on the size, the morphology, and the environment of the nanoparticles. However, this band is not observed for the Au@DTDTPA nanoparticles whose absorption spectra display a decrease of absorbance with a slight shoulder between 500 and 550 nm (Figure 3). The shape of the absorbance curve of Au@DTDTPA nanoparticles is characteristic of gold nanoparticles with core size <5 nm and confirms the data of TEM experiments [35–37]. The plasmon band is also not present in the absorption spectrum of Au@DTDTPA-Cy5, but two bands centered at 602 nm and 648 nm appear (Figure 3). In comparison to the UV-visible spectrum of Cy5, these bands can be attributed to the presence of Cy5 on the gold nanoparticles. It must be pointed out that a slight shift is observed when Cy5 is grafted onto the gold core (≈ 10 nm). As expected, the functionalization of Au@DTDTPA nanoparticles by Cy5-NH₂ renders the gold colloid fluorescent. After excitation at 646 nm, the photoluminescence spectrum displays an emission band centered at 669 nm (658 nm for free Cy5-NH₂), which is not visible on the spectrum of gold nanoparticles before the reaction (Figure 4).

The immobilization of Cy5 onto Au@DTDTPA nanoparticles is accompanied by a decrease in fluorescence lifetime (from 1.2 ns to 1.0 ns). When grafted to the gold nanoparticles, the fluorescence lifetime of Cy5 remains constant and different to the one of free Cy5 for at least 48 h. Such a difference indicates that there is no release of the organic dyes from Au@DTDTPA nanoparticles.

2.2. Internalization of the Au@DTDTPA-Cy5 Nanoparticles Monitored by Fluorescence Imaging

Owing to their small size (core diameter between 2 and 3 nm), the internalization of non-labeled Au@DTDTPA nanoparticles (i.e., without modification with organic dyes) is not easy to monitor with optical microscopy. High-angle annular dark-field scanning transmission electron microscopy (HAADF-STEM) was therefore used to characterize the intracellular localization of non-labeled Au@DTDTPA in U87 MG cells with high resolution (<10 nm). This technique uses the high atomic number of gold ($Z = 79$) to its advantage, compared with the elements from organic matter (H, C, N, O, P, S). Indeed, the images result from the electrons that cross the sample and are scattered at angles depending on the Z -numbers of the target atoms. Because the electrons are detected with an annular detector placed at variable height, the collection angle is set so that the contrast between elements of different Z is the maximum. To see the gold nanoparticles (Au@DTDTPA), a high-angle annular detector was used to obtain the signal of this high- Z element (white in the images). Several images were done in different cells and a signal corresponding to Au@DTDTPA was found in them, always in the cytoplasm. Images of U87 MG cells loaded with non-labeled Au@DTDTPA nanoparticles are shown in Figure 5. In the circle of Figure 5A, we can see a bright white zone in the cytoplasm of the cell, corresponding to the presence of the high- Z element. The zooms presented in Figure 5B,C show that this signal comes from small (<10 nm) high- Z particles located together in the cytoplasm. Their size determined from the HAADF-STEM images is slightly larger than the size of Au@DTDTPA nanoparticles measured from the TEM ones (about 5 nm in diameter vs. 2 or 3 nm) (Figure 5D). The difference (which remains moderate) can be explained by the lack of clarity at high magnification in HAADF-STEM images; this renders the measurements less accurate.

The fluorescence of the gold nanoparticles conferred by the grafting of the organic dyes allows monitoring their internalization in cells using less sophisticated means. After the incubation of glioblastoma cells (U87 MG) with Au@DTDTPA-Cy5, the superimposition of optical transmission and fluorescence images clearly reveals the presence of nanoparticles within the cytoplasm (Figure 6).

Although these gold nanoparticles exhibit a very reduced size, no fluorescence is detected in the nucleus. The presence of gold nanoparticles was confirmed by inductively coupled plasma-optical emission spectrometry (ICP-OES) analysis (Figure 7). Whatever the cells, the internalization increases with the incubation time. However, the amount of internalized gold nanoparticles and the impact of the functionalization of the gold nanoparticles by Cy5-NH₂ depend on the nature of the cells. The amount of gold nanoparticles and the impact of the functionalization on the internalization are lower in the case of HeLa cells than in the case of U87 MG cells. Even in the latter case, the impact of the functionalization on the internalization remains relatively low (<30%).

To better localize the NP action sites within the cell, colocalization studies of NPs and organelles were performed. In particular, the colocalization with mitochondria was measured using a fluorescent tracker (MitoTracker Green) having no spectral overlap with Cy5-labeled gold nanoparticles. Figure 8 shows a cell containing trackers (green) and Au@DTDTPA-Cy5 nanoparticles (red) after 6 h of incubation with the fluorescent gold nanoparticles.

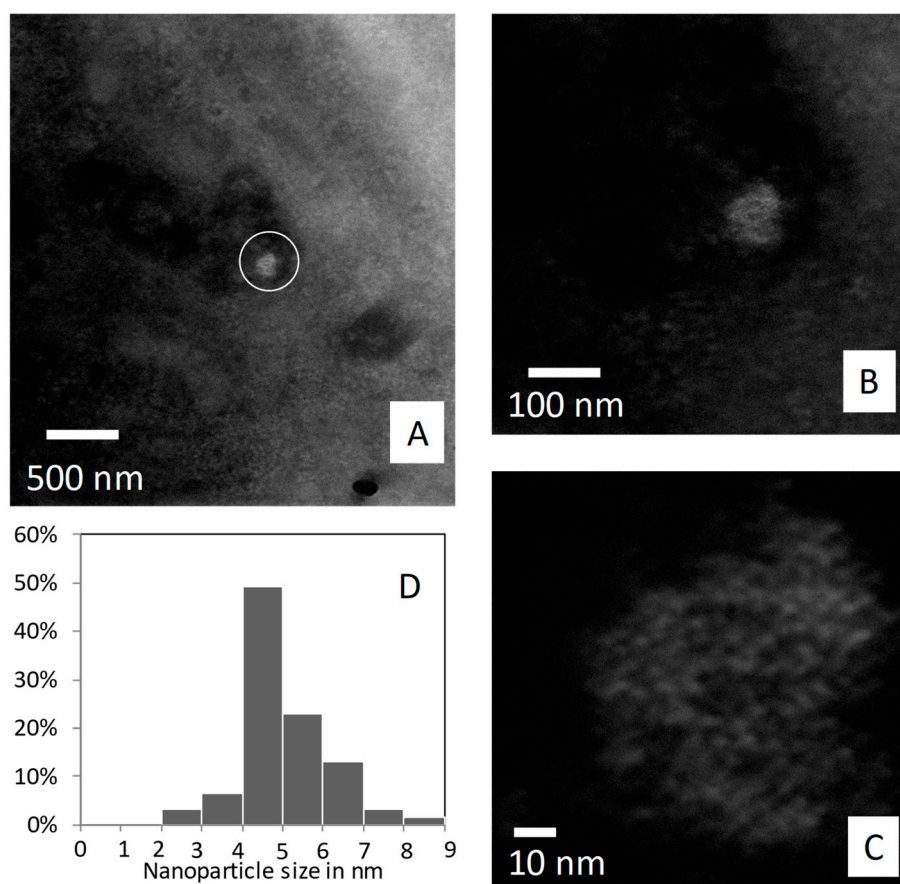


Figure 5. High-angle annular dark-field scanning transmission electron microscopy (HAADF-STEM) images. (A) Overall view of U87 MG cells containing Au@DTDTPA. The circle indicates a bright object containing atoms with a high atomic number that correspond to Au@DTDTPA. (B,C) High resolution images of the area in the circle of image A. (D) Size distribution of the bright object in the area in the circle of image A.

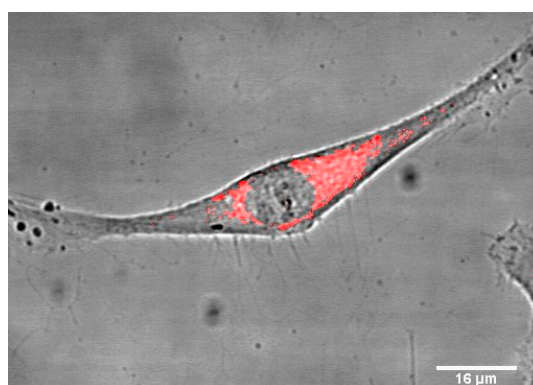


Figure 6. Confocal microscopy image of a glioblastoma cell (U87 MG) after 6 h of incubation with Au@DTDTPA-Cy5 nanoparticles (red), $[Au]_{incubation} = 5 \times 10^{-4} \text{ mol. L}^{-1}$.

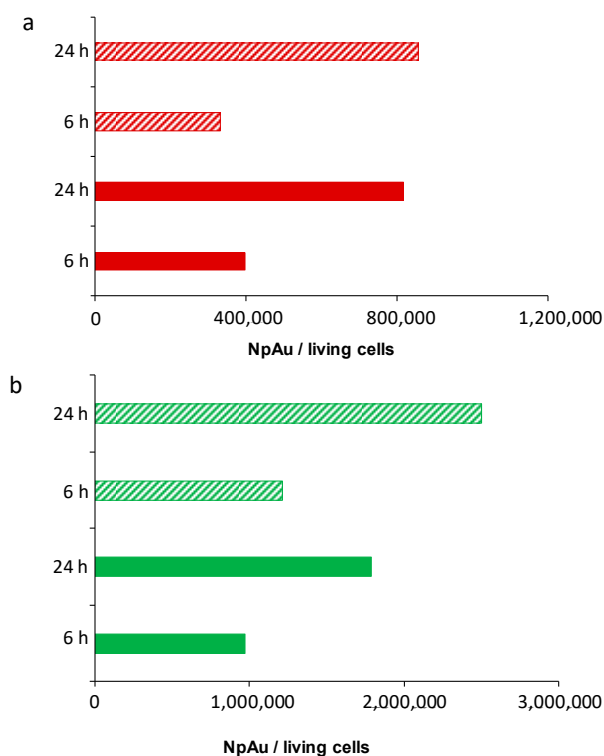


Figure 7. Inductively coupled plasma-optical emission spectrometry (ICP-OES) analyses of (a) HeLa and (b) U87 MG cells incubated with Au@DTDTPA (filled bars) and Au@DTDTPA-Cy5 (dashed bars) nanoparticles for 6 and 24 h.

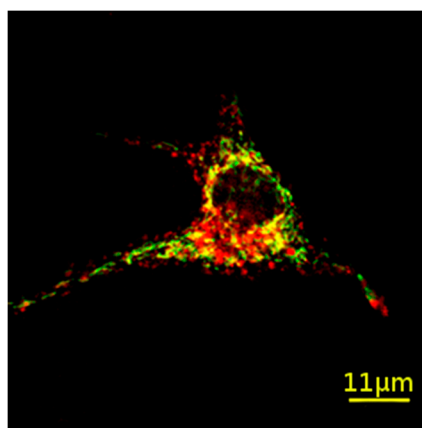


Figure 8. Fluorescence image obtained by confocal microscopy of U87 MG cell loaded with Au@DTDTPA-Cy5 nanoparticles (red) in the presence of MitoTracker Green (green). Yellow reflects the colocalization of fluorescent gold nanoparticles and mitochondria.

In addition to green and red zones, large yellow zones that correspond to regions where red and green are both present can be observed (Figure 8). The apparition of yellow-colored zones reflects therefore the colocalization of gold nanoparticles and mitochondria. The presence of radiosensitizing nanoparticles in the vicinity of the mitochondria is an unexpected but very interesting result that may explain the ability of these ultrasmall gold nanoparticles to improve the efficiency of radiotherapy.

Fluorescence imaging is not restricted to the observation of cells. This imaging modality is also a powerful preclinical tool since it can be applied for monitoring the diffusion of fluorescent nanoparticles *in vitro* in 3D cell culture and their biodistribution in animal models after intravenous injection [38,39]. Confocal microscopic images of U87 MG cells spheroid sections confirmed that Au@DTDTPA-Cy5

nanoparticles are able to reach the center of 800 μm diameter spheroids, highlighting the good diffusion abilities for these nanoparticles. In parallel, when the spheroids were dissociated to provide a single-cell suspension, a Cy5 fluorescence signal was observed in the cytoplasm of U87 MG cells, thus confirming the cellular uptake of Au@DTDTPA-Cy5 nanoparticles (Figure 9).

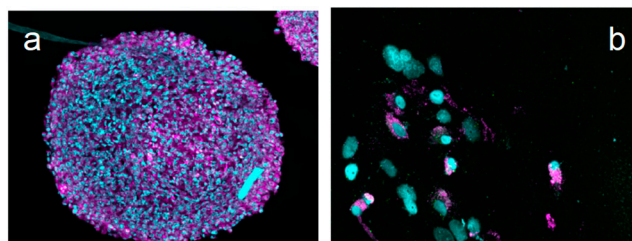


Figure 9. (a) Fluorescence imaging of a U87 MG cells spheroid section after 24 h exposure with Au@DTDTPA-Cy5 nanoparticles. (b) Fluorescence imaging of U87 MG single cells obtained after spheroid dissociation. Pink fluorescent signal corresponding to Cy5 was found in the cytoplasm, while cell nuclei were labeled with Hoechst 33342 (blue fluorescent signal).

2.3. In Vivo Fluorescence Imaging

Furthermore, the post-functionalization of Au@DTDTPA by aminated Cy-5 NIR dyes open the door to their in vivo follow-up by fluorescence imaging. The image acquired 30 min after intravenous injection of the fluorescent Au@DTDTPA-Cy5 nanoparticles clearly shows a preferential accumulation in the tumor which appears highly fluorescent in comparison to the rest of the body (Figure 10). Ex vivo organ imaging shows an accumulation of Au@DTDTPA-Cy5 nanoparticles in kidneys and in the tumor, whereas no signal was detected in the heart or spleen. This preliminary in vivo fluorescence imaging study confirms, despite the surface modification, the safe behavior of these gold nanoparticles which was previously revealed by MRI and SPECT [27,28]. These nanoparticles are indeed characterized by a preferential accumulation in the tumor and also by renal clearance.

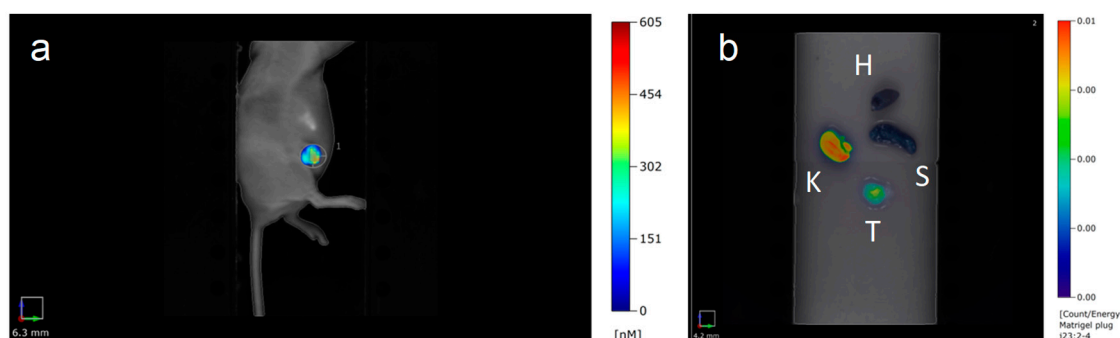


Figure 10. (a) Fluorescence imaging of a tumor-bearing mouse laid on its left flank after intravenous injection of Au@DTDTPA-Cy5 nanoparticles. (b) Fluorescence imaging of ex vivo organs (heart (H), kidney (K), spleen (S), and tumor (T)) after intravenous injection of Au@DTDTPA-Cy5 nanoparticles.

3. Materials and Methods

3.1. Au@DTDTPA Synthesis

The synthesis, based on the Brust method [40], consists of reducing a gold salt ($\text{HAuCl}_4 \cdot 3\text{H}_2\text{O}$) with NaBH_4 in the presence of thiols (stabilizers) that, by adsorption on growing particles, ensures control of the size and the colloidal stability. In this case, the chelator consists of a dithiolated derivative of diethylenetriaminepentaacetic acid (DTPA), named DTDTPA. The synthesis and characterization of the DTDTPA ligand has been described earlier [24,25].

Tetrachloroauric acid trihydrate ($\text{HAuCl}_4 \cdot 3\text{H}_2\text{O}$), sodium borohydride (NaBH_4), acetic acid (CH_3COOH), hydrochloric acid, sodium hydroxide (NaOH), methanol, and other organic solvents (reagent grade) were purchased from Aldrich (Sigma-Aldrich Chemie S.a.r.l., Saint-Quentin Fallavier, France).

For a typical preparation of gold nanoparticles, $\text{HAuCl}_4 \cdot 3\text{H}_2\text{O}$ (200 mg, 51×10^{-5} mol) was placed in a 250 mL round-bottom flask and dissolved with methanol (60 mL). In another flask, DTDTPA (256 mg, 50×10^{-5} mol), water (40 mL), and acetic acid (2 mL) were mixed. This solution containing DTDTPA was added to the gold salt solution under stirring. The mixture turned from yellow to orange. NaBH_4 (195 mg, 515×10^{-5} mole) dissolved in water (13.2 mL) was added to the gold-DTDTPA solution under stirring at room temperature. At the beginning of the NaBH_4 addition, the solution first became dark brown then a black flocculate appeared. The vigorous stirring was maintained for 1 h before adding aqueous hydrochloric acid solution (2 mL, 1 M). After the partial removal of the solvent under reduced pressure, the precipitate was retained on the polymer membrane and washed thoroughly and successively with 0.1 M hydrochloric acid, water, and acetone. The resulting black powder was dried (up to 200 mg of dry powder of Au@DTDTPA) and dispersed in aqueous solution of sodium hydroxide (NaOH 0.01 M) to have a final concentration of 50 mM in gold.

3.2. Functionalization of Au@DTDTPA by NIR Organic Dye Cyanine-5-Amine (Cy5-NH_2)

The preparation of the fluorescent-labelled nanoparticles (Au@DTDTPA-Cy5) was achieved by grafting near-infrared (NIR) organic dye (cyanine 5 derivative) onto the organic shell (DTDTPA) of the gold nanoparticles. Since the DTDTPA shell is rich in $-\text{COOH}$ groups, aminated Cy5 (Cy5-NH_2) was chosen for the functionalization of the gold nanoparticles. The condensation between $-\text{COOH}$ groups of Au@DTDTPA nanoparticles and $-\text{NH}_2$ of Cy5-NH_2 , which is promoted by EDC and NHS, yields amide function.

A solution of Au@DTDTPA (9 mL, 50 mM in gold) was adjusted to pH 5. For the activation of the carboxylic groups, EDC (397 mg) and NHS (477 mg) in deionized water (6.48 mL) were added to the colloid under stirring at room temperature. The agitation was maintained for 90 min. Afterward, the pH of the solution was adjusted to pH 7.5 and Cy5-NH_2 (4 mg) was added to the aqueous suspension of Au@DTDTPA nanoparticles. The solution was stirred for 15 min at room temperature and for 12 h at 4 °C.

After the reaction with Cy5-NH_2 , the nanoparticles were purified by dialysis against acidic medium (pH 5, molecular weight cut-off (MWCO): 6 kDa). The dialysis bath was changed four times (6, 20, 26, and 40 h after the immersion of the dialysis tube in the acid aqueous solution) until it became colorless. After the purification by dialysis, the gold nanoparticles were concentrated by centrifugation using centrifugal concentrators (Vivaspin[®], MWCO: 10 kDa) until a gold concentration of 50 mM.

3.3. Transmission Electron Microscopy

The size of the gold core was obtained from transmission electron microscopy (TEM) performed with a JEOL 2010 FEG microscope at 200 kV (INSA, Lyon, France) and a JEOL JEM 2100F microscope at 200 kV (ICB, Dijon, France). Drops of colloidal solutions were deposited on dedicated TEM carbon grids and observed after natural drying at room temperature. The treatment of the images and the determination of the size of the gold cores were achieved using Gatan DigitalMicrograph[™] software (3.10.01 for Gatan Microscopy Suite 1.5.1, Gatan, Pleasanton, CA, USA).

3.4. Measurements of ζ -Potential

The ζ -potential of the Au@DTDTPA and the Au@DTDTPA-Cy5 nanoparticles was directly determined using a Nanosizer ZS equipped with a He-Ne (633 nm) laser from Malvern Instruments at the Qualio Laboratory (Besançon, France). The colloids were diluted to obtain a concentration of 1 mM in gold (0.2 g Au/L), containing 0.01 M in NaCl and adjusted to the desired pH by the addition of NaOH or HCl 1 M.

3.5. Fluorescence Spectrometry

Fluorescence experiments were performed with a Fluorolog FL3-22 spectrometer (HORIBA Jobin Yvon, Kyoto, Japan) using Instrument Control CT software (2.2.13, Keysight Technologies, Santa Rosa, CA, USA), connected with the unit Spectra CQ. The wavelength of excitation was fixed at 646 nm and the scan was performed from 656 to 800 nm. The solutions were previously diluted to obtain a final concentration of 0.2 g Au/L and were analyzed in a standard quartz cuvette.

3.6. UV-Visible Spectrophotometry

UV-visible absorption spectra were recorded at room temperature using a SPECORD 210 (Analytic Jena, Jena, Germany) and WinASPECT software (2.2.0.0, Analytic Jena, Jena, Germany). The samples were previously diluted to a final concentration of 0.2 g Au/L and were analyzed in a standard quartz cuvette. The scan was performed from 400 to 800 nm.

3.7. Inductively Coupled Plasma-Optical Emission Spectrometry (ICP-OES)

The samples were mineralized in ultrapure aqua regia to a final concentration of at least 20 µg/L in gold. An ICP-OES (710 ES Varian/Agilent, Santa Clara, CA, USA) with axial torch with a concentric nebulizer and cyclonic spray chamber was used. The parameters fixed during measurement were as follows: power of 1.2 kW with argon auxiliary of 1.5 L/min and nebulizer pressure of 200 kPa. The emission lines used to measure the gold concentration were 267.594 nm, 242.794 nm, and 208.207 nm. The efficacy of the atomization is about 60% for gold. An ionizing buffer was employed for the measurements. The limit of detection of this technique is 20 µg/L.

3.8. Centrifugation

A Fisher Bioblock Scientific 2-16P centrifuge (Illkirch, France) with a rotor 1251 was employed for concentrating gold nanoparticles suspension after purification (dialysis). The colloids were placed in the upper compartment of Vivaspin[®] flasks equipped with a membrane (MWCO: 5 or 10 kDa). The centrifugations were performed at 238× g (1500 rpm).

3.9. Cell Culture

The HeLa cells (derived from cervical adenocarcinoma) and U87 MG cells (derived from glioblastoma) were purchased from ATCC France Office (Molsheim, France). They were cultivated in Dulbecco's Modified Eagle Medium (DMEM) (Life Technologies, Carlsbad, CA, USA) supplemented with 10% heat-inactivated fetal bovine serum (Sigma Aldrich, Saint-Louis, MO, USA), 100 U/mL penicillin (Sigma Aldrich, Saint-Louis, MO, USA), 100 µg/mL streptomycin (Sigma Aldrich, Saint-Louis, MO, USA), and 1% nonessential amino acids (Life Technologies, Carlsbad, CA, USA). Cells were maintained in a 5% CO₂ incubator (Heracell[®], ThermoFischer, Langenselbold, Germany) at 37 °C.

To favor the formation of spheroids, U87 MG single cells were seeded at 4×10^4 cells/mL in T75 culture dishes, with a hydrophobic poly(2-hydroxyethyl methacrylate) coating that prevents cell adhesion onto the bottom of the flask. Four days after seeding, the spheroids were transferred into a spinner (Dutscher, Brumath, France) and kept in culture for growing for at least ten days after seeding.

At the time of the experiments, U87 MG cells spheroids were incubated with 5×10^{-3} M Au@DTDTPA-Cy5 nanoparticles in 6-well plates for 24 h. The spheroids were rinsed twice with Hank's Balanced Salt Solution (HBSS) after exposure to nanoparticles. Then, half of the spheroids were embedded into Tissue-Tek[®] O.C.T. compound (Sakura[®] Finetek, Staufeu im Breisgau, Germany) and frozen in isopentane/ liquid nitrogen to prevent ice crystal formation. Fifty-micrometer cryostat sections were prepared, then fixed with formaldehyde 3.7%.

For the other half of the spheroids, enzymatic plus mechanical dissociation was performed using trypsin-EDTA 0.05% and a 21-gauge syringe needle to obtain a single-cell suspension without aggregates. Isolated cells were plated onto glass slides using cytocentrifugation. All slides (with

spheroid sections or isolated cells) were then stained with Hoechst 33342, before observation with a confocal microscope.

3.10. High-Angle Annular Dark-Field Scanning Transmission Electron Microscopy (HAADF-STEM)

U87 cells were plated on glass coverslips. While attached, they were incubated with 1 mmol/L of Au@DTDTPA for 1 h. The cells were then rinsed with PBS 1× and fixed in the mixture of 2.5 % glutaraldehyde and 4% paraformaldehyde in PBS 1×. After rinsing the cells with PBS 1× and distilled H₂O, they were dehydrated using ethanol in gradient concentrations until 100%. Next, the samples were embedded in resin step by step using a mixture of ethanol with increasing concentrations of Epon resin until 100%. After resin polymerization at 65 °C, the samples were cut using an ultramicrotome into 150 nm thick slices deposited on copper grids. The observation was performed on the microscopy platform IBiSA at the Institut Curie, Orsay, France with a Jeol 2200FS FEG electron microscope operating at 200 kV, using the 1nm probe and a camera length of 6 cm. ImageJ software (1.52a, National Institutes of Health, USA) (<https://imagej.nih.gov/ij/>, last accessed on: 23 April 2018) enabled a statistical analysis of internalized particles.

3.11. Confocal Microscopy

Confocal microscopy experiments were performed with a LEICA SP5 confocal system located at the Centre de Photonique Bio-Médical (CPBM), University Paris-Sud (Orsay, France) in a controlled chamber. The samples were kept at 37 °C and regulated in CO₂. The U87 MG cells were incubated with 0.5 mM of Au@DTDTPA-Cy5 for 6 h. Cyanine 5 was excited at 633 nm and the fluorescence emission was detected in the 650–750 nm range. The images were processed with the freely available ImageJ software.

For colocalization studies, the U87 MG cells were incubated for 12 h with 200 nM MitoTracker Green (Invitrogen – ThermoFisher Scientific, Waltham, MA USA). The trackers were washed out with PBS 1× before incubation for 6 h with 1 mM of Au@DTDTPA-Cy5. Organic dye was excited at 633 nm and the fluorescence emission was detected in the 650–750 nm range. The MitoTracker Green was excited at 488 nm and the fluorescence emission was detected in the 505–600 nm range. Images were recorded at three different depths (z-axis positions).

3.12. Animal Models

Animal studies were conducted using an approved protocol in accordance with the French ethics committee of Champagne-Ardenne and the French research ministry (APAFIS# 4373_v1). Female athymic BALB/c nu/nu mice were obtained from Charles River Laboratories (Ecully, France) at six weeks of age. Breast cancer MDA-MB-231 was orthotopically injected (5×10^6 cells) into the fourth mammary abdominal gland. Mice followed a special diet with an alfalfa-free diet (Envigo, Gannat, France) to reduce auto-fluorescence. When tumors reached 200 mm³, mice were imaged with FMT 4000 (PerkinElmer, Villebon-sur-Yvette, France).

3.13. In Vivo and Ex Vivo Fluorescence Imaging

For in vivo and ex vivo fluorescence experiments, 100 µL of Au@DTDTPA-Cy5 were injected into the tail vein of anesthetized mice. Mice were imaged in the decubitus lateral position with an FMT 4000 (PerkinElmer, Villebon-sur-Yvette, France) small animal scanner using a 635 nm excitation wavelength and a 650–670 emission filter. Then, 3D trans-illumination acquisitions were performed 30 min post-injection. Images were captured and reconstructed using TrueQuant (v3.1) software (PerkinElmer, Waltham, MA, USA).

4. Conclusions

The presence of DTDTPA at the surface of gold nanoparticles plays a crucial role in the growth control of the metallic core during the reduction of the gold salt by NaBH_4 , in the immobilization of metal ions used for medical imaging (MRI and nuclear imaging), and in the colloidal stability of the nanoparticles. This work demonstrates that DTDTPA ligands also act as grafting sites for post-functionalization with aminated NIR dye owing to the COOH moieties (3 COOH per ligand). The grafting of NIR Cy5-NH₂ dye onto the DTDTPA organic shell confers efficient fluorescence properties to the nanoparticles. This new development in nanoparticle design offers the possibility to monitor internalization and localization in cells by fluorescence microscopy, as well as biodistribution in small animals using fluorescence imaging. Although the internalization of non-labeled Au@DTDTPA nanoparticles can be monitored by HAADF-STEM, the follow-up by fluorescence imaging appears more attractive for at least two main reasons: (i) the fluorescence imaging is characterized by its ease of implementation and (ii) in contrast to HAADF-STEM, fluorescence imaging can be efficiently exploited for *in vivo* study in real time.

The surface modification of Au@DTDTPA nanoparticles by NIR dyes exerts no (or only a little) influence on their behavior in the presence of cells. The uptake (amount of gold nanoparticles in cells) and internalization kinetics are almost the same for HeLa and U87 MG cells than those observed for non-functionalized Au@DTDTPA nanoparticles. However, the fluorescence properties of Au@DTDTPA-Cy5 nanoparticles confer a crucial advantage for monitoring their fate after internalization in cells. The experiments performed with MitoTracker Green reveal the presence of gold nanoparticles in the vicinity of mitochondria. Knowing where the nanoparticles are constitutes a real advantage for exploiting the radiosensitizing effect of gold nanoparticles. In a previous study, we demonstrated that the most crucial factor for an efficient control of tumor growth is the localization of the radiosensitizers (gadolinium-based nanoparticles) rather than their concentration [18].

The post-functionalization of Au@DTDTPA nanoparticles by NIR dyes exerts also no influence on the biodistribution of the nanoparticles since the behavior after intravenous injection into tumor-bearing mice is the same for Au@DTDTPA-Cy5 and Au@DTDTPA [27,28]. The preferential accumulation in the tumor and the renal clearance are preserved after the post-functionalization. Although they rest on paradoxical phenomenon, both characteristics (tumor accumulation and renal clearance) are essential for therapeutic applications and, in peculiar, for radiosensitization [23]. The renal clearance allows the removal of non-biodegradable radiosensitizer excess. The radiosensitization will therefore be restricted to the tumor for better selectivity of the radiotherapy treatment.

In summary, the post-functionalization of Au@DTDTPA with NIR organic fluorophores (aminated Cy-5) opens the perspective of investigating the relationship between sub-cellular localization, *in vivo* biodistribution, and improvement of X-ray performances using these gold nanoparticles, a key step in the design of more efficient nanotheranostic agents.

Author Contributions: Conceptualization, S.P., J.D., E.P., S.L., R.B., and S.R.; methodology, G.J.S., O.C., A.C., E.P., and R.B.; validation, S.P., J.D., S.L., R.B., and S.R.; investigation, G.J.S., P.M., L.S., O.C., G.L., A.C., and F.B.H.; resources, F.B. and F.D.; data curation, E.P., A.C., J.D., and R.B.; writing—original draft preparation, R.B. and S.R.; writing—review and editing, S.P., J.D., S.L., R.B., and S.R.; visualization, G.J.S., P.M., L.S., A.C., and O.C.; supervision, S.L. and S.R.; project administration, S.L. and S.R.; funding acquisition, S.P., S.L., and S.R.

Funding: This work was supported by the “Agence Nationale de la Recherche” (project MULTIMAGE, ANR 2012 RPIB 0010), “Défi Nano” (project Proton, mission interdisciplinaire, CNRS), the European Commission for the financial support of the projects FP7-PEOPLE-2013-IEF 624370 and FP7-PEOPLE-2013-ITN-608163, and the Région Franche-Comté and Région Grand Est (PhD grant for G.J.S. and financial support for the project eNano-RX (Cancéropôle Est)) and the Université Paris Saclay-IRS NanoTheRad.

Acknowledgments: The authors are grateful to Sylvaine Linget who performed ICP-OES analyses (Qualio Laboratory, Besançon, France).

Conflicts of Interest: The authors declare no conflict of interest. The funders had no role in the design of the study; in the collection, analyses, or interpretation of data; in the writing of the manuscript; or in the decision to publish the results.

Abbreviations

Au@DTDTPA	gold nanoparticles coated by linear chelator
Au@DTDTPA-Cy5	gold nanoparticles coated by linear chelator and functionalized with cyanine 5
DTPA	diethylenetriaminepentaacetic acid (linear chelator)
DTDTPA	dithiolated derivative of diethylenetriaminepentaacetic acid
Au@TADOTAGA	gold nanoparticles coated by macrocyclic chelator
DOTA	1,4,7,10-tetraazacyclododecane-1,4,7,10-tetraacetic acid
DOTAGA	1,4,7,10-tetraazacyclododecan-1-glutaric acid-4,7,10-triacetic acid
TADOTAGA	DOTAGA functionalized by thioctic acid
Cy5-NH ₂	aminated derivative of cyanine 5
Z	atomic number
vs.	versus
MRI	magnetic resonance imaging
SPECT	single-photon emission computed-tomography
MRT	microbeam radiation therapy
pi	post-injection
EDC	<i>N</i> -(3-Dimethylaminopropyl)- <i>N</i> '-ethylcarbodiimide
NHS	<i>N</i> -hydroxysuccinimide
MWCO	molecular weight cut-off
TEM	transmission electron microscopy
UV	ultraviolet
ICP-OES	inductively coupled plasma-optical emission spectrometry

References

- Hainfeld, J.F.; Slatkin, D.N.; Smilowitz, H.M. The use of gold nanoparticles to enhance radiotherapy in mice. *Phys. Med. Biol.* **2004**, *49*, N309. [[CrossRef](#)]
- Hainfeld, J.F.; Smilowitz, H.M.; O'Connor, M.J.; Dilmanian, F.A.; Slatkin, D.N. Gold nanoparticle imaging and radiotherapy of brain tumors in mice. *Nanomedicine* **2013**, *8*, 1601–1609. [[CrossRef](#)]
- Schuemann, J.; Berbeco, R.; Chithrani, D.B.; Cho, S.H.; Kumar, R.; McMahan, S.J.; Sridhar, S.; Krishnan, S. Roadmap to clinical use of gold nanoparticles for radiation sensitization. *Int. J. Radiat. Oncol. Biol. Phys.* **2016**, *94*, 189–205. [[CrossRef](#)]
- Haume, K.; Rosa, S.; Grellet, S.; Śmiałek, M.A.; Butterworth, K.T.; Solov'yov, A.V.; Prise, K.M.; Golding, J.; Mason, N.J. Gold nanoparticles for cancer radiotherapy: A review. *Cancer Nano* **2016**, *7*, 8. [[CrossRef](#)]
- Rosa, S.; Connolly, C.; Schettino, G.; Butterworth, K.T.; Prise, K.M. Biological mechanisms of gold nanoparticle radiosensitization. *Cancer Nano* **2017**, *8*, 2. [[CrossRef](#)]
- Kuncic, Z.; Lacombe, S. Nanoparticle radio-enhancement: Principles, progress and application to cancer treatment. *Phys. Med. Biol.* **2018**, *63*, 02TR01. [[CrossRef](#)]
- McMahon, S.J.; Hyland, W.B.; Muir, M.F.; Coulter, J.A.; Jain, S.; Butterworth, K.T.; Schettino, G.; Dickson, G.R.; Hounsell, A.R.; O'Sullivan, J.M.; et al. Biological consequences of nanoscale energy deposition near irradiated heavy atom nanoparticles. *Sci. Rep.* **2011**, *1*, 18. [[CrossRef](#)]
- Kobayashi, K.; Usami, N.; Porcel, E.; Lacombe, S.; Le Sech, C. Enhancement of radiation effect by heavy elements. *Mutat. Res.* **2010**, *704*, 123–131. [[CrossRef](#)]
- Butterworth, K.T.; McMahon, S.J.; Currell, F.J.; Prise, K.M. Physical basis and biological mechanisms of gold nanoparticle radiosensitization. *Nanoscale* **2012**, *4*, 4830–4838. [[CrossRef](#)]
- Retif, P.; Pinel, S.; Toussaint, M.; Frochot, C.; Chouikrat, R.; Bastogne, T.; Barberi-Heyob, M. Nanoparticles for radiation therapy enhancement: The key parameters. *Theranostics* **2015**, *5*, 1030–1044. [[CrossRef](#)]
- Liu, Y.; Zhang, P.; Li, F.; Jin, X.; Li, J.; Chen, W.; Li, Q. Metal-based nanoenhancers for future radiotherapy: Radiosensitizing and synergistic effects on tumor cells. *Theranostics* **2018**, *8*, 1824–1849. [[CrossRef](#)]
- Scheinberg, D.A.; Villa, C.H.; Escorcía, F.E.; McDevitt, M.R. Conscripts of the infinite armada: Systemic cancer therapy using nanomaterials. *Nat. Rev. Clin. Oncol.* **2010**, *7*, 266–276. [[CrossRef](#)]
- Min, Y.; Caster, J.M.; Eblan, M.J.; Wang, A.Z. Clinical translation of nanomedicine. *Chem. Rev.* **2015**, *115*, 11147–11190. [[CrossRef](#)]

14. Kunjachan, S.; Ehling, J.; Storm, G.; Kiessling, F.; Lammers, T. Noninvasive imaging of nanomedicines and nanotheranostics: Principles, progress, and prospects. *Chem. Rev.* **2015**, *115*, 10907–10937. [[CrossRef](#)]
15. Dou, Y.; Guo, Y.; Li, X.; Li, X.; Wang, S.; Wang, L.; Lv, G.; Zhang, X.; Wang, H.; Gong, X.; et al. Size-tuning ionization to optimize gold nanoparticles for simultaneous enhanced CT imaging and radiotherapy. *ACS Nano* **2016**, *10*, 2536–2548. [[CrossRef](#)]
16. Porcel, E.; Liehn, S.; Remita, H.; Usami, N.; Kobayashi, K.; Furusawa, Y.; Le Sech, C.; Lacombe, S. Platinum nanoparticles: A promising material for future cancer therapy? *Nanotechnology* **2010**, *21*, 085103. [[CrossRef](#)]
17. Le Duc, G.; Miladi, I.; Alric, C.; Mowat, P.; Bräuer-Krisch, E.; Bouchet, A.; Khalil, E.; Billotey, C.; Janier, M.; Lux, F.; et al. Toward an image-guided microbeam radiation therapy using gadolinium-based nanoparticles. *ACS Nano* **2011**, *5*, 9566–9574. [[CrossRef](#)]
18. Dufort, S.; Le Duc, G.; Salomé, M.; Bentivegna, V.; Sancey, L.; Bräuer-Krisch, E.; Requardt, H.; Lux, F.; Coll, J.-L.; Perriat, P.; et al. The high radiosensitizing efficiency of a trace of gadolinium-based nanoparticles in tumors. *Sci. Rep.* **2016**, *6*, 29678. [[CrossRef](#)]
19. Lux, F.; Mignot, A.; Mowat, P.; Louis, C.; Dufort, S.; Bernhard, C.; Denat, F.; Boschetti, F.; Brunet, C.; Antoine, R.; et al. Ultrasmall rigid particles as multimodal probes for medical applications. *Angew. Chem. Int. Ed.* **2011**, *50*, 12299–12303. [[CrossRef](#)]
20. Alqathanni, M.; Blencowe, A.; Geso, M.; Ibbott, G. Quantitative 3D Determination of Radiosensitization by Bismuth-Based Nanoparticles. *J. Biomed. Nanotechnol.* **2016**, *12*, 464–471. [[CrossRef](#)]
21. Detappe, A.; Thomas, E.; Tibbitt, M.W.; Kunjachan, S.; Zavidij, O.; Parnandi, N.; Reznichenko, E.; Lux, F.; Tillement, O.; Berbeco, R. Ultrasmall silica-based bismuth gadolinium nanoparticles for dual magnetic resonance–computed tomography image guided radiation therapy. *Nano Lett.* **2017**, *17*, 1733–1740. [[CrossRef](#)]
22. Soo Choi, H.; Liu, W.; Misra, P.; Tanaka, E.; Zimmer, J.P.; Ito, B.; Bawendi, M.G.; Frangioni, J.V. Renal clearance of quantum dots. *Nat. Biotechnol.* **2007**, *25*, 1165–1170. [[CrossRef](#)]
23. Yu, M.; Zheng, J. Clearance pathways and tumor targeting of imaging nanoparticles. *ACS Nano* **2015**, *9*, 6655–6674. [[CrossRef](#)]
24. Debouttière, P.-J.; Roux, S.; Vocanson, F.; Billotey, C.; Beuf, O.; Favre-Réguillon, A.; Lin, Y.; Pellet-Rostaing, S.; Lamartine, R.; Perriat, P.; et al. Design of gold nanoparticles for magnetic resonance imaging. *Adv. Funct. Mater.* **2006**, *16*, 2330–2339. [[CrossRef](#)]
25. Alric, C.; Taleb, J.; Le Duc, G.; Mandon, C.; Billotey, C.; Le Meur-Herland, A.; Brochard, T.; Vocanson, F.; Janier, M.; Perriat, P.; et al. Gadolinium chelate coated gold nanoparticles as contrast agents for both X-ray computed tomography and magnetic resonance imaging. *J. Am. Chem. Soc.* **2008**, *130*, 5908–5915. [[CrossRef](#)]
26. Arifin, D.R.; Long, C.M.; Gilad, A.A.; Alric, C.; Roux, S.; Tillement, O.; Link, T.W.; Arepally, A.; Bulte, J.W.M. Trimodal gadolinium-gold microcapsules containing pancreatic islet cells restore normoglycemia in diabetic mice and can be tracked by using US, CT, and positive-contrast MR imaging. *Radiology* **2011**, *260*, 790–798. [[CrossRef](#)]
27. Alric, C.; Miladi, I.; Kryza, D.; Taleb, J.; Lux, F.; Bazzi, R.; Billotey, C.; Janier, M.; Perriat, P.; Roux, S.; et al. The biodistribution of gold nanoparticles designed for renal clearance. *Nanoscale* **2013**, *5*, 5930–5939. [[CrossRef](#)]
28. Miladi, I.; Alric, C.; Dufort, S.; Mowat, P.; Dutour, A.; Mandon, C.; Laurent, G.; Bräuer-Krisch, E.; Herath, N.; Coll, J.-L.; et al. The in vivo radiosensitizing effect of gold nanoparticles based MRI contrast agents. *Small* **2014**, *10*, 1116–1124. [[CrossRef](#)]
29. Laurent, G.; Bernhard, C.; Dufort, S.; Jiménez Sánchez, G.; Bazzi, R.; Boschetti, F.; Moreau, M.; Vu, T.H.; Collin, B.; Oudot, A.; et al. Minor changes in the macrocyclic ligands but major consequences on the efficiency of gold nanoparticles designed for radiosensitization. *Nanoscale* **2016**, *8*, 12054–12065. [[CrossRef](#)]
30. Butterworth, K.T.; Nicol, J.R.; Ghita, M.; Rosa, S.; Chaudhary, P.; McGarry, C.K.; McCarthy, H.O.; Jiménez Sánchez, G.; Bazzi, R.; Roux, S.; et al. Preclinical evaluation of gold-DTDTPA nanoparticles as theranostic agents in prostate cancer radiotherapy. *Nanomedicine* **2016**, *11*, 2035–2047. [[CrossRef](#)]
31. Caravan, P.; Ellison, J.J.; McMurry, T.J.; Lauffer, R.B. Gadolinium(III) chelates as MRI contrast agents: structure, dynamics, and applications. *Chem. Rev.* **1999**, *99*, 2293–2352. [[CrossRef](#)]
32. Miyawaki, A. Visualization of the spatial and temporal dynamics of intracellular signaling. *Dev. Cell* **2003**, *4*, 295–305. [[CrossRef](#)]
33. Hermanson, G.T. *Bioconjugate Techniques*, 2nd ed.; Academic Press: London, UK, 2008.
34. Ghosh, S.K.; Pal, T. Interparticle coupling effect on the surface plasmon resonance of gold nanoparticles: from theory to applications. *Chem. Rev.* **2007**, *107*, 4797–4862. [[CrossRef](#)]

35. Chen, S.; Kimura, K. Synthesis and characterization of carboxylate-modified gold nanoparticle powders dispersible in water. *Langmuir* **1999**, *15*, 1075–1082. [[CrossRef](#)]
36. Wu, Z.; Jin, R. On the Ligand's Role in the Fluorescence of Gold Nanoclusters. *Nano Lett.* **2010**, *10*, 2568–2573. [[CrossRef](#)]
37. Duff, D.G.; Baiker, A.; Edwards, P.P. A new hydrosol of gold clusters. *J. Chem. Soc. Chem. Commun.* **1993**, 96–98. [[CrossRef](#)]
38. Faure, A.-C.; Dufort, S.; Josserand, V.; Perriat, P.; Coll, J.-L.; Roux, S.; Tillement, O. Control of the in vivo Biodistribution of Hybrid Nanoparticles with Different Poly(ethylene glycol) Coatings. *Small* **2009**, *5*, 2565–2575. [[CrossRef](#)]
39. Kobayashi, H.; Ogawa, M.; Alford, R.; Choyke, P.L.; Urano, Y. New strategies for fluorescent probe design in medical diagnostic imaging. *Chem. Rev.* **2010**, *110*, 2620–2640. [[CrossRef](#)]
40. Brust, M.; Fink, J.; Bethell, D.; Schiffrin, D.J.; Kiely, C. Synthesis and reactions of functionalised gold nanoparticles. *J. Chem. Soc. Chem. Commun.* **1995**, 1655–1656. [[CrossRef](#)]



© 2019 by the authors. Licensee MDPI, Basel, Switzerland. This article is an open access article distributed under the terms and conditions of the Creative Commons Attribution (CC BY) license (<http://creativecommons.org/licenses/by/4.0/>).

Comprendre et améliorer les effets cliniques de la hadronthérapie

Résumé L'utilisation des faisceaux de particules chargées a amélioré à la fois la sélectivité et l'efficacité des traitements de radiothérapie. Ceux-ci permettent de réduire les toxicités induites dans les organes sensibles, et d'autre part d'augmenter le contrôle local des tumeurs, notamment au niveau des tumeurs radiorésistantes. De meilleures connaissances des effets du transfert d'énergie linéique (TEL), principalement au niveau du pic de Bragg, et de la radiolyse de l'eau ont fait progresser cette méthode de traitement. Cependant, de nombreux verrous scientifiques et techniques doivent encore être levés pour aller vers des traitements de hadronthérapie plus personnalisés. Par exemple, l'efficacité thérapeutique peut encore être améliorée en associant l'utilisation de nanoparticules métalliques à celle de rayonnements de TEL élevé. Les domaines de recherche concernés vont de la physique des particules et la chimie fondamentale jusqu'aux essais cliniques, impliquant différentes communautés de chercheurs à l'international.

Mots-clés Hadronthérapie, radiolyse de l'eau, rayonnement ionisant, électron, proton, particule alpha, ions lourds accélérés, pic de Bragg, nanoparticules.

Abstract Understanding and improving the clinical effects of hadrontherapy

Charged particles beams allowed to improve targeting and effectiveness of radiotherapy treatments. On the one hand, it reduces toxicities induced in the sensitive organs. On the other hand, it increases local control, in particular of radioresistant cancers. Better knowledge of the effects of linear energy transfer (LET), particularly at the Bragg peak, and of water radiolysis have advanced this treatment method. However, many scientific and technical obstacles still need to be resolved to move towards personalized particle therapy (hadrontherapy) treatments. For example, the effectiveness of treatments can be further improved by associating nanoparticles with elevated LET radiations. The current research ranges from particles physics and fundamental chemistry to clinical trials involving different research teams worldwide.

Keywords Water radiolysis, ionizing radiation, electrons, proton, alpha rays, swift heavy ions, Bragg peak, nanoparticles.

Vers la personnalisation

L'effet des rayonnements, autres que les photons de haute énergie X ou γ , sur la matière vivante a éveillé la curiosité scientifique très tôt après la découverte, il y a plus d'un siècle, de la radioactivité et de ses effets [1]. Ainsi, lorsque la matière vivante est la cible d'une particule alpha, elle subit visiblement des dégâts plus délétères que ceux occasionnés par une irradiation γ [2-4]. Les êtres vivants étant composés au minimum de 70 % d'eau, la recherche s'est naturellement orientée vers l'étude des effets des différents types de particules énergétiques sur l'eau, c'est-à-dire sur les effets du transfert d'énergie linéique (TEL, voir encadré 1). Par définition, le TEL caractérise l'énergie cédée à la matière par unité de longueur. La radiolyse de l'eau, processus physico-chimique dont les recombinaisons primaires comme celle de deux radicaux hydroxyle HO[•] en H₂O₂ s'effectuent en moins d'une μ s, est notamment caractérisée par des rendements radiolytiques différents lorsque l'on utilise des ions lourds à la place de photons X ou γ [5-6]. Les molécules biologiques telles que les protéines, l'ADN, les membranes, ainsi que les processus biochimiques sont susceptibles d'être affectés par ces rayonnements. Les interactions peuvent être directes si les particules passent à proximité de celles-ci, ou indirectes lorsque les espèces radicalaires produites par la radiolyse de l'eau réagissent avec ces molécules [7].

Les molécules biologiques endommagées vont modifier transitoirement le métabolisme cellulaire normal, conduisant soit à une réparation fidèle des dégâts, soit à une mutation ou à la mort. Les espèces radicalaires de l'oxygène (ERO, en

Encadré 1

Le transfert d'énergie linéique

Le transfert d'énergie linéique (TEL), autrement appelé pouvoir d'arrêt, est le paramètre qui décrit l'évolution de l'énergie E cédée au milieu traversé sur une épaisseur x par une particule énergétique*. Cette énergie cédée augmente sur le parcours de la particule au cours des collisions élastiques ou inélastiques ou par effet électrostatique. Le matériau se retrouve alors soit excité électroniquement, soit ionisé. Le TEL (= -dE/dx) régit donc le dépôt de la dose au sein de la matière traversée, le long de l'axe de propagation de la particule ionisante ; il est exprimé en eV/nm ou en keV/ μ m. Le TEL peut être calculé à partir de la relation de Bethe-Bloch [46]. Les photons X et γ , même énergétiques, sont absorbés par la matière selon une loi exponentielle régie par le processus d'absorption d'énergie. Ces particules ne sont pas arrêtées par la matière, mais absorbées. Cette nuance fait qu'on ne parlera pas de TEL pour les photons ; il concerne uniquement les particules chargées comme les électrons, les protons, les hélions et plus généralement les ions lourds, autrement appelés en physique des particules, les « hadrons », constitués de protons et de neutrons. Les neutrons énergétiques interagissent directement avec les noyaux atomiques ; on parlera alors de TEL nucléaire et cela n'affecte pas directement les ionisations, c'est-à-dire les états électroniques du matériau.

*On parle ici d'énergie très supérieure à l'énergie d'ionisation du matériau ; souvent les particules issues de fission d'isotopes radioactifs ont des énergies comprises entre quelques keV et des MeV.

anglais ROS) produites peuvent perturber la cellule en engendrant un stress oxydant pouvant également mener à la mort cellulaire.

Tableau I - Quelques exemples de particules ionisantes ayant différentes origines (naturelle ou artificielle), des énergies variées, et avec pour conséquences des parcours différents dans l'eau et des utilisations ou effets très divers.

Type de particules	Origine de production	Énergie maximale (MeV)	TEL moyen dans l'eau (keV/μm)	Parcours (m)	Utilisation/Impact
Électron (e ⁻)	Tritium (³ H)	0,018	2,6	5,5 x 10 ⁻⁶	Marquage moléculaire
	Soufre (³⁵ S)	0,167	0,5	320 x 10 ⁻⁶	
	Accélérateur linéaire	22	0,2	2 x 10 ⁻²	Radiothérapie (tumeurs superficielles, protocole flash)
Protons (H ⁺)	Van de Graff	3	21	140 x 10 ⁻⁶	Activation / Analyse
	Cyclotron	30	3,5	8,5 x 10 ⁻³	
	Cyclotron	200	0,3	20 x 10 ⁻²	Protonthérapie (pic de Bragg)
Alpha (α / ⁴ He ²⁺)	²¹⁰ Po	5,3	136	38,9 x 10 ⁻⁶	Alpha immunothérapie
	Van de Graff	3	180	17 x 10 ⁻⁶	Activation / Analyse
	Cyclotron	10	92	110 x 10 ⁻⁶	
Ions carbone (¹² C ⁶⁺)	Cyclotrons	< 1000	30	5-10 x 10 ⁻³	Hadronthérapie (pic de Bragg)
⁷ Li, noyau de recul	¹⁰ B + n → ⁷ Li + α	2,31	300	5-9 x 10 ⁻⁶	Thérapie par capture de neutron par le bore (BNCT)
Cocktail de particules (incluant e ⁻ et H ⁺ à ions lourds)	Rayonnement cosmique	> 100	-	> 10 ⁻²	Interaction avec spationaute
	Interaction laser de haute intensité/matière	10-200	-	> 10 ⁻³	Radiolyse à très haute résolution temporelle ou à débit de dose extrême

La hadronthérapie est une technique de traitement du cancer qui repose sur l'utilisation de faisceaux de particules chargées, comme les protons et les ions carbone. Pour appliquer ces rayonnements de TEL élevé à la radiothérapie, où l'objectif est d'éliminer les cellules tumorales à un stade où elles sont encore localisées, le médecin doit mettre en œuvre une stratégie qui tient compte de multiples paramètres. Ceux-ci sont liés à la cible mais aussi au rayonnement utilisé, choisi en fonction des faisceaux disponibles dans chaque centre de radiothérapie. La proximité d'organes sensibles, les mouvements respiratoires et cardiaques, la faible oxygénation dans le volume tumoral à traiter (appelée hypoxie) ainsi que la radiorésistance due au métabolisme de certains types de tumeur sont autant de paramètres critiques dont on peut maintenant tenir compte. En utilisant un faisceau de particules bien maîtrisé dans l'espace, dans le temps ainsi qu'en énergie, il sera techniquement possible de bénéficier des apports de l'effet FLASH [8]. Ces irradiations à très haut débit de dose permettent de délivrer la dose 600 à 2 000 fois plus rapidement qu'avec les irradiateurs actuels, ce qui a pour conséquence de limiter les effets secondaires aux tissus sains [9]. Tous ces paramètres concourent à rendre la radiothérapie plus personnalisée et plus prometteuse.

Nous allons décrire ici les caractéristiques des faisceaux de particules de TEL élevé, les rendements radiolytiques des entités produites et les conditions dans lesquelles ils sont utilisés en hadronthérapie. Enfin, nous présenterons la possibilité d'amplifier encore leurs effets, notamment par l'addition de nanoparticules métalliques dans la tumeur. Puis nous ferons le point sur les défis à relever pour personnaliser la hadronthérapie du futur.

Structure des dépôts d'énergie dans l'eau liquide

Les rayonnements nucléaires énergétiques – c'est-à-dire dépassant généralement le keV et souvent le MeV – peuvent ioniser les matériaux comme l'eau. Ces rayonnements peuvent être issus de radioéléments, naturels ou artificiels, dont on connaît l'activité mais que l'on ne peut pas déclencher, seulement *a minima* contrôler. De plus, la chimie de ces radioisotopes peut rendre complexe la compréhension des mécanismes sous rayonnement [10]. Avec les accélérateurs de particules mis au point par les ingénieurs au cours du XX^e siècle, la chimie sous rayonnement a progressé très vite en permettant aux chercheurs d'analyser uniquement l'effet de la particule sur la matière [11]. Le *tableau I* donne quelques exemples de ces particules, de leur énergie et de la façon dont elles peuvent être produites et utilisées. La valeur moyenne du TEL est également reportée. Celui-ci caractérise notamment la densité des ionisations des molécules rencontrées. Ainsi, dans chaque μm³ d'eau traversé, les concentrations de H₂O⁺ évoluent localement le long de l'axe de propagation de la particule.

Ceci reflète la variation du TEL le long de la trace [12] : plus le TEL est élevé, plus cette concentration est grande. Ainsi, à TEL élevé, la variation de concentration initiale de H₂O⁺ (dès le dépôt d'énergie effectué en quelques 10⁻¹⁶ s) rend le système réactionnel très hétérogène. A contrario, à TEL faible (pour des électrons de 10 MeV par exemple), les molécules ionisées sont réparties rapidement, en 10⁻⁶ s, et de façon homogène. Nous verrons que cela a des répercussions importantes sur le devenir du processus de radiolyse.

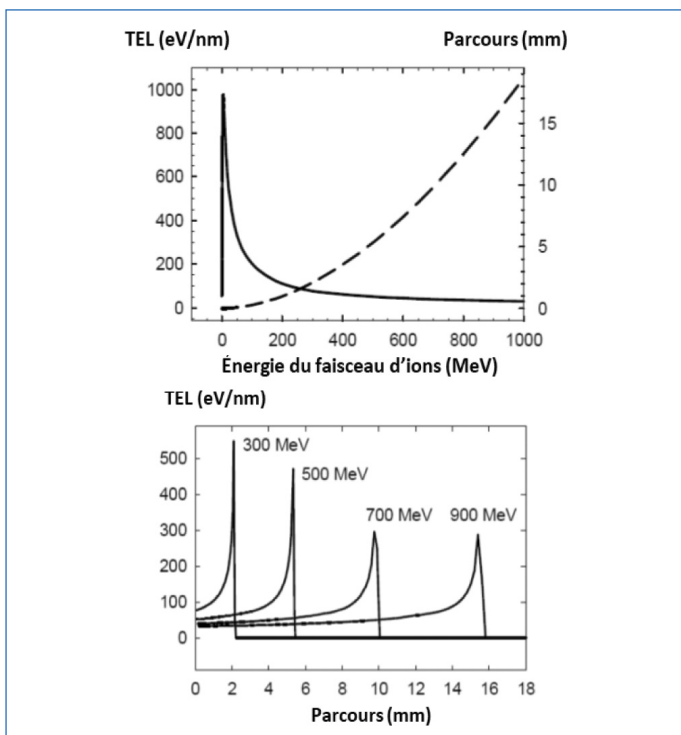


Figure 1 - Simulation des dépôts d'énergie des ions carbone C^{6+} d'énergie variée et leur parcours dans l'eau. La courbe en tirets est liée au parcours, alors que les courbes pleines donnent la variation du TEL [13].

Les fins de traces des ions accélérés et pic de Bragg

En traversant la matière, les particules chargées perdent leur énergie cinétique par collisions successives avec les molécules du milieu qu'elles rencontrent. En ralentissant, ces particules cèdent de plus en plus d'énergie et, arrivées à la toute fin de leur parcours, l'ultime dépôt d'énergie est exacerbé : c'est le pic de Bragg. La *figure 1* montre ce phénomène bien connu et qui peut être reproduit par le calcul en utilisant la formule de Bethe-Bloch (*encadré 1* p. 76).

Comme les particules chargées sont freinées jusqu'à l'arrêt, la valeur de leur TEL est maximale au pic de Bragg. La littérature donne généralement la valeur moyenne du TEL le long du parcours, comme on peut le constater dans le *tableau I* [10]. Bien connaître les processus chimiques de radiolyse en jeu en fonction d'une valeur de TEL permettrait de tirer une loi décrivant les concentrations des espèces chimiques en fonction du TEL local, c'est-à-dire pour un point de la courbe de pénétration de la particule et non plus seulement en fonction du TEL moyen. Cependant, les concentrations locales des espèces chimiques produites le long du parcours de la

particule ionisante doivent être mesurées à des temps courts, avant qu'elles n'aient eu le temps de trop diffuser et de réagir. Cela suppose donc une technique d'analyse résolue spatialement et temporellement. Les résolutions nécessaires seraient alors le micromètre pour la dimension spatiale, et la nano-seconde pour la dimension temporelle [14]. On pourrait ainsi distinguer les effets chimiques au pic de Bragg. Ceci est essentiel pour des protons de haute énergie (200 MeV, *tableau I*) qui possèdent des TEL moyens comparables à ceux des électrons ou des photons γ , montrant notamment que la valeur du TEL moyen n'est pas représentative des effets chimiques observés ou recherchés au pic de Bragg [15]. La description des effets du TEL sur le parcours d'une particule demeure donc un défi de taille. Les expériences qui pourraient y être associées nécessitent d'une part des particules de plusieurs centaines de MeV d'énergie pour avoir des parcours suffisants afin de réaliser une détection le long de la trace d'ionisation, et d'autre part générées sous forme d'impulsion très brèves (ns). Il existe quelques essais de rapprochement entre les effets chimiques et les valeurs de TEL, calculées sur des parcours très courts, mais en nombre encore insuffisants pour en tirer une loi [15].

Rendements radiolytiques des produits formés par radiolyse à TEL élevé

Les paramètres représentant les effets chimiques sont les rendements radiolytiques primaires des espèces formées ou recombinées, exprimés en molécule par 100 eV d'énergie déposée (le système international donne une unité : mole J^{-1}) [10]. Ces paramètres sont largement décrits dans la littérature, notamment pour la radiolyse γ de l'eau, « à TEL faible », et leur détermination est rappelée dans ce numéro dans l'article de F. Wang *et coll.* (voir p. 23). Des valeurs de ces rendements sont reportées dans le *tableau II*. Pour les TEL faibles, la distribution spatiale des espèces chimiques devient homogène en quelques dizaines de nanoseconde (10^{-9} s) par agitation thermique (mouvement brownien) après l'interaction physique des particules avec l'eau. Comme la densité d'ionisation initiale est faible (i.e. TEL faible), les espèces chimiques (radicaux et molécules) interagissent peu pendant leur diffusion et par conséquent, les rendements évoluent peu jusqu'aux valeurs des rendements primaires. Il est possible de définir pour les TEL plus élevés qui produisent initialement des densités d'ionisation très fortes, des rendements radiolytiques primaires différentiels sur le parcours de la particule ionisante. Il n'existe que trop peu de mesures de ces rendements différentiels [16]. Il serait pourtant fort utile de les

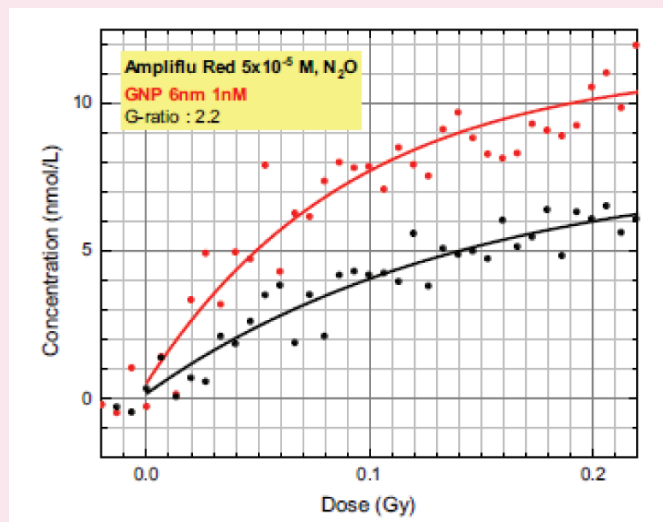
Tableau II - Rendements radiolytiques des espèces issues de la radiolyse de l'eau soumise à deux types de particules, de TEL moyens différents.

	Trace de 1 μ m	Rendements primaires (μ mol/J)						
		H ₂	H ₂ O ₂	HO \cdot	HO ₂ \cdot /O ₂ \cdot^-	e $^-$ _{aq}	H $^+$	H ₃ O $^+$
Trace d'un e $^-$ de TEL = 0,27 eV/nm		0,05	0,07	0,28	~ 0	0,28	0,06	0,28
Trace d'ion lourd accéléré de TEL > 100 eV/nm		> 0,15	> 0,09	< 0,1	~ 0,01	< 0,10	-	< 0,10

Encadré 2

Les méthodes de détermination des rendements radiolytiques primaires et dépendant du temps pour des particules de TEL élevé

Comme pour les TEL faibles, les mesures des rendements radiolytiques se font soit par mesure directe résolue en temps (radiolyse pulsée avec des ions lourds [14], soit par mesure « post mortem » lorsque des molécules stables peuvent être analysées et dosées par des techniques ayant un temps de réponse ou une mise en œuvre plus longue (chromatographie, spectrométrie de masse). En général, ces dernières ont une sensibilité plus poussée mais elles nécessitent soit de connaître le mécanisme chimique ayant conduit à la formation de l'espèce dosée, soit de simplifier le mécanisme chimique en ajoutant des espèces connues pour « capturer » préférentiellement des radicaux. La méthode de capture (en anglais « scavenging ») relie la concentration (C) du capteur au temps (t) de capture par la relation $t = 1/kC$, k étant la constante de vitesse de la réaction de capture. Sa mise en œuvre a permis de mettre en évidence les recombinaisons radicalaires dans les traces d'ionisation [47]. Une fois que l'on peut mesurer la concentration d'une espèce, on peut remonter à son rendement de formation primaire (G) par la relation $C = d \times G$, où d est la dose. La pente à l'origine de la fonction $C = f(d)$ donne le rendement primaire G. Cette détermination est représentée dans la figure [30].



Représentation graphique de la concentration de l'espèce formée Résorufine en fonction de la dose en rayonnement alpha, menant à la détermination du rendement primaire : pente à l'origine.

déterminer, notamment au pic de Bragg (voir encadré 2). La description des effets se résume souvent à l'observation de recombinaisons des radicaux libres qui voient leurs rendements baisser. En contrepartie, on constate une augmentation des rendements de H_2 et H_2O_2 . Le rendement du radical superoxyde HO_2^*/O_2^- s'expliquerait, quant à lui, par la forte densité d'ionisations qui permettrait des multi-ionisations de molécules d'eau [15].

Application à la hadronthérapie

Efficacité balistique

Par rapport à la radiothérapie classique qui utilise des rayons X, cette approche présente d'abord une efficacité balistique [17-18]. Comme illustré en figure 2, pour les photons, la dose maximum, qui correspond à l'énergie déposée en profondeur, est atteinte quelques centimètres après la pénétration du faisceau dans le patient. La dose

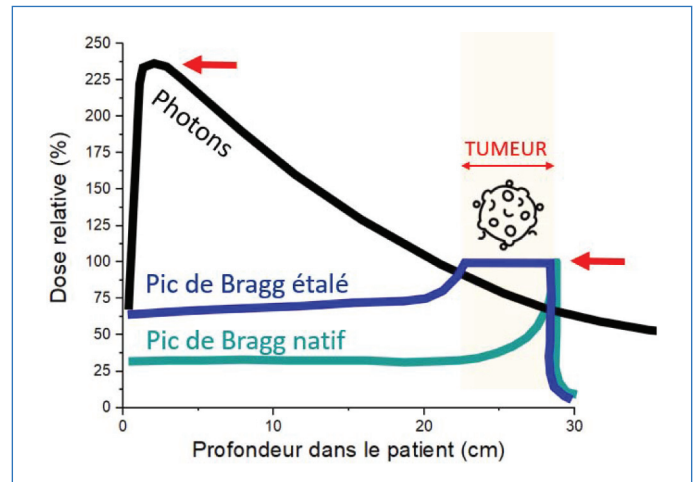


Figure 2 - Dose déposée dans le patient en fonction de la nature du rayonnement (faisceau de photons en noir, faisceau de hadrons natif en vert, faisceau de hadrons étalé en bleu).

déposée dans le patient diminue ensuite progressivement après ce maximum. Ce maximum se trouve bien avant d'atteindre la tumeur pour les tumeurs profondes, ce qui montre que les tissus sains situés en amont de la tumeur sont largement irradiés. D'autre part, le dépôt de dose se poursuit après la tumeur, ce qui fait que les tissus situés derrière reçoivent également une quantité non négligeable de rayonnement. En revanche, le parcours en profondeur des particules de haut TEL dans la matière étant très différent, il permet d'obtenir un traitement qui épouse mieux la forme de la tumeur. D'une part, les faisceaux chargés pénètrent dans le patient pratiquement sans diffusion [19] ; d'autre part, comme introduit précédemment, le dépôt de dose en profondeur est beaucoup plus ciblé et prend la forme du pic de Bragg. En faisant varier l'énergie des particules et donc en superposant successivement ces pics, il est possible d'obtenir un pic de Bragg étalé (appelé SOBPs : « spread out Bragg peak ») afin d'irradier toute la tumeur de façon homogène.

En pratique, il existe deux méthodes pour réaliser cette conformation du faisceau à la tumeur. La première est une **mise en forme passive**. Le faisceau est fixe et produit avec une énergie donnée, puis il est modifié par l'insertion d'éléments sur son trajet (modulateur, diffuseurs, collimateur, compensateurs...) qui vont permettre de couvrir tout le volume tumoral. Cette méthode est la plus ancienne et la plus robuste. La deuxième méthode est plus récente et repose sur une **mise en forme active** du faisceau, qui permet de traiter des tumeurs de différentes tailles sans interposer d'accessoires sur le trajet du faisceau. Il s'agit d'un balayage actif (appelée PBS : « pencil beam scanning ») où, grâce à un système électromagnétique, le faisceau très fin balaie latéralement toute la tumeur. Puis, en faisant varier l'énergie du faisceau (et donc la position du pic de Bragg), toutes les couches de la tumeur sont successivement irradiées. Cette méthode est celle qui se développe le plus car elle permet de délivrer des faisceaux d'intensité modulée. Historiquement, le faisceau était horizontal et ne permettait pas d'autre angle d'irradiation du patient. L'apparition de bras isocentrique permet maintenant de choisir cet angle d'irradiation librement de façon similaire aux installations de radiothérapie classique.

Quelle que soit la méthode de délivrance du faisceau hadronique, ce dépôt d'énergie ciblé induit une densité d'ionisations maximale dans les cellules cancéreuses à détruire et permet d'épargner considérablement les tissus sains,

notamment ceux qui se trouvent derrière la tumeur. De ce fait, les effets secondaires généralement observés avec la radiothérapie, aigus ou tardifs, peuvent être considérablement réduits avec l'utilisation de faisceaux de haut TEL. La *figure 3* présente la comparaison de deux traitements photons ou protons pour un patient atteint d'une tumeur intracrânienne (tumeur supra-sellaire). Dans le cas des protons, on note que la distribution de la dose est beaucoup plus adaptée au volume tumoral, avec une réduction considérable de la dose délivrée aux tissus sains, notamment l'isodose verte représentant 50 % de la dose prescrite recouvre beaucoup plus de tissus sains en traitement photons qu'en protons.

Efficacité biologique

Outre leur efficacité balistique, les particules de haut TEL ont également une efficacité biologique supérieure à celle des photons. Les dépôts d'énergie localisés dans le pic ont pour conséquence une augmentation de la complexité des dommages provoqués aux cellules tumorales, notamment à leur ADN. Les lésions multiples, qui sont produites et regroupées localement sous forme de grappes [20-21] sont difficilement réparables [22] et conduisent à une instabilité génomique [23-24] augmentant la probabilité de mortalité cellulaire [25] à l'origine de l'effet thérapeutique.

C'est pour rendre compte de la différence d'efficacité entre les rayonnements à l'échelle cellulaire que l'efficacité biologique relative (EBR) a été introduite (voir *encadré 3*). Selon la position de la cellule cible par rapport au pic de Bragg (et selon les TEL des particules la traversant), la capacité à induire la mort cellulaire est 1,1 à 3 fois supérieure pour les ions carbone que pour les photons [26].

Pour les rayonnements photoniques, la quantité d'énergie déposée n'est pas suffisante pour entraîner la mort et il faut plusieurs trajectoires de faisceaux pour que la cellule accumule les dommages et finisse par mourir. En revanche, pour les ions, la quantité d'énergie déposée augmente et il faut moins de trajectoires pour entraîner la létalité, ce qui se traduit par une augmentation de l'EBR [27]. Une EBR maximale est atteinte quand une seule trajectoire délivre en moyenne assez d'énergie pour tuer la cellule. Les rayonnements à haut

TEL sont donc plus agressifs et permettent ainsi d'éradiquer des tumeurs radiorésistantes pour lesquelles les traitements classiques seraient inefficaces [22]. C'est notamment le cas des tumeurs dites « hypoxiques » où la concentration en oxygène est faible (*encadré 3*), ce qui est un facteur d'échec thérapeutique [28-29]. En effet, dans ce type de tumeur, les faisceaux de photons ou de protons sont trois fois moins efficaces. Cette diminution de l'efficacité est réduite à deux lorsque des ions carbone sont utilisés et disparaît quasiment avec des ions encore plus lourds (comme l'argon). On pourrait associer en partie ces différences au pouvoir de produire de l'oxygène moléculaire avec des TEL élevés à partir de la production primaire du radical superoxyde $O_2^{\cdot-}$, ou de l'eau oxygénée. De plus, le phénomène de stabilisation des radicaux par O_2 a beaucoup moins d'influence dès lors que des dommages produits sont directement létaux, comme en présence de rayonnement de TEL élevé [30-31].

Encadré 3

Efficacité biologique relative et effet oxygène

L'efficacité biologique relative (EBR) d'un rayonnement à haut TEL par rapport au rayonnement de référence (rayons X) se définit comme le rapport des doses nécessaires pour produire un effet biologique identique. Cet effet est en général un taux de survie cellulaire égal à 10 %. L'effet oxygène est aussi appelé OER (« oxygen enhancement ratio »). Il représente le ratio entre la dose nécessaire pour atteindre une même réponse biologique, que l'on soit en présence ou en l'absence d'oxygène. Les particules de haut TEL sont moins sensibles à l'effet oxygène.

Indications

La hadronthérapie présente donc des avantages indéniables. Son efficacité balistique en fait une technique privilégiée pour traiter les tumeurs situées à proximité directe d'organes sensibles comme le tronc cérébral, les nerfs optiques ou la moelle épinière. Il s'agit également d'une technique de traitement particulièrement appropriée pour les cancers pédiatriques car le volume de tissus sains irradiés et la dose totale au patient sont diminués, ce qui limite les toxicités à long terme et le risque de cancer secondaire [28]. D'autre part, son efficacité biologique permet de traiter des tumeurs radiorésistantes pour lesquelles le taux de récurrences et d'échec thérapeutique sont élevés.

À la fin 2018, 190 000 patients avaient été traités avec des protons à travers le monde, 28 000 avec des ions carbone et 3 500 avec d'autres ions [32]. Le Japon et les États-Unis restent les pays les mieux équipés même si la hadronthérapie se développe progressivement à travers le monde, comme illustré en *figure 4*. En France, un troisième centre de traitement a ouvert à Caen en 2018, après ceux de Nice (2016) et Orsay (2010). Dans notre pays, seuls des traitements par protons sont actuellement proposés, et les indications qui font l'objet d'un remboursement par l'assurance maladie sont restreintes aux tumeurs primitives de l'œil, chordomes et chondrosarcomes de la base du crâne et du rachis, ainsi qu'à certaines tumeurs de l'enfant. Les autres indications sont moins consensuelles et font encore l'objet de recherches et de comparaisons [33].

Le principal frein au développement des traitements avec des particules de haut TEL reste la taille et le coût des installations. Les experts ont estimé le coût d'un investissement initial pour un centre de protons entre 40 et 50 millions d'euros,

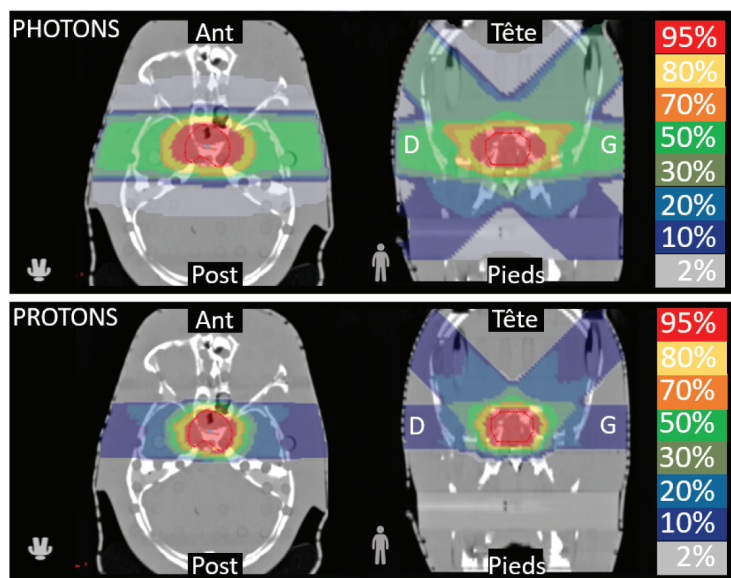


Figure 3 - Comparaison de deux traitements : avec des photons (en haut) et avec des protons (en bas) pour la même tumeur supra-sellaire (crâne) (publié avec l'aimable autorisation de l'Institut Curie, Orsay (CPO)/L. de Marzi).

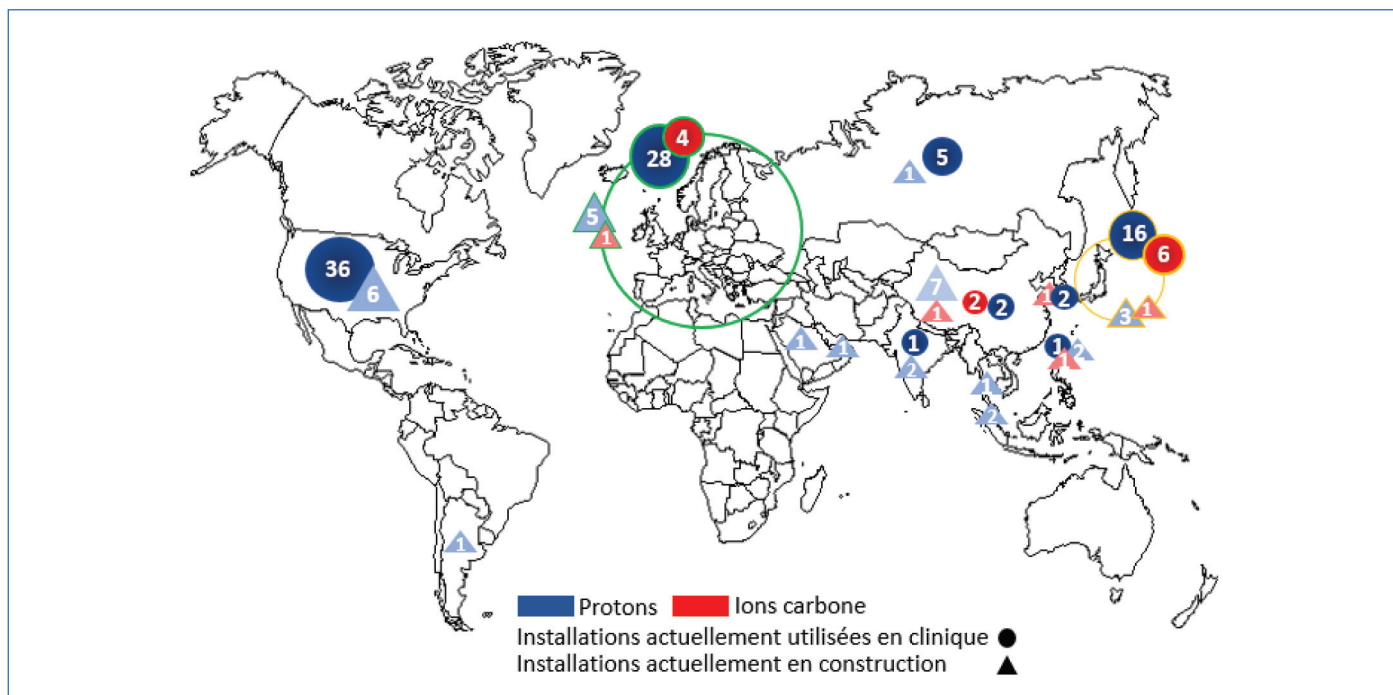


Figure 4 - Installations de hadronthérapie dans le monde (carte établie d'après les données du PTCOG [32]).

c'est-à-dire quatre fois supérieur à celui d'un centre de radiothérapie conventionnel [33]. Les écarts sont encore plus importants lorsqu'il s'agit d'une installation avec des ions carbone.

Enjeux et recherches

La hadronthérapie fait à l'heure actuelle l'objet de nombreuses recherches et développements.

Les interactions nucléaires qui peuvent se produire dans le patient entre le faisceau d'ions (comme les ions carbone) et les tissus biologiques induisent la production de particules secondaires (protons, α ...). Ceci se traduit par une queue de fragmentation après le pic de Bragg (*figure 2*) qui doit être prise en compte dans la planification du traitement du patient. Cependant, la production de rayonnements secondaires suite à la fragmentation ouvre des possibilités majeures dans le développement d'une thérapie guidée par l'image et le contrôle des traitements [34]. L'amélioration de l'imagerie clinique, qui est un des enjeux majeurs, est nécessaire pour contrôler la position du patient en temps réel et pouvoir l'irradier de manière précise. Les mouvements du patient, qu'ils soient fortuits (mouvement involontaire) ou non (respiration, battements cardiaques) provoquent un déplacement de la cible qu'il faut gérer. Les irradiations FLASH, mentionnées précédemment, permettraient de limiter les effets secondaires. La réduction de la taille des faisceaux d'irradiation, avec notamment l'utilisation de faisceaux de protons submillimétriques (minibeams) dix fois plus petits que les faisceaux cliniques actuels, permettrait de préserver davantage les tissus sains tout en assurant un contrôle tumoral équivalent ou supérieur à la protonthérapie conventionnelle [35]. En parallèle, l'intégration des données radiobiologiques (et notamment de l'EBR) dans les modèles des systèmes de planification de traitement constitue une avancée. Enfin, le développement de thérapies combinées, notamment avec les nanoparticules, est un axe de recherche fondamental visant à produire un effet différentiel entre la tumeur et les tissus sains situés à proximité.

L'effet des nanoparticules comme agents théranostiques : radio-amplification et imagerie

Lorsque les tumeurs sont très résistantes, et notamment lorsqu'elles sont très hypoxiques, la hadronthérapie peut ne pas suffire à les éradiquer. L'escalade de dose est limitée par les tissus situés avant la tumeur qui reçoivent une dose non négligeable durant le traitement de la tumeur.

Ainsi, pour amplifier localement l'effet des radiations dans le volume à traiter, une des approches consiste à enrichir les cellules tumorales avec des nanoparticules (NP) constituées d'atomes lourds. Ces composés de matériaux denses (or, gadolinium, platine) sont suivis par imagerie car ils permettent d'augmenter le contraste de la plupart des modalités de diagnostic utilisées en clinique (scanner, IRM...). Le principe radio-amplificateur de ces nanoparticules repose sur une augmentation de l'émission électronique. Suite à leur activation par le rayonnement primaire ou le rayonnement secondaire issu d'ionisations préalables dans le milieu, une désexcitation en cascade s'ensuit, entraînant l'émission de photons de fluorescence et d'électrons secondaires autour de la nanoparticule [36-37].

Une grande partie des électrons émis sont des électrons Auger de basse énergie ($< 1\text{keV}$) [38] issus de la désexcitation des atomes de la nanoparticule que le faisceau chargé avait activée par interaction coulombienne. D'autres processus, comme l'activation plasmonique, peuvent également contribuer à l'émission d'électrons de basse énergie [39]. Ces différentes étapes constituent l'étape physique qui se produit environ 1 femtoseconde après l'interaction du faisceau dans la matière (*figure 5*).

Ces électrons vont interagir avec leur environnement composé d'eau et induire la production de nombreux radicaux. Les nanoparticules ayant perdu de nombreux électrons restent fortement chargées positivement et vont pouvoir également capturer des électrons des molécules d'eau environnantes, entraînant leur dissociation et une

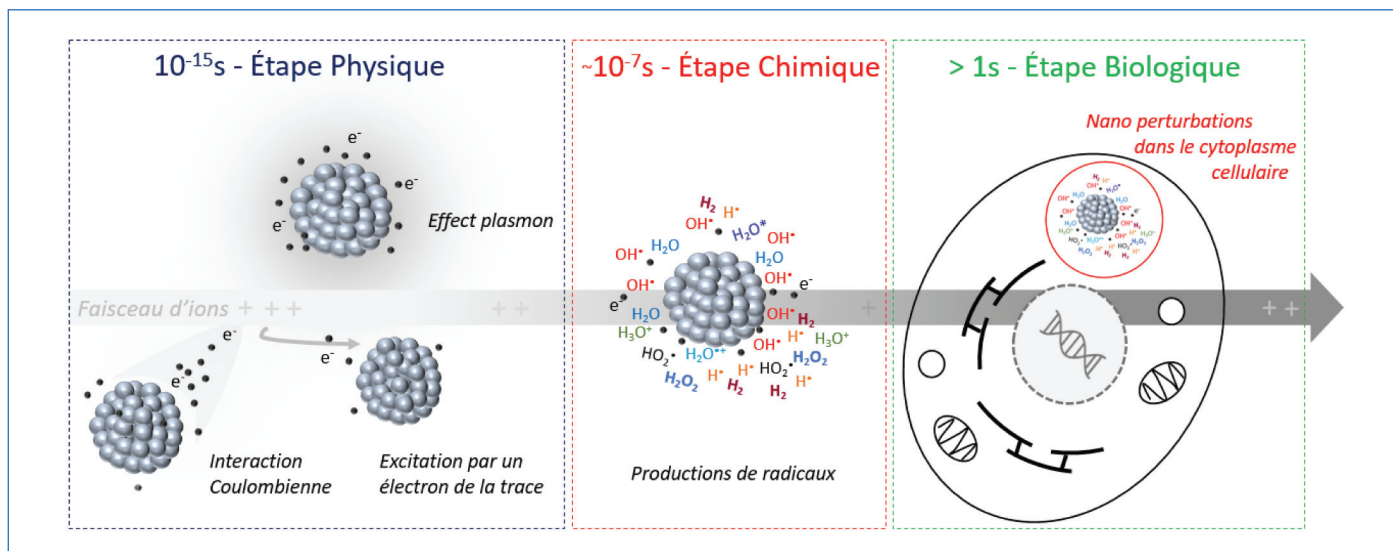


Figure 5 - Déroulé des étapes et des phénomènes intervenant suite à l'interaction d'un faisceau d'ions énergétiques sur une solution aqueuse contenant des nanoparticules métalliques. La production locale de radicaux libres, autour des nanoparticules, est plus importante que dans le solvant seul. Les effets, notamment la radiosensibilisation de la cellule ciblée, sont alors localement amplifiés.

production supplémentaire de radicaux. Ces espèces radicalaires fortement réactives vont créer des dommages biologiques multiples et donc complexes à réparer, dans un volume de quelques nm³ autour de la nanoparticule. Par exemple, la présence de NP de platine peut augmenter de 93 % certains dommages moléculaires provoqués par une irradiation de protons de 150 MeV [40]. La quantification de l'augmentation de la production de radicaux en est encore à un stade très préliminaire, mais une étude récente a montré que l'irradiation alpha d'une faible concentration de NP d'or produisait une radiolyse supplémentaire, traduite par une surproduction de radicaux hydroxyle et d'électrons [30]. Ceci corrobore l'étude pionnière menée par Usami *et coll.* [41-42] qui visait à démontrer le rôle majeur des radicaux de l'eau, et notamment OH[•], dans l'amplification des dommages biologiques produits en présence de complexes de platine, sous irradiation ionique. L'amplification des dommages par trace d'ions était supérieure en fin de parcours, là où le TEL était le plus haut ; une observation également rapportée par Schlathöler *et coll.* en 2016 [40]. Les nanoparticules métalliques sont localisées dans le cytoplasme cellulaire et n'ont jamais été observées dans le noyau [36, 43-44]. L'effet radio-amplificateur des nanoparticules qui se traduit par une augmentation de la mortalité cellulaire est donc initié dans le cytoplasme. Celui-ci est induit par la production d'amas radicalaires capables de provoquer des perturbations dans leur voisinage immédiat et d'induire des dommages cellulaires complexes.

Des essais cliniques prometteurs

La physique des particules, la chimie sous rayonnement et la biologie cellulaire partagent des objectifs communs. Parmi ceux-ci se trouve l'objectif de faire progresser la médecine, notamment dans la lutte contre le cancer, en améliorant la qualité des soins apportés aux malades. La hadronthérapie, qui repose sur des interactions à TEL élevé, se situe à l'interface de ces domaines de recherche. Au cours des dernières années, des progrès considérables ont été accomplis, notamment dans la compréhension des effets du rayonnement sur la matière ou dans l'analyse des mécanismes physico-chimiques impliqués dans la radiolyse de l'eau. Cependant, il reste encore

de nombreux défis, notamment dans la description des effets du TEL le long du parcours des particules. Ceux-ci nécessitent le développement de techniques d'analyse poussées, qui soient résolues spatialement et temporellement, et requièrent en outre des faisceaux de particules très énergétiques. Les efficacités balistique et biologique des hadrons expliquent le développement à travers le monde d'installations cliniques utilisant des protons ou des ions carbone. Ainsi, des dizaines d'essais cliniques sont actuellement réalisés pour démontrer selon les indications la supériorité de la hadronthérapie sur les autres techniques de traitement par rayonnement [45]. En parallèle, les avancées réalisées en termes de délivrance de la dose (thérapies FLASH et minibeam notamment) génèrent de nombreux espoirs pour réduire les effets secondaires du patient et augmenter le contrôle local des tumeurs. Les thérapies combinées, basées sur l'utilisation de nanoparticules métalliques, se développent dans cet objectif, comme en témoignent les différents essais cliniques menés notamment en France, entre autres à Grenoble (métastases cérébrales) et à Villejuif (cancer du col de l'utérus).

Les auteurs remercient l'initiative de Recherche Stratégique NanoTheRad de l'Université Paris-Saclay.

- [1] G. Baldacchino, L'apport des ions accélérés dans l'épopée de la chimie sous rayonnement, *Hist. Rech. Contemp.*, **2017**, 6, p. 47-54, <https://doi.org/10.4000/hrc.2849>
- [2] R.M. Anderson *et al.*, Effect of linear energy transfer (LET) on the complexity of alpha-particle-induced chromosome aberrations in human CD₃₄⁺ cells, *Radiat. Res.*, **2007**, 167, p. 541-50.
- [3] R. Hirayama *et al.*, Contributions of direct and indirect actions in cell killing by high-LET radiations, *Radiat. Res.*, **2009**, 171, p. 212-18.
- [4] A. Ito *et al.*, Contribution of indirect action to radiation-induced mammalian cell inactivation: dependence on photon energy and heavy-ion LET, *Radiat. Res.*, **2006**, 165, p. 703-12.
- [5] A. Appleby, H.A. Schwarz, Radical and molecular yields in water irradiated by γ -rays and heavy ions, *J. Phys. Chem.*, **1969**, 73, p. 1937-41.
- [6] W.G. Burns, R. Barker, Dose-rate and linear energy transfer effects in radiation chemistry, *Radiat. Kinet.*, **1965**, 3, p. 303-68.
- [7] C. Von Sonntag, *The Chemical Basis of Radiation Biology*, Taylor & Francis, **1987**.
- [8] A. Patriarca *et al.*, Experimental set-up for FLASH proton irradiation of small animals using a clinical system, *Int. J. Radiat. Oncol. Biol. Phys.*, **2018**, 102, p. 619-26.
- [9] V. Favaudon *et al.*, Ultrahigh dose-rate FLASH irradiation increases the differential response between normal and tumor tissue in mice, *Sci. Transl. Med.*, **2014**, 6, 245ra93.

- [10] J.W.T. Spinks, R.J. Woods, *An Introduction to Radiation Chemistry*, Wiley, **1990**.
- [11] J.F. Wishart, B.S.M. Rao, *Recent Trends in Radiation Chemistry*, World Scientific Publishing Co., **2010**.
- [12] J.A. LaVerne, Track effects of heavy ions in liquid water, *Radiat. Res.*, **2000**, *153*, p. 487-96.
- [13] G. Baldacchino, Y. Katsumura, Chemical processes in heavy ions track, in *Recent Trends in Radiation Chemistry*, J.F. Wishart, B.S. Madhava Rao, World Scientific, **2010**, p. 231-54.
- [14] G. Baldacchino, Pulse radiolysis in water with heavy-ion beams: a short review, *Radiat. Phys. Chem.*, **2008**, *77*, p. 1218-23.
- [15] S. Yamashita, M. Taguchi, G. Baldacchino, Y. Katsumura, Radiation chemistry of liquid water with heavy ions: steady-states and pulse radiolysis studies, in *Charged Particle and Photon Interactions with Matter. Recent Advances, Applications, and Interfaces*, Y. Hatano, Y. Katsumura, A. Mozumder (eds), CRC Press, Taylor and Francis Group, **2011**, p. 325-54.
- [16] S. Yamashita *et al.*, Water radiolysis with heavy ions of energies up to 28 GeV: 1. Measurements of primary *g* values as track segment yields, *Radiat. Phys. Chem.*, **2008**, *77*, p. 439-46.
- [17] W.H. Bragg, R. Kleeman, XXXIX. On the α particles of radium, and their loss of range in passing through various atoms and molecules, *The London, Edinburgh, and Dublin Philosophical Magazine and Journal of Science*, **1905**, *10*, p. 318-40.
- [18] F.H. Attix, *Introduction to Radiological Physics and Radiation Dosimetry*, Wiley, **1986**.
- [19] T. Kamada *et al.*, Carbon ion radiotherapy in Japan: an assessment of 20 years, *Lancet Oncol.*, **2015**, *16*, p. 93-100.
- [20] Y. Hagiwara *et al.*, 3D-structured illumination microscopy reveals clustered DNA double-strand break formation in widespread γ H2AX foci after high LET heavy-ion particle radiation, *Oncotarget*, **2017**, *8*, p. 109370-81.
- [21] Y. Hagiwara *et al.*, Clustered DNA double-strand break formation and the repair pathway following heavy-ion irradiation, *J. Radiat. Res.*, **2019**, *60*, p. 69-79.
- [22] M. Durante, R. Orecchia, J.S. Loeffler, Charged-particle therapy in cancer: clinical uses and future perspectives, *Nat. Rev. Clin. Oncol.*, **2017**, *14*, p. 483-95.
- [23] E. Sage, N. Shikazono, Radiation-induced clustered DNA lesions: repair and mutagenesis, *Free Radic. Biol. Med.*, **2017**, *107*, p. 125-35.
- [24] M. Durante, F.A. Cucinotta, Heavy ion carcinogenesis and human space exploration, *Nat. Rev. Cancer*, **2008**, *8*, p. 465-72.
- [25] Y. Lorat *et al.*, Nanoscale analysis of clustered DNA damage after high-LET irradiation by quantitative electron microscopy: the heavy burden to repair, *DNA Repair (Amst)*, **2015**, *28*, p. 93-106.
- [26] C. Rodriguez-Lafrasse, J. Balosso, De la trace des ions carbone à l'efficacité thérapeutique de l'hadronthérapie, *Cancer/Radiothérapie*, **2012**, *16*, p. 16-24.
- [27] M. Tubiana, J. Dutreix, A. Wambersie, *Radiobiologie*, Ed. Hermann, **1986**.
- [28] J. Thariat *et al.*, Apports de la protonthérapie à la radiothérapie d'aujourd'hui, pourquoi, comment ?, *Bull. Cancer*, **2018**, *105*, p. 315-26.
- [29] M.R. Horsman, J. Overgaard, The impact of hypoxia and its modification of the outcome of radiotherapy, *J. Radiat. Res.*, **2016**, *57*, p. i90-i98.
- [30] G. Baldacchino *et al.*, Importance of radiolytic reactions during high-LET irradiation modalities: LET effect, role of O₂ and radiosensitization by nanoparticles, *Cancer Nanotechnol.*, **2019**, *10*, 3.
- [31] J. Chapman, A. Reuvers, J. Borsa, C. Greenstock, Chemical radioprotection and radiosensitization of mammalian cells growing in vitro, *Radiat. Res.*, **1973**, *56*, p. 291-306.
- [32] Particle Therapy Co-Operative Group (www.ptcog.ch).
- [33] *Protonthérapie, indications et capacité de traitement*, Institut national du cancer, **2016**.
- [34] V. Reithinger, Assurance qualité des traitements par hadronthérapie carbone par imagerie de particules promptes chargées, Université Claude Bernard-Lyon I, **2015**.
- [35] Y. Prezado *et al.*, Proton minibeam radiation therapy widens the therapeutic index for high-grade gliomas, *Sci. Rep.*, **2018**, 16479.
- [36] S. Lacombe, E. Porcel, E. Scifoni, Particle therapy and nanomedicine: state of art and research perspectives, *Cancer Nanotechnol.*, **2017**, *8*, 9.
- [37] Z. Kuncic, S. Lacombe, Nanoparticle radio-enhancement: principles, progress and application to cancer treatment, *Phys. Med. Biol.*, **2018**, *63*, 02TR01.
- [38] S.J. McMahon *et al.*, Biological consequences of nanoscale energy deposition near irradiated heavy atom nanoparticles, *Sci. Rep.*, **2011**, *1*, p. 1-10.
- [39] K. Haume *et al.*, Transport of secondary electrons through coatings of ion-irradiated metallic nanoparticles, *Eur. Phys. J. D*, **2018**, *72*, 116.
- [40] T. Schlathöler *et al.*, Improving proton therapy by metal-containing nanoparticles: nanoscale insights, *Int. J. Nanomedicine*, **2016**, *11*, p. 1549-56.
- [41] N. Usami *et al.*, Fast He²⁺ ion irradiation of DNA loaded with platinum-containing molecules, *Int. J. Radiat. Biol.*, **2005**, *81*, p. 515-22.
- [42] N. Usami *et al.*, Mammalian cells loaded with platinum-containing molecules are sensitized to fast atomic ions, *Int. J. Radiat. Biol.*, **2008**, *84*, p. 603-11.
- [43] E. Porcel *et al.*, Gadolinium-based nanoparticles to improve the hadrontherapy performances, *Nanomedicine Nanotechnology, Biol. Med.*, **2014**, *10*, p. 1601-08.
- [44] G.J. Sánchez *et al.*, Fluorescent radiosensitizing gold nanoparticles, *Int. J. Mol. Sci.*, **2019**, *20*, 4618.
- [45] K. Bettayeb, Les promesses de l'hadronthérapie, *CNRS Le journal*, **2018**, <https://lejournal.cnrs.fr/articles/les-promesses-de-lhadrontherapie>
- [46] J. Lindhard, A.H. Sorensen, Relativistic theory of stopping for heavy ions, *Phys. Rev. A*, **1996**, *53*, p. 2443-56.
- [47] G. Baldacchino *et al.*, Determination of the time-dependent OH-yield by using a fluorescent probe: application to heavy ion irradiation, *Chem. Phys. Lett.*, **2009**, *468*, p. 275-79.

Pauline MAURY, doctorante, **Erika PORCEL**, maître de conférences, **Sandrine LACOMBE**, professeure, Université Paris-Saclay¹, et **Gérard BALDACCHINO***, ingénieur-chercheur, expert sénior du CEA Paris-Saclay².

¹ Université Paris-Saclay, CNRS, Institut des Sciences Moléculaires d'Orsay.

² Université Paris-Saclay, CEA, CNRS, LIDYL, Gif-sur-Yvette.

*gerard.baldacchino@cea.fr

Congrès SCF2021

28 - 30 juin 2021

Cité des Congrès de Nantes

Chimie, Lumière, Couleur

Week-end Grand Public
au Muséum de Nantes : 26-27 juin 2021

www.scf2021.fr | contact@scf2021.fr

- Ouverture des inscriptions fin novembre 2020
- Date limite de soumission : 15 février 2021

Titre : Evaluation de stratégies thérapeutiques combinées basées sur l'utilisation de rayonnements et de nanoparticules en utilisant un modèle cellulaire 3D

Mots clés : modèle cellulaire 3D ; nanoparticules ; radiations ; hadronthérapie ; ECM ; hypoxie

Résumé : Dans l'arsenal thérapeutique contre le cancer, la radiothérapie (RT) occupe une place majeure. Utilisée pour plus d'un patient sur deux, cette stratégie reste limitée du fait des dommages collatéraux qu'elle induit sur les tissus sains et de la radiorésistance de certains cancers. Des stratégies thérapeutiques alternatives plus performantes sont donc nécessaires. Dans ce contexte, l'utilisation de nanoagents capables d'amplifier l'effet de la RT a été proposée. Leur couplage avec un faisceau d'ions lourds, plus sélectif et plus efficace que les RX conventionnels, constitue une solution aux perspectives intéressantes pour améliorer les traitements. Pour évaluer le potentiel de protocoles anticancéreux, le recours à des modèles précliniques est indispensable. A l'échelle *in vitro*, les cultures cellulaires monocouches sont traditionnellement utilisées mais apparaissent dépassées car elles échouent notamment à prédire l'effet du microenvironnement cellulaire. Le but de ma thèse était d'évaluer l'efficacité de stratégies combinant nanoparticules (NPs) et radiations en utilisant un modèle cellulaire optimisé dans ce but. Ce modèle *in vitro*, établi en trois dimensions (3D) inclut une matrice extracellulaire (ECM) à base de collagène. Un autre avantage majeur du système réside dans le contrôle de la concentration en oxygène à l'intérieur de l'échantillon, permettant de retrouver un niveau similaire à celui des tumeurs normoxiques et hypoxiques.

J'ai d'abord mis au point les méthodes expérimentales permettant de préparer ce modèle de façon reproductible puis une caractérisation a été effectuée grâce à des méthodes de microscopie spécifiques. J'ai montré que des méthodes d'analyse classiques peuvent être employées pour étudier les réponses cellulaires aux traitements. Ce modèle *in vitro* 3D a ensuite été utilisé avec succès dans le cadre d'un essai clinique de traitement basé sur l'utilisation de NPs de Gadolinium (AGuIX®) combinées à de la radiothérapie externe (X - 6 MV) et de la curiethérapie (Y - 380 keV).

Ces travaux montrent que ces NPs amplifient de 15% l'effet des RX (à 1.8 Gy) et de 30% l'effet des Y (à 5.25 Gy). La méthode développée pour quantifier l'enrichissement des NPs dans les tumeurs de patients à partir des images IRM, ainsi que les fractions de survie cellulaire obtenues sont des pré-requis importants au développement de nouveaux outils dosimétriques capables de calculer des distributions de dose en présence de NPs. Une autre stratégie repose sur l'utilisation de nouveaux agents multimodaux, conçus pour administrer des molécules actives de façon ciblée dans la tumeur. Dans le cadre de mes travaux, j'ai évalué l'efficacité de nanoagents organométalliques (MOFs), véritables « nanocages » capables d'incorporer un agent anticancéreux comme la Gemcitabine. Des modèles cellulaires classiques (2D) et optimisés (3D) ont été utilisés pour évaluer l'efficacité de la combinaison de ces agents avec des irradiations par faisceaux d'ions carbone (290 MeV/uma) ou hélium (150 MeV/uma). Ces travaux ont permis de démontrer l'efficacité de cette combinaison, même en conditions hypoxiques, avec une amplification à 2 Gy de 45% à 55% selon le faisceau utilisé. L'utilisation du modèle 3D a par ailleurs permis de mettre en évidence la capacité de ces nanoparticules à migrer au sein de l'ECM et à être internalisées par les cellules. Grâce à ce travail, un nouveau type de nanoagents permettant d'améliorer les performances de la hadronthérapie a été mis en exergue.

Ces travaux ont donc débouché sur l'optimisation d'un modèle *in vitro* 3D dont les caractéristiques permettent de prédire l'efficacité de traitements combinés, dans des conditions plus proches de celles des tumeurs tout en restant facile d'utilisation et reproductible. Il peut ainsi être utilisé en parallèle d'essais précliniques en vue d'évaluer rapidement l'efficacité d'un traitement, ou pour estimer le potentiel de nouveaux nanoagents en développement.

Title : Evaluation of therapeutic strategies based on radiations and nanoparticles using a 3D cell model

Keywords : 3D cell model; nanoparticles; radiations; hadrontherapy; ECM; hypoxia

Abstract : Radiotherapy (RT) plays a crucial role in the therapeutic arsenal against cancer. Used for more than 50% of patients, this strategy remains limited due to the collateral damage induced on healthy tissues and the radioresistance of some cancers. Thus, the development of alternative strategies of treatment remains a great challenge.

In this context, the use of nanoagents capable of amplifying the effect of RT has been proposed. Their combination with particle therapy, which is more selective and more efficient than conventional XR, is a promising solution for improving the performances of cancer treatments. In this perspective, preclinical models are essential to evaluate the potential of new therapeutic strategies. For a rapid and easy evaluation, monolayer cell cultures are commonly used. These models, though, appear outdated as they fail to predict the effects of the cell environment.

Thereby, the goal of my thesis was to evaluate the efficiency of strategies combining nanoparticles (NPs) and radiations using a three-dimensional cell model (3D) composed of an extracellular matrix (ECM) able to better reproduce the microenvironment and tumor features.

A major advantage of the system is the control of the oxygen concentration inside the sample to mimic the oxygenation level in tumors (normoxic and hypoxic).

I first developed the experimental methods to prepare this model and characterize it using specific microscopy methods. Classical methods were employed to quantify cell responses to treatments.

The 3D model was then successfully used to evaluate a new protocol of treatment in parallel to a clinical trial. The treatment consists in the addition of Gadolinium-based NPs (AGuiX[®]) with external radiation (X-rays - 6 MV) and brachytherapy (Y - 380 keV).

This work demonstrated the efficacy of NPs to amplify the effect of X-rays by 15% (at 1.8 Gy) and the effect of Y (at 5.25 Gy) by 30%. The method that we have developed to quantify the enrichment of NPs in the tumor from patients MR images as well as radiobiological results obtained are important prerequisites for the development of new dosimetric tools capable of calculating dose distributions in the presence of NPs. Another strategy of treatment is based on the use of new multimodal agents, designed to deliver and, potentially, control the release of active molecules in tumors. As part of my work, I have evaluated the efficacy of organometallic nano-agents (MOFs), "nanocages" capable of incorporating anti-cancer agents such as Gemcitabin. Classical 2D and new 3D cell models were used to evaluate the efficacy of these agents combined with carbon ions (290 MeV/uma) or helium ions (150 MeV/uma) radiations. This work demonstrated the efficacy under normoxic and hypoxic conditions, with an amplification at 2 Gy of 45% to 55% depending on the irradiation beam. Thanks to the 3D model, it was also established that these new NPs migrate through the ECM and penetrate into the cells. Finally, this work highlighted a new type of nanoagent that improves the performances of particle radiation treatment.

In summary, this work resulted in to the production of a 3D *in vitro* model whose characteristics allow predicting the effectiveness of combined treatments under conditions closer to those of tumors while remaining easy to use and reproducible. It can be used in parallel with preclinical trials to rapidly assess the efficacy of a treatment or to estimate the potential of new nanoagents.